Christian Timo Poppe

Process simulation of wet compression moulding for continuous fibre-reinforced polymers

Christian Timo Poppe

Process simulation of wet compression moulding for continuous fibre-reinforced polymers

Process simulation of wet compression moulding for continuous fibre-reinforced polymers

by
Christian Timo Poppe

SKIT Scientific Publishing

Karlsruher Institut für Technologie
Institut für Fahrzeugsystemtechnik

Process simulation of wet compression moulding
for continuous fibre-reinforced polymers

Zur Erlangung des akademischen Grades eines Doktors der
Ingenieurwissenschaften von der KIT-Fakultät für Maschinenbau des
Karlsruher Instituts für Technologie (KIT) genehmigte Dissertation

von Christian Timo Poppe, M.Sc.

Tag der mündlichen Prüfung: 15. Oktober 2021
Referentin: Dr.-Ing. Luise Kärger (KIT)
Korreferent 1: Prof. Philippe Boisse (INSA Lyon)
Korreferent 2: Prof. Dr.-Ing. Frank Henning (KIT)

Abstract

Interdisciplinary development approaches for system-efficient lightweight design unite a comprehensive understanding of materials, processes and methods. This applies particularly to continuous fibre-reinforced plastics (CoFRPs), which offer high weight-specific material properties and enable load path-optimised designs.

This thesis is dedicated to understanding and modelling Wet Compression Moulding (WCM) to facilitate large-volume production of CoFRP structural components. WCM combines simultaneous infiltration and draping during processing, allowing for comparatively low cavity pressures ($<$ 20 bar) and short cycle times ($<$ 3 min).

In this regard, the first part of this work (cf. Chapter 2) focuses on a systematic analysis of the relevant physical process mechanisms. The first experiments using a transparent tool allow for in-situ visualisation of the flow front progression during moulding. The trials demonstrate a strong interdependence between draping and infiltration during processing. Although relevant, current modelling approaches cannot capture this interaction of local deformation and anisotropic fluid propagation sufficiently.

The second part (cf. Chapter 3) is dedicated to systematically evaluating the impact of low-viscous infiltration on the deformation mechanism. Novel and modified test benches are developed in order to investigate dry and infiltrated membrane, bending, compaction and contact behaviour. The trials show that infiltration with a low-viscous matrix significantly reduces friction between and within the rovings leading to reduced shear resistance, bending stiffness, and tangential contact stresses. This improves drapeability allowing for more complexly shaped parts. Conversely, infiltration further induces rate-dependency, which can diminish drapability at higher viscosities and processing speeds. Moreover,

i

the relevance of these experimental findings for process modelling is evaluated through hyper- and hypoviscoelastic material formulations validated on a complex demonstrator. Investigating the deformation mechanism shows that the infiltrated material state should be considered to describe membrane and bending behaviour. Moreover, it becomes apparent that a modelling of the compaction in the thickness direction and an accurate prediction of local fibre volume content are essential for WCM modelling.

A monolithic fully-coupled simulation approach for combined textile forming and resin infiltration is proposed in the third part of this thesis (cf. Chapter 4), utilising the equivalence of Fourier's law for heat conduction and Richard's law for porous media throughflow. The process model is based on modular superimposed finite elements representing a single textile layer. Usage of continuum shells allows for a three-dimensional material formulation, which makes non-linear compaction during forming considerable. A user-developed superimposed fluid element (user-element) describes the three-dimensional resin propagation considering the current deformation state and the local fibre orientation. In this manner, a fully-coupled analysis in ABAQUS/EXPLICIT is employed for a mutual explicitly formulated solution of deformation and pressure field. Comparison with experimental trials demonstrate an accurate prediction of textile forming and simultaneous infiltration within a single simulation run.

Finally, the inherent Fluid-Structure Interaction (FSI) in WCM can cause additional undesired process defects such as flow-induced fibre displacement (FiFD). This can have severe negative impacts on the infiltration behaviour and the structural properties of the final part (cf. Chapter 5). Since existing analytical solutions are not sufficient, a numerical prediction of FiFD is investigated in the last chapter of the work. For this purpose, a bilateral FSI is implemented and validated using Terzaghi's effective stress approach. A comparison with planar experimental results from literature show a good prediction of FiFD during WCM.

Conclusively, the results of the thesis support a time- and cost-efficient process and product design at an early stage. The outcomes underline the applicability and validity of the developed methods. However, they likewise indicate the scope for further development. Particularly an implementation of heat transfer and curing are worthwhile additions towards a comprehensive process model.

Kurzfassung

Entwicklungsansätze für den systemeffizienten Leichtbau vereinen Werkstoff-, Prozess- und Methodenverständnis. Dies gilt im Besonderen für endlosfaserverstärkte Kunststoffe (FVK), die hohe gewichtsspezifische Materialeigenschaften bieten und lastpfadoptimierte Konstruktionen ermöglichen. Diese Dissertation widmet sich dem Verständnis und der Modellierung der Nasspresstechnologie, um die Groß-serienproduktion von endlosfaserverstärkten Strukturbauteilen zu unterstützen. Nasspressen kombiniert gleichzeitiges Drapieren und Infiltrieren während der Verarbeitung, was vergleichsweise geringe Werkzeuginnendrücke ($<$ 20 bar) und Zykluszeiten ($<$ 3 min) ermöglicht.

Der erste Teil dieser Arbeit (siehe Kapitel 2) fokussiert sich auf eine systematische Analyse der relevanten, physikalischen Prozessmechanismen. Versuche mit einem transparenten Werkzeug ermöglichen eine in-situ-Visualisierung des Fließfrontverlaufs während der Formgebung. Die Versuche verdeutlichen die starke Wechselwirkung zwischen Drapierung und Infiltration während der Verarbeitung. Diese Wechselwirkung wird durch herkömmliche, sequenzielle Modellierungsansätze nicht erfasst.

Der zweite Teil (siehe Kapitel 3) widmet sich der Bewertung des Einflusses der niedrigviskosen Infiltration auf relevante Deformationsmechanismen. Hierzu werden neuartige und modifizierte Prüfstände verwendet, um das trockene und infiltrierte Membran-, Biege-, Kompaktierungs- und Kontaktverhalten zu untersuchen. Die Ergebnisse zeigen, dass die Infiltration mit einer niedrigviskosen Matrix die Reibung zwischen und innerhalb der Rovings signifikant verringert, was direkt auch die Scherfestigkeit, Biegesteifigkeit und tangentiale Kontaktspannungen reduziert. Die verbesserte Drapierbarkeit ermöglicht komplexere Bauteilgeometrien. Jedoch induziert die Infiltration auch eine Ratenabhängigkeit,

die die Umformbarkeit des Textiles bei höheren Viskositäten und Verarbeitungs-geschwindigkeiten gleichermaßen verschlechtern kann. Die Relevanz dieser experimentellen Erkenntnisse für die Prozessmodellierung werden anhand von Modellen bewertet und abschließend an einem komplexen Demonstrator validiert. Simulationen zeigen, die Infiltration sollte bei der Beschreibung des Membran- und Biegeverhaltens berücksichtigt werden. Die Kompaktierung ist zudem für eine genaue Vorhersage des lokalen Faservolumengehalts entscheidend. Demgegenüber ist eine herkömmliche Kontaktmodellierung zwischen Halbzeug und Werkzeug ausreichend, da nur relativ geringe Spannungen auftreten.

Im dritten Teil dieser Arbeit (vgl. Kapitel 4) wird ein monolithischer Simulationsansatz für die kombinierte Textilumformung und Harzinfiltration entwickelt, der auf der Äquivalenz des Fourierschen Gesetzes für die Wärmeleitung und des Richardschen Gesetzes für die Durchströmung eines porösen Mediums beruht. Das Prozessmodell basiert auf überlagerten finiten Elementen zur Beschreibung der Einzelschicht. Die Verwendung von Kontinuumsschalen ermöglicht eine Berücksichtigung der Kompaktierung während der Umformung. Ein entwickeltes Fluid-Element (User-Element) beschreibt die dreidimensionale Harzausbreitung unter Berücksichtigung des aktuellen Verformungszustandes und der Faserorientierung. Auf diese Weise wird eine vollständig gekoppelte Analyse in ABAQUS für eine gemeinsame explizit formulierte Lösung von Verformungs- und Druckfeld genutzt. Der experimentelle Vergleich zeigt eine gute Vorhersagegüte.

Die inhärente Fluid-Struktur-Interaktion (FSI) im Nasspressen kann zu unerwünschten Prozessdefekten wie strömungsinduzierter Faserverschiebung (eng: FiFD) führen. Dies kann negative Auswirkungen auf Infiltration und strukturellen Eigenschaften des fertigen Bauteils haben. Im letzten Kapitel der Arbeit wird die numerische Vorhersage von FiFD untersucht (siehe Kapitel 5). Zu diesem Zweck wird ein beidseitige FSI implementiert und validiert. Ein Vergleich mit experimentellen Ergebnissen zeigt eine gute Vorhersagegüte von FiFD während der viskosen Kompaktierung.

Die Erkenntnisse dieser Arbeit unterstützen eine frühzeitige zeit- und kosteneffiziente Prozess- und Produktgestaltung. Die Ergebnisse verdeutlichen die Anwendbarkeit und Validität der entwickelten Methoden. Sie zeigen aber gleichermaßen wichtige Forschungs- und Implementierungsfelder wie Wärmetransport und Aushärtung auf.

Danksagung

Diese Arbeit entstand während meiner Tätigkeit als wissenschaftlicher Mitarbeiter am Institut für Fahrzeugsystemtechnik (FAST), am Institutsteil für Leichtbautechnologie, des Karlsruher Institut für Technologie (KIT) und in enger und vertrauensvoller Kooperation mit dem Fraunhofer Institut für Chemische Technologie (ICT). Die in dieser Arbeit dargestellten Forschungsergebnisse entstand im Rahmen der folgenden Forschungsprojekte:

Besonderer Dank gilt meiner Betreuerin Frau Dr.-Ing. Luise Kärger. Durch ihre offene, direkte und hoch motivierte Leitung des Institutsteils für Leichtbautechnologie, sowie durch ihre fachliche Expertise wurden die hier dargestellten Ergebnisse erst ermöglicht. Das von ihr geschaffene produktive, großartige Arbeitsklima am Institut erlaubt wissenschaftliches Arbeiten und Forschen auf

höchstem Niveau. Ihr kritisches Feedback und ihre Ansprechbarkeit haben über die Jahre maßgeblich zur meiner persönlichen und der inhaltlichen Entwicklung der Arbeit beigetragen.

Ebenso danke ich Herrn Prof. Philippe Boisse für die Übernahme des ersten Korreferats. Es ist mir eine große Ehre, einen international anerkannten Experten auf dem Gebiet der Umformsimulation für Faserverbundhalbzeuge als Teil meiner Prüfungskommission gewonnen zu haben.

Darüber hinaus danke ich Prof. Dr.-Ing. Frank Henning für die Übernahme des zweiten Korreferats. Nur durch den von ihm geschaffenen interdisziplinären und institutsübergreifenden Forschungsverbund konnte diese Arbeit in enger Kooperation mit dem Frauenhofer ICT gelingen. Für die vertrauensvolle Zusammenarbeit in den Themen Werkstoffcharakterisierung, Prozessentwicklung und Industriekooperation bedanke ich mich herzlich.

Weiterhin bedanke ich mich bei meinen großartigen Kollegen, Studierenden und Freunden vom Institutsteil für Leichtbautechnologie, Institut für angewandte Materialen – Werkstoffkunde (IAM-WK) und dem Fraunhofer ICT für die herausragende Unterstützung und eine unglaublich angenehme Zusammenarbeit bedanken. Namentlich danke ich Dominik Dörr, Fabian Albrecht, Clemens Zimmerling, Constantin Krauß, Bastian Schäfer, Siegfried Galkin, Julian Seuffert, Nils Mayer und Sarah Müller, welche mit vielen guten Anregungen, Diskussionen und ihrem Fachwissen entscheidend unterstützt haben.

Der abschließende Dank gebührt meiner tollen Familie, namentlich meinen Eltern Martin Poppe und Ulrike Poppe, sowie meinem Bruder Johannes Poppe, ohne deren beständige Unterstützung ich dies nie hätte erreichen können. Außerdem bedanke ich mich herzlichst bei geschätzten Freunden und Freundinnen für die tollen Zeiten und Diskussionen. Dies gilt im Besonderen meiner lieben Katja. Danke für die liebevolle Unterstützung der letzten Jahre.

Karlsruhe,
Dezember 2021

Christian T. Poppe

Contents

Acronyms and nomenclature

Acronyms

1D, 2D, 3D	One-, two, three-dimensional
BC	Boundary condition
BET	Bias-extension test
BJS	Beavers-Joseph-Saffman interface condition
CAE	Computer-aided Engineering
CEL	Eulerian Lagrangian Method
CF	Carbon fibre
CIP	Carrier-integrated processing
CoFRP	Continuous fibre-reinforced polymers
CoFRTP	Continuous fibre-reinforced thermoplastics
CoF	Coefficient of Friction
COS	Coordinate system (Frame)
CRTM	Compression Resin Transfer Moulding
CV	Control Volume
DIC	Digital Image Correlation
DPE2D	Darcy-Progression-Element with 2D formulation
DPE3D	Darcy-Progression-Element with 3D formulation
DSC	Differential Scanning Calorimetry

FE/CV	Finite Element with additional Control Volume
FEA	Finite Element Analysis
FEM	Finite Element Method
FiFD	Flow-inducted fibre displacement
FSI	Fluid-Structure-Interaction
FV	Finite Volume
FVC	Fibre volume content (in equations ϕ)
IP	Integration point
HPRTM	High Pressure Resin Transfer Moulding
IBET	Infiltrated bias-extension test
KES	Kawabata bending test
LCA	Life Cycle Assessment
LCM	Liquid Compression Moulding
M3D3	Triangular membrane element in ABAQUS
NCF	Non-crimped fabric
OAT	Off-axis tension test
PF	Picture frame
PP	Ply-Ply interface
RBT	Rheometer bending test
RTM	Resin Transfer Moulding
(S)RVE	(Statistical) Representative Volume Element
S3R	Triangular reduced integrated shell element in ABAQUS
SC6R	Reduced integrated continuum shell element (SC) in ABAQUS
TP	Tool-Ply interface
UD	unidirectional

VARI	Vacuum-assisted Resin Injection
VD	Finite Differences
WCM	Wet Compression Moulding
WF	Woven fabric

Applied subroutines in ABAQUS/EXPLICIT

VUMAT	User-defined material behaviour
VUGENS	User-defined bending behaviour
VUINTERACTION	User-defined contact behaviour
VUEXTERNALDB	User-defined runtime operations and information exchange
VUFIELD	User-defined node-based operations
VUSFLD	User-defined integration point-based operations
VUEL	User-defined finite elements

Scalar symbols

Latin

a	In-plane anisotropy ratio of $\boldsymbol{K}$
$a_{\mathrm{con},i}$	Contact state flag at every proximity point i
$A_1^{(i)}$	Current area of surface i
A^{el}	Element area (2D elements)
A_{sl}	Sledge contact area
b	Specimen width
B_i	Elastic bending stiffness
$B_{\mathrm{w}}^{\mathrm{Can}}$	Width-normalised cantilever bending stiffness

c_p	Heat capacity
$c_\mathrm{t,con}$	Tangential penalty contact stiffness
$c_\mathrm{N}^\mathrm{P}, c_\mathrm{N}^\mathrm{T}$	Penalty stiffness during normal pressure/tension (contact)
C_hyd	Hydraulic capacity
$C_\mathrm{s}^{(n)}$	Averaged contact state $[-1, 1]$ at interface
$d_\mathrm{t,con}$	Tangential penalty contact damping
d_s	Shear damping
$d_\mathrm{N}^\mathrm{P}, d_\mathrm{N}^\mathrm{T}$	Contact damping during normal pressure/tension
$E_{\mathrm{f},i}$	Fibre moduli
$E_{\mathrm{f},i}^\mathrm{init}$	Initial fibre moduli
$E_{\mathrm{f},i}^\mathrm{end}$	Maximal fibre moduli
E_3^Mat	Modelled part of the thickness modulus during compaction
E_3^Lock	Additional material locking modulus during compaction
E_3^lim	Final locking modulus during compaction
E_0^SC	Base stiffness of the continuum shell element in $\boldsymbol{e}_3$
f	Point force
$f_\mathrm{T,3}^\mathrm{max}$	Maximal tacking force (contact)
f_raw	Measured raw force (Tensile testing machine)
f_shear	Measured shear-related reaction force
f_fric	Frictional forces in bearings
f_fluid	Fluid-induced forces
f_comp	Compaction forces in $\boldsymbol{e}_3$
F_g	Length-related weight force of the specimen
g_z	Z-component of gravity vector $\boldsymbol{g}$
G_{12}	In-plane shear module

h	Ply thickness
h_{cav}	Cavity height
h_{rim}	Flow channels height
h_{exo}	Specific reaction enthalpy
i, j, n, m, l, k	Frequently used indices
I_i	Set of N invariants $i = [1, N]$
$I_{12}^{\text{e,init}}, I_{12}^{\text{e,mid}}, I_{12}^{\text{e,lock}}$	Parameter for invariant-based membrane model
J	Jacobian matrix
k_k^{P1}	Polynomial coefficients of P1 with $k = [1, 3]$
k_l^{P2}	Polynomial coefficients of P2 with $l = [1, 4]$
K_{f1}	Permeability in weft direction (woven fabric, fibre frame)
K_{f2}	Permeability in warp direction (woven fabric, fibre frame)
K_3	Permeability in thickness direction
K_f	Permeability in fibre direction (UD-NCF)
$K_\perp$	Permeability perpendicular to fibre orientation (UD-NCF)
K_{11}^0	Undeformed permeability in weft direction (woven fabric)
K_{22}^0	Undeformed permeability in warp direction (woven fabric)
K_r	Permeability in radial direction
l_{bend}	Bending length during cantilever
L	Total edge length
m_{sl}	Sledge weight
m_{prox}	Proximity point number associated with the current salve node
M	Bending moment
M_0	Initial threshold bending moment

p	Fluid pressure
p_{inj}	Injection pressure
$p_k^{(N)}$	Nodal pressure at node N of every element k
p_{N}	Normal contact pressure
r	Point heat source
r_{ff}	Flow front position (radial)
r_{inj}	Injection radius
r_N^{Scan}	Scanning radius for node N (interface flows)
$r_{i,\text{MP}}^{\text{Scan}}$	Scanning radius for element midpoint i (interface flows)
R_{bend}	Bending radius
$R_{2,\varGamma}$	Yield surface for coupling $\varepsilon_\perp$ and γ_{12} (UD-NCF)
$R_{12,\varGamma}$	Yield curve for shearing (UD-NCF)
s	Curvilinear coordinate of the spline (edge)
S	Saturation
S_k	Saturation of element k
$S_{\theta,\tau}$	Scale factor for tangential contact stress
t	Time
t_{inj}	Injection time
t_{soak}	Soaking time before processing
T	Temperature
T_g	Glass transition temperature
u_{raw}	Measured raw displacement
u_{comp}	Measured displacement during compaction
$u_{\text{comp,ply}}$	Measured displacement per ply during compaction
$u_\perp$	In-plane disp. perpendicular to fibre orientation (UD-NCF)

u_{T}	Tool displacement
$\dot{u}_{\mathrm{T}}$	Tool velocity
$\dot{V}^{(i)}_{\mathrm{flow},k}$	Flow rate at each surface i of every element k
v_{Fluid}	Fluid velocity
$V_{k,1}$	Current element volume
V_k^{void}	Void volume of each element k
V_k^{fluid}	Fluid volume of each element k
V_k^{fibre}	Fibre volume of each element k
$V_{k,\mathrm{fluid}}^{+}$	Local fluid overflow volume of each element k
$w_{\mathrm{A},0}$	Measured areal weights in undeformed state
$w_{\mathrm{A}}^{\gamma_{12}}$	Measured areal weights at different shear states
w_{sp}	Width of the bended specimen
$y_{\mathrm{state}}^{\mathrm{mem}}$	Membrane state in each element
W_{diss}	Dissipation energy
x_{ff}	Flow front position (linear)
$x_{\mathrm{Loc},i}$	Strip position i along the specimen

Greek

α	Degree of cure
α_{max}	Maximal reachable degree of cure
$\alpha_{\varGamma}$	Drag coefficient for interface slip
β_{rot}	Ellipse rotation angle
β_0^{+}, β_1^{+}	Penalty parameter for pressure field modification
γ_{12}	In-plane shear angle
γ_1	Angle between $\boldsymbol{X}_1$ and $\boldsymbol{f}_1$

γ_2	Angle between $\boldsymbol{X}_2$ and $\boldsymbol{f}_2$
$\gamma_{12,\text{lock}}$	In-plane locking angle
$\dot{\gamma}_{12}$	In-plane shear rate
$\dot{\gamma}_{\text{eq}}$	Scalar equivalent of the deformation rate
Γ_{porous}	Domain interface
$\varepsilon_{\text{f},1}$	Strain in weft direction (woven fabric)
$\varepsilon_{\text{f},2}$	Strain in wrap direction (woven fabric)
$\varepsilon_\perp$	In-plane strain perpendicular to fibre orientation (UD-NCF)
ε_3	Compressive strain
$\varepsilon_{\text{I-III}}$	Material parameter for compaction behaviour
$\varepsilon_{3,\text{s}}^{\text{lim}}$	Start compression strain for locking
$\varepsilon_{3,\text{e}}^{\text{lim}}$	End compression strain for locking
η	Viscosity
η_{PP}	Contact viscosity (Ply-Ply)
η_{D}	Bending viscosity
$\eta_{\text{t,con}}$	Tangential contact viscosity (Cross model parameter: μ_0, μ_∞, m, n)
θ	Relative fibre angle at interface
Θ_{S}	Stokes domain
Θ_{D}	Darcy domain
Θ_{fill}	Filling domain boundary
Θ_{sat}	Saturated domain boundary
κ_{11}^{TS}	Transverse shear stiffness in weft direction
κ_{22}^{TS}	Transverse shear stiffness in warp direction
κ_{12}^{TS}	In-plane transverse shear stiffness
$\dot{\kappa}$	Curvature rate

$\bar{\kappa}^{\mathrm{el}}$	Averaged mean curvature
μ_{TP}	Coefficient of friction (Tool-Ply)
μ_{PP}	Coefficient of friction (Ply-Ply)
$\mu_{\mathrm{t,con}}$	Contact CoF
ξ_3	Normal contact distance
$\xi_{\mathrm{T},3}^{\max}$	Displacement at maximal tacking force
ξ_3^{TT}	Normal contact tracking thickness
ρ	Density
τ	Tangential contact stress
τ_{crit}	Tangential contact yield stress (user-defined contact)
$\tau_{+1,0,-1}^{\max}$	Center and factor levels for maximal tangential (built-in contact)
ϕ_{can}	Cantilever plate angle
Φ_{set}	Level set function
ϕ	Fibre volume content (FVC)
φ	Porosity
Φ	Isotropic contact yield function (sliding)
ψ	Stored strain energy function
ω	Deflection angle
$\dot{\omega}$	Deflection rate

Vector symbols (1st order)

Latin

$\boldsymbol{b}_{\mathrm{grav}}^{\mathrm{vec}}$	Fluid body force vector due to gravity
$\boldsymbol{f}$	External body forces

$\boldsymbol{f}_\text{d}$	Viscous drag forces (FSI)
$\boldsymbol{f}_\text{g}$	Gravity-induced drag forces (FSI)
$\boldsymbol{f}_\text{p}$	Pressure-induced drag forces (FSI)
$\boldsymbol{g}$	Gravity
$\boldsymbol{M}_\text{sec}$	Section moments
$\boldsymbol{n}$	Outward normal surface vector
$\boldsymbol{N}_\text{sec}$	Section forces
$\boldsymbol{N}$	Normal contact forces
$\boldsymbol{p}_k^\text{vec}$	Nodal pressure vector
$\boldsymbol{r}^\text{diff}$	Nodal diffusive flux vector
$\boldsymbol{S}^\text{+,vec}$	Nodal source vector for pressure modification
$\boldsymbol{t}$	Tangential surface vector
$\boldsymbol{t}_{\text{seg},i}$	Line segment with $i = [1, 2]$
$\boldsymbol{T}$	Tangential contact forces
$\boldsymbol{u}$	Displacement
$\boldsymbol{v}_\text{D}$	Macroscopic fluid velocity (Darcy)
$\boldsymbol{v}_\text{f}$	Fluid velocity
$\boldsymbol{v}_\text{s}$	Solid velocity
$\boldsymbol{Z}$	Combined contact forces

Greek

$\boldsymbol{\xi}_t$	Tangential in-plane contact slip with $t = [1, 2]$

Tensor symbols (2nd and higher order)

Latin

$\boldsymbol{B}$	Operator matrix based on the shape functions
$\boldsymbol{C}$	Right Cauchy-Green deformation
$\mathbb{C}$	Stiffness tensor
$\boldsymbol{D}$	Rate-of-deformation
$\boldsymbol{E}$	Green-Lagrange strain
$\boldsymbol{f}_{\text{R}}$	Nodal reaction force matrix
$\boldsymbol{F}$	Deformation gradient
$\boldsymbol{G}$	Metric coefficients
$\boldsymbol{I}$	Unit tensor
$\boldsymbol{J}$	Jacobian matrix
$\boldsymbol{K}$	Permeability
$\boldsymbol{M}^{\text{mass}}$	Mass matrix
$\boldsymbol{N}_{\text{shape}}$	Linear shape function matrix
$\boldsymbol{P}^{*}$	Nominal stress tensor
$\boldsymbol{R}$	Orthogonal rotation tensor
$\boldsymbol{S}$	2nd Piola-Kirchhoff stress
$\boldsymbol{U}$	Right stretch tensor

Greek

$\boldsymbol{\varepsilon}$	Logarithm strain
$\boldsymbol{\lambda}$	Heat conduction
$\boldsymbol{\sigma}$	Cauchy stress
$\boldsymbol{\tau}$	Kirchhoff stress

Coordinate frames and configurations

Note. For the 2D case applies $i, j = [1, 2]$ and for the 3D case $i, j = [1, 3]$.

$\mathscr{B}_0$	Initial (reference) configuration
$\mathscr{B}_1$	Current configuration
$\{\boldsymbol{e}_i\}$	Orthogonal Green-Naghdi's frame
$\{\boldsymbol{f}_i\}$	Non-orthogonal principal material frame
$\{\boldsymbol{g}^i\}$	Covariant non-orthogonal frame
$\{\boldsymbol{g}_j\}$	Contravariant non-orthogonal fram
$\{\boldsymbol{x}_{\mathrm{rot},i}\}$	Rotated, orthogonal ellipse frame
$\{\boldsymbol{X}_i\}$	Fixed, orthogonal assembly COS on ABAQUS
$\{\boldsymbol{\varsigma}_i\}$	Isoparametric element configuration
$\{\boldsymbol{\xi}_i\}$	Orthogonal contact COS at proximity point

Operators, math symbols and additional notations

$\mathrm{div}(\bullet)$	Divergence
$\mathrm{grad}(\bullet)$	Gradient
$\mathrm{det}(\bullet)$	Determinant of a matrix
$\mathrm{tr}(\bullet)$	Trace
$(\bullet)^{\top}$	Transpose of a matrix, e.g. $A_{ij}^{\top} = A_{ji}$
$(\bullet)^{-1}$	Inverse of a matrix
$\cdot$	Single contraction, e.g $(\boldsymbol{A} \cdot \boldsymbol{B})_{ijkl} = A_{ij} B_{jk}$
$:$	Double contraction, e.g. $(\boldsymbol{A} : \boldsymbol{B})_{ijkl} = A_{ij} B_{ij}$
$\otimes$	Dyadic product, e.g. $(\boldsymbol{A} \otimes \boldsymbol{B})_{ijkl} = A_{ij} B_{kl}$
$(\bullet)^{\circ}$	Volumetric part

$(\bullet)^{\text{dev}}$	Deviatoric part
$(\bullet)^{*}$	Normalised by norm
$\dot{(\bullet)}$	Material time derivative
$(\bullet)'$	First order spatial derivative
$(\bullet)''$	Second order spatial derivative
$\lvert\bullet\rvert$	Absolute value
$\lVert\bullet\rVert$	Euclidean tensor norm
$\bar{\bullet}$	Averaged quantity
$\tilde{\bullet}$	Voigt notation
$\hat{\bullet}$	With respect to ABAQUS' Green-Naghdi's frame $\{e_i\}$
$\bullet^{\text{e}}$	Elastic part
$\bullet^{\text{v}}$	Viscous part
$\bullet^{\text{p}}$	Plastic part
$\bullet^{0}$	In undeformed reference configuration/state
$\triangle\bullet$	Incremental value during explicit time integration

Clarifications. The term 'pre-infiltrated' or 'infiltrated' is consistently used throughout this thesis to address a fully-infiltrated material from micro- to macro-scale. In this work, the term 'weak FSI' describes a one-sided coupling between fabric deformation and fluid progression where only the current deformation affects the pressure field, but not vice versa. In this regard, a 'strong FSI' addresses a both-sided coupling.

1 Introduction

This chapter motivates the presented thesis (cf. Section 1.1) and provides an overview of the related literature (cf. Section 1.2). Subsequently, the main objectives are defined (cf. Section 1.3). This chapter concludes with an outline of this thesis (cf. Section 1.4) and the applied material in Section 1.5.

1.1 Motivation

Lightweight design is a development strategy, which aims to realize functionality through a system of minimum mass while ensuring its reliability. Therefore, it implies a holistic development strategy to enhance the system's efficiency through the combined optimal use of material, process and joining innovations [1, 2]. When focusing on composite materials, it becomes particularly evident that a comprehensive approach is required. These materials provide exceptionally high lightweight potential due to their excellent weight-specific material properties and their capability to be tailored to specific applications. However, they also pose high requirements for product and process design, both economically and technically [3].

While the aerospace industry successfully applied high-performance composite materials for years [4], the automotive sector still primarily uses traditional materials such as steel and discontinuous glass fibre-reinforced composites [5]. This difference originates from different requirements in

the respective industries. In the aerospace industry, smaller quantities and reduced part complexity, compared to the automotive industry, limit the necessary investments for manufacturing processes. Moreover, minimised aircraft downtime increases weight-reduction benefits, thereby compensating the initially higher material prices of high-performance composite materials.

Compared to the aerospace industry, similar lightweight construction achievements are harder to accomplish within the automotive industry. First, the intense price competition dominates material selection. Second, low scrap rates and high throughput rates require robust manufacturing processes. Besides, the demanding transition of the automotive industry towards more sustainable mobility involves high levels of investments, which only partially benefit lightweight construction [6, 7]. Additionally, life cycle assessment (LCA) and economically affordable recycling concepts for composite applications are necessary for providing sustainable lightweight composite solutions for the future [8, 9]. Besides, high growth potential is forecasted [10] for composite materials within the automotive sector if critical success factors such as structural reliability, robust process technology and continuous design concepts are implemented [7].

Among composite materials, continuous fibre-reinforced polymers (Co-FRP) provide the highest lightweight potential. The automotive industry demands low cycle times, which, for thermoset-based CoFRPs, can only be achieved via Resin Transfer Moulding (RTM) or Wet Compression Moulding (WCM). Here, cycle times between 1.5 and 3 minutes can already be achieved by a combination of dry engineering textiles/fabrics and fast curing resin systems [2, 9, 11]. Alternatively, continuous fibre-reinforced thermoplastics (CoFRTP) are gaining importance due to low cycle times, material efficiency and recyclability [3]. They are produced from tape-layed, pre-infiltrated and pre-consolidated stacks, which are pre-heated and thermoformed.

CoFRTP are well suited for structural components [12]. Nevertheless, full exploitation of the existing lightweight potential of this material class can only be achieved by an optimal adjustment of applied material, defect-free manufacturing and appropriate design. This provides a challenging and complex task, where interdisciplinary expertise is required [13,14]. For example, structural performance can be improved by a load-path-oriented fibre layout. At the same time, interdependencies between individual process steps (forming, infiltration and curing) need to be considered to prevent defects such as dry spots, fibre undulations, gaps, or wrinkles.

For these reasons, detailed knowledge about the occurring physical mechanisms and their reliable modelling as well as consideration throughout the whole manufacturing process is essential to enable time- and cost-effective process and product design [2, 15]. Several methods and guidelines have been successfully developed and applied in various engineering disciplines.

Following a Concurrent Engineering approach, Kärger et al. [15] have introduced a virtual process chain (CAE chain) for composite materials (cf. Figure 1.1).
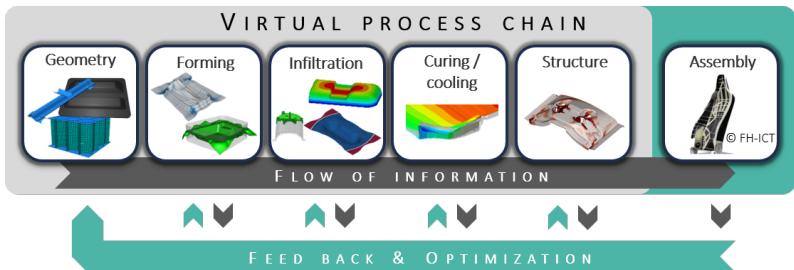

Figure 1.1: Illustration of a continuous CAE chain for virtual analysis of manufacturing and structural behaviour of continuous fibre-reinforced polymers (CoFRP) [15].

The individual process steps are virtually modelled and relevant information is retained and passed on successively to subsequent simulation steps. These CAE chain can be modularly adapted to all commonly used

thermoset and thermoplastic composites. Yet, this approach heavily relies on suitable experimental expertise and corresponding process models for the individual process steps. This work is specifically about developing such a model for draping and infiltration during WCM to incorporate the advantages of high-performance composite materials into reliable processes and part designs (cf. Figure 1.1). The following, selected literature outlines the extensive research conducted in multiple fields and disciplines related to composite processing and simulation approaches of CoFRP.

1.2   State of the art

First, commonly processed CoFRP materials and their respective manufacturing processes are outlined (cf. Section 1.2.1). Second, material characterisation methods related to forming (cf. Section 1.2.2) and mould-filling (cf. Section 1.2.3) under consideration of process conditions and their interdependencies are presented. Based on this, relevant simulation approaches in both areas are introduced in Sections 1.2.4 and 1.2.5.

1.2.1   Composite materials and processing

CoFRP materials are made out of fibrous reinforcements embedded into a polymer-based 'matrix'. Fibres contribute high stiffness and strength, whereas the matrix material ensures their geometrical arrangement, shape and load transmission, as well as environmental protection [16]. This modular concept provides one of the main advantages of composite materials as it enables highly tailored solutions [1, 12]. As outlined in the following, this interaction between fibres and matrix causes several mutual dependencies during processing. For example, the forming behaviour of CoFRPs are governed by fibrous material [17] but simultaneously affected by the fluid pressure and curing state [18]. Similarly, mould-filling

strongly depends on the matrix viscosity [19], but the resulting in-mould pressure is directly affected by the local fibre volume (FVC) content and fibre orientation [20]. The inherent anisotropy of composites originating from the fibre architecture needs to be considered during forming and mould-filling [21].

1.2.1.1 Reinforcements

CoFRP, similar to other reinforcements polymers, benefit from the high tensile stiffness of the embedded fibres. The fibre's shape also provides statistical 'size effect', which originates from the smaller the volume of the filaments, which reduces chances for imperfection. Depending on the intended application, different reinforcements such as natural fibres (e.g. wool, hemp, banana), organic fibres (e.g. polyethene, aramid, carbon) or an-organic fibres (e.g. glass) are applied. This work focuses on carbon fibres (CF) for high-performance applications. For this material, fibre production itself already leads to a strong predefined orientation on the molecular scale, introducing anisotropy even before the material is composed. Comprehensive reviews on this matter are exemplarily provided by Schürmann [16] or Long [22].

CoFRPs are commonly distinguished into dry and pre-impregnated textiles. Woven fabrics and non-crimped fabrics (NCF) are the most widespread representatives of dry engineering textiles for shell-like structures [1, 23]. The individual material behaviour of fabrics differs depending on pre-treatment, fibre material and either weaving architecture or stitching and yarn pattern [16]. These materials are usually processed using RTM or WCM. Pre-impregnated textiles are often referred to as 'prepregs', are infiltrated with a thermoset or thermoplastic resin before the actual forming process. Furthermore, thermoset prepregs can utilize bi-staged resin

systems to support handling after preforming before subsequent processing and solidification. Thermoplastic prepregs, often denoted as organo-sheets and unidirectional (UD) tapes, are processed using stamp- or thermoforming [1, 2, 24].

1.2.1.2 Matrix materials

The chemical structure of the matrix material significantly affects processing by contributing to density, hygrothermal expansion behaviour, drapeability and viscosity [16]. Furthermore, it is decisive for the structural behaviour of the final part by affecting its stiffness (transverse), thermal application limits, possible warpage, thermal expansion limits and relaxation.
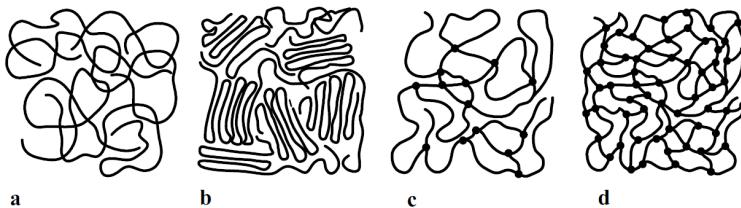
Figure 1.2: Chemical structure of polymers | (a) amorphous thermoplastic; (b) semi-crystallised thermoplastic; (c) elastomer; (d) spatially cross-linked thermoset [16].

Thermoset polymers (e.g. epoxy or vinyl resins) provide the highest final part performances due to a strong three-dimensional (3D) cross-linking (curing) during processing (cf. Figure 1.2 (d)). Their major drawback is difficult recyclability [25]. Their curing behaviour depends on the local temperature history and strongly affects resin rheology. This directly affects the mould-filling during processing and must be carefully monitored and controlled [19, 26, 27].

In contrast, thermoplastic polymers (e.g. polyamide, polypropylene) are not reactively cross-linked (cf. Figure 1.2 (a,b)), which makes solidification

reversible. However, this comes at the cost of reduced mechanical performance compared to the thermoset systems. During processing of thermoplastics, temperatures and corresponding crystallisation of the polymer must be carefully adjusted as material properties change significantly around glass transition temperature T_g [28–30].

1.2.1.3 Fast CoFRP processing

When targeting cycle times below three minutes, as required for automotive mass production, only three processes are applicable and economically relevant for CoFRP. RTM and WCM with fast-curing polymers and thermoforming processes using thermoplastic organosheets or tape laminates [2]. Other established liquid moulding techniques, such as Vacuum-assisted Resin Injection (VARI), cannot achieve comparable processing times due to long infiltration paths and a considerable amount of manual process steps [21, 26].

Resin Transfer Moulding. The conventional RTM process is an in-mould resin-injection process, which is established in industry for many decades [26]. It consists mainly of a preforming and an injection step with subsequent curing as illustrated in Figure 1.3. Significant effort and research have been conducted to qualify this process for large volume production [2, 26, 31, 32]. Handling and dosing equipment for highly reactive resins are supplied to meet these requirements [21, 27, 33, 34]. Furthermore, modifications of the process route and control including increased injection pressure (High Pressure (HP-RTM)) [35, 36] and an additional compression phase (CRTM) during mould closure [31, 32, 37–40] are proposed.

The preforming step (cf. Figure 1.3 (top)) includes draping of a flat pre-product into a complex, 3D shaped dry (bindered or non-bindered) fabric. Corresponding operations can also contain near-net shaped forming and application of binder and activation of the applied binder to ensure
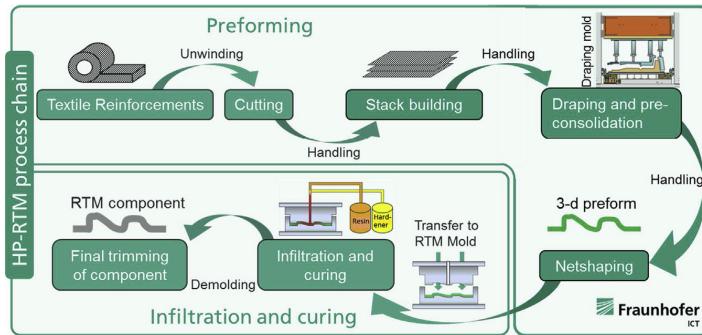
Figure 1.3: Schematic illustration of main process steps preforming, injection and curing during HPRTM for manufacturing of complex CoFRPs [2].

dimensional stability for further processing [26]. Effects and defects can occur during draping. Expected effects are reorientation of fibres during large deformations, inter-ply slip between individual layers of the stack and changes in the FVC. Common draping defects are gapping, undulations or wrinkles. Both, effects and defects influence subsequent infiltration, curing and final part performance [2, 17, 41].

To prevent these defects, the draping behaviour is often systematically manipulated by introducing additional membrane tension forces through local grippers or global blank holders [22, 42–45]. The occurrence of draping defects has been successfully reduced by these concepts. Especially the occurrence of wrinkles has been reduced, in which mechanisms and remedies are understood comprehensively [46–49]. The downside of additional blank holder applications is required additional material, which prevents near-net shaped forming [2]. Moreover, draping effects could be provoked or intensified by misplaced grippers [42, 45, 50] .

Furthermore, alternative strategies to prevent such defects are suggested in the literature. Nezami et al. [45] have presented a piezo-active manipulation concept based on metal layers to reduce the intra-ply friction

and improve drapeability. Another possibility is a sequential draping process based on a segmented tooling sequence or active local robot-based manipulation of the stack. This concepts aim to resemble the manual smooth-out movement of wrinkles within a fully automatised forming process [51,52]. Instead of draping a part as a whole, the draping task itself can be simplified using a segmentation into sub-preforms. Moreover, the local drapeability of fabrics can be directly influenced by stitching patterns [53, 54] of UD-NCF or weaving architectures of woven fabric [55]. An appropriate assembly of the sub-preforms can minimise loss of mechanical performance [56]. Forming simulation, which will be outlined in Section 1.2.4, can provide vital support for the outlined challenges.

The injection and curing step (cf. Figure 1.3 (bottom)) comprises the dosing of the highly-reactive resin into the fully or partly closed mould cavity as well as the curing of the manufactured CoFRP [19, 26]. High injection rates, initialised curing before injection and fast cavity vacuumisation can enable cycle times between three to five minutes [31]. Challenges primarily arise from the usage of high reactive resin systems [27, 34], which can lead to increased viscosity and thus to high cavity pressures [2, 31]. This may even result in adverse effects such as local fibre-washout [57,58] e.g. pressure-induced undulations or flushing out rovings, or macroscopic flow-induced fibre displacements (FiFD) of several decimetres [58–60]. Furthermore, air entrapments [21, 22, 61] and in partly saturated regions, especially on micro-scale [62–66] and local resin channels [67] may occur.

The aforementioned effects can complicate the manufacturing process and reduce its robustness. Similar to the numerical prediction of preforming, mould-filling simulation can provide crucial support in terms of mould design development, optimisation of injection strategy and the prediction of dry spots (cf. Section 1.2.5) [15, 21, 61, 68].

Wet compression moulding. WCM is a closed-mould process, which was established more broadly in the automotive within the last decade,

exemplary of as part of large volume production of structural parts within the car bodies of the BMW i3 and i8 [11, 69, 70]. As illustrated in Figure 1.4, two process variants can be distinguished.
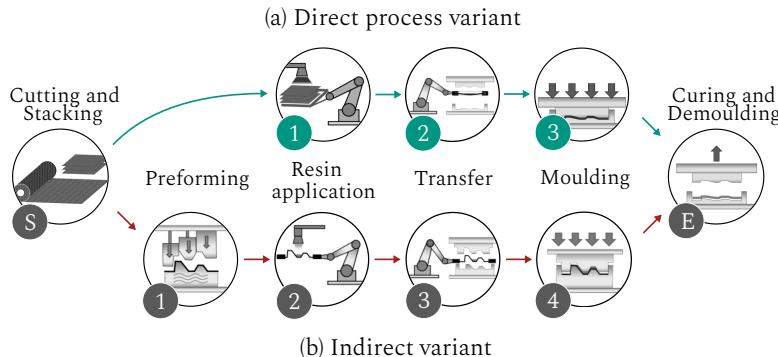
Figure 1.4: WCM steps | (a) Direct process with simultaneous draping and infiltration; (b) Indirect variant, where the resin is applied on-top of the already preformed part.

Starting with the direct process variant (cf. Figure 1.4 (a)), individual fabric layers are cut (S), stacked (1) and resin is applied on the topside (2), by using a wide slit nozzle. The resin seeps into the fibrous stack, while the partly infiltrated stack is transferred into the mould. In the third, most crucial step (3), infiltration and textile forming occur simultaneously [69, 71]. Thus, in contrast to RTM, injection is not a process step subsequent to forming. Due to a large pre-infiltration of the stack, thickness-dominated flow progression and short infiltration distances are achieved. This results in comparatively low cavity pressures, making WCM more attractive compared to conventional liquid composite moulding processes such as the above introduced RTM/CRTM [9, 72, 73].

In contrast, the indirect process variant (cf. Figure 1.4 (b)) comprises an additional preforming step (1). Here, the resin is applied on top of the already preformed stack (2). The moulding step (4) resembles almost completely the CRTM compression step. As draping and infiltration are decoupled within the indirect process variant, the RTM-related mechanism, challenges and numerical methods outlined above are involved.

The direct WCM variant is economically more attractive although more difficult to model, since draping, infiltration and curing take place simultaneously during moulding. The latter can minimise cycle times down to two to three minutes [2, 74]. Like for other liquid compression moulding (LCM) processes, experimental and numerical investigations of WCM show strong mutual dependencies between involved physical mechanisms, especially between resin flow and textile forming [9, 11, 69, 75]. The combination of forming and infiltration step disqualifies sequential modelling approaches as outlined above for RTM.

Available literature focuses on an experimental assessment of key process parameters, advanced tooling concepts or the effects of process parameters on structural performance. Among the first, Bergmann et al. [11, 74] have outlined correlations between part quality and process boundary conditions such as stack weight, mould temperatures, resin amount, infiltration time and moulding sequence. They evaluate the part quality using surface characteristics such as wrinkles, undulations and dry spots. A physical-based process analysis is prevented by overlapping of the discussed effects.

Beyond that, Bockelmann [9] investigated the through-thickness infiltration during moulding using fluorescent photography. Using this information, he proposes a new tooling and infiltration concept based on a spatially distributed resin carrier frame. This carrier-integrated processing (CIP) can be used to achieve very homogenous infiltration results inside the stack and increases process robustness due to a much closer controlled fluid progression. Moreover, he presents an LCA comparing

WCM (with and without the proposed CIP) to the conventional RTM. Energy consumption, energy costs and environmental impact favours an application of WCM because cycle times are shorter and cavity pressures are lower. Both reduce the required amount of pressing forces and dwell times, leading to smaller and less energy and capital-consuming process equipment.

Also focusing on a direct comparison between RTM and WCM, Stanglmaier [70] investigated the infiltration quality and structural performance with special emphasis on thickness transition areas and local patches. He shows that a shafted layout of the wall thickness transitions is recommendable. Infiltration of these shafted areas and can be achieved without reducing the mechanical performance of the final part. However, positioning and fixing of the material transitions must be ensured during infiltration. A generalisable dimensioning concept for transition areas has not been presented.

Albrecht et al. [73] experimentally compared the two WCM process variants (cf. Figure 1.4) by applying it to the manufacturing of a complex sledge-shaped demonstrator part. Not only lower processing times could be achieved for the direct variant, but infiltration quality in terms of dry spots is also better for simultaneous infiltration. This results from an earlier infiltration of critical areas before significant deformations take place inside the mould. The results directly indicate the importance of coupled draping and infiltration.

In addition, a comprehensive study of the direct WCM process has been provided by Senner [69]. He focuses on the in-mould forming behaviour and tool design, aiming to increase process robustness. Neglecting infiltration, he proposes geometrical relations for blank holders and crimp seals dimensioning (german: Quetschsicken).

Focusing on structural performance, Heudorfer et al. [76] have investigated the influence of resin amount and infiltration time on the interlaminar shear strength and the tensile strength. They report the amount

of resin to be decisive for the obtained mechanical properties of their part. Yet, the scattering of their results prevents a unambiguous conclusion.

An analysis of the compressive-strength-after-impact of non-crimped fabrics manufactured using the WCM process has been presented by Lee et al. [77] recently. They show that a good mechanical impact performance could be achieved if a low void content can be realised.

Thermoplastic tape forming. Manufacturing of continuous fibre reinforced thermoplastics (CoFRTP) utilizes semi-finished products such as organosheets or UD tapes to achieve low cycle times [2,3]. Organosheets are fully pre-impregnated plates with embedded woven fabrics. UD tapes are impregnated stripes with unidirectional reinforcement supplied on a role [30,78]. This tape enables the usage of near-net shaped laminates, which reduces waste and increases material usage rate [1,79].
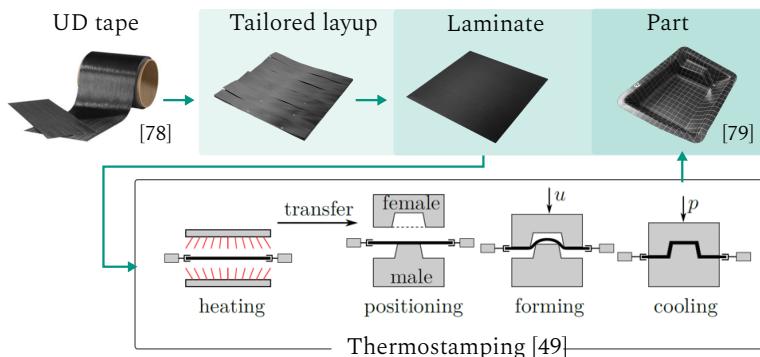
**Figure 1.5:** Illustration of the thermoplastic tape forming process chain including pre-consolidation of the laminate and subsequent thermostamping into a complex geometry (based on [49,78,79]).

A common processing route is shown in Figure 1.5. The UD tape stripes are layed to form a tailored laminate. For pre-consolidation, transversal pressure is applied while the laminate cools down below the melting

temperature. Subsequent drying of the laminates can prevent deconsolidation during reheating [80] but increases energy consumption. Before processing, the pre-consolidated laminate is heated well above melting temperature, usually applying an infrared heater or convection ovens and thermoformed into a complex shaped part [79]. Afterwards, additional cooling time is required. During this time, transverse pressure is applied [49].

Analogously to the RTM preforming step, forming defects such as winkling, gapping, or fibre undulations can result from the manufacturing process and are studied extensively in literature [24, 49, 78, 81, 82]. In general, the presence of the viscous polymer can favour sticking and stacking (thickness direction) between the plies, which leads to increased contact stresses and lower drapeability if the temperature history is not carefully adjusted [49, 83]. Depending on the material, local crystallisation can significantly affect the material behaviour during processing.

Using thermoplastic prepregs, Sachs [78] has demonstrated that unidirectional reinforcements tend to provoke more wrinkling than similar organosheets in critical areas. Furthermore, increasing relative fibre orientation between individual plies of the stacked laminate tends to increase the likelihood for wrinkling [84]. Substantial temperature- and rate-dependencies are reported for all deformation mechanisms during forming. These findings suggest utilising process simulation at an early stage during the process and part development [28, 85–87] to prevent time- and cost-consuming iterations for part and process design [2, 49].

1.2.2   Characterisation of forming behaviour

CoFRPs are multi-scale materials. In this regard, deformation mechanism can be described on a macro-, meso- and micro-scale [22, 88–90]. Whereas a microscopic view aims to investigate the forming behaviour of individual filaments inside a roving [91, 92], the mesoscopic scale focuses

on the interaction and compaction of rovings for different fabric architectures and proper consideration of stitching patterns during deformation [93–96]. This thesis focuses on a macroscopic view. At this scale, the CoFRP is considered as a homogenised, anisotropic continuum.

Macroscopic forming behaviour of a CoFRP stack during moulding refers to several different deformation mechanisms, which are commonly categorised into intra-ply and inter-ply mechanisms (cf. Figure 1.6) [24,49,97].
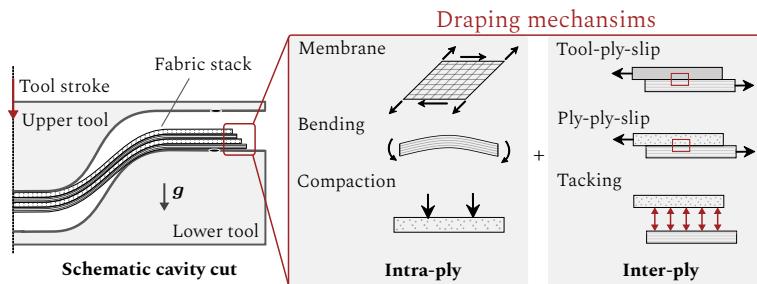
Figure 1.6: Macroscopic deformation mechanism during forming, categorised into intra-ply and inter-ply mechanism.

Moreover, possible tacking between the contact interfaces due to impregnation may occur. In-plane shearing is normally the dominant deformation mode as the shear stiffness is several orders of magnitude lower than the tensile stiffness of the fibres. For unidirectional NCFs, membrane behaviour is additional strongly influenced by the stitching pattern and yarn behaviour [51, 96].

Experiments reveal a high membrane stiffnesses in fibre direction and comparably low bending stiffnesses. The latter originates from the intra-roving slip between the filaments [98]. Moreover, transverse compaction determines the resulting forming forces and the final thickness of the plies. Consequently, compaction is an important deformation mode and is decisive for the infiltration as it strongly affects the local FVC.

Several experimental setups are proposed in literature to characterise the macroscopic deformation mechanisms (cf. Figure 1.6) introduced here. The most relevant ones are outlined in the following.

1.2.2.1 Intra-ply shear and tensile behaviour[1]

Membrane related deformation mechanisms of engineering textiles during draping (cf. Figure 1.6) are usually divided into in-plane shear, fibre tensioning and longitudinal fibre-compaction. Moreover, interwoven fibres can lead to a 'tension-shear coupling', which interconnects both mechanisms and leads to increased shear resistance when fibre tension is present [42].

For the characterisation of the shear behaviour of dry woven and UD-NCF, the Bias-Extension Tests (BET) [98, 100, 101] or Picture Frame (PF) tests [100, 102–104] are usually applied (cf. Figure 1.7 (a,b)). Both tests have advantages and disadvantages [105, 106]. Still, comparable results are reported for woven fabrics [100, 107, 108]. While the BET provides a straightforward and often simpler characterisation of shearing, several authors observed drawbacks in terms of mesoscopic effects such as inter-tow slip, crosspoint slip and fibre bending during the characterisation of dry fabrics [101, 106, 109]. These effects prevent a direct extraction of the mechanical properties with analytical solutions [49].

On the contrary, the deformation modes for shear and tension can be decoupled using PF tests. This enables an investigation of shear-tension-coupling for woven fabrics [42, 44, 110–112] or UD-NCFs [69], where feasibility depends on the yarn stiffness. However, misalignment and in-plane bending of the fibres can provide challenges when adopting the

---

[1]   Section 1.2.2.1 contains extracts of: C. Poppe, D. Dörr, F. Henning, L. Kärger: *Experimental and numerical investigation of the shear behaviour of infiltrated woven fabrics*, Composites Part A, 114:327-337, 2018 [99].

(a) Picture Frame [42]   (b) BET [42]   (c) Off-Axis-Tension [105]
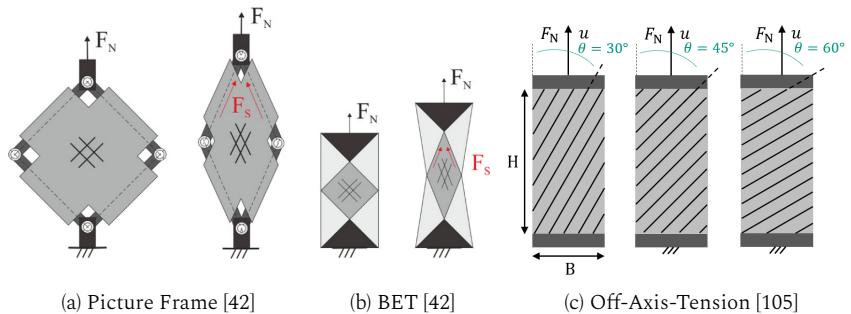
Figure 1.7: Shear characterisation setups for engineering textiles.

PF test [42, 44, 103, 113]. Schirmaier et al. [51, 105] has proposed Off-Axis-Tension (OAT) trials for a more comprehensive characterisation of unidirectional NCF (cf. Figure 1.7 (c)). So far, no test benches for the shear characterisation of engineering fabrics infiltrated with a low-viscous fluid have been proposed in literature.

For prepreg, organosheets and thermoplastic UD-tapes, strong dependencies between the matrix material state (viscosity) and mechanical properties during shear are reported in comprehensive investigations [49, 82, 85, 86, 98, 114]. For thermoplastic UD tapes, the well-established torsion bar test, which has been proposed by Haanappel et al. [85] is usually applied.

The relevance for an experimental assessment of the fibre tension behaviour depends on the material type. For woven reinforcements, non-linear and tensile behaviour is observed in both fibre directions [115–117]. Initial undulations are eventually stretched out during tensile load, which leads to increasing tensile forces during testing. No biaxial and only less pronounced non-linear behaviour is observed for the tensile behaviour of biaxial NCFs [118]. On the contrary, high sensitivity to the clamping situation is reported for the transverse tensile behaviour of unidirectional NCF due to a strong impact of yarn behaviour and stitching pattern [105].

1.2.2.2 Intra-ply bending[1]

To characterise bending behaviour, a systematic deflection is applied on the specimen often by utilising gravity-induced slag or rotating measurement devices. A comprehensive review on bending characterisation has been presented by Boisse et al. [47].

The cantilever test, also referred to as Peirce test [120, 121] (cf. Figure 1.8 (a)), is commonly applied for bending characterisation of dry woven fabrics. The Peirce method [120] assumes a linear relationship between curvature and bending moment. Bilbao et al. [122] and Liang et al. [123, 124] have presented an additional optical measurement technique to analyse the shape and deformation of the specimens during testing. Their work demonstrates that the moment-curvature-relation is non-constant, with a maximum at the clamped end. A modified cantilever test, which has been presented by Bilbao et al. [122], enables the investigation of elasto-plastic bending behaviour by applying variable bending length in addition to optical evaluation. An additional effort through optical detection and evaluation methods is required to obtain bending rate and plastic behaviour during cantilever tests. This is necessary, because the curvature rate distribution along the specimen's length is nonlinear. In this regard, the cantilever test is most suitable for straightforward determining the elastic bending stiffness [47]. [47, 125–128] and UD-NCF [51].

Beyond that, vertical arrangements of the tests have been presented, e.g. by Dangora et al. [126] (cf. Figure 1.8 (a)), which aim to reduce the influence of gravity loadings for small deflations and to enable rate-dependent characterisation.

The Kawabata bending test (KES-FB2) [130] and its expansions impose a constant curvature and curvature rate distribution on the specimens by

---

[1]   Section 1.2.2.2 contains extracts of: C. Poppe, T. Rosenkranz, D. Dörr, L. Kärger: *Comparative experimental and numerical analyis of bending behaviour of dry and low-viscous infiltrated woven fabrics*, Composites Part A, 124:105466, 2019 [119].

(a) Peirce's Cantilever test (horizontal) [125]; (vertical) [126]

(b) Kawabata KES-FB2 bending test [122]

(c) Rheometer-Bending-Test [129]

(d) Three-point bending test [47]
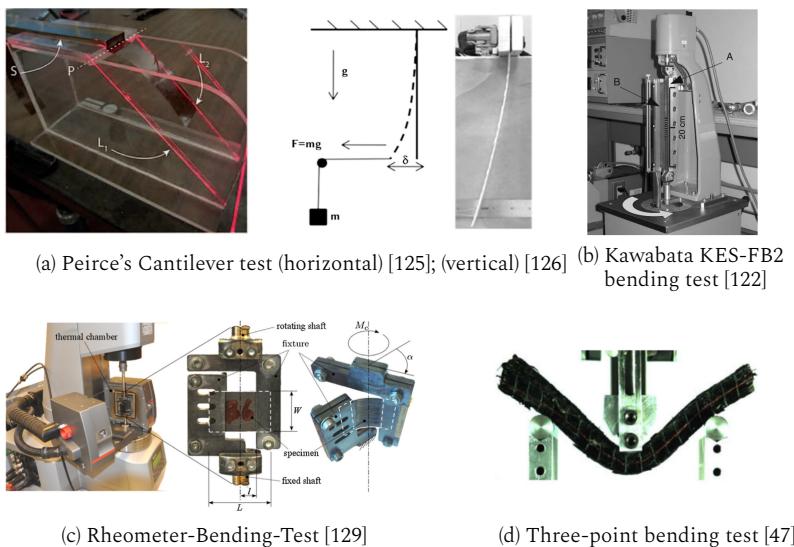
Figure 1.8: Common bending characterisation setups.

rotation of one of the two clamps (cf. Figure 1.8 (b)). This test gives direct access to the moment-curvature-relation, even when several loading and unloading cycles are applied. Nonlinear and hysteretic material response is reported for several materials [122, 131, 132] due to internal friction between the rovings and filaments [133, 134]. In contrast to the cantilever test, the KES-FB2 enables rate-dependent bending characterisation.

The most significant modification of the KES-FB2, the rheometer bending test (RBT), was presented by Sachs [87, 129] and allows for an investigation of the rate- and the temperature-dependent bending response of thermoplastic composites (cf. Figure 1.8 (c)).

Moreover, Boisse et al. [47] have proposed to apply a three-point bending test for thick interlock fabrics (cf. Figure 1.8 (d)). This test produce originates from cured composites in solid-state [135,136], because they require a sufficiently large bending stiffness of the material, which is only achievable by either thick laminates or short specimens [47].

No attempts have been published to characterise the bending behaviour of engineering fabrics infiltrated with a low-viscous fluid. The required viscosity range during testing ($20-250\,\text{mPas}$) is significantly lower than comparable pre-impregnated semi-finished products investigated in literature.

1.2.2.3 Intra-ply compaction[1]

During the last decades, compaction (consolidation) of composites has been subject of many studies. Most of the available literature is related to LCM processes such as RTM [138–144] or VARI [145]. This originates from the strong relationship between compaction and local FVC, which is decisive for the infiltration behaviour in this process. Moreover, it is vital for an accurate prediction of the final part thickness, FVC and tool forces during moulding [59, 61, 146, 147]. Furthermore, compaction is an ongoing research topic within the processing of thermoplastic UD tapes, to reduce voids during consolidation [148].
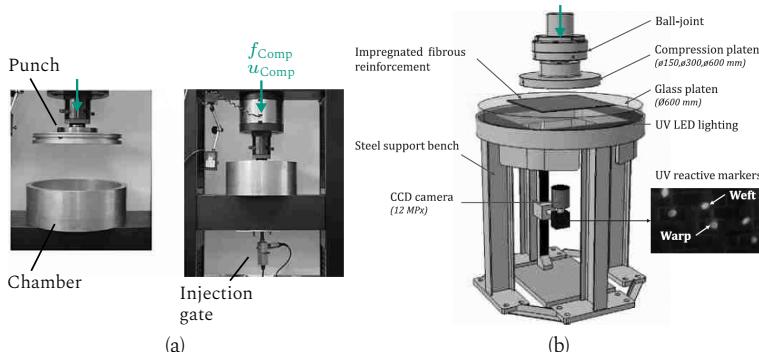

Figure 1.9: Common setups for transverse compaction tests with (a) additional injection gate [149] or (b) additional optical tacking of in-plane deformation [147].

---

[1] Section 1.2.2.3 contains extracts of: C. Poppe, C. Krauß, F. Albrecht, L. Kärger: *A 3D process simulation model for wet compression moulding*, Composites Part A, 145:106379, 2021 [137].

Compaction behaviour is commonly investigated straightforward using plate-to-plate or punch-to-plate tools on tensile testing machines [149]. More sophisticated approaches additionally allow for an controlled injection [146], optical tracking of in-plane deformation [147] or fluid pressure during compaction [75] (cf. Figure 1.9).

A characteristic non-linear shape for the reaction forces can be expected when engineering textiles are subjected to transverse compaction [150]. Similar to other deformation modes, stress relaxation, rate-dependency and hysteresis effects need to be taken into account for most woven reinforcements and prepregs [149,151,152]. Beyond that, even higher reaction forces are received when dry textiles are additionally subjected to shear deformation, which originates from increased material density as outlined by Ivanov and Lomov [153]. Moreover, obtained reaction forces increase further when pre-infiltrated specimens are exposed to compaction because of the superimposed fluid pressures below the punch, for example, shown by Bickerton and Abdullah [149]. In contrast to membrane and bending behaviour, investigation of the compaction behaviour of dry and low-viscous infiltrated specimens is common in literature.

1.2.2.4 Inter-ply behaviour

Experimental characterisation of inter-ply slip is commonly conducted via relative motion between two interfaces with controlled transverse pressure. Several configurations (cf. Figure 1.10) are proposed in literature [78]. They can be applied to tool-ply and ply-ply interfaces. A benchmark study by Sachs et al. [87] have revealed consistent results for the presented setups for the same material. Special attention is recommended in terms of systemic errors. Those can originate from mesoscopic effects and fibre architecture, leading to stick-slip-effects [154–156] or inhomogeneous load distributions within the interface clamped area. Enlargement of the contact area and application of pull-through tests are recommended to alleviate these problems.

(a) Pull-out-test   (b) Pull-through-test   (c) Horizontal sledge
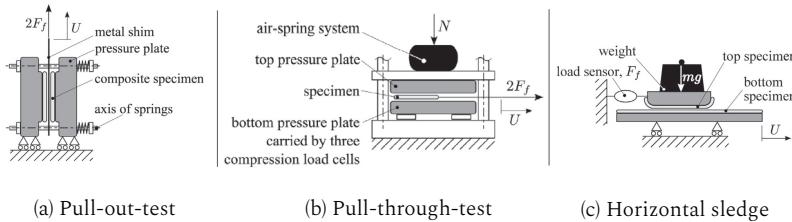
Figure 1.10: Common setups for interface friction characterisation (extract from [87]).

In literature, pressure- and rate-dependency is reported for dry woven fabrics [87, 155–160], unidirectional NCF [93], pre-impregnated organo-sheets [161, 162] and UD-tapes [83, 85, 163].

Regarding low-viscous infiltrated contact interfaces, Hüttl et al. [156] have compared the Coefficient of Friction (CoF) obtained from dry and pre-infiltrated specimens using a horizontal sledge in combination with a fluid reservoir. For tool-ply contact interfaces, infiltration increases the measured tangential stresses compared to the dry reference. In contrast, they report that infiltration decreases the tangential stresses for the inter-ply contact. Rate dependency has not been investigated as always a constant velocity of 100 mm/min was applied.

Despite tangential friction, tacking in normal direction can an important issue for pre-infiltrated textile interfaces. For thermoplastic UD-taps [49, 83, 85] an explicit tacking-stiffness is considered during modelling. However, a direct experimental assessment with process-related boundary conditions is challenging. A comprehensive review focusing on prepreg tacking during automated fibre placement has been published by Budelmann et al. [164] recently. Yet, the outlined mostly peel-based setups cannot be directly applied, as detachment during forming is commonly not caused by peeling.

1.2.3 Characterisation of mould-filling

Besides draping, the relevant macroscopic mechanisms during WCM are mould-filling related. These interconnected mechanisms can be subdivided according to infiltration, heat transfer and curing (cf. Figure 1.11).
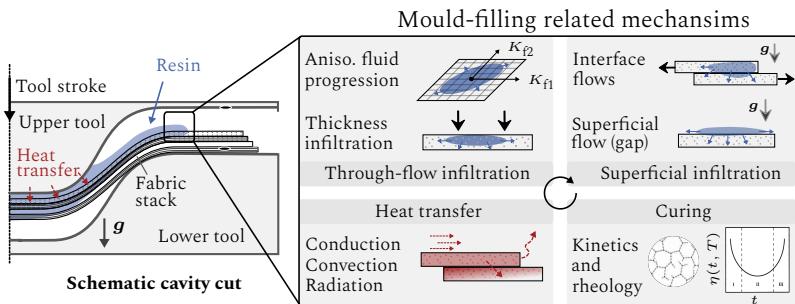
Figure 1.11: Macroscopic mould-filling-related mechanism, categorised according to through- and superficial flow mechanism and accompanied by non-isothermal curing of the matrix.

The above-outlined forming behaviour (cf. Figure 1.6) results in a deformed, anisotropic porous fibre network, which is being simultaneously infiltrated by the resin during moulding. Infiltration on the macro-scale can be categorised into through- and superficial-flow related mechanism. Whereas throughflow accounts for fluid progression within the deformed stack, superficial squeeze-flow results from fluid being pushed over the stack surface by contact with the tooling or from one ply into another. In addition, curing within the thermoset polymer is initialised through contact with the hot tool surfaces [19, 27]. Curing history affects the resin's viscosity and resulting residual stresses.

In general, a macroscopic view focuses on the prediction and optimisation of mould-filling and injection strategies on part level [19, 32]. Similar to draping, infiltration is a multi-scale phenomenon (cf. Figure 1.12), including different mechanisms for the micro- or meso-scale that are homogenised when a macroscopic view is adopted [2, 61].
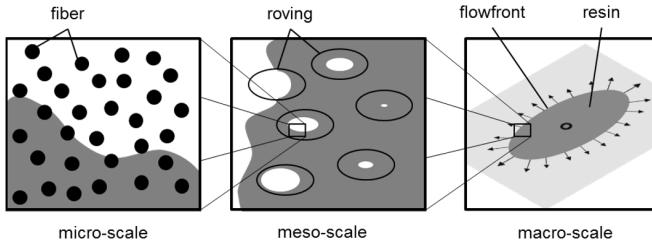
Figure 1.12: Illustration of micro-, meso- and macro-scale during injection of CoFRPs [2].

At the micro-scale, resin flow inside the rovings is investigated, whereas meso-scale focuses on the flow between them. Investigations at both scales focus on minimising void formation and virtual material characterisation [64, 165, 166].

For a characterisation of the material, infiltration of the stack foremost depends on the ratio between permeability tensor of the fibrous medium $\boldsymbol{K}$ and the matrix' viscosity η as Darcy's law proved suitable for a description [167]:

$$\boldsymbol{v}_{\mathrm{D}} = \frac{\boldsymbol{K}(\phi)}{\eta\,\varphi}\,\mathrm{grad}\,(p)\,. \tag{1.1}$$

Here, $\boldsymbol{v}_{\mathrm{D}}$ is the macroscopic fluid velocity, which takes the porosity $\varphi = 1 - \phi$ and the FVC ϕ into account.

The origin of Darcy's law will be outlined in more detail within Section 1.2.5. The related literature describing the experimental characterisation of permeability (cf. Section 1.2.3.1 as well as resin reaction kinetics and chemo-rheology (cf. Section 1.2.3.2) is outlined in the following.

1.2.3.1 Permeability

An accurate determination of permeability is important for all LCM processes as it strongly affects infiltration behaviour and flow front progression during injection or moulding [21]. Consequently, comprehensive research has been conducted in this field for more than 40 years [138].

Among others, Arbter et al. [168] and Vernet et al. [169] have provided comprehensive reviews, recommendations and worldwide benchmarks.

At macroscopic scale, Darcy's law (cf. Eq. 1.1) suitably describes the fluid progression within a homogenous porous medium. During characterisation, a constant pressure or injection rate is applied to a one-dimensional (1D) flow scenario. A predefined measurement gap is used, which needs to be completely occupied by the porous medium (textile). A 1D formulation of Darcy's law is subsequently applied to calculate the permeability based on the pressure difference between inlet and outlet in the stationary regime. This approach implies that the completely saturated permeability is characterised [170, 171]. In contrast, the transient permeability can be obtained by optical tracking of the flow front [75, 172–176] or with a linear array of pressure sensors [177, 178]. The transient permeability is better suited for mould-filling-related parameter extraction, as the flow front progresses through a dry textile resembles the boundary conditions during the injection. A comparison of saturated and unsaturated permeability measurements in literature is given by Park et al. [171]. They outline the discrepancies between both approaches and the reasons for the general uncertainty during permeability measurements.

Several studies focus on the anisotropy of the permeability tensor, which arises from in-plane shearing [153, 169, 175, 179]. Demaria et al. [20, 173] have shown that geometrical reorientation of fibres and change of FVC are the two key factors responsible for the change of permeability during deformation. Similar to shear characterisation (cf. Figure 1.7), picture frame-like clamping frames are applied [153, 174, 176, 179]. They are used to achieve a conditioned shear deformation state [169] before infiltration. Moreover, the in-plane anisotropy ratio $a = K_{11}^0/K_{22}^0$ between the fibre orientations depends on the weaving of the fabric. For balanced woven fabrics, the ratio is $a = 1$, leading to a perfectly radial flow front in undeformed state [19, 20]. In the same sense, unidirectional NCFs can be addressed as strongly in-balanced fabric with a significantly higher

permeability in fibre direction than in a perpendicular direction of the yarn [178, 180, 181].

Several authors reported an impact of nesting phenomena apart from shearing when multi-ply stacks are characterised [21, 169, 179, 182]. This originates from inhomogeneous interfaces between the single plies of the stack, allowing for an interlock of the rovings. Due to this effect, homogeneity of the porous medium increases, whereas permeability decreases because possible flow paths are closed [179].

In addition to in-plane, transverse permeability in thickness direction K_{33} is an increasingly important field of research. Being among the first, Weizenböck et al. [183] has proposed to use spatially distributed thermocouples to evaluate the 3D permeability tensor, including its component in thickness direction. Unfortunately, they encounter problems with local flow paths and flow-induced compaction. For these reasons, similar measurement principles as outlined above are also employed for the transverse direction [38, 181, 184]. Similarly, a 1D flow in thickness direction is utilised to calculate the permeability based on Darcy's law. Several layers (> 10) are needed to obtain a reasonable stack thickness. Thus an impact of nesting phenomena systematically affects the results. If possible, it is recommended to using the same number of plies during characterisation and processing. Moreover, a homogenous distribution of the injected fluid through hole-plates or honeycombs is a necessary precondition for reliable results [185, 186].

Apart from experimental trials, analytical [180, 187–189] and numerical models [190–192] on meso-scale can be used to estimate permeability values based on the textile's architecture. At meso-scale, Representative Volume Elements (RVEs) or Statistical Representative Volume Elements (SRVEs) are being applied frequently for engineering textiles [190, 191, 193], but also for nonwovens [194, 195]. Moreover, advanced

numerical methods are used to investigate the validity and prediction accuracy of existing analytical approximations, such as, for example, the Kozeny-Carman equation [196].

1.2.3.2 Reaction kinetics and chemo-rheology of resins

Reaction kinetics and the corresponding cross-linking of the monomers to polymers is crucial for a comprehensive assessment of LCM processes. To start with, viscosity changes by several orders of magnitude during processing while transitioning from liquid to solid-state. As the required injection- (RTM) or in-mould pressure (WCM) correlates with matrix viscosity, it is decisive for both infiltration quality and processing times [18]. Secondly, the individual curing cycle determines whether the resin reaches a fully cured final state, directly affecting the glass-transition-temperature (T_g), fracture toughness and ultimately the structural performance of the part [11, 76]. Moreover, process-induced strains due to chemical shrinkage and thermal strains due to cooling of the part after demoulding can lead to intolerable distortions of the final part [18].

A characterisation of the reactive behaviour of thermoset resin systems is mainly carried out using Differential Scanning Calorimetry (DSC). For a comprehensive review of related studies, the interested reader is directed to Yousefi et al. [197]. Alternative characterisation methods, which should only be named here, are Raman Spectroscopy, Dialectric Analysis (DEA), Fourier-Transform Infrared Spectroscopy (FTIR), or Near-Infrared Spectroscopy (NIR) [18, 198, 199].

DSC compares the heat flux of a reactive sample and non-reactive reference (cf. Figure 1.13 (a)) to extract the exothermal heat that is released during cross-linking as illustrated in Figure 1.13 (b). A baseline needs to be defined to separate the obtained heat flow peak from the total enthalpy. The enclosed area (cf. Figure 1.13 (b)) represents the total specific reaction enthalpy h_{exp}, which further integrated with time yields the degree of cure $\alpha(t, T)$.
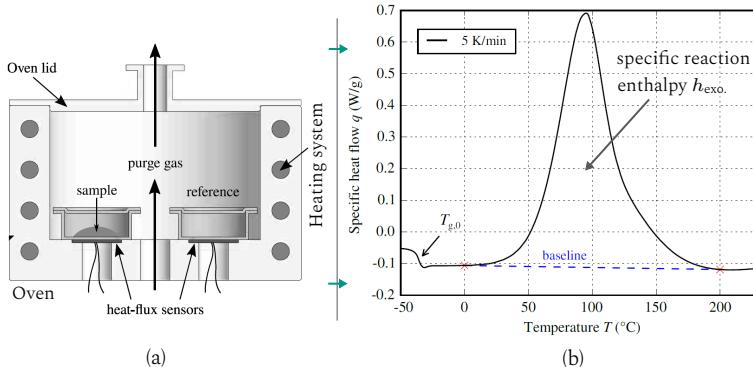
Figure 1.13: (a) Schematic illustration of the measurement principle of an DSC analysis [18]; (b) Exemplary heat flow evolution during non-isothermal DSC of an epoxy resin [27].

DSC measurements can be carried out under isothermal or non-isothermal conditions. The former suffers from an accurate estimation of the starting temperature due to initialised curing before heating of the samples is completed [200]. In contrast, starting temperature can be set sufficiently low to prevent prior curing for non-isothermal DCS measurement. However, isothermal trials are straightforward and can be conducted with less effort compared to non-isothermal measurements.

LCM processes are usually carried out under isothermal conditions, e.g. constant tool temperature to reduce cycle times [21, 22]. The resulting curing can be near isothermal or non-isothermal, depending on the specific mould-filling setup. In combination with fast-curing resin systems, this invokes several challenges. First, cross-linking is strongly time- and temperature-dependent, which makes fast curing prone to vitrification effects. This is initialized when the curing temperature catches up with T_g, resulting in an decrease of the maximal reachable degree of cure $\alpha_{max} < 1$ [18, 201, 202]. Secondly, physical ageing may occur, making parameter identification and extrapolation for modelling significantly more demanding. [18, 27]. It is not clear whether to apply isothermal or

non-isothermal measurements [202, 203]. Bernath et al. [27] have shown that combining non-isothermal and cyclic DSC runs can provide a comprehensive and large database for reliable parameter identification of fast curing resins. These highly reactive resins are required to achieve short cycles times during WCM. For modelling of these resin kinetics, empirical or mechanistic models are available in literature. A comprehensive review has been provided by Halley et al. [199]

Beyond reaction kinetics, which yields $\alpha(t, T)$, the directly related chemorheological behaviour of the resin system is required, which eventually gives the current viscosity $\eta(\alpha(t, T))$ during curing (cf. Figure 1.11) [2]. For the chemo-rheological behaviour, parallel-plate rheometry is usually applied for thermoset resins [198, 204, 205]. Thereby, the resin is injected into a gap between two plates. A constant or cyclic angular velocity is applied on one of the plates and the resulting moment is recorded at the other one. A shear stress in the gap is induced, which allows for a calculation of the viscosity η under consideration of geometrical factors [204].

1.2.4 Forming simulation

Forming simulation aims to model and predict the draping behaviour of CoFRPs via suitable kinematic assumptions (kinematic approaches) or constitutive material modelling (mechanics-based approaches) [89, 206]. While the former neglects physics-based modelling and exclusively relies on geometrical mapping algorithms, the latter can predict the material behaviour under consideration of process-related boundary conditions using constitutive modelling [2]. Finite Element Analysis (FEA) allows a direct implementation of constitutive models based on the introduced deformation mechanism (cf. Section 1.2.2) and is therefore commonly used for mechanics-based approaches.

In the following, a short overview of kinematic forming simulation is given in Section 1.2.4.1, succeeded by a survey of the most relevant FE forming simulation approaches in Section 1.2.4.2.

1.2.4.1 Kinematic approaches

The transition between an initially planar semi-finished product and the final 3D part shape can be predicted using kinematic assumptions in conjunction with suitable geometrical mapping algorithms (cf. Figure 1.14). As Lim and Ramakrishna [206] have pointed out in their review, it is generally assumed that material deforms incompressible and inextensible in the fibre directions.
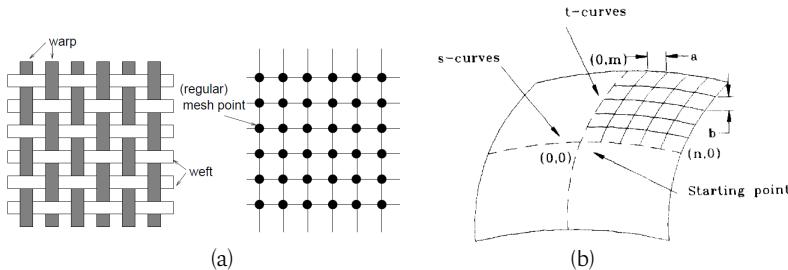
Figure 1.14: Kinematic approaches | (a) Topology of the initial mesh points for a plain weave fabric [207]; (b) Exemplary grid definition on a 3D surface originating from the predefined starting point [208].

For unidirectional reinforcements, a simple shear deformation is assumed, whereas a pure shear (Trellis shear) deformation is assumed for woven reinforcements [206, 207]. This implies a constant thickness for the incompressible unidirectional material as the area remains constant. In contrast, woven fabric material thickens during shearing as the area changes.

The main advantage of kinematic approaches is the comparably low computing effort [208]. Consequently, the first approaches reach far back to the mid-50s [209]. A large number of publications and models have been

proposed within the last decades, constantly improving prediction accuracy and robustness [206, 207, 210–214]. The two crucial shortcomings of such approaches imply the need for a predefined starting point (cf. Figure 1.14 (b)) and the neglected material behaviour under process conditions. Thus, these techniques are only suitable for a fast approximation and a first reasonable guess of the expected final fibre orientations after draping. More complex interactions between material and tooling are neglected, such as contact in multi-layer stacks, blank holder, seals, gripper, temperature or infiltration state. Therefore, they are not suitable for modelling WCM. The only exceptions are manual processes such as hand-draping [215, 216], because the starting point and the smooth-out directions can be similarly realised in experiments and simulation.

1.2.4.2 Finite Element forming simulation

To overcome the shortcomings of the kinematic approaches, mechanics-based formulations using Finite Element Method (FEM) have become state-of-the-art. Constitutive modelling is used to describe the individual deformation mechanisms of this multi-scale material. By this means, their internal structure can be described, enabling a prediction of their behaviour during processing. Based on the material resolution, approaches are distinguished according to micro-, meso- and macro-scale (cf. Section 1.2.2). Figure 1.15 illustrates the multi-scale character of woven fabric and summarises the commonly applied modelling approaches, including their aims of each scale. At the micro-and meso-scale level, individual constituents of the textile materials are modelled using either discrete 1D and 2D elements (micro-scale) or 2D and 3D elements, respectively. This allows for direct consideration of the heterogeneous fabric structure and corresponding modelling of local draping effects [88]. This detailed resolution comes at the costs of high computational effort (for example $> 50\,\mathrm{h}$ at multiple cores).
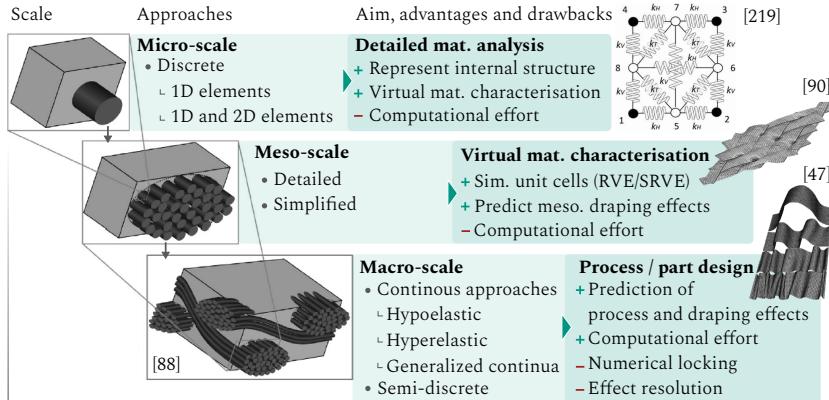
Figure 1.15: Comparison of FE-based multi-scale modelling approaches for CoFRP and corresponding aims, advantages and drawbacks.

Consequently, these models are mostly applied for RVEs or small and relatively simple single-ply forming tasks. This may still be beneficial when virtual material characterisation prevents expensive trials. In contrast, the homogenised description of the material behaviour on macro-scale aims to enable a virtual process design and predict draping effects for large structures and multi-ply stacks. Micro- and mesoscopic effects are commonly neglected to achieve this. Industry aims for simulation run times between 7 and 10 h on High-performance Clusters (HPCs) for overnight results.

Micro-scale approaches – detailed material analysis. Such approaches are usually assembled networks of 1D springs, truss or beam elements [88, 220] (cf. Figure 1.16 (a)). Valentini et al. [219] have proposed a comparable network for very compliant knitted meshes. By introducing rotational springs, a prediction of in-plane and out-of-plane bending is achieved [221, 222].
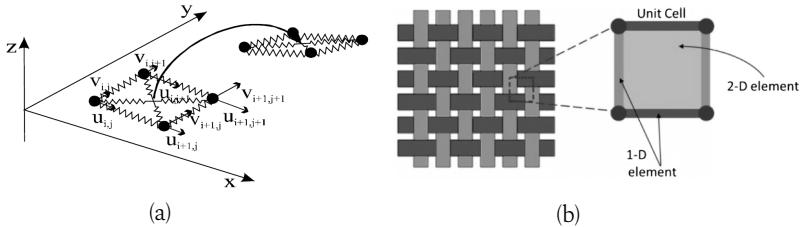
Figure 1.16: Illustration of discrete approaches | (a) Shear deformation illustrated by Boubaker et al. [222]; (b) Representation of a unit cell based on 1 and 2D elements [126].

Using 1D elements provides a straightforward approach to account for mesoscopic effects via conventional elements [49]. The main limitation originates from a missing element surface, which prevents a proper contact formulation and modelling multi-ply stacks. For example, a unit cell can be comprising a 2D element surrounded by 1D elements along the edges (cf. Figure 1.16 (b)). Moreover, additional 2D elements such as membrane or shells can be used [126].

First approaches based on membrane and truss elements [223, 224] neglected the bending behaviour. Subsequent approaches utilized truss and shell elements [225] and later bar and shell elements to capture the out-of-plane bending behaviour [126,226]. Moreover, Harrison et al. [81,227] have applied truss and bar elements [228] to predict the in-plane and out-of-plane bending behaviour of engineering fabrics and organosheets. They show that the in-plane bending stiffness is an important mechanism, enabling the modelling of shear transition zones during BET. Similar effects are observed for second-order gradient approaches [229–231]. Additionally, micro-scale modelling approaches have been comprehensibly discussed by Boisse et al. [217], Jauffres et al. [232], Syerko et al. [218] and Bussetta & Correia [88].

Meso-scale approaches – virtual characterisation. A detailed modelling of the internal structure of CoFRPs can also be accomplished using 2D shell or 3D volume elements to represent a unit cell or small samples on a meso-scale (cf. Figure 1.17). This also implies the need for a contact formulation between individual rovings represented by the elements. Two types of approaches can be distinguished on meso-scale [88]:

(a)   (b)
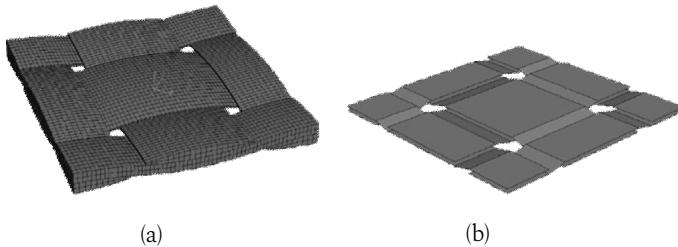
Figure 1.17: Comparison of mesoscopic unit cells by Boisse et al. [217] | (a) Detailed model based on volume elements; (b) Simplified model using shell elements.

Detailed approaches (cf. Figure 1.17 (a)) aim to model the material structure of a unit cell as accurately as possible. They aim to enable virtual material characterisation [218, 233]. The only application of such a solely detailed approach for a small single layer forming setup of woven fabric has been proposed by Tavana et al. [234], whose model could predict local effects such as yarn movement and material locking. However, these approaches are currently too computational time intensive for an application to larger structures. An elegant alternative for this problem has been proposed by Iwata et al. [235, 236] by using a coupled macro-meso approach. Here, a first macroscopic run is conducted to obtain transient boundary conditions, which are then used to solve a detailed mesoscopic model in critical areas during a subsequent simulation run. Detailed models for engineering fabrics in literature allow for a prediction of local forming effects such as yarn buckling [126, 236, 237], in-plane tensile and shear behaviour as well as tension-shear-coupling [153, 220, 238–241] or compaction [140, 143, 151, 153, 237].

Simplified mesoscopic approaches aim to reduce the degrees of freedom involved and thereby the computational expense. A reduced prediction accuracy is acceptable as long as key geometrical features are still considered. This is achieved by reducing the degrees of freedom for modelling of the roving geometry using only a few solid [93, 242, 243] or shell [244, 245] elements (cf. Figure 1.17 (b)). This still allows for discrete modelling of the yarn for NCFs via bar elements.

Macro-scale approaches – process simulation.   Compared to micro- or meso models, continuous approaches assume a homogenous medium on the macro-scale (cf. Figure 1.15) and the related deformation mechanisms (cf. Figure 1.6) are modelled through constitutive equations [217].

In general, macroscopic approaches are distinguished according to hypoelastic, hyperelastic, higher-order and semi-discrete formulations. The key advantage of such macroscopic formulations is their comparably low computational effort. This enables the prediction of the final fibre orientations and draping effects for large structures (Edge: $1 - 3\,\text{m}$) and multiply stacks (> 8 plies) under consideration of process-related boundary conditions e.g. temperature, blank holder forces [2, 15]. These approaches are therefore well-suited for virtual process development and assurance of manufacturability for CoFPRs.

Several macroscopic models are already applied in industry as part of commercial codes, for example PAMFORM, ANIFORM or recently SIMU-DRAPE. Comprehensive reviews on FE forming simulation modelling approaches on macro-scale have been presented by Boisse et al. [47, 89], Gereke et al. [23] and Bussetta and Correia [88]. Three main aspects require consideration when macro-scale modelling approaches based on FEM are adopted:

To start with, a *decoupling of membrane and bending behaviour* is required [47, 246]. This originates from the homogenised material description on

macro-scale, which neglects relative fibre motion during bending defor-
mation. The application of conventional shell theories for CoFRPs fails
to predict the low bending stiffness originating from the low transverse
shear stiffness (relative fibre motion) while modelling the high tensile
stiffness of the fibres of a fabric [48]. An intrinsic decomposition of the
material formulation based on the virtual work or internal virtual energy
is required [49, 102, 114, 246] to address this correctly for conventional
shell-based approaches. Furthermore, a discrete decomposition based on
superimposed membrane and shell elements is purposeful [85, 103, 247,
248]. Enhanced approaches for an accurate prediction of the bending be-
haviour by generalised continua [47] or 3D formulations to account for
transverse compaction is still in the subject of research [30, 249–252].

A second general issue is the correct consideration of *fibre-reorientation*
during large shear deformation on the macro-scale. This is caused by
the initially orthogonal frame $\{e_1, e_2\}$ becoming non-orthogonal $\{f_1, f_2\}$
during shear deformation (cf. Figure 1.18).
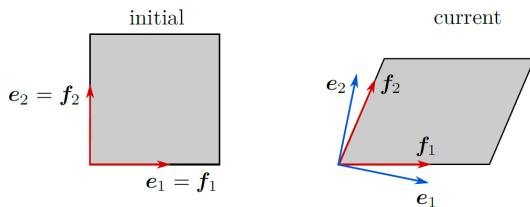
Figure 1.18: Schematic illustration of the rotation of an orthogonal frame (Green-Naghdi's
frame) $\{e_1, e_2\}$ and principal material orientations $\{f_1, f_2\}$ during pure shear
deformation [49].

As the axial stiffness of the fibres is several orders of magnitude higher
than the corresponding shear stiffness, the material formulations need
to account for the current non-orthogonal fibre orientations (principal
material directions). This requirement applies to all continuous formula-
tions, whether hypo-, hyperelastic or else.

Finally, a third main aspect focuses on *numerical locking phenomena*, such as unintended and physically implausible (artificial) stiffening effects, which originate from non-compatibility between specified deformation states and their discretisation in FEM. The relevance of these effects strongly depends on the selected integration scheme (full, selective-reduced, reduced) and the applied element shapes (triangular, quadrilateral, etc.). Integration scheme and shape functions specify which energy modes contribute to the deformation state [253, 254]. Preventing locking and hourglassing provides key challenges, especially for solid-shell and comparable 3D formulations [249–251].

Yu et al. [255] observe an intra-ply shear locking for non-aligned material and element orientations. Building on that, Hamila and Boisse [253] have conducted a comprehensive investigation of numerical locking phenomena utilising the BET. Their study highlights the inability of a fully integrated four-node element for a tension-free motion for any mesh. They refer to it as tension locking because the inextensibility in the fibre direction results in artificial fibre strains and 'spurious tensions'. They propose a selectively reduced integration scheme combined with a stabilisation procedure, where the latter only applies to the non-constant part of the in-plane shear deformation [253]. This approach allows the treatment of non-aligned meshes. Similarly, Thije and Akkerman [256] investigate the effects of mesh aligning and reduced integration on numerical shear locking. They show that aligned meshes, reduced integrated or additional methods are needed to prevent locking. Thije and Akkerman [256] ultimately propose and verify a new triangular multi-field element, which introduces additional degrees of freedom for the strain. Nevertheless, Dörr [49] argues that the increased computational effort presumably prevents its use for a wide range of application.

In the following, underlying ideas and differences between hypoelastic, hyperelastic and generalised continua approaches are summarised. Additional information can be found in the review papers mentioned above

(cf. Figure 1.15) and by a comparative study by Kim [257]. Ultimately, a short overview on semi-discrete approaches is presented.

Hypoelastic approaches.   These approaches relate the rate-of- deformation to the stress rate and is defined for the physically linear case by [254]

$$\boldsymbol{\sigma}^{\triangledown} = \mathbb{C} \colon \boldsymbol{D}, \tag{1.2}$$

where $\boldsymbol{\sigma}^{\triangledown}$ represents an objective rate of the Cauchy stress $\boldsymbol{\sigma}$, $\boldsymbol{D}$ the rate-of-deformation tensor and $\mathbb{C}$ the fourth-order elasticity tensor [48, 49]. The introduction of an conventionally objective stress-rate, as for example Green-Naghdi-rate or Jaumann-rate, implies that an orthogonal fixed frame (cf. Figure 1.18, $\{\boldsymbol{e}_1, \boldsymbol{e}_2\}$) is introduced. An incremental time integration as presented by Hughes and Winget [258] enables a hypoelastic formulation of constitutive equations with respect to the current deformation according to

$$\boldsymbol{\sigma}^{n+1} = \boldsymbol{\sigma}^n + \triangle\boldsymbol{\sigma}^{n+1} \qquad \text{with} \qquad \triangle\boldsymbol{\sigma}^{n+1} = \mathbb{C} \colon \triangle\boldsymbol{\varepsilon}^{n+1}. \tag{1.3}$$

Here, $\triangle\boldsymbol{\varepsilon}^{n+1}$ is the logarithmic strain increment within an according time step n. As illustrated in Figure 1.18, hypoelastic models need to be formulated in accordance with the current principal material directions. Incremental stress calculation needs therefore to be performed within a non-orthogonal frame [90]. As demonstrated by Dörr [49] or Williams [103], the latter can be achieved by introducing an additional fibre-parallel frame as illustrated in Figure 1.19. Utilizing the normalized right stretch tensor U_{ij}^*, a mapping between the Green-Naghdi's frame $\{\boldsymbol{e}_i\}$ and a normalized co- $\{\boldsymbol{g}_i^*\}$ and contravariant $\{\boldsymbol{g}^{*i}\}$ non-orthogonal frame can be achieved according to [48,49]

$$\boldsymbol{e}_i = U_{ij}^{*\top} \boldsymbol{g}^{*j} \quad \text{and} \quad \boldsymbol{g}_i^* = U_{ij}^* \boldsymbol{e}_j \quad \text{with} \quad U_{ij}^{*\top} = \frac{1}{||\boldsymbol{g}_i||} U_{ij}. \tag{1.4}$$
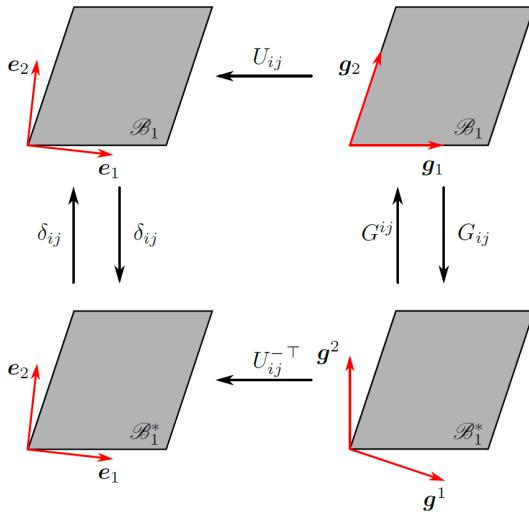
Figure 1.19: Schematic illustration of the transformations in the current configuration $\mathscr{B}_1$ between Green-Naghdi's frame $\{\boldsymbol{e}_i\}$ and the covariant $\{\boldsymbol{g}_i\}$ and contravariant $\{\boldsymbol{g}^i\}$ fibre parallel frame [49].

The orthogonality condition of co- and contravariant base is satisfied by $\boldsymbol{g}^i \cdot \boldsymbol{g}_j = \delta_j^i$. Doing so enables to formulate Equation 1.3 with respect to a non-orthogonal fibre-parallel frame via incremental stress summation within the current configuration [49]

$$[{}^{t+dt}\Delta\boldsymbol{\sigma}^{\mathrm{e}}]_{\{\boldsymbol{g}_i^* \otimes \boldsymbol{g}_j^*\}} = [\mathbb{C}]_{\{\boldsymbol{g}_i^* \otimes \boldsymbol{g}_j^* \otimes \boldsymbol{g}_k^* \otimes \boldsymbol{g}_l^*\}} : [{}^{t+dt}\Delta\boldsymbol{\varepsilon}]_{\{\boldsymbol{g}^{*k} \otimes \boldsymbol{g}^{*l}\}}, \qquad (1.5)$$

This implicates an inherent path dependency of such a material formulation, that can be problematic for non-monotonous, physical nonlinear deformations. Following this approach, hypoelastic and hypoviscoelastic models have been successfully applied for engineering textiles [90,259–261], thermoplastic organosheets [86,262] and UD-tapes [48].

Hyperelastic approaches. A second, common approach to formulate the constitutive material behaviour for large deformations is based on a

stored strain energy function ψ (potential), from which the second Piola-Kirchhoff stress tensor $\boldsymbol{S}$ can be derived by derivations according to [254]

$$\boldsymbol{S} = 2\frac{\partial\psi(\boldsymbol{C})}{\partial\boldsymbol{C}}. \tag{1.6}$$

Here, $\boldsymbol{C}$ is the right Cauchy-Green tensor. The energy function ψ can also be expressed by a set of invariants I_i of the left or right Cauchy-Green tensor [263]

$$\boldsymbol{S} = 2\sum_{i=1}^{N}\left(\frac{\partial\psi}{\partial I_i}\frac{\partial I_i}{\partial\boldsymbol{C}}\right). \tag{1.7}$$

For material modelling, a St. Venant-Kirchhoff material model is widely applied [254]. It yields a physically linear relation between the second Piola-Kirchhoff stress tensor $\boldsymbol{S}$ and the Green-Lagrange strain $\boldsymbol{E}$

$$\boldsymbol{S} = \mathbb{C}\colon \boldsymbol{E}, \tag{1.8}$$

based on the fourth order elasticity tensor $\mathbb{C}$. The elegance of this approach originates from the fact that the second Piola-Kirchhoff stress provides the work conjugate to the Green-Lagrange strain with respect to the initial undeformed configuration $\mathscr{B}_0$. Thus, in contrast to a hypoelastic formulation, hyperelastic constitutive equations can be formulated with respect to the reference configuration. This is beneficial because the principal material orientations can be aligned with the Cartesian base vectors, leading to an intrinsical consideration of the fibre reorientation during large shear deformation [49, 103]. Additionally, $\boldsymbol{S}$ (cf. equation 1.8) can be directly mapped to the current, non-orthogonal configuration $\mathscr{B}_1$ by [254]

$$\boldsymbol{\tau} = \boldsymbol{F}\cdot\boldsymbol{S}\cdot\boldsymbol{F}^{\top} \quad\text{and}\quad \boldsymbol{\sigma} = \frac{1}{J_1}\boldsymbol{\tau} \quad\text{with}\quad J_1 = \det(\boldsymbol{F}), \tag{1.9}$$

where $\boldsymbol{F}$ is the deformation gradient, $\boldsymbol{\tau}$ the Kirchhoff and $\boldsymbol{\sigma}$ the Cauchy stress (cf. Figure 1.20). Another advantage compared to hypoelastic formulations is the path and time step independence, as the stored internal energy solely depends on the total deformation $\psi = \psi(\boldsymbol{F})$ [254].
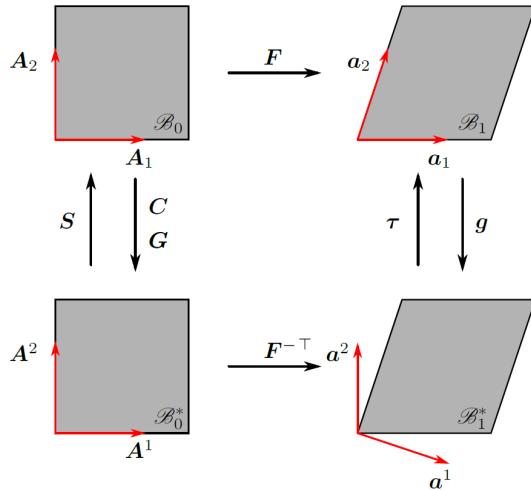
Figure 1.20: Schematic illustration of the definition of the metric and stress tensors as mapping between the covariant initial $\mathscr{B}_0$ and covariant current $\mathscr{B}_1$ and the according contravariant configurations $\mathscr{B}_0^*$ and $\mathscr{B}_1^*$ [49].

Consequently, hyperelastic material formulations are widely applied in forming simulation [217]. Strain-based definitions (cf. equation 1.6) have been among the first utilized by Thije et al. [264] and Haanappel et al. [85] for thermoforming simulation. Rate-dependency of the pre-impregnated material can be introduced via an isotropic, linear or non-linear Voigt-Kelvin approach, where the viscous part is addressed by a Cross model [265]. Dörr [49,114] applies a hyperviscoelastic material formulation within a physically decomposed user element, which captures both viscoelastic membrane and bending behaviour. Moreover, he introduces a non-linear

generalized Maxwell approach to model the viscoelastic behaviour during thermoplastic UD tape forming more accurately.

Beyond that, several invariant approaches are present in literature (cf. Figure 1.6). The first approaches have been presented by Aimène et al. [266], Peng et al. [267] and Dridi et al. [268] for woven fabrics. Gong et al. [269] have introduced tension-shear-coupling via coupled dependencies of the invariants. Peng et al. [270] and Gong et al. [271] have presented modifications of their approaches for woven fabrics, which special emphasis on prepregs and organosheets.
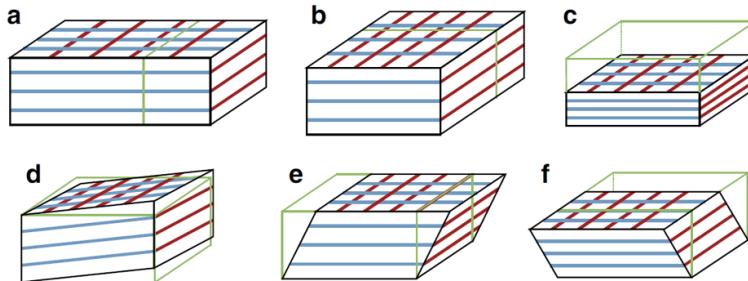
Figure 1.21: Macroscopic deformation modes of an interlock reinforcement | (a,b) in-plane stretches; (c) Transverse Compaction; (d) in-plane shear; (e,f) transverse shear [272].

Using additional invariants for compaction and out-of-plane shear (cf. Figure 1.21) an expansion to three dimensions is possible [249,273]. Guzman-Maldonado et al. [28, 82] have introduced thermo-mechanical behaviour to this 3D approach to simulate the thermoforming process.

Recent work by Denis et al. [274] captured dissipative effects during non-monotonous shear-deformation, which is usually neglected in the macroscopic simulation approaches, but yet experimentally observed for decades [132].

Generalized continua approaches. Another promising approach focuses on second order gradient approaches [249]. Despite solely using a first-order energy potential ψ_{I}, the authors propose to introduce additional terms based on a second-order energy potential ψ_{II}, which can be expressed as [275]

$$\psi(\boldsymbol{C}, \text{grad}(\boldsymbol{C})) = \psi_{\text{I}}(\boldsymbol{C}) + \psi_{\text{II}}(\text{grad}(\boldsymbol{C})). \qquad (1.10)$$

Here, the second-order energy potential ψ_{II} is formulated via spatial derivatives of the Right Cauchy-Green deformation tensor $\boldsymbol{C}$. Using this approach, the in-plane shear transition zones of the BET have been successfully modelled for the first time with a macroscopic approach [229, 230, 275] as such approaches allow to capture in-plane bending stiffness. Moreover, local in- and out-of-plane bending of thick interlock fabrics during three-point bending tests are modelled using kinematic measures for the second-order energy potential ψ_{II} [249, 272, 275]. As Dörr [49] points out, for thin reinforcements, the common approach to account for membrane and bending behaviour in a decoupled fashion resembles the introduction of a second-order energy potential in the case of out-of-plane bending, because it allows for an independently formulated strain energy potential based on the kinematic measure of curvature. An application of such a second gradient approach to forming simulation is for example provided by Barbagallo et al. [276]. In any case, the promising goal to consider mesoscopic effects on macroscopic scale demands for further research.

Semi-discrete approaches. Finally, an intermediate approach can be applied, which can be referred to as *Semi-discrete approaches* [49,88]. Based on a decomposition of an element into unit cell representation and combined contribution to the constitutive equitation of each cell, the virtual work can be formulated based on yarn tension and shear deformation [277, 278]. Initially presented by Boisse et al. [279], Hamila et al.

[277] have introduced out-of-plane bending stiffness. Several adaptations of this approach for woven engineering fabrics [246, 280], thermoplastic prepregs [123, 281] and biaxial NCF [109] have been proposed in literature [23, 88].

1.2.5 Mould-filling simulation

Mould-filling simulations at macro-scale aim to model the injection of large complex structures. As a consequence of the mould-filling related mechanisms introduced in Figure 1.11, this implies modelling the porous media throughflow and possible superficial fluid domains. The former requires consideration in all LCM process, including WCM, as a void-free, homogenous infiltration of the stack is desired for the final part [26]. For WCM, superficial fluid is normally avoided via spreading distributed resin application, pre-heating of stack and resin, and suitable impregnation times before processing [9, 69]. It is avoided because it reduces process robustness and favours process defects such as FiFD. Hence, the relevance and occurrence of superficial flows depend on applied process parameters and the complexity of the part geometry [73]. Similar to porous media flow, modelling heat tranfer and isothermal or non-isothermal curing is important for all LCM processes [21]. Similar applies to residual strain-induced warpage [18].

Like draping, mould-filling must be treated as a multi-scale phenomenon (cf. Figure 1.12). Flow progression between and around the filaments of a roving refers to the micro-scale. A meso-scale view is adopted when a roving's filaments are considered a homogenous porous medium surrounded by fluid. Similar to draping, these two views are usually solely applied for the development of analytical or empirical equations e.g. Gebart model [180] or virtual material characterization using representative unit cells [282–286]. Similar to forming simulation, only macroscopic approaches

can be solved efficient enough to describe industrial-scale part dimensions [2]. Following the scope of this work, this section focuses on macroscopic modelling.

In the following sections, first the governing equations are outlined (cf. Section 1.2.5.1). In Section 1.2.5.2, their numerical implementation and different discretisation strategies are described based on the individual requirements of relevant processes. Eventually, a brief introduction on modelling Fluid-Structure-Interaction (FSI) in mould-filling is presented (cf. Section 1.2.5.3).

1.2.5.1 Governing equations

The two governing equations for compressible fluids are mass and momentum conservation. The angular momentum balance is intrinsically satisfied by the symmetry of the stress tensor. Both mass and momentum equation relate a change of mass or momentum within a considered volume to a possible flux of these quantities over the control volumes' surfaces [287]. Assuming an incompressible and Newtonian fluid allows for further simplification and assumptions. For mass conservation, incompressibility yields a divergence-free control volume (CV) according to

$$\frac{\partial \rho}{\partial t} + \text{div}\,(\rho \boldsymbol{v}) = 0 \xrightarrow[\rho=\text{const.}]{} \text{div}\,(\boldsymbol{v}) = 0, \qquad (1.11)$$

where the fluid density is denoted by ρ and the velocity vector by $\boldsymbol{v}$. Conservation of momentum in differential form is given by

$$\frac{\partial (\rho \boldsymbol{v})}{\partial t} + \text{div}\,((\rho \boldsymbol{v}) \otimes \boldsymbol{v}) = -\text{grad}\,(p) + \text{div}\,(\boldsymbol{\tau}) + \rho \boldsymbol{f}, \qquad (1.12)$$

where $\boldsymbol{\tau}$ represents the viscous friction tensor, p the isotropic pressure and $\rho \boldsymbol{f} = \rho \boldsymbol{g} + \boldsymbol{s}$ are external body forces (e.g. gravity vector $\boldsymbol{g}$ or a source $\boldsymbol{s}$). From left to right, the first term of Equation 1.12 refers to the change of momentum over time in a fixed material frame, whereas the second

term accounts for in- and outflow of the control volume (convection). The third and fourth term account for normal and shear forces respectively originating from fluid pressure and friction acting on the control volume (CV).

For an isotropic Newtonian fluid, the scalar shear forces $\tau = \eta \dot{\gamma}$ are expressed based on the scalar share rate

$$\dot{\gamma}_{\text{eq}} = \sqrt{2 \boldsymbol{D}^{\text{dev}} : \boldsymbol{D}^{\text{dev}}}, \tag{1.13}$$

which can be calculated based on the deviatoric part of the strain rate tensor according to

$$\boldsymbol{D}^{\text{dev}} = \boldsymbol{D} - \boldsymbol{D}^{\circ} \quad \text{with} \quad \boldsymbol{D}^{\circ} = \frac{1}{3} \text{tr}\left(\boldsymbol{D}\right) \boldsymbol{I}, \tag{1.14}$$

where $\boldsymbol{I}$ is the second order unit tensor and the strain rate tensor is expressed according to

$$\boldsymbol{D} = \frac{1}{2} \left(\text{grad}(\boldsymbol{v}) + \text{grad}\left(\boldsymbol{v}^{\top}\right) \right). \tag{1.15}$$

While resin is injected or redistributed, low Reynolds numbers $\text{Re} \leq 1$ are present, which allows to neglect inertia effects $(\text{div}\left((\rho\boldsymbol{v}) \otimes \boldsymbol{v}\right) \to 0)$ compared to internal friction. Furthermore, quasi-stationary state can be assumed $(\partial(\rho\boldsymbol{v})/\partial t \to 0)$. Moreover, an external body force $\boldsymbol{s} \to 0$ can be neglected, as solely gravity needs to be taken into account. This leads to the widely applied Stokes equation [21]

$$0 = -\text{grad}(p) + \eta \, \text{div}\left(\text{grad}(\boldsymbol{v})\right) + \rho\boldsymbol{g}, \tag{1.16}$$

which, when integrated over a homogenised porous CV, yields the Brinkman equation

$$0 = -\text{grad}(p) + \eta \, \text{div}\left(\text{grad}(\tilde{\boldsymbol{v}})\right) - \eta \boldsymbol{K}^{-1} \boldsymbol{v}_{\text{D}} + \rho\boldsymbol{g}. \tag{1.17}$$

Here, a volume-averaged velocity $\boldsymbol{v}_{\mathrm{D}} = \varphi \boldsymbol{v}_{\mathrm{f}}$ is introduced to account for the fibre volume (porosity $\varphi = (1 - \phi)$) in the porous medium. This introduces the permeability $\boldsymbol{K}$ of the porous medium. Further, viscous forces are usually neglected as the permeability values are very small ($\eta \operatorname{div}(\tilde{\boldsymbol{v}}) \to 0$).

Ultimately, this leads to the well-known and frequently applied Darcy equation [167]

$$\boldsymbol{v}_{\mathrm{D}} = -\frac{\boldsymbol{K}}{\eta \, \varphi}(\operatorname{grad}(p) - \rho \boldsymbol{g}) \tag{1.18}$$

for a flow of an incompressible Newtonian fluid through a porous medium. For RTM, the pressure gradients dominate Equation 1.18 – gravity can be neglected [19, 288]. In case of VARI or WCM body forces due to gravity need to be accounted [9, 73].

During mould-filling, saturated $S = 1$ and unsaturated flow $0 \leq S < 1$ domains are present and interconnected by the current flow front position. Darcy's law can be combined with mass conservation and rewritten using a point-wise defined saturation between $S = 0$ (dry, flow front) and $S = 1$ (saturated domain), which is known as Richard's law

$$\frac{\partial S(t)}{\partial t} = \operatorname{div}\left(-\frac{\boldsymbol{K}(S, \phi)}{\eta}\operatorname{grad}(p)\right) . \tag{1.19}$$

To solve these partial non-linear differential equations, three typical boundary conditions can be prescribed to the edges of the control volume [287]. Dirichlet conditions impose fixed values such as a predefined inlet pressure or velocity. In contrast, Neumann conditions impose gradient-based conditions for pressure or velocity. A rather rarely used superposition of both types is termed as Robin condition [21].

1.2.5.2 Numerical approaches

The numerical implementation of these equations for mould-filling applications has been studied extensively within the last 30 years, mainly focused on injection during VARI or RTM processes [2, 19, 21, 61]. For the latter, simulation models based on anisotropic porous medium through-flow have been state-of-the-art for many decades and part of several commercial software codes [19, 34, 289–291]. Moreover, consideration of non-isothermal flows and reactive flows is important to determine the fluid's viscosity and thus the resulting fluid progression and mould pressure [32, 65, 66, 292].

The capabilities of the models strongly depend on their intended field of application and the amount of deformation captured by the approach. Accordingly, several modelling and discretisation strategies and solving techniques have been proposed in literature. They range from Finite Volume (FV) [32, 39, 293] to Finite Differences (FD) [294] techniques. Moreover, conforming [289–291] and non-conforming [19, 34] FE-based formulations with additional control volumes (FE/CV) [290, 295–298] to account for mass conservation and interface flows are adopted. Coupled approaches using discrete interfaces such as the Eulerian-Lagrangian-Methods (CEL) [299, 300] are applied.

Using FV-based formulations is beneficial because it allows for straight-forward integration of the equations over the cell volume [293]. Moreover, mass conservation is ensured intrinsically because interface flows are determined based on the cell centre values of the elements on both sides – thus ensuring matching interface values. A 1D compaction can be modelled using a moving mesh, as has been demonstrated by Seuffert et al. [39]. This can enable the modelling of the CRTM process for minor challenging geometries. Although rather exceptional, FV-based formulations can be used for solid mechanics, including large deformations as Cardiff et al. [293] have demonstrated using a Lagrangian cell-centred FV solution methodology for the simulation of metal forming processes.

Mould-filling or simultaneous fluid progression has not been addressed in Cardiff's work.

However, most of the proposed models utilise FE-based formulations of the Navier-Stokes equation [301], Stoke's equation [296, 302], Brinkman's equation [303] or Darcy's equation [289, 290, 295]. Following the conventional FEM approach, the equations are implemented in their weak form [254] using element shape functions for spatial discretisation and a distinct number of integration points. Although providing challenges in terms of mass conservation [295, 304, 305], these formulations allow for a simulation of the direct coupling between fluid progression and solid mechanics during large deformations [61, 299, 306, 307].

Implicit time integration schemes are usually applied to achieve an unconditionally stable solution for the fluid velocity and pressure field [61]. Nonetheless, the models that have been proposed in literature are not able to account for sufficiently large deformations and relative slip between the layers as required for draping. Hence, no direct adaption of any of the existing mould-filling model to account for WCM process modelling is feasible.

Flow front reconstruction. Regardless of whether single-phase (only fluid) or multiphase (air+fluid) flows are modelled [308], a transient reconstruction of the current flow front position is required in each time step [309], often referred to as Moving-Boundary-Problem. To overcome this difficulty without remeshing, methods like for example the Volume-of-Fluid (VoF) approach are used [309–311] (cf. Figure 1.22).

To reconstruct or numerically approximate the interface within the cells around the flow front, a transient level set function $\Phi_{\text{set}} \in [0, 1]$ can be introduced (cf. Figure 1.22 (b)). Similar to the saturation S in Richard's law (cf. Equation 1.19), the level set function indicates the ratio between pure fluid and air (void).
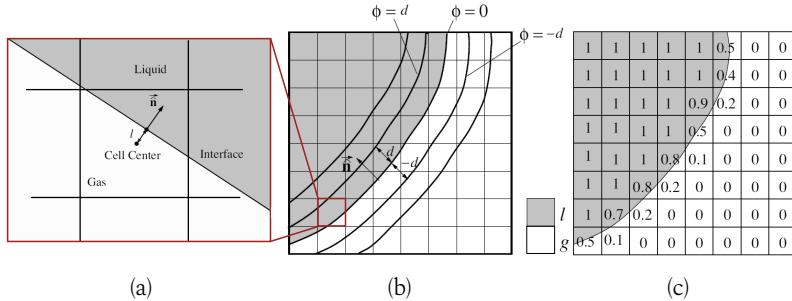
Figure 1.22: Illustration of the VoF method [311] | (a) Linear gas-fluid interface reconstruction; (b) Isolines around the interface; (c) Resulting cell-based saturation.

Porous interface coupling.   A suitable coupling between porous through-flow and superficial pure fluid regions provides challenges in terms of modelling, even without deformation of the porous medium (cf. Figure 1.23). This applies in particular to a gap flow in CRTM [39], as well as to other LCM processes such as VARI and WCM [26, 88, 307] (cf. Figure 1.23 (a)). As outlined in Figure 1.23 (b), Stokes flow (cf. Equation 1.16)
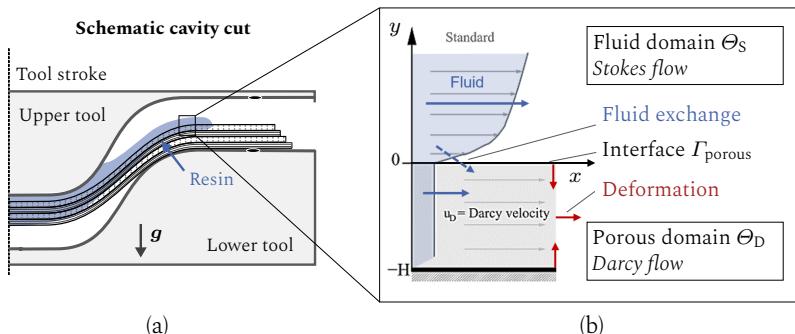
Figure 1.23: Porous interface coupling | (a) Schematic view cut of possible flow progression during mould closure in WCM; (b) 1D illustration of the velocity profile in superficial and porous domain (expansion based on [312]).

is usually assumed for the superficial (fluid) domain Θ_S, whereas Darcy's law (cf. Equation 1.18) is utilized to model the flow through the porous

domain Θ_D [313]. As both equations are different systems of partial differential equations, it has not yet been completely clarified what kind of conditions should be imposed at the interface Γ_{porous}. Moreover, it is not yet clear whether a strict interface can account for the, in reality, heterogeneous transition zone between pure fluid and porous domain. [312]. For example, experiments using 1D flow channels with porous media inserts have revealed that the straightforward approach of ensuring continuity of mass flow (velocity) and pressure (stress) at the interface, as illustrated in 1.23 (b), provides a rather bad prediction [312].

Consequently, several different approaches have been proposed within the last decades as this provides a general issue in many engineering fields. Levy et al. [314] suggest to distinguishes between near-parallel and near-normal flow scenarios, which enables further assumption at the interface. The Beavers-Joseph interface condition [315] introduces a tangential slip coefficient $\alpha_{\Gamma_{\text{porous}}}$ at the interface. Saffman [316] modifies these conditions by proposing a proportional relationship between shear stress and tangential velocity at the interface. The resulting Beavers-Joseph-Saffman (BJS) condition is frequently applied and provides a good comparison with experimental results [317]. Recently, Le Bars and Worsters [318] have introduced a viscous transition zone to the interface, which allows adjusting the interface Γ_{porous} in normal direction.

So far, the only 3D applications of a fully-coupled Stokes-Darcy model can be found in the field of VARI simulation [299, 307, 319]. In all cases the BJS interface condition is imposed at the interface, which implies mass conservation and continuity of stress (pressure) at the interface $\Gamma_{\text{porous}} = \Theta_S \cap \Theta_D$ according to [307]

$$\boldsymbol{v}_S \cdot \boldsymbol{n}_S = \boldsymbol{v}_D \cdot \boldsymbol{n}_D \quad \text{with} \quad \boldsymbol{n}_S = -\boldsymbol{n}_D \tag{1.20}$$

$$2\boldsymbol{n} \cdot \boldsymbol{D}(\boldsymbol{v}_S) \cdot \boldsymbol{t} = \frac{-\alpha_{\Gamma_{\text{porous}}}}{\sqrt{\text{tr}\,(\boldsymbol{K})}}(\boldsymbol{v}_S - \boldsymbol{v}_D) \cdot \boldsymbol{t} \tag{1.21}$$

$$p_S = p_D. \tag{1.22}$$

Here, n donates the outward normal vector of the interface between both domains $[\varTheta_S, \varTheta_D]$, t the unit tangential interface vector, D the Eulerian strain-rate (cf. Equation 1.15) associated with the Stokes' velocity field and K is the permeability of the porous medium. The drag coefficient $\alpha_{\varGamma_{\text{porous}}}$ controls the tangential velocity discontinuity at the interface.

Dereims et al. [307] have implemented in an implicit, iteratively coupled code using FE/CV within a mini-element formulation, to introduce solid mechanics, fluid-structure-interaction and finite strain of the porous media to the simulation of a stiffened panel. Although they provide a good prediction for the thickness variation during VARI, the model cannot be applied for draping-like deformations occurring during WCM.

1.2.5.3 Fluid-Structure-Interaction

Whenever fluid is injected into the completely (RTM) or partly closed mould (CRTM), it imposes drag forces on the porous medium [71,313,320, 321]. This means, spatial velocity and pressure changes impose forces on the fibre bed. As Tucker [322] and Pillai [187] have illustrated (cf. Equation 1.24), three terms contribute to the total fluid-solid-interaction

$$f_T = f_d + f_g + f_p \qquad (1.23)$$
$$\text{with}$$
$$f_d = \varphi \eta K^{-1} (v_f - v_s) \quad \text{and} \quad f_p = -\text{grad}\,(\varphi)\, p, \qquad (1.24)$$

namely viscous fluid drag forces f_d, gravity-induced pressure gradients f_g and fluid pressure (from drag) f_p. These forces are volume-averaged [N/mm^3] and act on the porous medium. Viscous drag is dominated by the relative velocity of fluid and solid, whereas the gradient of porosity governs the form drag. In LCM processes, gravity-induced drag f_g can be neglected as the pressure due to injection or compaction is usually significantly higher [59, 147]. Similarly, form drag f_p can mostly be neglected as porosity gradients are in most cases low compared to in-plane

pressure gradients [grad $(\varphi) \ll$ grad (p)]. Yet, strong local flow-induced displacements can contradict this assumption [59] as this results in increased porosity gradients.

It is commonly distinguished between weak and strong FSI. The term 'weak' refers to a one-sided coupling, whereas 'strong' FSI implies a both-sided coupling between fluid pressure and deformation, each directly affecting the other. FSI has several practical implications for CoFRP composite processing as Figure 1.24 illustrates. Recently, Hautefeuille et al.
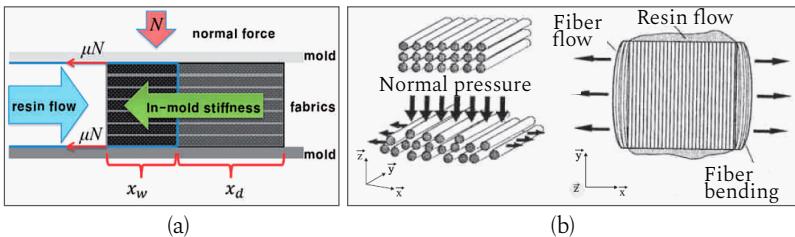
Figure 1.24: FSI-related effects during processing | (a) Fibre washout during HP-RTM [57]; (b) FiFD during transverse compaction [323].

[59, 147] and Bodaghi et al. [58] have demonstrated the ongoing relevance and challenges regarding a proper process control to prevent FiFD during RTM. As illustrated in Figure 1.24 (a), the equilibrium between resin flow-induced drag and in-mould stiffness of the fabric determines whether the stack is being infiltrated or shifted. Normal forces and frictional conditions in the dry (x_d) and wet (x_d) domain inside the mould are of high relevance. Seong et al. [60] have demonstrated by experiments that two types of deformations must be distinguished. A local flow-induced deformation is expected when flow forces exceed the in-mould stiffnesses of the material and frictional forces are sufficiently high. In contrast, a global (rigid body) sliding of the reinforcement is triggered when the flow forces exceed the frictional forces at the interfaces.

During RTM injection, relatively high injection pressure values are expectable (> 20 bar). However, similar challenges also arise during other

LCM processes (e.g. WCM) and especially during compaction of wholly or partly infiltrated fibre beds (cf. Figure 1.24(b)). As Hautefeuille et al. [59,147] have demonstrated for compaction of a completely saturated UD-NCF material, macroscopic FiFD of several centimetres can arise when there is an increase of viscosity due to an onset of curing or when a high compaction rates are applied. Moreover, they demonstrate the strong interdependency between a local in-plane deformation, which increases the permeability, and a resulting global pressure drop in the specimen. They show that a reliable calculation of the pressure field must account for local changes of FVC and permeability [59]. Hence, approximations based on a homogeneously defined permeability may only be applied to the point before local compaction, or flow-induced displacement within the stack occurs.

Analytical solutions are limited to 1D scenarios [321]. One example is, the model to predict fibre-washout during RTM developed by Bodaghi et al. [57] (cf. Figure 1.24 (a)). Generally, the complexity and non-linearity of the mechanisms inhibit a suitable analytical assessment for manufacturing-related cases. Hence, most models that consider strong FSI use Terzaghi's effective stress approach [321], usually based on FE/CV formulations [61, 290, 299, 307].

For WCM, FSI is of particularly high importance since draping and infiltration occur simultaneously. During draping and compaction, relatively high fluid pressure may occur in some saturated areas of the mould before the stack is properly constrained. Hence, suitable modelling of these effects to support process design is desired. From the presented literature survey, it is concluded that a FE/CV approach seems most promising.

1.3 Objectives

Given the literature survey in Section 1.2, the majority of recent research focuses on experimental studies in the context of WCM. They consistently reveal a strong interaction between forming and mould-filling during processing. Nonetheless, a comprehensive process analysis based on the physical mechanisms has not been proposed. In several studies, solely the indirect relationship between process parameters and obtained result on part level is investigated [11, 72, 73]. In other studies, infiltration
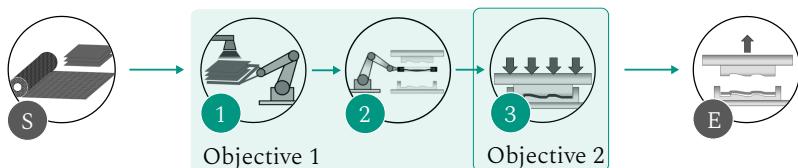
Figure 1.25: Direct WCM process route (cf. Figure 1.4) | Objectives 1: Physics-based process analysis; Objective 2: Development of a macroscopic process model.

and the presence of fluids are completely or partially neglected [69, 324]. Moreover, no suitable material characterisation methods for low-viscous infiltrated engineering textiles have been presented in literature so far.

Beyond that, numerical methods to account for simultaneous draping and infiltration are non-existent for WCM [9,72,75]. Although several promising models and concepts are proposed in literature for forming [17,88] and mould-filling [2,21] simulation, none of the proposed models in literature can be adapted to WCM.

Given these challenges, the following two main objectives of this thesis are derived for direct WCM (cf. Figure 1.25):

Objective 1. Systematic analysis of the interrelated material behaviour of textile and fluid during WCM processing with special emphasis on a comprehensive, physics-based understanding of significant mechanisms and their interdependencies to ultimately enable process modelling.

Objective 2. Development and validation of a macroscopic WCM process simulation model, allowing for a simultaneous description of draping and fluid progression under consideration of process boundary conditions.

Delimitation. This work focuses on the interaction between draping and infiltration under processing conditions. Although important, heat transfer and curing are neglected during experiments, material characterisation and modelling in this thesis. Moreover, implementation of heat transfer and curing require on a suitable process simulation model of WCM, which is first developed in this work.

1.4 Outline

A comprehensive process analysis is conducted in **Chapter 2**. Motivated and illustrated via experimental trials using a double dome geometry with transparent tooling, key process mechanism are identified and structured in Section 2.2. Moreover, three process phases during mould closure are proposed to illustrate the relevance of the identified requirements for process simulation. These are subsequently summarised in Section 2.3.

Chapter 3 is solely dedicated to the material characterisation, modelling and evaluation of the viscous draping of a woven fabric during processing. This includes the macroscopic deformation mechanisms for membrane, bending and inter-ply behaviour in dry and infiltrated state, as well as an

application to a complex demonstrator geometry (cf. Section 3.4). Apart from the infiltrated material's viscosity, fluid progression and pressure are neglected in this chapter. Finally, the results are concluded and discussed in Section 3.5.

Chapter 4 describes the path towards a macroscopic simulation approach that can predict fluid progression during moulding. A forming-driven strategy is proposed based on superimposed user elements and additional control volumes (FV/CV). First, its general suitability is demonstrated via an expansion of a conventional draping model (superimposed membrane + shell elements) with a superimposed 2D fluid progression element based on Darcy's law (DPE2D). In Section 4.3 a 3D and fully-coupled expansion of both draping and fluid progression model (DPE3D) is presented and validated using the double dome trials with woven fabric. The fluid drag is not considered in this chapter (weak FSI).

Using the verified model, its suitability to prediction FiFD is investigated in **Chapter 5**. Therefore, the process model is parametrised to describe a anisotropic unidirectional NCF. Experimental trials are conducted to adapt the membrane, bending, compaction behaviour and the permeability tensor (cf. Section 5.2). Viscous compaction trials are conducted to verify the implemented strong FSI (cf. Section 5.3.3). A parametric study highlights the importance of a suitable contact formulation and its coupling to the current flow front position (cf. Section 5.3.4). Moreover, a comparison with experimental results from literature is given in Section 5.3.5.

Finally, a summary of the obtained results is presented in **Chapter 6** followed by possible further steps towards a comprehensive WCM process model are proposed based on the combined advantages and current limitations of the presented model.

1.5 Investigated materials

Two different non-bindered materials are investigated in this work. A plane weave carbon fabric (cf. Figure 1.26) and a unidirectional carbon NCF (cf. Figure 1.27).

Woven fabric. For the majority of the tests, a balanced 12K plane weave carbon fabric (T700SC-12K-50C by ZOLTEK) is used. This applies to the systematic analysis of viscous draping mechanism (cf. Section 3) and the development of a two- and 3D process simulation model in Section 4. Its areal weight is $w_{A,0} = 330 \pm 10\,\text{g/m}^2$ and roving width is $5.0 \pm 0.5\,\text{mm}$, while initial spacing measures $2.0 \pm 0.3\,\text{mm}$.

Figure 1.26: Woven fabric.

UD-NCF. A non-crimped fabric containing unidirectional ZOLTEK fibres (Panex PX35) is used in Section 5 as it more affected by FiFD due low yarn stiffness in perpendicular direction. The areal weight of this material is $w_{A,0} = 333 \pm 10\,\text{g/m}^2$ and the initial thickness of a single ply measures $0.5 \pm 0.2\,\text{mm}$ with a roving width of $5.0 \pm 0.2\,\text{mm}$. The non-bindered carbon fibres are intertwined using polyester yarn with tricot stitch (cf. Figure 1.27).

Figure 1.27: UD-NCF.

Silicone oil. Silicone oils (QUAX GMBH, Otzberg, Germany) with different but constant viscosities are applied during all trials to avoid additional uncertainties due to non-isothermal curing effects. The investigated viscosity range of $20 - 250\,\text{mPa\,s}$ is chosen according to typical process limits.

2   Process analysis

Abstract

This chapter focuses on the physical mechanisms during WCM. Experimental trials on a double dome geometry with transparent tooling are presented, which allow for in-situ visualisation of the flow progression during moulding. The experiments demonstrate a strong mutual dependency between draping and mould-filling. Furthermore, a comparison between a woven fabric and UD-NCF material highlights a decisive impact of transversal permeability for the final resin distribution within the stack.

A systematic structuring of the identified mechanisms during processing based on available literature and own experimental results is proposed. By taking a modelling perspective, four interacting and complementary areas of physical mechanisms are identified. The first area addresses the viscous draping of the partly infiltrated stack. A suitable FE-based forming simulation approach is required, which addresses membrane, bending, compaction and contact behaviour for large deformations. Furthermore, the second area of physical mechanisms concerns fluid progression. For this, a suitable fluid submodel must predict the simultaneous fluid progression during moulding. An FE/CV-based approach for this submodel seems to be well suited considering large deformations. The coupling of both submodels further enables addressing the third area of mechanisms, namely FSI-based effects such as flow-induced fibre displacement. Moreover, heat transfer and curing are important to predict the local viscosity of the resin (fourth area). Since these four areas of physical mechanisms are not equally relevant during mould closure, process phases (draping-, coupled- and fluid-phase) are proposed to investigate the requirements for process simulation. These are summarised at the end of this chapter.

This chapter focuses on the physical mechanisms during WCM. Based on this analysis, it aims to identify key requirements for process simulation. In Section 2.1, experimental trials using a transparent double dome geometry are conducted for an in-depth investigation of the interactions between draping and mould-filling. Four areas of interrelated physical mechanism are identified (cf. Section 2.2) by combining the experimental results with the discussed literature. Finally, the findings are concluded by summarising the key requirements for process simulation (cf. Section 2.3). Although this chapter mainly focuses on a woven fabric (WF) material, additional trials are conducted with a uni-directional non-crimped (UD-NCF) fabric to investigate the impact of the significantly lower permeability in thickness direction.

2.1   Experiments with transparent tooling[1]

Experimental trials on a double dome-shaped geometry are conducted to understand the interaction between stack deformation and infiltration in WCM processes. To enable an optical tracking of the fluid progression, a transparent tooling as shown in Figure 2.1 is used. All trials are conducted in cooperation with the Fraunhofer ICT (Pfinztal, Germany). The tool was manufactured by PELZ TECHNIK GMBH in Heilbronn (Germany). The tool dimensions are outlined in Figure 2.1 (b). An electronically controllable actuator with integrated position control (EMMS-AS-140-L-HS-RSB motor combined with ESBF-BS-100-400-5P cylinder by FESTO) is used for a path-controlled closing. A circumferential blank holder is included in the upper mould. Fluid progression is tracked by two cameras, filming from above (Camera 1) and the bottom side using a 45° mirror (Camera 2).

---

[1]   Section 2.1 contains extracts of: C. Poppe, F. Albrecht, C. Krauß, L. Kärger: *A 3D process simulation model for wet compression moulding*, Composites Part A, 145:106379, 2021 [137].
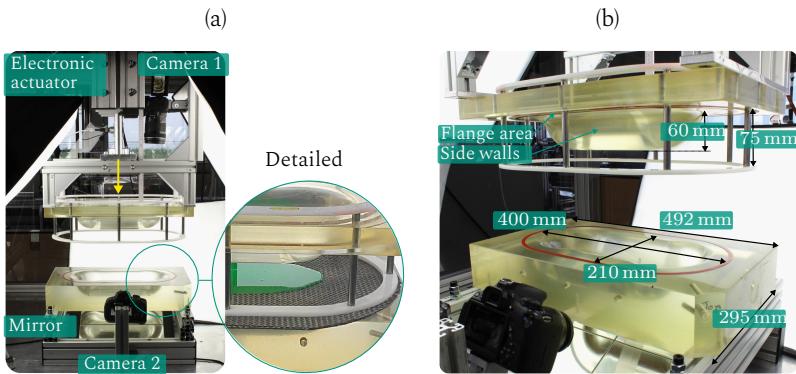
Figure 2.1: (a) Setup of Double Dome trials with transparent tooling, (b) Tool dimensions [137].

Experimental procedure.   An undeformed four-ply stack $[\pm 45]_4$ of woven fabric is placed on the lower tool to conduct a trial. A distinct amount of coloured silicon oil (120 ml) with constant viscosity is centrally applied on the top layer. All trials are conducted using a closing profile with a total duration of 4 s to close the cavity from 62 mm to 2 mm gap height. During the first two seconds, a constant closing speed of 25 mm/s is applied which is reduced to 5 mm/s for another two seconds when a remaining cavity gap of 12 mm is reached (cf. Table 2.1). Closing speed is reduced towards the end of moulding [73]. Additional sealing is placed inside the upper and lower tool to prevent leakage. The investigated configurations are summarised in Table 2.1.

Table 2.1: Transparent double dome trials | Trial configurations.

Material	η (mPas)	Amount (ml)	Soak time t_{soak} (s)	Speed $\dot{u}_\text{T}$ (mm/s)
WF	20	120	15	$25 \rightarrow 5$
WF	200	120	30	$25 \rightarrow 5$
UD-NCF	20	120	15	$25 \rightarrow 5$
UD-NCF	100	120	30	$25 \rightarrow 5$

Viscosity values are chosen to explore the processing limits. These limits depend on the fabric's permeability in thickness direction (K_{33}), the prior infiltrated area of the stack, the resins viscosity and the soaking time before processing. Pre-trials and permeability measurements show (cf. Table A.1), that the values for K_{33} of the UD-NCF are approximately 63 % lower (FVC of $\varphi = 0.3$), than the values obtained for the woven fabric in uncompressed state. Moreover, an increase of K_{33} with decreasing number of layers is observed for the woven fabric, caused by small gaps between the crosspoints [325]. Therefore, a lower viscosity of 100 mPas is used for the UD-NCF trials. To ensure reproducibility, a constant soaking time of t_{soak} 15 s or 30 s in case of the trials with increased viscosity is waited for before starting a test. The soaking times are selected to provide a comparable fluid spreading at the topside of the stack during all trials. Each trial is conducted three times.

During the evaluation, captured video footage is optically corrected and synchronized to the current remaining cavity height provided by the cylinder position. Moreover, each ply's initial and final (infiltrated) weight is measured to estimate the final resin distribution within the stack. Since no curing takes place, the final state is evaluated by separating the single plies after draping. The stack absorbed between $77 - 83\,\%$ of the applied fluid. Thus, some fluid remained within the lower tool.

Results. During mould closure, stack deformation and fluid distribution lead to noticeable differences between dry and viscous reaction forces (cf. Figure 2.2). This difference to the dry forming forces increases with decreasing cavity height. It is expected that the infiltrated deformation behaviour primarily causes the differences between 60 and 10 mm. Significant fluid progression occurs mainly within the last 5 mm of tool closure. In this final phase of moulding, the measured forces are higher for the trials with a viscosity of 200 mPas mainly because the required infiltration pressure increases along with the fluid's viscosity. Moreover, rate-depend reaction forces are observed for the pre-infiltrated trials (20

and 200 mPas). In contrast to the dry reference, obtained reaction forces decrease when the closing speed is reduced from 25 to 5 mm/s.
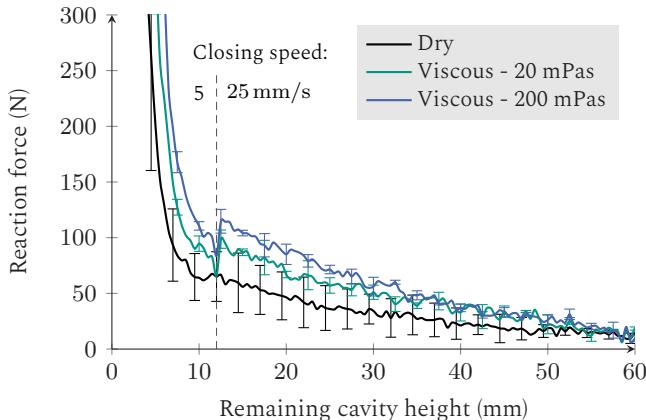

Figure 2.2: Reaction forces for dry and viscous forming of the woven fabric material using the double dome geometry with transparent tooling [137].

The results in terms of fluid progression during processing of woven fabric material are shown in Figure 2.3. Trials using a low-viscous oil are presented in the top row. The bottom row displays the results of the high-viscous oil trials. In both cases, pictures at discrete, remaining cavity heights (50 - 2 mm) indicated by the numbers (1) to (6) are presented. All images are subdivided into a top and bottom view to directly assess the infiltration in thicknesses direction.

The low-viscous fluid application leads to pronounced leaking (drops) in thickness direction before mould closure, as for example indicated in the top left picture (1). This is further intensified by small gaps within the four-ply stack, which facilitates gravity-induced infiltration of the fluid in the thickness direction. As can be seen, by following the pictures from left to right, this also results in a homogenous infiltration of the stack, as the flow front in the top and bottom plies progress quite similarly. This is illustrated, for example, by the top pictures (3) and (4), which show cavity
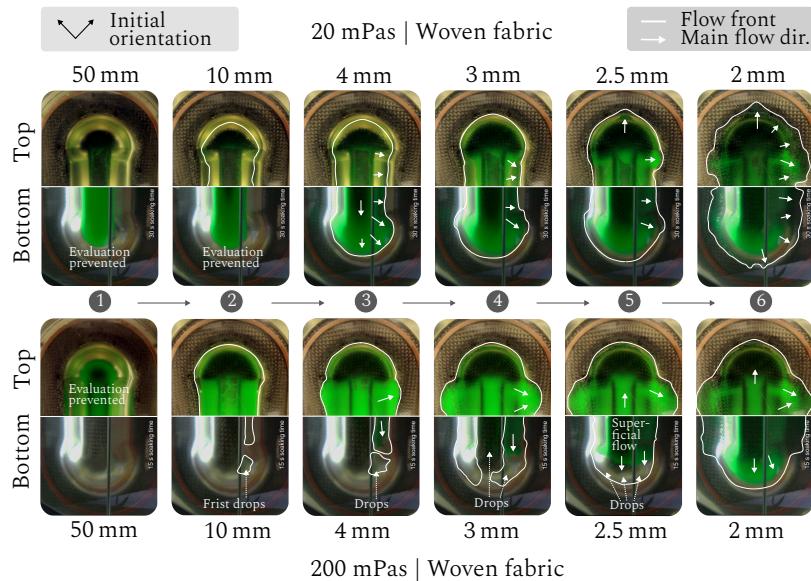
Figure 2.3: Flow front progression during viscous moulding for a four-ply woven fabric stack at different remaining cavity heights using constant viscosities of 20 (top) and 200 mPas (bottom). Photos are taken from the top and bottom sides during moulding. Fluid dripping or tool curvature can prevent a determination of the flow front position in some regions [137].

heights of 4 to 3 mm. Additionally, the homogeneity of the final infiltration state is reflected by the bar charts of the final infiltration-induced weight increase of each ply for the fully closed mould, which is presented in Figure 2.4 (a). Towards the end of the tool stroke (5,6), the additionally accumulated fluid in the lower mould is forced back into the stack.

In contrast to the trials with the low-viscous fluid, the high viscosity of 200 mPas prevents leakage in thickness direction before moulding (cf. Figure 2.3, bottom row). No fluid apart from first drops can be detected at the bottom view until a cavity height of 4 mm is reached, as shown in picture (4). Consequently, the stack is infiltrated mostly from top to bottom, like images (3) to (6) show. Thus, the differences between the top and bottom-sided fluid progression remain until the mould is almost closed

(6). As the same amount of resin is applied, the observed fluid progression is more superficial, as less fluid infiltrates in thickness direction.
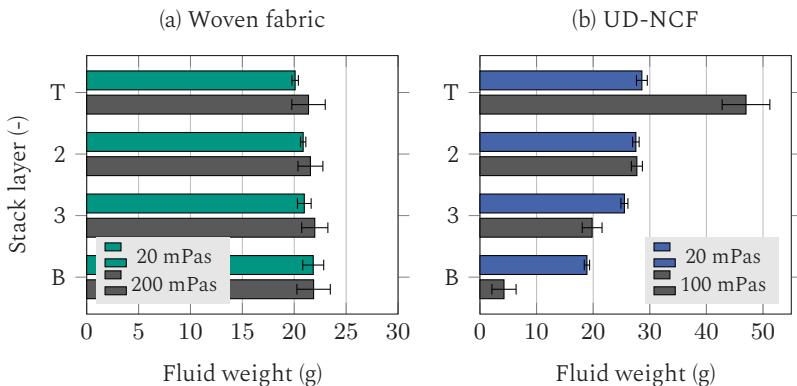

Figure 2.4: Comparison of final infiltration | Fluid weight per layer (T=Top, B=Bottom) indicating the infiltration state for (a) woven fabric; (b) UD-NCF. A significant inhomogeneity for the final resin distribution in thickness direction is only observed for the UD-NCF trials, particularly for the high viscosity.

In this work, the term 'superficial flow' describes the fluid progression on the stack's top side. This is additionally indicated by the intensity of the green coloured matrix, which shows noticeable differences between the low and high viscosity for cavity heights ≥ 3 mm. Moreover, the first infiltrated regions within the bottom ply arise at the side walls (cf. Figure 2.1 (b)) where the largest deformations occur and not within the mostly undeformed centre.

Although the final infiltration state does not differ significantly between both viscosities (cf. Figure 2.4 (a)), the infiltration path is considerably different and the infiltration remains more superficial for the 200 mPas trials. This is reasonable because through-the-thickness flow increases with viscosity, favouring fluid spreading on top of the stack instead of through it.
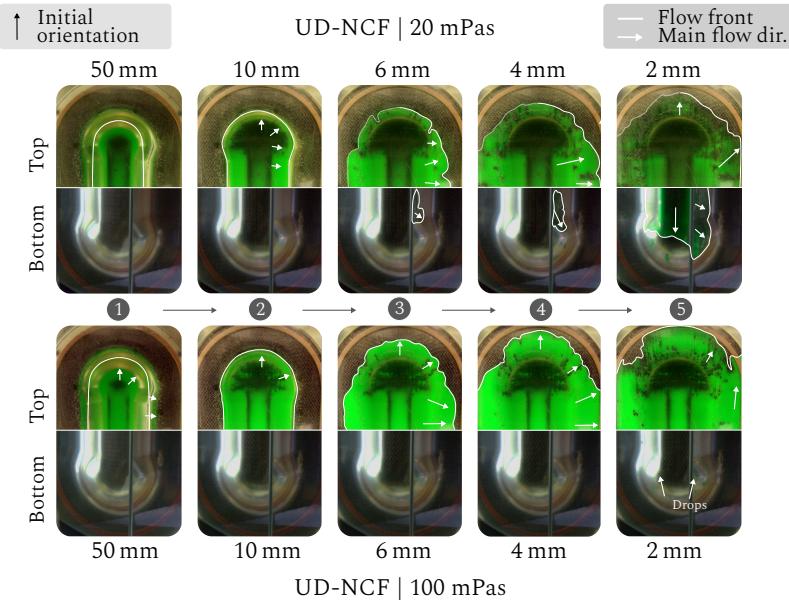
Figure 2.5: Flow front progression during viscous moulding at different remaining cavity heights with constant viscosities of 20 mPas (top) and 100 mPas (bottom) for a four-ply stack of UD-NCF.

The fluid progression for the UD-NCF material is demonstrated in Figure 2.5. Although similarities in terms of fluid progression exist, the infiltration in thickness direction is significantly hindered. For both viscosities (20 and 100 mPas), the fluid progresses mostly superficial and only towards full mould closure infiltrates the bottom ply. In contrast to the WF, a distinct inhomogeneous stack infiltration in thicknesses direction is observed for the final state (cf. Figure 2.4 (b)).

Discussion. The experimental results give an insight into the physical mechanisms during WCM. During moulding and compaction of the pre-infiltrated stack, fluid redistribution (forced infiltration) and internal dissipation (friction) within the superimposed fluid lead to increased moulding forces (cf. Figure 2.2 (b)). Similar observations have been published for

various liquid moulding processes [19, 143, 144, 149]. Furthermore, the results demonstrate that increased reaction forces are only dominant within the final 15 % of the tool stroke when first regions are completely saturated and compaction becomes the dominant deformation mechanism.

Furthermore, stack deformations and fluid progression are interrelated. First, the shape of the stack determines which part of the mould is currently occupied by the porous medium. Second, the permeability is directly affected by the local FVC. Consequently, local deformations are important for fluid progression. The infiltration in thickness direction demonstrates this, as the infiltration does not originate from the stack centre but the deformed side wall regions (cf. Figure 2.3 (4)). It is assumed that the stack deformations in this side walls cause this due to a partial reorientation of the higher in-plane permeability components K_{11} and K_{22} (cf. Table A.1) in thickness direction.
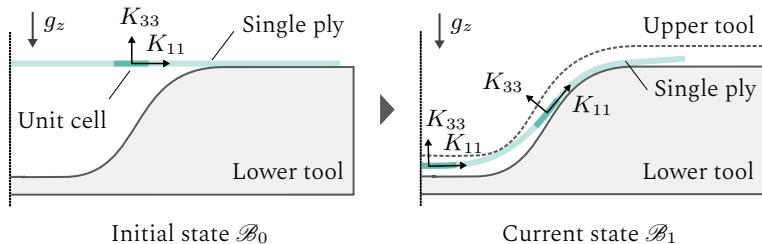
Figure 2.6: Comparison of a unit cell in initial $\mathscr{B}_0$ and current $\mathscr{B}_1$ deformation state, which leads to increased permeability in thickness direction (g_z) due to reorientation of the permeability tensor components K_{11} and K_{22}.

This facilitates infiltration in this region as $K_{11,22} > K_{33}$. At the same time, minor shearing in the region cannot compensate this. Experimental results further demonstrate that the resulting in-mould fluid progression and final infiltration quality is strongly affected by the ratio of fluid viscosity and stack permeability, especially in thickness direction. Although this has been reported in literature [9, 21, 72], the experiments for the first

time demonstrate the consequences of permeability and stack deformation for the resulting fluid progression on part level during WCM. For the WF, permeability values in thickness direction for low compaction states lead to a fairly homogenous final infiltration state for both investigated viscosities (cf. Figures 2.3 and 2.4 (a)). Yet, the fluid progresses more superficial when a higher viscosity of 200 mPas is applied. In contrast, the low transversal permeability values of UD-NCF prevent a homogenous final saturation of the stack (cf. Figure 2.5 and 2.4 (b)) for both applied viscosities. For UD-NCF, this results in a widespread infiltration of the top side, whereas the bottom side remains almost dry. Processing of UD-NCF would require increased soaking times before moulding and reduced closing speeds.

Concluding the experimental results, it is demonstrated that draping and infiltration do appear simultaneously. However, viscous draping (I) dominates the overall results for a large part of the tool stroke, whereas infiltration does so towards the end of moulding (III). Three process phases during mould can be identified as Figure 2.7 illustrates.
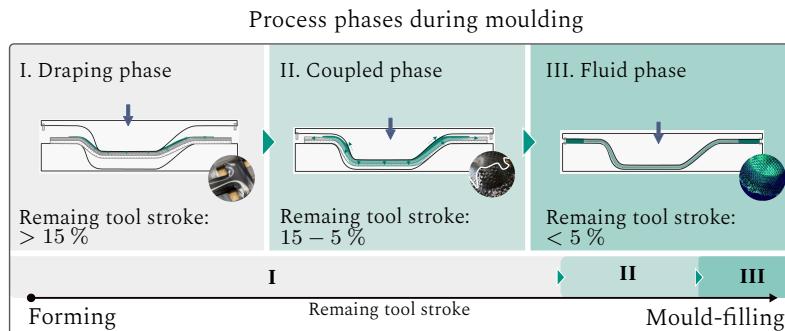

Figure 2.7: WCM process phases | Viscous draping dominates the first part of the moulding sequence. Coupled effects and fluid progression only dominate towards lower cavity heights. The provided percentages are geometry-dependent.

I. Draping phase.   Within roughly $80-85\%$ of the tool stroke, the partly pre-infiltrated textile stack is formed. This 'draping phase' is dominated by the macroscopic draping mechanisms (cf. Figure 1.6). Fluid pressure and drag forces remain low compared to forming forces. Due to gravity, resin seeps into the deforming stack or is being redistributed superficially by contact with the tool. Curing, which is neglected in this trials, is usually of minor importance as no large areal contact with the hot tool surface has taken place yet.

II. Coupled phase.   When compaction or superficial squeezing begins, the pressure in the fluid raises in the already saturated regions of the mould. This 'coupled phase' is critical for FSI since the stack is not fully constrained yet, but already locally exposed to increased fluid drag. Fluid flow, superficial or within the stack, matters in this stage [9, 73]. For industrial applications, the superficial fluid is avoided wherever possible for the sake of process robustness.

III. Fluid phase.   Finally, a 'fluid phase' is entered (remaining tool stroke $<5\%$), which is dominated by infiltration effects such as flow through porous media and, in trials with reactive matrix, curing. Here, draping is almost completed, apart from compaction. This last phase resembles a CRTM compressions step (cf. Section 1.2.1.3). As the process forces significantly depend on the fluid pressure, FSI-related mechanisms remain important.

Taking into account the outlined interactions and the high importance of the draping mechanism during the three process phases, it seems beneficial to follow a forming-driven approach.

2.2 Physical mechanisms from a modelling perspective

This section aims to cluster the relevant mechanisms during WCM to support and enable process modelling. For this work, a modelling viewpoint is taken. Identified mechanisms are structured by their physical area and the way they may be virtually described. Hence, the occurring mechanisms could also be clustered differently if, for example, a process developer or part designer view would be taken. Given the outlined experimental (cf. Section 2.1) and available results from the literature (cf. Section 1.2), Figure 2.8 proposes a systematic ordering of the occurring mechanisms by introducing four relevant areas of physical mechanisms. Each of them contains related mechanisms that should be addressed within a comprehensive modelling approach. The quarters (Q1), (Q2) and (Q4) can be investigated both individually or combined. Only FSI (Q3) requires existing submodels for direct coupling of viscous draping and fluid progression.

1. Viscous draping. The first area of physical mechanisms contains the viscous draping behaviour of the partly infiltrated textile stack. The deformation mechanisms of the processed CoFRP (cf. Figure 1.6) need to be addressed, both with experiments and numerical methods. These are commonly separated into intra-ply and inter-ply mechanisms. The intra-ply mechanisms address membrane, bending, and compaction behaviour, whereas the contact model captures the interfaces' inter-ply behaviour. As outlined in Section 1.2.2, several characterisation setups for each of the mechanisms have been proposed in literature. However, experimental characterisation of low-viscous infiltrated material states requires modifications of existing setups.

Regarding modelling, an FE-based simulation model with an explicit time integration scheme seems to be best suited for this area, given large deformations and contact slip requirements. A large number of macroscopic
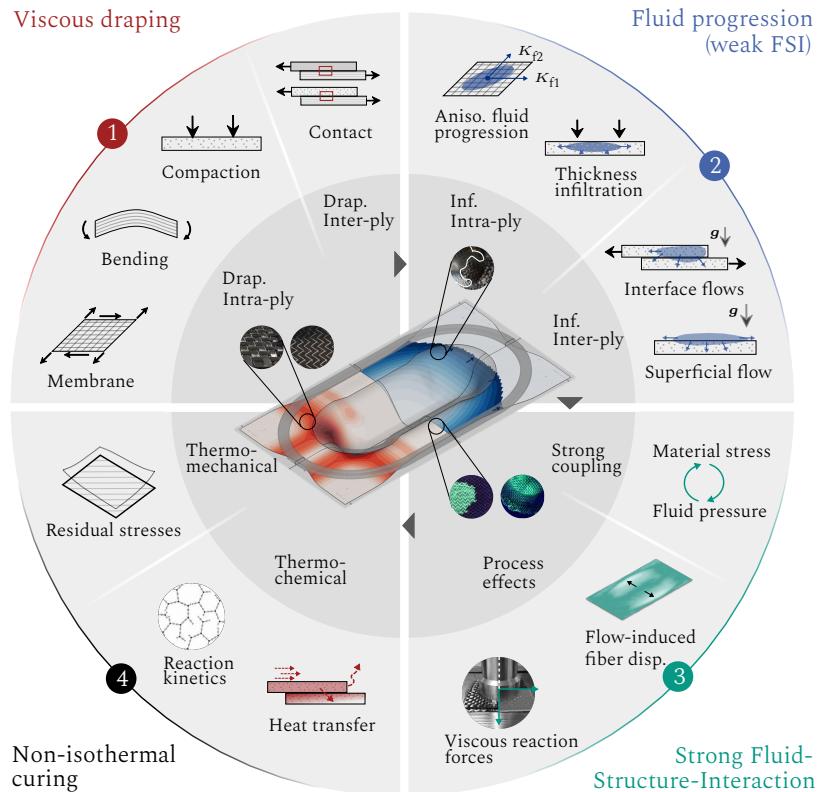
Figure 2.8: Important areas of physical mechanisms for WCM modelling clustered into four Quarters (Q1-4), taking a modelling perspective. The sequence is motivated by the relevance and coupling of the mechanism during moulding.

forming models for engineering textiles and thermoforming has been proposed in literature (cf. Section 1.2.4). As outlined, compaction is often neglected by existing forming simulation models [249, 251]. Nonetheless, it has to be addressed by the WCM process modelling due to the interaction with fluid progression. Beginning with a conventional shell-based approach, an expansion to capture out-of-plane compaction is desired.

71

The infiltration state is best addressed in a homogenous manner using viscoelastic material formulation.

2. Fluid-progression.   The second area of physical mechanisms comprises the mould-filling-related mechanisms (cf. Figure 1.11). They are also separate into intra-ply mechanisms, such as anisotropic fluid progression and thickness infiltration within the porous network, and inter-ply mechanisms related to the interfaces between the plies and superficial flows. The presented experimental results in Section 2.1 demonstrate that infiltration takes place simultaneously during moulding and is strongly affected by the local deformation state of the stack. Moreover, infiltration in through-thickness direction has a significant affect on the final infiltration state. This agrees with existing literature discussed in Sections 1.2.1.3 and 1.2.3.

Modelling of the second quarter requires an coupled fluid submodel, which takes the current state of deformation into account (weak FSI). Since this submodel is subjected to large deformations, a FE/CV-based formulation seems to be most promising given the existing literature (cf. Section 1.2.5.2). In contrast to RTM mould-filling, the fluid pressure in WCM is relatively low during most of the tool stroke. Consequently, gravity needs to be taken into account. This implies a 3D formulation for the fluid submodel to capture the experimentally observed infiltration in thickness direction.

3. FSI.   The third quarter in Figure 2.8 addresses process effects that originate from the strong interaction between stack deformation (Q1) and infiltration (Q2). This interaction is decisive for process effects, for example increased moulding forces during pre-infiltrated compaction. Moreover, undesirable process defects, such as flow-induced fibre displacement (FiFD) [59, 147] or mesoscopic fibre washing [58] from fluid drag originate from strong FSI during processing (cf. Section 1.2.5.3).

Although this area might be a direct consequence of the combined first ones, it is addressed as a separate area of mechanisms in this work. On the one hand, modelling of strong FSI requires existing submodels for viscous draping (Q1) and fluid progression (Q2). On the other hand, a suitable coupling between both submodels needs to be implemented and validated. Given the lack of a distinct interface between fluid and porous medium at macro-scale, existing literature suggest implementing an effective stress approach based on Terzaghi's law (cf. Section 1.2.5.3). One more, this favours a superimposed FE/CV-based formulation for the fluid submodel, as it allows for a combined response of draping and fluid submodel at the nodes of each element.

4. Non-isothermal curing. Finally, the last quarter contains the non-isothermal curing of the resin system during and after moulding. This includes heat transfer within the partly- and fully infiltrated stack, reaction kinetics and rheology of the thermoset resin [18]. Leading to changes in viscosity and residual stresses due to shrinkage or thermal expansion, capturing this mechanism allow to consider the temperature-time cycle during processing as well as possible related process effects such as warpage (cf. Section 1.2.3.2).

From a modelling perspective, this area (Q4) expands the three already introduced quarters by a temperature degree of freedom. In this regard, heat transfer occurs within the viscous draping model and is affected by the convective transport in the fluid model, e.g. relative fluid velocity. As viscosity changes, it affects the stresses and pressure predicted in both submodels, which implies FSI.

2.3 Concluded requirements for process simulation

On the basis of the experimental results in Section 2.1 and process analysis in Sections 2.2, the following requirements for a macroscopic process simulation for direct WCM are proposed:

1. Development of draping and fluid submodels that can be coupled and solved simultaneously
2. The draping submodel provides the deformed shape of the porous network by capturing the macroscopic deformation mechanisms during large deformations, which includes:
   2.1 Constitutive models for dry and pre-infiltrated intra-ply deformation mechanisms, namely membrane and bending
   2.2 Implementation of these constitutive equations into a FE-based approach using an explicit time integration scheme to account for large areal contact
   2.3 Expansion of these approaches to a 3D element formulation that allows for compaction during moulding
   2.4 Implementation for a contact formulation for inter-ply modelling between adjacent plies and between tools and plies
   2.5 Suitable tool modelling including geometries and relevant process boundary conditions, e.g. blank-holders or seals
3. Development and validation of a fluid submodel, describing the simultaneous fluid progression under consideration of the current deformation state of the porous textile. This implies:
   3.1 An FE/CV-based formulation of Stokes or Darcy's law ensuring mass conservation
   3.2 Prediction of anisotropic fluid progression and the resulting pressure distribution within the stack
   3.3 Modelling of forced fluid redistribution during compaction

    3.4 A method to account for fluid exchange at stack interfaces, including the consideration of large slip at the interface.

    3.5 An approach to model superficial fluid under consideration of the tool cavity

4. Expansion of FSI by a strong coupling between the draping-related material stresses and fluid-induced drag forces

5. Development of a heat transfer submodel, superimposed to the existing elements or directly embedded in one of the other submodels – ABAQUS's coupled thermo-mechanical analysis supports an introduction of the temperature degree of freedom

6. Introduction of curing kinetics and rheology by suitable models to enable viscosity, residual stresses and shrinkage predictions based on the temperature evolution

7. Overall numerically efficient implementation allowing for coupling of the submodels in a scalable manner

3   Viscous draping

Abstract

This chapter is dedicated to the systematic experimental investigation and numerical modelling of viscous draping behaviour of a pre-infiltrated woven fabric. A macroscopic FE forming simulation model is adopted for modelling, which accounts for a predefined infiltration state in a homogenised manner. Unlike other pre-impregnated materials, e.g. thermoplastics, the viscosity values of the matrix material are significantly smaller (20-250 mPas). This complicates the characterisation of pre-infiltrated textiles under processing conditions. Thus, established characterisation methods require modification. As for over 85 % of the tool stroke, the fluid pressure remains insignificant; it is neglected in this chapter.

For a systematic evaluation of membrane, bending and contact behaviour, experimental trials are conducted focusing on the impact of infiltration on the deformation mechanisms. Results show that infiltration with a low-viscous fluid significantly reduces friction between and inside the rovings. This reduces shear resistance, bending stiffness and tangential contact stresses, which improves drapeability. At the same time, infiltration introduces a rate-dependency. This may, in turn, reduce drapeability when higher viscosities and deformation rates are present. Thus, the initially improved drapeability decreases with ongoing curing during processing. Hence, precise timing between draping, infiltration and curing is decisive for process control.

Beyond that, the individual relevance of the pre-infiltrated deformation mechanisms for a comprehensive process simulation is assessed via numerical studies with parametrised material models. Moreover, a good agreement between experimental trials and simulation is achieved for a complex demonstrator. Results suggest to account for infiltration during membrane and bending deformation. In contrast, a built-in contact model without normal traction seems sufficient for the draping WCM submodel with the investigated material.

3.1   Membrane behaviour[1]

Membrane deformation due to in-plane shear provides a particularly important deformation mechanism for engineering textiles, including woven fabrics. It allows for a shape transition from a two-dimensional (2D) stack into a 3D part via fibres reorientation at the crosspoints. In addition, a small elongation in the fibre direction is possible when undulations at the crosspoints are stretched out. This is a geometrical property resulting from the applied textile architecture – the fibres themselves are considered inextensible. In-plane fibre compression is not considered as this normally results in out-of-plane buckling [47]. In the following, the woven fabric, as introduced in Section 1.5, is subjected to shear deformation in the dry and pre-infiltrated state using silicon oil to ensure a constant viscosity.

3.1.1   Experimental assessment

A reproducible and homogeneous infiltration state of the specimens during testing is assumed to be of importance because of three main infiltration-related mechanisms that are expected to have an impact on the internal friction of the rovings and hence on the measured shear behaviour response (cf. Figure 3.1 (a)). It is expected, that the resin may form a lubrication layer between the rovings at the crosspoints, which could change the frictional conditions (1), depending on fluid viscosity and possibly slip-rate. Moreover, preliminary investigations show that the resin seeps into the rovings and thickens them (cf. Figure 3.1 (b)), which is expected to influence shear behaviour due to a change in bending stiffness (2) and compaction behaviour (3) of the rovings. These mechanisms significantly depend on a homogeneous infiltration state of the specimens.

Hence, to ensure a homogeneous infiltration state during testing, the characterisation set-up should provide shear testing in a fluid reservoir.
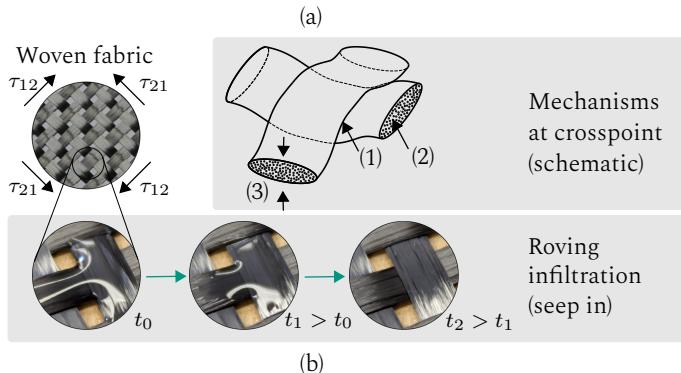
Figure 3.1: Illustration of assumed infiltration-related mechanisms affecting the shear response | (1) Change of friction at crosspoints, (2) within the roving and (3) compaction behaviour [99].

The usage of pre-infiltrated specimens within a common vertical BET (cf. Section 1.2.2.1) would prevent a homogenous infiltration state during testing. Beyond that, the changing residual weight of the specimen would be superimposed in the measured force, complicating a correct evaluation of the material response. These reasons suggest a horizontal alignment for the experimental setup.

3.1.1.1 Infiltrated bias-extension test (IBET)

The new proposed test is designed as a horizontal BET within an additional fluid reservoir (cf. Figure 3.2). As shown in Figure 3.2 (b), the rear fixture remains fixed during testing, while a steel rope with a low bending stiffness displaces the front fixture. The rope is mounted on the load cell of a tensile testing machine.
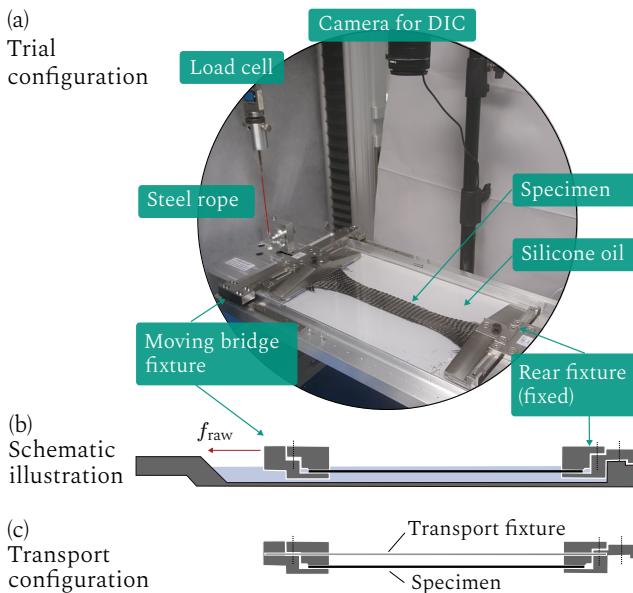
Figure 3.2: Design of the modified test (IBET); (a) Picture of the set-up in a tensile testing machine; (b) Schematic vertical section view; (c) Transfer configuration [99].

To ensure a reproducible initial positioning and prevent the initial specimen's deformation, it is clamped outside the fluid reservoir using an additional preparation table. An additional transportation fixture illustrated in Figure 3.2 (c) is used to position the undeformed fabric into the reservoir. The fixture is designed to apply high forces to ensure a suitable clamping of the specimen even within the fluid environment. An additional layer of thin rubber is used in the clamped areas to distribute normal forces and raise friction. Additional heater units can be used to heat the fluid reservoir.

Evaluation methodology. Due to the horizontal design, additional forces are superimposed to the shear resistance of the specimens. This includes frictional forces within the linear bearings (f_{fric}), which are determined using calibration tests without specimens. Furthermore, fluid resistance

is taken into account for impregnated tests as a function of viscosity and velocity ($f_{\mathrm{fluid}}(\eta, v)$), determined by prior calibration tests. Furthermore, compliance of the steel rope is taken into account via f_{raw}. Hence, the resulting forces (f_{shear}) are calculated from the raw signal (f_{raw}) by

$$f_{\mathrm{shear}} = f_{\mathrm{raw}} - f_{\mathrm{fric}} - f_{\mathrm{fluid}}(\eta, v), \tag{3.1}$$

where $f_{\mathrm{fluid}}(\eta, v)$ is not considered for dry tests. All calibration tests are conducted 10 times.

Shear angles within the mid-segment and the outer shape of the specimens are measured with an optical system during all tests. This includes a camera system with a downstream in-house DIC-Tool based on an enhancement of an open-source MATLAB script. A pattern is applied to each specimen, which is detected and tracked by the DIC algorithm. All presented results are based on the optically measured angle within the mid-segment.

Experimental procedure.　An Inspekt 50 static tensile testing machine by Hegewald & Peschke (Nossen, Germany) in combination with a 100 N load cell is used to record the force-displacement curves during testing. Silicone oils with three different viscosities (20, 135 and $250 \pm 3\,\mathrm{mPas}$) are used as test fluids. Since rate-dependency of the infiltrated material is expected, three different velocities 100, 350 and 700 mm/min are tested. The specimens remain within the fluid for two minutes before the testing to ensure a complete and homogeneous infiltration. Five to eight specimens are tested for every configuration, depending on the actual scattering. Beyond that, additional uni-axial tests with dry samples (280 x 140 mm) within a BET set-up are conducted to parametrise the elongation behaviour in the fibre direction, which is needed for parametrisation of the numerical model in Section 3.1.2.

3.1.1.2 Preliminary investigations

Before the infiltrated trials, additional dry tests are performed to validate the horizontal positioning of the specimen, the impact of mesoscopic effects and the resulting prediction accuracy of the textiles' locking angle.

IBET Validation. For the validation of the IBET, dry sample results are compared to a conventional BET. It is observed that the results are in good agreement (cf. Figure 3.3). However, the standard deviation for the IBET is slightly increased, especially for low shear angles and forces, due to the uncertainties within the forces determined by equation (3.1). Moreover, gravity leads to some sag of the dry specimens ($\approx 1\,\mathrm{cm}$), which does not measurably influence the results.
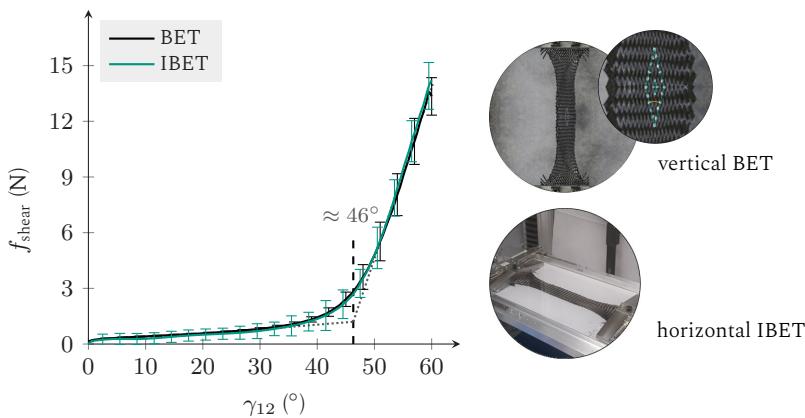

Figure 3.3: Dry specimen response during conventional BET and the modified IBET and illustration of optically tracked pattern [99].

Besides that, sag vanishes for infiltrated tests. Hence, the horizontal IBET design provides comparable results to the BET and can consequently be applied for the shear characterisation of infiltrated woven fabrics.

Mesoscopic effects.   Before the main trials, additional picture frame shear tests are conducted to ensure a valid prediction of the materials locking angle despite mesoscopic effects, such as a relative slip of fibres and fibre bending. These effects have also been reported for comparable materials [108, 326].
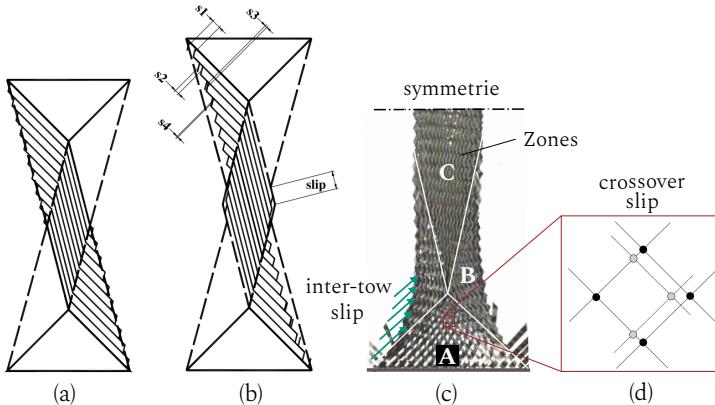
Figure 3.4: Comparison of mesoscopic effects | (a,b) Schematic illustration for BET by [106]; (c) Compared own results with IBET [99]; (d) Illustration of crossover slip [106].

Similar to the findings that have been published by Harrison et al. [108] (cf. Figure 3.4 (a,b)), crossover and inter-tow slip occurs during higher shear angles within the Zone C as illustrated in Figure 3.4 (c). Beyond that, in-plane bending of the fibres and rovings in Zone A are found, as exemplarily reported by Bel et al. [109]. According to Harrison et al. [108], the BET can predict the material locking angle correct, despite the oc-curring mesoscopic effects. Additional PF tests with dry specimens are conducted to validate this for the here applied material. It is assumed that a validation of the dry material state is sufficient, because a comparison of the final deformation states did not indicate any correlation between mesoscopic effects or the slip distances of the rovings and their infiltra-tion state. Nearly identical local slip is found in all specimens, leading to one curve for the outer shape of the textiles (cf. Figure 3.15).

Locking angle. A common way to determine the locking angle of the material is based on the intersection of two tangents using the shear-force curve (cf. Figure 3.3). This approach requires homogenisation of the shear forces when comparing PF and BET results [110]. Unfortunately, the above outlined mesoscopic effects may affect the measured shear forces for the BET. Moreover, PF results could be affected by pre-tension of the fibre due to misalignment of the fibres or roving bending [327]

An alternative approach solely using kinematic information is used to determine the material locking angle to prevent a possible impact of these effects. In the case of the BET or IBET, the locking angle is determined by a noticeable change of the slope between displacement and resulting material shear angle as illustrated in Figure 3.5 (black filled dot)).
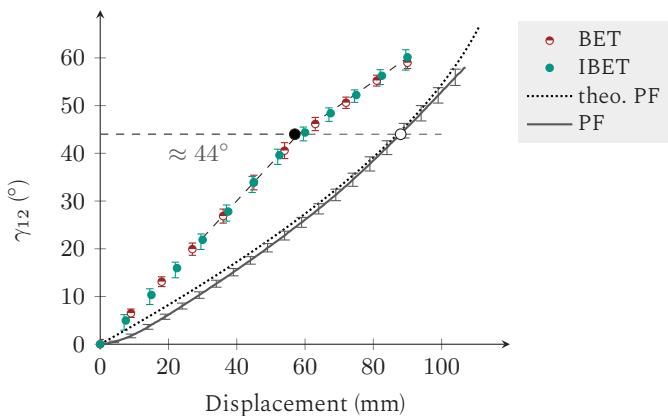

Figure 3.5: Comparison of the determined locking angle of BET, IBET and PF using the angle-displacement curves of [99].

This marks the point where tensioned fibres in Zone C (cf. Figure 3.4) have fully closed the gaps between the rovings and get into contact with each other. Further shear deformation due to compaction of the rovings

is possible. Therefore the shear angle still increases. From here onwards, higher tensions in Zone C favour mesoscopic slip.

Regarding the PF, the material locking angle is identified by comparing theoretical and measured shear angle. (cf. Figure 3.5(white filled dot)). Due to crosspoint friction, the measured shear angle lags slightly behind. This deviation is constantly reduced during shearing due to increased fibre tension until the material starts to lock. Similar to the BET, this leads to a change in the slope of the displacement-angle curve. However, this change is less pronounced due to the fully constrained boundary of the specimens during PF trials.

Using the displacement-shear-curves of the PF, BET and IBET pre-trials (cf. Figure 3.5), a comparable locking angle of $44 \pm 2\,°$ is found. This result is comparable to the locking angle ($46\,°$) determined with the shear-force curve in Figure 3.3 using BET and IBET. It is concluded that the IBET can predict the locking angle accurately. This indicates a negligible influence of mesoscopic effects below the locking angle. Furthermore, the results show that the commonly applied approach for the locking angle determination using the shear-force curve yields comparable outcomes. Consequently, the latter method is used to evaluate the locking angle in the following infiltrated trials.

Fibre elongation.   Due to undulation implied by the woven's architecture, minor elongation in fibre direction is possible. Additional uni-axial tensile tension tests are conducted in the dry state for parametrisation. The experimental result are displayed in Figure 3.11 of Section 3.1.2.

3.1.1.3 IBET results

The experimental results of the main trials are shown in Figures 3.6 to 3.8, including additional detailed views on the below-locking angle region of

0 to 40 °. The resulting curves of the dry specimens can be used as a reference line since the dry results are rate-independent at room temperature.
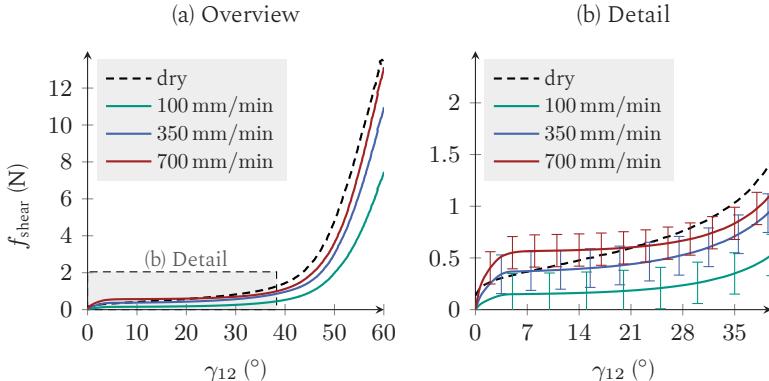
Figure 3.6: Experimental results using the IBET | Infiltration state: 20 mPas [99].

A general viscosity dependency is observable through an offset between results at the same deformation rate but varying viscosity. Beyond that, a rate-dependency is observed by means of increasing shear force response for higher deformation velocities as exemplarily shown in Figure 3.9 for a constant velocity of 100 mm/min. The corresponding results at 350 mm/min and 700 mm/min are shown supplemented in Appendix A.2. Furthermore, the locking angle shifts towards lower shear angles with increasing shear rate. This can be exemplified by the the 250 mPas fluid results, where the locking angle decreases from 48 to 43 ° ($\gamma_{\text{lock}}^{(100)} = 48°$, $\gamma_{\text{lock}}^{(350)} = 46°$, $\gamma_{\text{lock}}^{(700)} = 43°$). Moreover, the characteristics of the curves (shape) of the infiltrated specimens sometimes differ from the dry ones, at least at lower shear angles as illustrated by the detailed views in Figures 3.6 to 3.8. While the dry curves provide a relatively constant incline until the locking region is reached, the curves obtained from
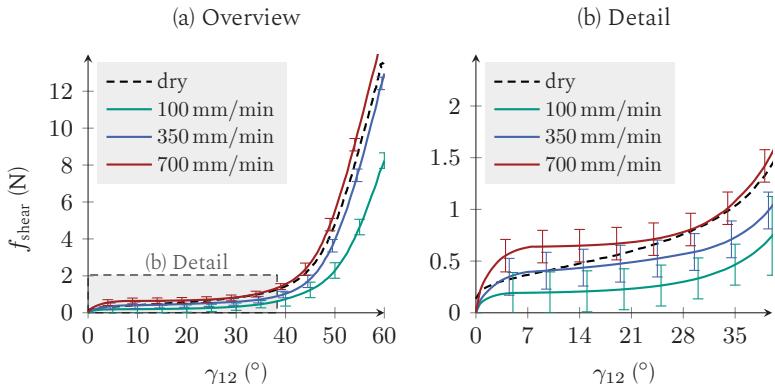
Figure 3.7: Experimental results using the IBET | Infiltration state: 135 mPas [99].
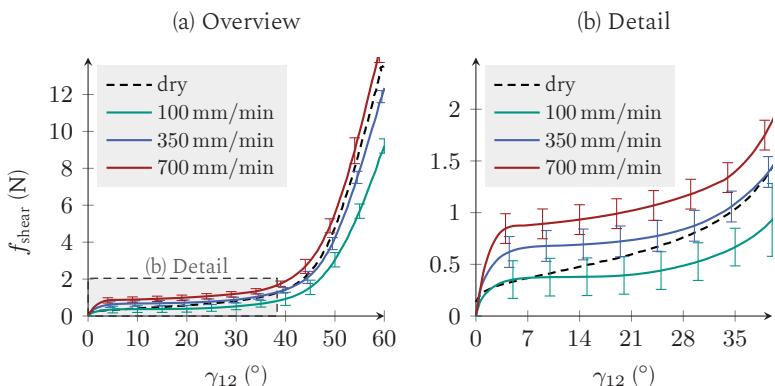
Figure 3.8: Experimental results using the IBET | Infiltration state: 250 mPas [99].

the infiltrated trials provide a partly constant shear force below a locking angle of 20°.

It can be concluded that a low viscosity (20 mPas) reduces the shear resistance of the fabric compared to the dry specimens, especially in combination with low deformation rates (cf. Figure 3.6). On the contrary, a high viscosity (250 mPas) leads to an increased shear resistance compared to the dry specimens, for example, when comparing the relative positions of

the viscous curves to the dry curves in the detailed plots 3.6 to 3.8. Additionally, these plots show that the rate-dependency increases with rising viscosity as the offset between the infiltrated curves enlarges.
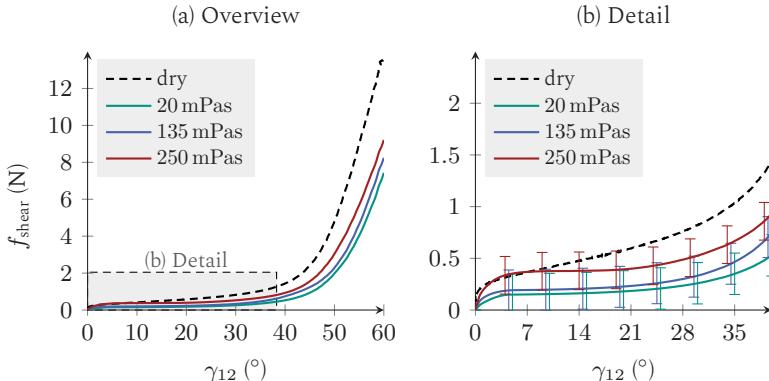
Figure 3.9: Experimental results using the IBET | Comparison at constant velocity of 100 mm/min [99].

3.1.1.4 Discussion

Since mesoscopic effects (sliding and in-plane bending) occur when applying the IBET set-up, their impact on the locking angle is investigated in advance to the main trials through additional PF tests in dry state. Results revealed that the IBET set-up is a reliable and quick test method, well suited for infiltrated shear characterisations of a wide range of shear angles, including an accurate prediction of the locking angle (cf. Figure 3.5). This is in accordance with recommendations and findings in literature [47, 101, 106, 109]. The impact of mesoscopic effects proved negligible below the locking angle and not noticeably affected by the infiltration state. This holds even for the here investigated relatively coarse woven fabrics.

The experimental results reveal a rate- and infiltration-dependent material response of the infiltrated woven fabric. Shear resistance of the material can be significantly reduced by infiltration with low viscosity fluids (20 mPas). Even for the highest tested deformation rates, the obtained shear resistance around the locking angle is lower than the dry reference. Beyond that, shear resistance generally increases with increasing viscosity and deformation rate, leading to values twice as high as the dry specimens (cf. Figure 3.8), at least in some parts of the investigated range. In addition, differences in the characteristic of the infiltrated curves and a shift of the locking angle are observed.

The experimental findings should be discussed in the context of the afore outlined infiltration-related mechanisms displayed in Figure 3.1. Their contribution to the material shear response is shown in Figure 3.10.
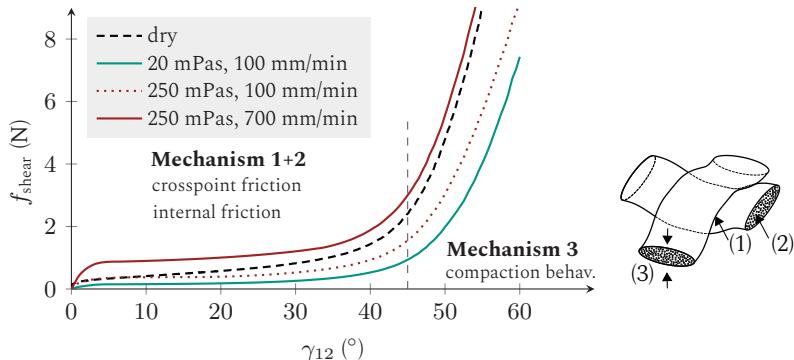
Figure 3.10: Impact and origin of infiltration-related differences during shear deformation | (1) Crosspoint friction, (2) intra-roving friction and (3) roving compaction [99].

Below locking, crosspoint friction and bending stiffness (inner friction) are reduced by the low-viscous infiltration and increased by the presence of higher viscous fluids compared to the dry reference. Towards locking, the compaction resistance of the rovings is reduced by the low-viscous infiltration, whereas the increased viscosity only slightly increases the shear response compared to the dry reference. Consequently, drapeability in

terms of shear behaviour is significantly affected by the fluid's presence and its current viscosity. Drapeability can be either increased by low-viscous infiltration and reduced deformation rate or decreased by higher viscosities and deformation rate.

3.1.2 Membrane modelling

First, a modelling approach for membrane behaviour is presented and parametrised. Afterwards, effects on part level are investigated and evaluated.

3.1.2.1 Constitutive equations for the membrane behaviour

The implemented hyperviscoelastic formulation is based on invariants of the Green-Lagrange strain tensor

$$\boldsymbol{E} = \frac{1}{2} \cdot (\boldsymbol{F}^\top \cdot \boldsymbol{F} - \boldsymbol{I}) \tag{3.2}$$

and the resulting rate-of-deformation tensor [254], which is given by

$$\boldsymbol{D} = \frac{1}{2}(\dot{\boldsymbol{F}} \cdot \boldsymbol{F}^{-1} + \boldsymbol{F}^{-T} \cdot \dot{\boldsymbol{F}}^\top). \tag{3.3}$$

Two deformation modes, elongation in both fibre directions and shear, are taken into account and thus contribute to the potential of free energy ψ given by $\psi(I_1^e, I_2^e, I_{12}^e, I_{12}^v) = \psi^{\text{elong}}(I_1^e, I_2^e) + \psi^{\text{shear}}(I_{12}^e, I_{12}^v)$, where I_1^e and I_2^e provide the elastic strain in the two fibre direction and $I_{12}^{e,v}$ the elastic and viscous shear strain.

Fibre elongation. Fibre elongation is modelled using a nonlinear hyperelastic formulation based on the elastic invariants of the Green-Lagrange strain tensor

$$I_i^e = \boldsymbol{E} : (\boldsymbol{G}_i \otimes \boldsymbol{G}_i) = \varepsilon_{\text{f},i}^e, \tag{3.4}$$

where $\boldsymbol{G}_i$ provide the initial fibre orientations ($i = 1, 2$). The elastic components for the second Piola-Kirchhoff tensor $\boldsymbol{S}$ are calculated using the invariants from Equation (3.4) coupled with the nonlinear elastic moduli $E_{\mathrm{f},i}(\varepsilon_{\mathrm{f},i}^{\mathrm{e}})$

$$S_i^{\mathrm{e}} = \varepsilon_{\mathrm{f},i}^{\mathrm{e}} \, E_{\mathrm{f},i}(\varepsilon_{\mathrm{f},i}^{\mathrm{e}}). \tag{3.5}$$

The nonlinear fibre moduli $E_{\mathrm{f},i}$ are functions of the corresponding directional strains $\varepsilon_{\mathrm{f},i}^{\mathrm{e}}$ using the second order polynomial (P1),

$$E_{\mathrm{f},i}(\varepsilon_{\mathrm{f},i}^{\mathrm{e}}) = \begin{cases} E_{\mathrm{f},i}^{\mathrm{init}} & [\, \varepsilon_{\mathrm{f},i} \leq \varepsilon_{\mathrm{f},i}^{\mathrm{init}} \,] \\ k_1^{\mathrm{P1}} \varepsilon_{\mathrm{f},i}^{\mathrm{e}\,2} + k_2^{\mathrm{P1}} \varepsilon_{\mathrm{f},i}^{\mathrm{e}} + k_3^{\mathrm{P1}} & [\, \varepsilon_{\mathrm{f},i}^{\mathrm{init}} < \varepsilon_{\mathrm{f},i}^{\mathrm{e}} \leq \varepsilon_{\mathrm{f},i}^{\mathrm{end}} \,] \\ E_i^{\mathrm{end}} & [\, \varepsilon_{\mathrm{f},i}^{\mathrm{e}} > \varepsilon_{\mathrm{f},i}^{\mathrm{end}} \,] \end{cases} \tag{3.6}$$

with the polynomial coefficients k_k^{P1} with $k = [1, 3]$. The initial, ondulation fibre stiffness is donated by $E_{\mathrm{f},i}^{\mathrm{init}}$, whereas the $E_{\mathrm{f},i}^{\mathrm{end}}$ provides the finally measured stiffness. Continuity is enforced with boundary conditions during parameter identification.

In general, ABAQUS uses a polar decomposition of the deformation gradient into the symmetric stretch (deformation) tensors $\boldsymbol{U}$ and the orthogonal rotation tensor $\boldsymbol{R}$, which defines a material fixed frame $\{\boldsymbol{e}_i\}$. This multiplicative decomposition is given by:

$$\boldsymbol{F} = \boldsymbol{R} \cdot \boldsymbol{U} . \tag{3.7}$$

The second Piola-Kirchhoff tensor $\boldsymbol{S}$ is transformed (pushed) to the material fixed frame via the stretch tensor $\boldsymbol{U}$ by

$$\hat{\boldsymbol{\sigma}} = \frac{1}{J} \cdot (\boldsymbol{U} \cdot \boldsymbol{S} \cdot \boldsymbol{U}), \tag{3.8}$$

where J is the determinant of the deformation gradient $J = \det(\boldsymbol{F})$ [254].

The experimental results of dry uni-axial tension tests (cf. Figure 3.11) are used to parametrise the material behaviour in fibre direction. An impact

of infiltration is neglected due to the dominating fibre stiffnesses. Material parameters are obtained via a gradient-based optimisation of the polynomial values using a virtual representation of the uni-axial test. The results are illustrated in Figure 3.11. The identified parameters are presented in Appendix A.1.1 in Table A.2.
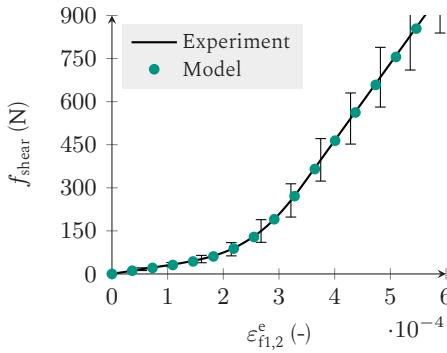
Figure 3.11: Parametrisation | Dry uni-axial tension tests in fibre direction [99].

Shear behaviour. A nonlinear hyperviscoelastic shear behaviour is assumed based on the invariants of the Green-Lagrange strain tensor $\boldsymbol{E}$ and the rate-of-deformation tensor $\boldsymbol{D}$

$$
\begin{aligned}
I_{12}^{\mathrm{e}} &= \frac{1}{2}\left[\boldsymbol{E}:(\boldsymbol{G}_1 \otimes \boldsymbol{G}_2) + \boldsymbol{E}:(\boldsymbol{G}_2 \otimes \boldsymbol{G}_1)\right] \\
I_{12}^{\mathrm{v}} &= \left[\boldsymbol{D}:(\boldsymbol{g}_1 \otimes \boldsymbol{g}_2) + \boldsymbol{D}:(\boldsymbol{g}_2 \otimes \boldsymbol{g}_1)\right].
\end{aligned}
\tag{3.9}
$$

The rate-of-deformation tensor $\boldsymbol{D}$ is defined with respect to co- and contravariant fibre parallel frame $\boldsymbol{g}_i$. The elastic shear components of the second Piola-Kirchhoff tensor $\boldsymbol{S}$ are calculated by

$$
S_{12}^{\mathrm{e}} = S_{21}^{\mathrm{e}} = I_{12}^{\mathrm{e}}\, G_{12}(I_{12}^{\mathrm{e}}),
\tag{3.10}
$$

where $G_{12}(I_{12}^{\mathrm{e}})$ provides a nonlinear shear modulus, which uses is described by a second- and third-order polynomial. The first polynomial is used to account for the constant mid-sector of the measured curves. The third-order polynomial accounts for shear locking according to

$$G_{12}(I_{12}^{\mathrm{e}}) = \begin{cases} G_1 & [0 \le I_{12}^{\mathrm{e}} \le I_{12}^{\mathrm{e,init}}] \\ k_1^{\mathrm{P2}} I_{12}^{\mathrm{e}^2} + k_2^{\mathrm{P2}} I_{12}^{\mathrm{e}} + k_3^{\mathrm{P2}} & [I_{12}^{\mathrm{e,init}} < I_{12}^{\mathrm{e}} \le I_{12}^{\mathrm{e,mid}}] \\ G_2 & [I_{12}^{\mathrm{e,mid}} < I_{12}^{\mathrm{e}} \le I_{12}^{\mathrm{e,lock}}] \\ k_4^{\mathrm{P2}} \left(I_{12}^{\mathrm{e}} - \gamma_{12}^{\mathrm{e,lock}} \right)^3 + G_2 & [\gamma_{12} > I_{12}^{\mathrm{e,lock}}]. \end{cases} \quad (3.11)$$

The polynomial coefficients k_l^{P2} with $l = [1, 4]$ are calculated under the assumption of $\mathcal{C}^0$ continuity between the regions $1 - 2$ and $2 - 3$ (Figure 3.12).
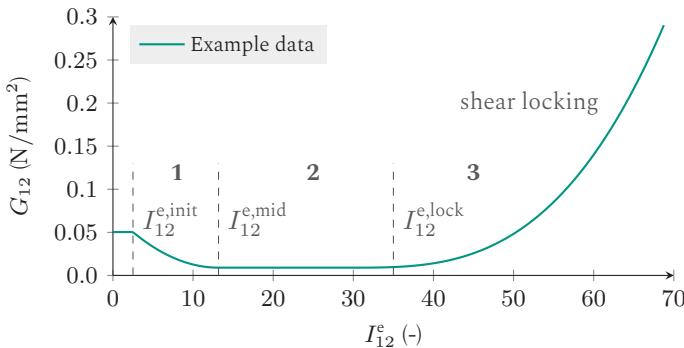
Figure 3.12: Modelling of the non-linear shear modulus with respect to initial configuration using three parts [99].

The viscous shear components of the Kirchhoff stress tensor τ_{12}^{v} are given by

$$\tau_{12}^{\mathrm{v}} = \tau_{21}^{\mathrm{v}} = 2d_{\mathrm{s}}(\eta)I_{12}^{\mathrm{v}}, \quad (3.12)$$

where $d_s(\eta)$ donates the viscosity dependent damping. The Kirchhoff stress tensor $\boldsymbol{\tau}^v$ is transformed (pulled) to the initial configuration by means of the deformation gradient $\boldsymbol{F}$ using Equation 1.20.

Finally, the elastic shear stress is superimposed to the viscous shear part according to a Voigt-Kelvin approach by

$$\boldsymbol{S}(I_{12}^e, I_{12}^v) = \boldsymbol{S}^e(I_{12}^e) + \boldsymbol{S}^v(I_{12}^v) \tag{3.13}$$

and transformed (pushed) to the Green-Naghdi frame $\{\boldsymbol{e}_i\}$ using Equation 3.8.

Virtual BET tests with the same specimen dimensions and boundary conditions are conducted (cf. Figure 3.15 (a)) to obtain the shear material parameters. Reverse parameter identification is used via a comparison of the measured averaged force-displacement curves and the ones predicted by the virtual setup (cf. Figure 3.13 and Figure 3.14).
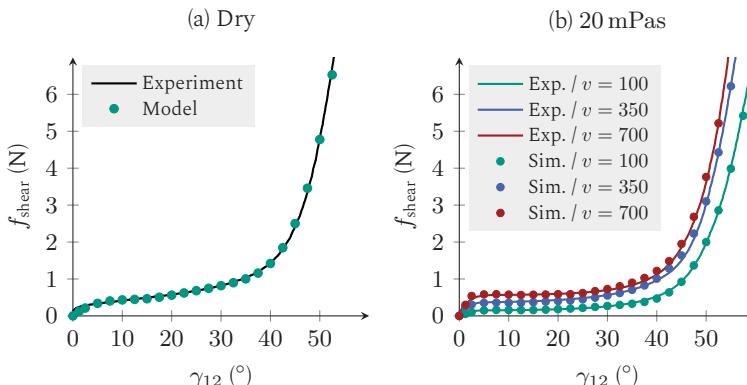
Figure 3.13: Parametrisation dry and 20 mPas | Rate- and viscosity dependent shear behaviour (mm/min) [99].

(a) 135 mPas   (b) 250 mPas
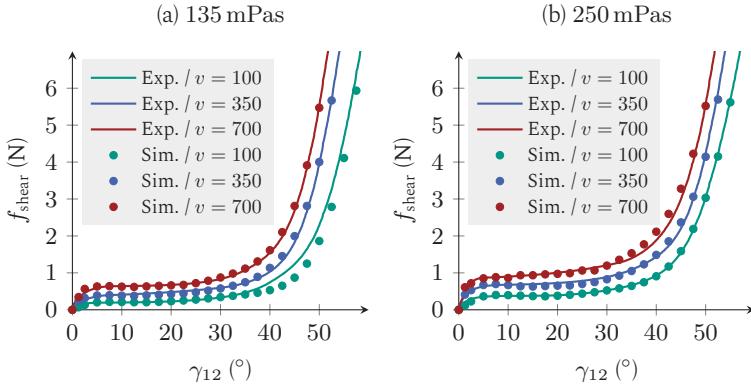
Figure 3.14: Parametrisation 135 and 250 mPas | Rate- and viscosity dependent shear behaviour (mm/min) [99].

Furthermore, the outer contour of the numerical sample is tracked and compared to experimental results (cf. Figure 3.15(b)). Parametrisation values are presented in Tables A.3 and A.4. The numerical results are in good agreement with the experimental ones.

(a) Comparison of shape   (b) Comparison of contour
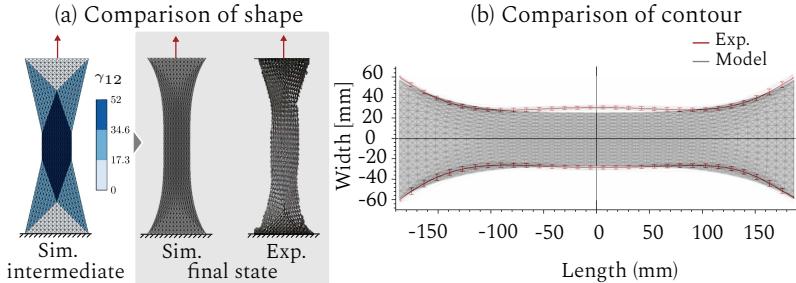
Figure 3.15: Comparison of exp. and numerical shape (a) and (b) contour during BET [99]. The simulation results in (a) show the shear zones before locking and the final shape in the fully locked state.

Due to mesoscopic fibre slip, which cannot be taken into account by the macroscopic approach, test curves cannot be matched simultaneously for the outer contour (cf. Figure 3.15) and the force-displacement curve for

95

shear angles above 55 °. No significant differences are observed for the outer contour during all trials - dry and infiltrated. To match the force-displacement curves combined with the specimen's outer contour using a macroscopic approach, either local parameters have to be assigned or homogenised fibre slippage mechanisms have to be taken into account [229, 230, 275].

3.1.3 Numerical study

The presented membrane model implemented in a subroutine for user-defined material behaviour (VUMAT)[1] is used to evaluate the influence of the rate- and viscosity-depended shear behaviour on part level utilising FE forming simulations for a double dome geometry. The shear rates resulting from the tool stroke amplitude during the forming simulation runs are within the characterised range.

Setups. Forming simulations of single woven plies with initial fibre orientations of 0/90 and ± 45 ° are performed in ABAQUS/explicit. The tools are modelled as discrete rigid surfaces and the tool stroke, which is implemented via a displacement boundary condition ($v_{tool} = 20$ mm/s), corresponds to real process conditions. Since the double dome geometry is double-symmetric, only one quarter is simulated with corresponding symmetry boundary conditions. Each ply is modelled by means of 49.600 triangular membrane and superimposed shell elements [328].

Bending behaviour is modelled with an orthotropic elastic stiffness of B_i = 300 N/mm² within a non-orthogonal material frame using a VUGENS subroutine similar to [328]. In this manner, the change of fibre orientation is accurately taken into account for arbitrary shear angles. A user-defined integration in the subroutine replaces the membrane part of the

---

[1]   Based on a material subroutine originally developed for UD tapes [49]

shell element over the thickness of the shell element. Moreover, a transverse shear stiffnesses of $\kappa_{11}^{TS} = \kappa_{22}^{TS} = 1\,\mathrm{N/mm^2}$ and $\kappa_{12}^{TS} = 0\,\mathrm{N/mm^2}$ are applied for the bending section.

The tool-ply contact is modelled via the built-in general contact algorithm in ABAQUS, using a constant friction coefficient of $\mu_{TP} = 0.3$. FE forming simulation runs using dry and infiltrated (20, 135, 250 mPas) states for the membrane behaviour are carried out. The bending and contact behaviour remain constant to enable the isolated observation and evaluation of the influence of fibre tension and infiltration-depended shear.

Results. Two critical zones of the double dome geometry are selected and evaluated for both initial fibre orientations (cf. Figure 3.16). The zones are evaluated using the highest 10 % of the occurring shear angle values and are selected according to the highest shear regions during forming.
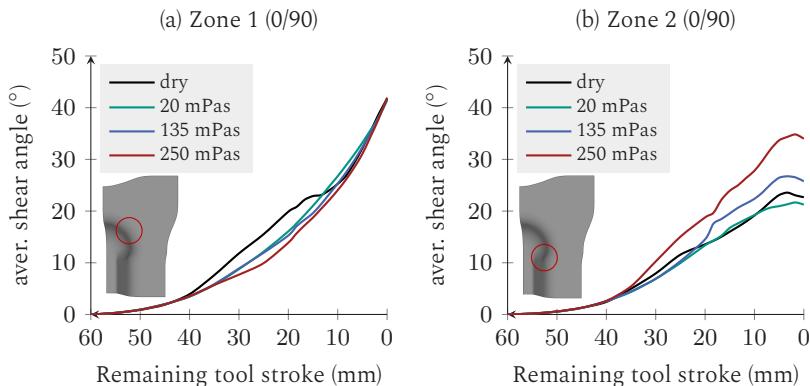
Figure 3.16: Numerical results 0/90° | Averaged shear angles based on the top 10 % values in the zones [99].

Results for Zone 1 (0/90) (cf. Figure 3.16 (a)) show, that the initial and final shear angles are in good agreement for all viscosities, but differences up to 9 ° arise during forming. In Zone 2 and 0/90 ° fibre orientation (cf. Figure 3.16 (b)), differences arise and remain even for the final fibre orientation (tool closed).
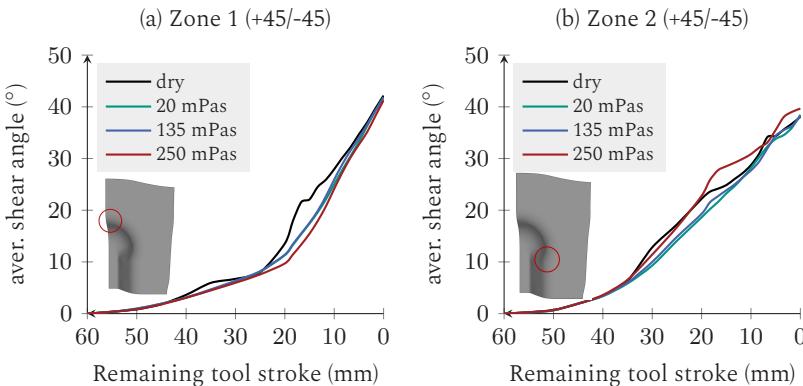
Figure 3.17: Numerical results ±45° | Averaged shear angles based on the top 10 % values in the zones [99].

As fibres are continuous, deformation in both zones is interconnected. While the results for the highest tested viscosity (250 mPas) provide the lowest shear deformation in Zone 1, it provides the highest in Zone 2. Similar results are found the fibre orientation of ±45° (cf. Figure 3.17). However, no significant impact of the infiltration state for the final fibre orientations is predicted for this setup.

Furthermore, the spatial shear distribution is compared for the 0/90 setup. As differences arise already during forming, Figure 3.18 provides exemplary field plots for the shear angle distribution with respect to different infiltration states (dry, 20, 135, 250 mPas) and a remaining tool cavity of 4.5 mm. A similar plot is provided for the fully closed mould in Figure 3.19 Similar to the zone plots above, differences are more distinct for Zone 2. The differences persist when the mould is closed completely.
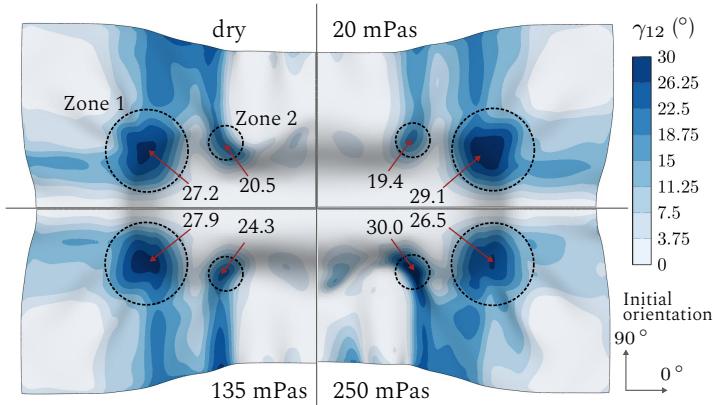
Figure 3.18: Numerical results | Comparison of the shear angle distribution at a remaining cavity of 4.5 mm and an initial fibre orientation of 0/90° [99]. The outlined values are the obtained maxima in the zones.

Discussion   Numerical results on component level reveal an influence of the infiltration on the resulting shear angle distribution. As illustrated in previous paragraphs, shear angle distributions can be significantly effected during forming (cf. Figures 3.18 and 3.19).
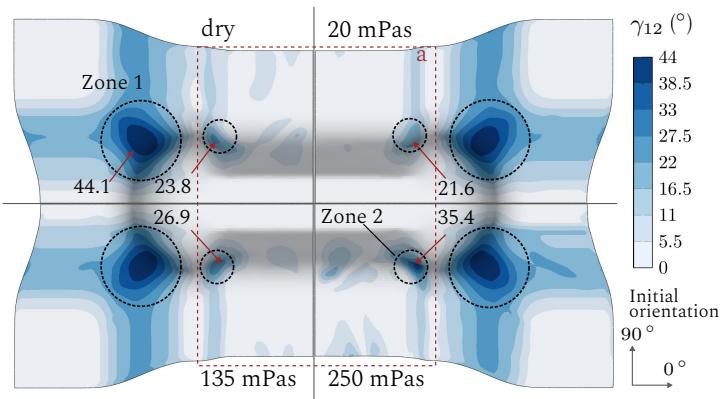
Figure 3.19: Numerical results | Comparison of the shear angle distribution for a fully draped 0/90° woven fabric single ply [99]. The outlined values are the obtained maxima in the zones.

No impact of infiltration on the predicted final shear angle distribution is observed for Zone 1, the half-dome of the double dome geometry, for both fibre orientations (cf. Figures 3.16, 3.17). This is due to the predefined kinematic shape imposed by the tool cavity and only applies to rather simple geometries. The kinematic constraints are also the reason for the interconnection of the results in Zones 1 and 2. Still, differences within the second zone remain for an initial fibre orientation of 0/90°. As continuous reinforcements are investigated, an interaction between the zones is reasonable. In the case of the 0/90° trials, this interaction reduces the local impact of tool constraints.

Infiltration with low-viscosity results in increased shear deformation in the main Zone 1 (cf. Figure 3.18) during moulding. The opposite applies for the higher viscosity of 250 mPas. Although the differences within Zone 1 vanish due to the outlined kinematic conditions, significant differences remain for Zone 2 (cf. Figure 3.19). Here, the material distribution seems to differ depending on the infiltration state, despite the absence of wrinkles. Beyond that, further investigations on more complex geometries and forming setups support the here outlied results. In general, it is investigated that the impact of infiltration increases when no blank holders constrain the deformation and when the number of interacting zones increases. Moreover, the rate-dependency leads to an increased effect of rather fast deformations, whereas the impact recedes for slower draping rates.

However, some limitations have to be highlighted. First, only the in-plane behaviour is adjusted for the infiltration of the fluid. This allows a decoupled investigation of this mechanism but also limits the resilience of the results on part level since infiltration will also influence bending and contact behaviour, which is therefore addressed in the following sections. Moreover, increasing viscosity due to curing and coupling with the resin propagation during forming is neglected in this study. Regarding modelling, a tension-shear or shear-compaction coupling is neglected, which can be important if grippers or global blank holders are applied.

The here discussed key experimental and numerical results regarding pre-infiltrated membrane behaviour are placed in a larger context at end of this chapter in Section 3.5.

3.2 Bending behaviour[1]

Bending provides another important deformation mechanism during forming. Moreover, the interaction of membrane and bending behaviour is crucial for possible draping defects such as wrinkling. [47]. In order to address viscous bending sufficiently, experimental characterisation and evaluation of dry and pre-infiltrated specimens are needed. This is carried out using the two different characterisation approaches, namely a slightly modified cantilever test [120] and a Rheometer bending tests (RBT), which is normally applied to for thermoplastic UD-tapes [85]. Subsequently, both approaches are compared, discussed and their suitability regarding bending characterisation of infiltrated fabrics is evaluated (Section 3.2.5).

3.2.1 Modified cantilever test

3.2.1.1 Setup and procedure

A slightly modified cantilever test is used in this study, which contains an additional wire as illustrated in Figure 3.20 (a). Typically, the specimens are clamped between two plates and pushed over an $41.5°$ edge at constant speed (here, $\dot{u} = 2\,\text{mm/s}$). In contrast to tests with dry fabrics, infiltrated specimens may initially stick to the upper plate. Therefore, a thin wire with a diameter of $0.5\,\text{mm}$ is positioned just behind the edge

---

(7 mm) between the moving top plate and the textile (Figure 3.20(a)). This ensures a reproducible test procedure, as the detachment is comparable for all tests. The width of the specimens measures 100 mm. Two different fibre orientations are investigated (0/90° and ±45°). A constant amount of silicon oil (10 ml) is being homogenous distributed on the full length of the specimen prior to testing. Moreover, an additional soaking time of 1 min is waited to ensure infiltration. Each test configurations was repeated 7-10 times, to ensure at least 7 reliable results.
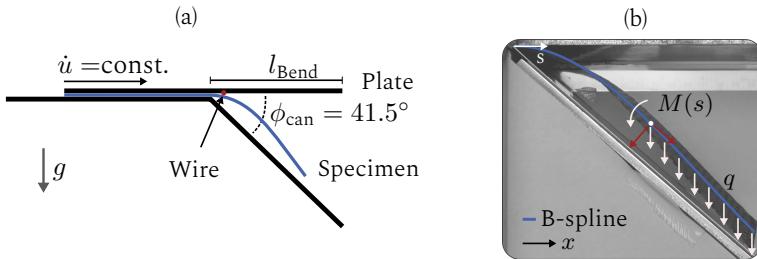
Figure 3.20: Modified cantilever test | (a) Schematic illustration; (b) Optical evaluation: Bending moment $M(s)$ resulting from the specimen's weight per unit length q on a cross-section for the curvilinear coordinate s on a fitted B-spline. The [119].

After the free end of the specimen is initially detached by contact with the wire, the test is be performed as usual. The wire is only used for the detachment from the top plate and does not have further contact with the specimen. The bending stiffness B_w^{Can} normalised by its width, is calculated by means of the overhang length l_{Bend}

$$B_w^{Can} = \frac{F_g}{b} \frac{l_{bend}^3}{8} \frac{\cos(\phi_{can}/2)}{\tan(\phi_{can})} \quad \text{with} \quad F_g = g_z \frac{m_{spec} + m_{resin}}{l_{bend}}, \quad (3.14)$$

which is measured when the free end of the specimen initially touches the lower plate (see Figure 3.20(a)). In standard commercial devices, ϕ_{can} = 41.5°-plates are used. An empirical correction factor for large deformations ($\cos(\phi_{can}/2)$) has been introduced by Peirce [120]. Boisse et

al. [47] have been shown that the usage of this empirical correction factor minimises the resulting errors to 4.4% for a deflection angle of $60\,^\circ$ in comparison to a FE solution. The length-related gravity force F_{g} of the specimens is determined by measurement of the infiltrated specimen weight prior to and after the test (see Equation 3.14) to account for possible weight changes during testing. The maximal weight change for the lowest viscosity $20\,\mathrm{mPas}$ was 10.2%. The averaged weights are assumed for evaluation.

An optical evaluation method similar to the approaches that have been presented by Bilbao et al. [122, 127] and Liang et al. [123] is implemented to quantify the curvature distribution along the specimens during the cantilever experiments. For this purpose, an edge detection algorithm combined with a spline fitting is implemented using an in-house code within MATLAB. The moment $M(s)$ at every point p on the curvilinear coordinate s (cf. Figure 3.20 (b)) can be calculated by

$$M(s_{\mathrm{p}}) = \int_{s_{\mathrm{p}}}^{L} q(s - s_{\mathrm{p}}) \cos(\phi_{\mathrm{can}}(u)) \mathrm{d}s \quad \text{and} \quad \kappa(s_{\mathrm{p}}) = \frac{s''}{(1 + s'^2)^{2/3}}, \tag{3.15}$$

where q is the weight per unit length, L the total length of the profile. Regarding the calculation of the curvature $\kappa(s_{\mathrm{p}})$, s' and s'' denote the first and second derivative of the detected edge fitted with a B-spline. The analytical solution is based on the Kirchhoff theory. Thus, the cross-section remains normal to the mid-surface during deformation. Therefore, transverse shear is not considered with this approach [95]. The average curvature rate $\dot{\kappa}$ is estimated using the curvature history

$$\dot{\kappa} \approx \frac{\triangle \bar{\kappa}}{\triangle t} \quad \text{with} \quad \triangle \bar{\kappa} \approx \frac{1}{\left(l_{b,t_1}^{\max} - l_{b,t_1}^{\min}\right)} \left(\sum_{i=l_{b,t_1}^{\max}}^{l_{b,t_1}^{\min}} |\kappa_{i,t_2} - \kappa_{i,t_1}| \right) \ [t_2 > t_1]. \tag{3.16}$$

Here, the incremental average curvature difference $\triangle \bar{\kappa}$, which is incrementally calculated along the currently detectable length of the specimens edge l_{b,t_1}, is divided by the incremental time period $\triangle t = t_2 - t_1$

between the two compared states. Due to low light exposure conditions directly under the top plate, the curvature rate could only be detected after one-third of the experiment duration.

The execution of the experiments with the infiltrated specimens did not cause major problems compared to the dry ones. As before for the membrane trials, constant infiltration time, an exact amount of resin and homogeneous distribution across the specimen are crucial. Nevertheless, it cannot be determined whether a resin flow occurs along the specimen (rovings) during the tests. However, no dripping of test fluid is detected during the tests for the investigated material combination. This might result from the rovings' good capability to absorb the fluid [329].

3.2.1.2 Results

A comparison between the experimentally determined bending stiffnesses of dry and infiltrated specimens (Equation 3.14) is shown in Figure 3.21 using boxplots.
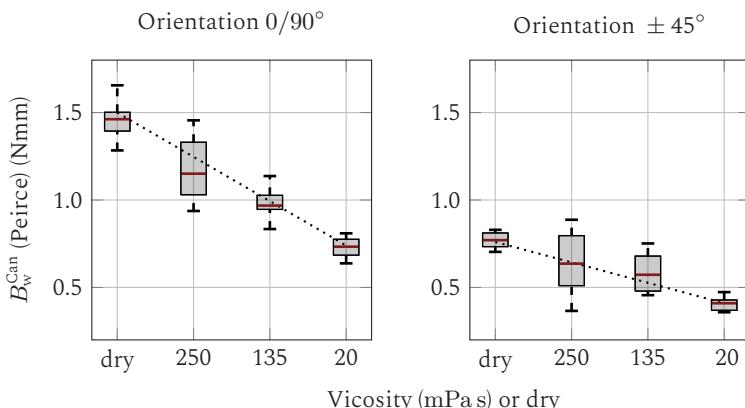
Figure 3.21: Results of the cantilever tests | The red lines within the Boxplots represent median, upper and lower bounds of the 25 and 75 percent quantile and the whiskers indicate the total value range of the bending stiffness $B_{\mathrm{w}}^{\mathrm{Can}}$ (based on [119]).

The bending stiffness of infiltrated specimens decreases significantly compared to dry specimens for both fibre orientations (> 50 %). The lower the viscosity of the infiltrated specimens, the lower the bending stiffness. The absolute reduction within the stiffness values of 0/90° specimens is about twice the ±45° ones, whereas the relative reduction is comparable.

A comparison with the results of the optical measurements is shown in Figure 3.22 using the optically detected moment-curvature curves. The Peirce straights ($M = \kappa \cdot B_w^{\text{Can}}$) match the optical results suitably. This validates the general capability of the applied optical detection method.
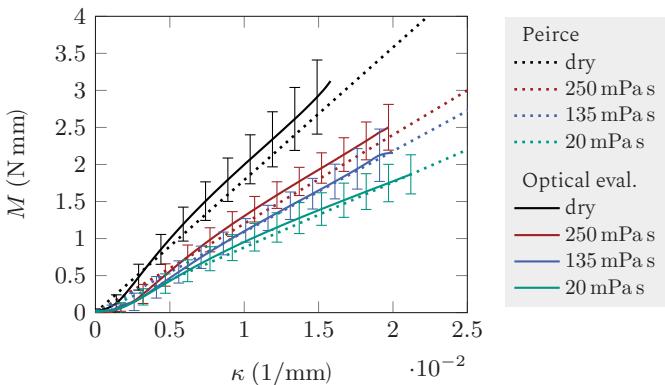
Figure 3.22: Results of the cantilever tests | Comparison between the optical detected moment-curvature-curves predictions of the Pierce method (based on [119]).

Furthermore, Equation 3.16 is used to estimate the average curvature rates $\dot{\kappa}$ during the cantilever test according to Table 3.1. Since the bending stiffness and weight of the specimens vary, so does the averaged curvature rate. The dry specimens are implicitly exposed to the lowest rates, while the low-viscous infiltrated ones are implicitly exposed to the highest when tested with the cantilever test.

Table 3.1: Optically estimated mean curvature rates during cantilever trials.

Inf. state	dry	20 mPas	135 mPas	250 mPas
$\dot{\kappa}^{\mathrm{Can}}$ ($\cdot 10^{-4}$ 1/mms)	3.3 ($\pm$1.4)	5.2 ($\pm$1.8)	5.9 ($\pm$2.1)	6.7 ($\pm$2.2)

Discussion. Experimental results reveal a consistent correlation between viscosity of the infiltration fluid and the bending stiffness of the specimens. This applies for the two investigated fibre orientations. The friction state mostly determines the bending stiffness of the rovings between the filaments. Consequently, an infiltration of the contact interfaces between the rovings and filaments reduces the frictional forces (lubrication) and results in a reduced bending stiffness of the specimens. In this regard, it is expected to find according correlations between bending stiffness and infiltration for unidirectional non-crimped fabrics (UD-NCF).

The optically determined moment-curvature-curves are in good agreement with the analytical solution provided by Peirce (cf. Figure 3.22). The curves' shapes are consistent with the results that have been published Liang et al. [123, 124]. Thus, the implemented optical evaluation provides reliable. The optical measurement results confirm that cantilever tests conducted with infiltrated specimens automatically involve varying rates during testing. This is neglected during the common evaluation procedure for dry specimens.

3.2.2 Rheometer trials

3.2.2.1 Setup and procedure

An enlarged rheometer bending test similar to the one that has been presented by Sachs et al. [129] is applied according to Figure 3.23. Tests with specimens containing a free test area of 70 x 60 mm are conducted. The

enlarged set-up is recommended for coarser fabrics to increase the number of cross points and, therefore, the experiments' reproducibility. The corresponding curvature rates can be assessed based on the assumption that a perfect arc with a constant curvature is formed along the specimen according to [330]

$$\frac{d\kappa_i}{dt} = \frac{\dot{\omega}_i^{\text{Rheo}}(t)}{2R_{\text{bend}} \cdot \cos^2(\omega_i(t)/2)} \quad \text{with} \quad \kappa_i = \frac{\tan(\omega_i^{\text{Rheo}}(t)/2)}{R}. \quad (3.17)$$

Here, ω provides the rotation angle of the rheometer and R_{bend} the bending radius. This implies that clamping conditions are assumed to be frictionless and that the bending stiffness is constant (homogenous) along the specimen. Three discrete angular velocities are investigated since a rate-dependency of the infiltrated material is expected (Table 3.2).

Table 3.2: Investigated curvature rates based on Equation 3.17.

$\dot{\omega}_i^{\text{Rheo}}$ (rpm)	0.1	1	10
$\dot{\kappa}_i^{\text{Rheo}}$ (1/mms)	$1.65 \cdot 10^{-4}$	$1.65 \cdot 10^{-3}$	$1.65 \cdot 10^{-2}$

Special attention is being paid to the clamping to reduce friction as far as possible. For this, both sides of the specimens are taped symmetrically to create a more homogeneous surface, as shown in Figure 3.23(b). Furthermore, care is taken to avoid wetting of the contact interfaces. The specimen's tested area (red box in Figure 3.23(b)) is placed within the fluid for one minute before testing to ensure a complete and homogeneous fluid distribution state. Five to eight specimens are tested for every configuration, depending on the actual scattering. In addition to the first deflection, further 2.5 cycles between $-60°$ and $60°$ are tested as illustrated in
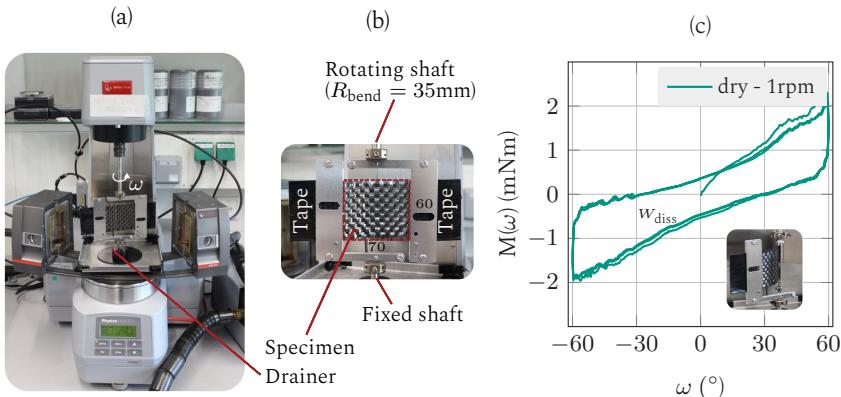
Figure 3.23: (a) Anton Paar MCR501 rheometer with enlarged bending test; (b) Detailed view; (c) Exemplary plot of the measured data [119].

Figure 3.23(c), to investigate the hysteresis behaviour of the dry and infiltrated specimens. The dissipation energy W_{diss} is represented by the enclosed area of one full cycle according to

$$W_{\text{diss}} = \int_{\omega_0}^{\omega_1} M\left(\omega\right) \, d\tilde{\omega},\tag{3.18}$$

which can be calculated as the integral of the measured moment-angle-curves $M(\omega)$. The execution of the rheometer tests with infiltrated woven fabrics did not cause problems and can therefore be recommended. In addition, only minor dropping of infiltration liquid could be detected during the tests. Hence sufficiently homogeneous fluid distribution is assumed.

3.2.2.2 Results

Regarding the first deflection, a significant influence of both, viscosity and bending rate is observed (cf. Figure 3.24). The bending stiffness of the low-viscous infiltrated specimens decreases along with the fluid's viscosity, as shown in Figure 3.24 (a). Moreover, the bending stiffness shows a

rate-dependent response (cf. Figure 3.24 (b)). It is worth mentioning that the dry specimens reveal a distinct rate-dependency, too.
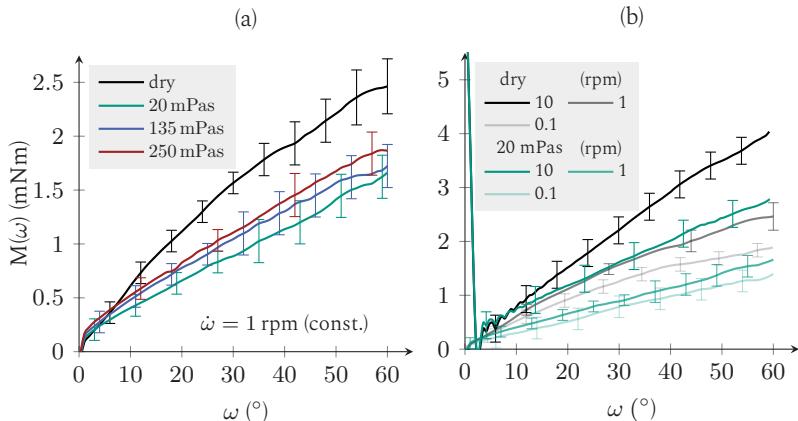
Figure 3.24: Rheometer tests | (a) Impact of the infiltration state at constant deflection rate of 1 rpm; (b) Impact of the bending rate on the moment-angle-curve $M(\omega)$ [119].

Regarding the results of the hysteresis behaviour (cf. Figure 3.25), similar dependencies in terms of infiltration viscosity and bending rate are found. However, the differences are slowly diminishing with an increasing number of load cycles (cf. Figure 3.25). The first deflection and hysteresis plots for the infiltration viscosities 135 and 250 mPas are supplemented in Appendix A.2.2.

Infiltration significantly reduces the initial threshold moment M_0 (cf. Figure 3.25 (b)), evaluated according to [122, 134] as shown in Figure 3.26).

As illustrated in Figure 3.25, the second and third cycle curves are almost identical, which indicates that an almost stationary state of the hysteresis behaviour is reached already within the third cycle. Consequently, the dissipation energies W_{diss} remain nearly constant between the second and

third cycle. The intensity of this effect depends on the viscosity of the infiltrated fluid.
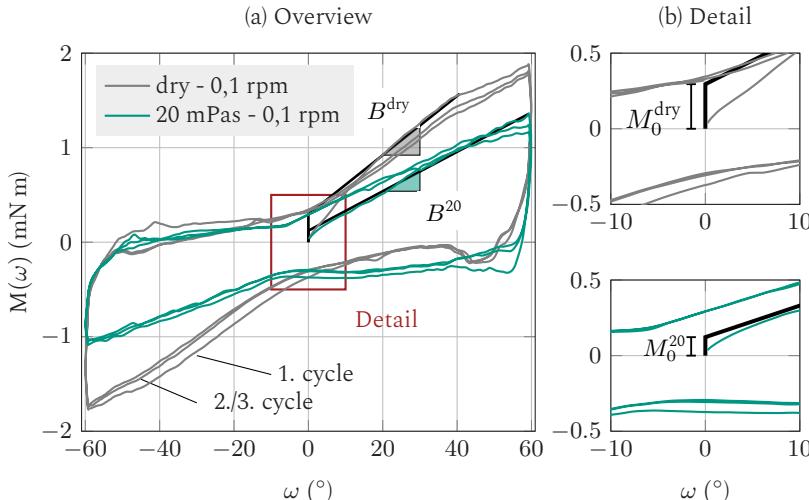
Figure 3.25: Rheometer tests | (a) Hysteresis behaviour of dry and infiltrated specimen; (b) Corresponding initial threshold moment M_0 based on [122, 134] [119].

The dependencies between dissipated energy, infiltration viscosity and bending rate (cf. Figure 3.26) show similar qualitative dependencies as results of the first deflection (cf. Figure 3.24 (a,b)). Consequently, the bending behaviour of the woven fabric is shown to be viscoelastic-plastic, even for dry specimens.

3.2.2.3 Discussion

As outlined in the discussion of the cantilever test, internal (micro) friction between the rovings and filaments is the main mechanism governing the bending behaviour of woven fabrics. In this regard, infiltration of the contact interfaces between the filaments and inside the rovings alters the frictional behaviour. This decreases the bending stiffness of the specimen. The impact of rate-dependency is similarly noticeable in the
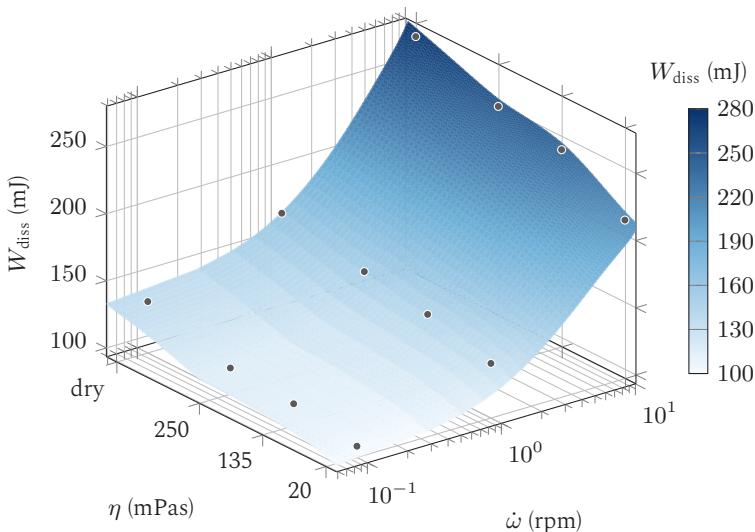
Figure 3.26: Rheometer tests | Surface plot and data grid of dissipation energies W_{diss} of the last rheometer cycle for varying viscosities η and angular velocities $\dot{\omega}$ [119].

RBT within dry and infiltrated fabrics. This suggests that the fibre coating cannot be neglected and contributes to the obtained results. Consequently, infiltration and coating contribute collectively to the measured viscosity- and rate-dependent material behaviour. This effect will probably not be measurable for pre-impregnated semi-finished products since the viscosity of these matrices is significantly higher.

Furthermore, dissipation energies W_{diss} (cf. Figure 3.26) during multiple load cycles and initial threshold moments M_0 (cf. Figure 3.25) are additionally investigated based on the suggestions that have been presented by Grosberg et al. [134], Dahl et al. [133] and Bilbao et al. [122]. Results show a consistent impact of the viscosity on both parameters. The tendency of the hysteresis behaviour towards a stationary state could originate from levelling phenomena on the contact interfaces and from the coating between the filaments, as Tourlonias et al. [91] have been shown

on single fibres. The implications of these effects have also been considered by Cao et al. [331] during their shear behaviour benchmark study using the term 'mechanical conditioning'. Consequently, the measured bending behaviour is viscoelastic and shows pronounced hysteresis effects. For the dry specimens, this was not expected.

3.2.3 Comparison of experimental results

In this section, both the cantilever and RBT tests are compared in terms of their characterisation results. Subsequently, their suitability for the bending characterisation of infiltrated fabrics is discussed.
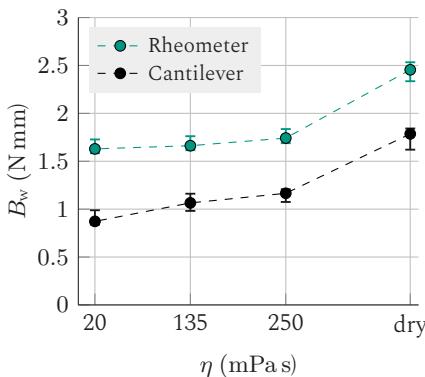
Figure 3.27: Comparison of the experimental results | Direct comparison of the normalised bending stiffnesses B_w (median values) at corresponding rates (cf. Table 3.3) [119].

A direct comparison between the two tests is enabled by additional optical determination of the curvature rates during the cantilever test corresponding to each infiltration viscosity (cf. Figure 3.22). The corresponding bending stiffness values measured with the RBT are interpolated with

respect to the cantilever base deflection rates. Since both tests used differently dimensioned specimens, the bending stiffnesses are normalised by the width w_{sp} according to

$$B_w = \frac{E\,h_0^3}{12\,w_{sp}},\tag{3.19}$$

where $h_0 = 0.3\,\mathrm{mm}$ provides the initial ply thickness. The results show a qualitative but no quantitative correlation (cf. Figure 3.27). Infiltration reduces the bending stiffness in both cases.
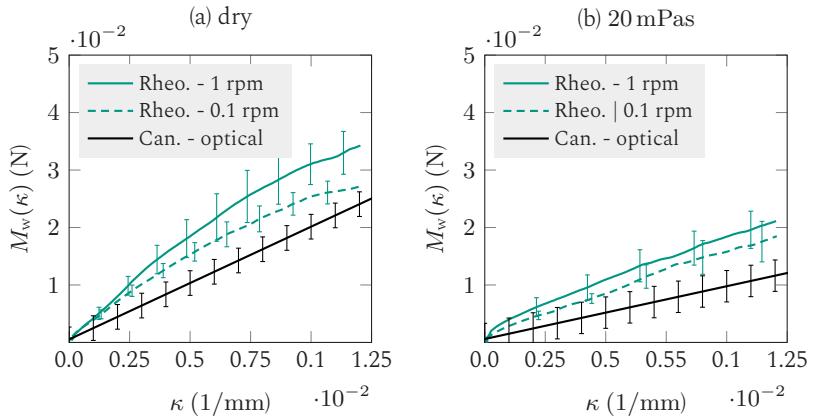
Figure 3.28: Comparison of the experimental results | Exemplary width-based moment-curvature-curves for the (a) dry and (b) infiltrated specimens with $20\,\mathrm{mPas}$ [119].

Still, bending stiffness measured by the rheometer test is systematically higher. Consequently, the normalised moment-curvature-curve $M_w(\omega)$ of the cantilever tests (cf. Figure 3.28) remains below the rheometer curves, even though the average curvature rate values of the cantilever tests lies between the rheometer rate ($\dot{\kappa}_{\mathrm{Rheo.}}^{1\,\mathrm{rpm}} > \dot{\kappa}_{\mathrm{Can.}} > \dot{\kappa}_{\mathrm{Rheo.}}^{0.1\,\mathrm{rpm}}$).

Discussion and evaluation. The effect of infiltration on the bending behaviour of woven fabrics is investigated employing two approaches. The bending stiffnesses determined by the RBT are about 25-44 % higher than the ones from the cantilever test. This difference is significantly higher than the uncertainties arising from the optical evaluation or averaging the curvature rates. The systematic deviation indicates that the test benches themselves caused the differences, including their applied boundary conditions. A potential influence of the specimen size cannot be excluded completely. However, it is assumed to be of minor importance since the specimen sizes are large enough to provide a sufficient number of crosspoints in both cases.

Three contributing effects are identified to explain the diverging results (cf. Figure 3.29). First, friction in the clamped area of the rheometer bend-

1. Friction in clamping   2. Specimen compaction   3. Infiltration
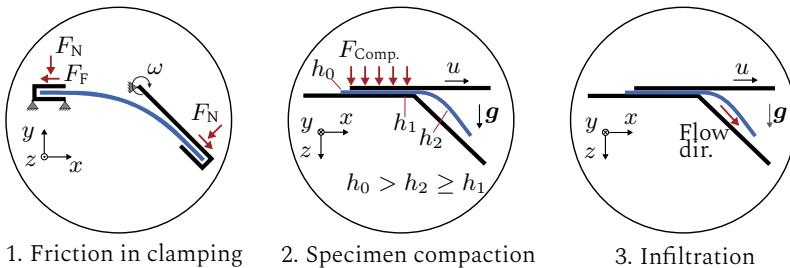
Figure 3.29: Assumed contributions to the systematic deviation between the cantilever and RBT results; (1),(2) systematic effects; (3) infiltration-specific effect [119].

ing test (cf. Figure 3.29 (1)) has a reported impact on the measured result [87], leading to increased values. We expect that friction contributes partly to an increased bending stiffness when measured by the RBT, as a completely frictionless state cannot be achieved. Regarding the cantilever test, the fabric could already be pre-compacted when tested [122] due to the weight of the top plate (cf. Figure 3.29 (2)). This reduces thickness h_2 in comparison to the initial thickness h_0, which is commonly used for the evaluation (cf. Equation 3.19). Compaction affects the physical and geometrical properties of the fabric due to an increased transversal shear

stiffness and a reduced second moment of area. While the physical effect leads to an increased bending stiffness, the latter leads to the contrary. Only additional experimental investigations can enable an evaluation of the individual importance and relevance of the discussed effects. Unfortunately, the compaction of the specimens could not be measured in this study. In any case, it is important to emphasise that higher compaction forces, apart from the ones needed to apply proper boundary conditions, should be avoided during cantilever tests. Comparing effects 1 and 2 (cf. Figure 3.29), we expect the impact of compaction to be more decisive than the effect friction with the clamps of the RBT as the thickness is accounted cubically.

Finally, the infiltration itself could lead to differences between the two test results. Potentially, a flow of the test fluid within the specimen does not directly contribute to the measured results of the RBT. However, it directly contributes during cantilever tests, where some loss of fluid mass within the specimens could not be avoided. This can affect the weight distribution. Yet, a fluid flow within the specimens or major dripping from the specimens could not be detected during the experiments. Moreover, the systematic deviation is also valid between the dry specimens, where a possible impact of infiltration is excluded. Consequently, the effect of infiltration is expected to be of minor importance in this case.

Further investigations are required to clarify the origin of the observed systematic difference. Based on the obtained results, an application of the RBT is recommended for dry and low-viscous infiltrated specimens. On the one hand, it allows for more in-depth material analytics. On the other hand, RBT trials do not suffer from possible adverse impacts of compaction (cf. Figure 3.29 (2)) or fluid redistribution (cf. Figure 3.29 (3)).

3.2.4 Modelling of bending

3.2.4.1 Constitutive equations for the bending behaviour

A hypoelastic bending formulation in combination with a Voigt-Kelvin approach is used within a non-orthogonal fibre-parallel frame given by the normalised covariant base vectors $\boldsymbol{g}_i$ and the corresponding dual contravariant base vectors $\boldsymbol{g}^i$. The elastic objective Cauchy stress rate $\boldsymbol{\sigma}^{\nabla}$ within the fibre-parallel frame is given by

$$[\boldsymbol{\sigma}^{\nabla}]_{\{\boldsymbol{g}_i\otimes\boldsymbol{g}_j\}} = [\mathbb{C}_{\text{bend}}]_{\{\boldsymbol{g}_i\otimes\boldsymbol{g}_j\otimes\boldsymbol{g}_k\otimes\boldsymbol{g}_l\}} : [\boldsymbol{D}]_{\{\boldsymbol{g}^k\otimes\boldsymbol{g}^l\}}, \tag{3.20}$$

where $\mathbb{C}_{\text{bend}}$ is the fourth order elasticity tensor for the bending model. The incremental elastic Cauchy stress $\Delta\boldsymbol{\sigma}^{\text{e}}$ in the fibre-parallel frame is obtained by integration of Equation 3.20 in time [258], which yields

$$[^{t+dt}\Delta\boldsymbol{\sigma}^{\text{e}}]_{\{\boldsymbol{g}_i\otimes\boldsymbol{g}_j\}} = [\mathbb{C}_{\text{bend}}]_{\{\boldsymbol{g}_i\otimes\boldsymbol{g}_j\otimes\boldsymbol{g}_k\otimes\boldsymbol{g}_l\}} : [^{t+dt}\Delta\varepsilon]_{\{\boldsymbol{g}^k\otimes\boldsymbol{g}^l\}}, \tag{3.21}$$

Here $\triangle\varepsilon$ is the strain increment in the fibre parallel frame, that is obtained from the strain increment in Green-Naghdi's frame $\boldsymbol{e}_i$ by means of the normalised right stretch tensor $\boldsymbol{U}^*$ by

$$[^{t+dt}\Delta\varepsilon]_{\{\boldsymbol{g}^i\otimes\boldsymbol{g}^j\}} = [\boldsymbol{U}^*]_{\{\boldsymbol{e}_i\otimes\boldsymbol{g}_j\}}^{\top} \cdot [^{t+dt}\Delta\varepsilon]_{\{\boldsymbol{e}_i\otimes\boldsymbol{e}_j\}} \cdot [\boldsymbol{U}^*]_{\{\boldsymbol{e}_i\otimes\boldsymbol{g}_j\}}. \tag{3.22}$$

To account for the viscoelastic bending behaviour, the incremental viscous Cauchy stress $\triangle\boldsymbol{\sigma}^{\text{v}}$ is added to the incremental elastic Cauchy stress $\triangle\boldsymbol{\sigma}^{\text{e}}$ within the fibre-parallel frame, which yields the total stress at the end of the increment

$$[^{t+dt}\boldsymbol{\sigma}^{\text{vk}}]_{\{\boldsymbol{g}_i\otimes\boldsymbol{g}_j\}} = [^{t}\boldsymbol{\sigma}^{\text{vk}} + ^{t+dt}\Delta\boldsymbol{\sigma}^{\text{e}} + ^{t+dt}\Delta\boldsymbol{\sigma}^{\text{v}}]_{\{\boldsymbol{g}_i\otimes\boldsymbol{g}_j\}}. \tag{3.23}$$

The superscript 'vk' represents the applied visco-elastic Voigt-Kelvin approach. The incremental viscous Cauchy stress $\Delta\boldsymbol{\sigma}^{\text{v}} = [^{t+dt}\boldsymbol{\sigma}^{\text{v}}]_{\{\boldsymbol{g}_i\otimes\boldsymbol{g}_j\}} - [^{t}\boldsymbol{\sigma}^{\text{v}}]_{\{\boldsymbol{g}_i\otimes\boldsymbol{g}_j\}}$ is determined via

$$[^{t+dt}\boldsymbol{\sigma}^{\text{v}}]_{\{\boldsymbol{g}_i\otimes\boldsymbol{g}_j\}} = 2\eta_{\text{D}}(\dot{\gamma}_{\text{eq}})[\mathbb{I}]_{\{\boldsymbol{g}_i\otimes\boldsymbol{g}_j\otimes\boldsymbol{g}_k\otimes\boldsymbol{g}_l\}} : [^{t+dt}\boldsymbol{D}]_{\{\boldsymbol{g}^k\otimes\boldsymbol{g}^l\}}. \tag{3.24}$$

The non-linear viscosity $\eta_{\text{D}}(\dot{\gamma}_{\text{eq}})$ depends on an equivalent of the deformation rate, $\dot{\gamma}_{\text{eq}}$ which is obtained by Equation 1.13.

Finally, the section moment $\left[^{t+dt}\boldsymbol{M}_{\text{sec}}\right]$ within the fibre-parallel frame is determined by the total moment $[^{t}\boldsymbol{M}_{\text{sec}}]$ and the numeric integration of the incremental stress over the initial thickness t_0 of the shell element

$$[^{t+dt}\hat{\boldsymbol{M}}_{\text{sec}}]_{\{\boldsymbol{g}_i\otimes\boldsymbol{g}_j\}} = [^{t}\boldsymbol{M}_{\text{sec}}]_{\{\boldsymbol{g}_i\otimes\boldsymbol{g}_j\}} + \int_{t_0} \left(^{t+dt}[\Delta\boldsymbol{\sigma}^{\text{e}} + \Delta\boldsymbol{\sigma}^{\text{v}}]_{\{\boldsymbol{g}_i\otimes\boldsymbol{g}_j\}}\right) \bar{f}_{33}^2 z\,dz,$$

(3.25)

where f_{33} is the deformation gradient in thickness direction, resulting from assumption of material incompressibility. The bending moments are returned to the solver after being transformed to the Green-Naghdi's frame. Section forces are neglected ($\hat{\boldsymbol{N}}_{\text{sec}} = 0$) to suppress the membrane part within the shell element.

To account for the infiltrated material state, a nonlinear elasticity $E(\dot{\gamma}_{\text{eq}})$ and a nonlinear viscosity $\eta_D(\dot{\gamma}_{\text{eq}})$ are implemented using Equation 3.26 by means of formulations based on an isotropic Cross model [265], where mechanical properties depend on the introduced rate equivalent $\dot{\gamma}_{\text{eq}}$,

$$E\left(\dot{\gamma}_{\text{eq}}\right) = \frac{E_0 - E_\infty}{1 + m_1\,\dot{\gamma}_{\text{eq}}^{1-n_1}} + E_\infty \quad \text{and} \quad \eta_D\left(\dot{\gamma}_{\text{eq}}\right) = \frac{\eta_0 - \eta_\infty}{1 + m_2\,\dot{\gamma}_{\text{eq}}^{1-n_2}} + \eta_\infty. \quad (3.26)$$

The outlined bending model is suitable to describe the observed rate- and viscosity-dependent bending behaviour but involves some noteworthy limitations. The hypoviscoelastic formulation implies a path-dependency that can affect the results for mainly non-monotonous bending deformations due to the non-linearity of the elastic part of the constitutive equation. Therefore, a generic geometry containing only a single punch is going to be applied in Section 3.2.5, which results in a mostly monotonous bending deformation on the fabrics. Furthermore, the model cannot account for warpage or spring back effects in the presented form. Thus, obtained results are only reliable until the tool is closed completely.

3.2.4.2 Parametrization

The cantilever test and RBT experimental results are used to parametrise two bending models, henceforth called cantilever and rheometer model.

Both approaches are parametrised separately using inverse FEA-based material parameter extraction. For time efficiency, and in contrast to the numerical study, an implicit integration scheme is applied during parametrisation[1]. For this, the outlined model is implemented within a UGENS subroutine. An in-house script using the gradient-based Nelder-Mead algorithm [332] is applied to identify and optimise suitable material parameters for both bending models.

For the parametrisation of the cantilever bending model, the above-outlined modelling approach is reduced to a purely hypoelastic approach ($\eta_D \to 0$) using constant elasticity moduli E_i^{can}, that are determined for each viscosity according to Table 3.3. The specimen tip displacement at the free end is used as the optimisation goal.

Table 3.3: Material parameter of the cantilever model.

	dry	*20 mPas*	*135 mPas*	*250 mPas*
E_i^{can} (MPa)	788.49	418.05	477.84	526.58

Regarding parametrisation of the bending model using the Rheometer dataset, a simulation set-up similar to [328] is applied with predefined deflection rates ($\dot{\omega}_i = 0.1, 1, 10$ rpm). The parametrisation results shown in Figure 3.30 are in good agreement with the experimental ones.

A comparison of both models' identified absolute and relative elasticity moduli compared to the dry stiffnesses is presented in Figure 3.31 at corresponding curvature rates of the cantilever test (cf. Table 3.1). The systematic differences obtained by experimental trials with the two different setups (cf. Figure 3.31 (a)) is reflected by the absolute values.

Moreover, the relative comparison shows that the identified elasticity values of the cantilever model decrease faster than the ones for of rheometer model (cf. dashed lines in Figure 3.31 (b)). This originates from the purely

---

[1] The implicit material model and RBT setup originate from [49]
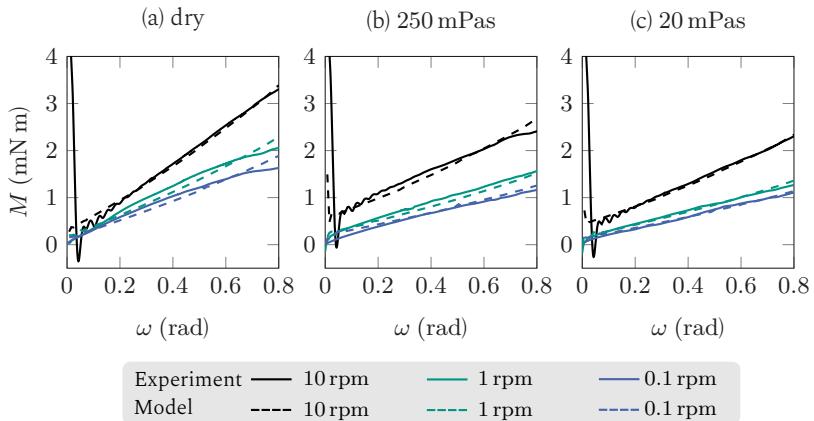
Figure 3.30: Parametrisation results for the rheometer model for the dry and infiltrate state for deflection rates [119].

elastic approach in the cantilever bending model, which must compensate for the missing rate-dependency via the elasticity modules.
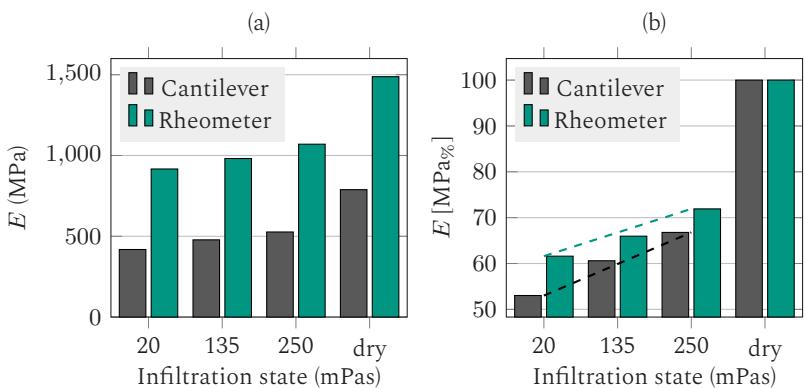
Figure 3.31: Comparison of parametrisation results | Elasticity moduli for different viscosities (mPas) at corresponding rates; (a) absolute, (b) relative to dry reference [119].

3.2.5 Numerical study

FE forming simulation model. To assess the process relevance of the experimental bending trials, a numerical sensitivity study is conducted using FE forming simulation runs with one and two plies on a generic box-shaped[1] geometry. On the macroscopic scale, the intra-ply mechanisms, namely membrane and bending behaviour, have to be decoupled since conventional shell theories can not describe the high membrane stiffnesses compared to the relatively low bending stiffness caused by intra-roving slip between filaments, which reduces the transverse shear stiffness. This is already explained in more detail in Section 1.2.4.2.

The outlined approach is implemented through three user-subroutines within the commercially available FE solver ABAQUS/explicit (cf. Table 3.4). Superimposed membrane and shell elements represent each single

Table 3.4: Numerical modelling | Outline and origin of the applied material models.

Deformation mechanism	Material formulation	ABAQUS Implementation	References & modifications
Membrane	hyperelastic	VUMAT	[99] (Sec. 3.1.2)
Bending	hypoviscoelastic	VUGENS	$[48, 328] + B_i(\eta, \dot{\omega})$
Interface (TP)	Coulomb friction	Built-in	[333]
Interface (PP)	Eq. 3.27	VUINTERACTION	$[83, 334]$ (low,high)

ply of the stacked laminate. To model membrane behaviour, the above presented hyperviscoelastic membrane model (cf. Section 3.1.2) is applied within a VUMAT subroutine. A dry material state is used for the

---

[1] The geometric was originally designed by Dr. Tobias Joppich at the Fraunhofer ICT, 2016

membrane model in this study, which provides a purely hyperelastic material formulation. For the above introduced bending model (cf. Section 3.2.4), an existing hypoviscoelastic model that has been published by Dörr et al. [328] is applied and modified to account for the experimentally measured viscosity-dependent bending behaviour. The subsequently presented model is implemented via a VUGENS subroutine. In addition to the already implemented rate-dependency following a Voigt-Kelvin approach, a nonlinear elasticity is implemented in combination with a Cross model. The observed plasticity behaviour is neglected in this numerical study because the visco-elasticity is expected to be the more significant mechanism, as the experimental results presented in Section 3.2.2.2 indicate. Moreover, the experimentally obtained hysteresis behaviour is not considered throughout this approach - a common assumption given the mostly monotonous deformations during draping.

Two contact pairs are distinguished, Tool-Ply (TP) and Ply-Ply (PP) interface (cf. Table 3.4). A conventional Coulomb friction law ($\mu_{TP} = 0.25$) within the general contact algorithm in ABAQUS is used to describe the TP interaction. The interface mechanisms for the PP contact, namely tacking in normal direction and friction, are considered by a penalty-based contact formulation [335] using a user-defined contact model that has been proposed by Dörr et al. [334] within the VUINTERACTION subroutine. The critical tangential stress τ_{crit}, which is regularised by a yield function, is given by

$$\tau_{crit} = \mu_{PP}\, p + \eta_{PP}\, v + \tau_{PP,0}, \tag{3.27}$$

where μ_{PP} is the tangential coefficient of friction and $\tau_{PP,0}$ accounts for the sticking. Rate-dependencies are suppressed within the contact model, limiting rate-dependency solely to the applied bending model ($\eta_{PP} \rightarrow 0$). Modelling of the interface behaviour is discussed in more detail in Section 3.3.

To account for the interdependency between membrane and bending behaviour [47, 85], which is connected by the PP contact formulation, two sets of PP contact parameters are used according to Table A.5 (Appendix A.2.2). For the low contact setting, the sticking parameter $\tau_{PP,0}^{low}$ is parametrised by experiments with dry woven fabrics [336], whereas $\tau_{PP,0}^{high}$ is set to mostly suppress relative slip between the plies (high contact setting). In this manner, the low contact setting represents a process situation in which plies can easily slide relative to each other, e.g. due to lubrication with low-viscous resin within the WCM process. In contrast, the high contact setting represents a process situation where plies mostly stick together and relative slip is mostly prevented. The latter approximates lubrication states with a partially cured resin or situations where chemical binders or high normal forces are applied. The contact parameters are kept constant in both cases to investigate the influence of the bending behaviour exclusively. In the following, the constitutive equations and modifications for the bending behaviour of infiltrated fabrics are presented and parametrised. Subsequently, numerical results of the sensitivity study are shown and discussed.

Setups. As outlined in Table 3.5, several forming simulation runs are performed in ABAQUS with an explicit time integration scheme. The dry specimens and the specimens infiltrated with 20 mPas represent the extreme values of the experimentally obtained bending stiffnesses (see. Figure 3.31). Therefore, only these two viscosities are used for the sensitivity study. Three sets of setups are compared, a comparison among the single ply setups (S1-S4), a comparison among the two-ply setups with low frictional conditions (S5-S8) and a similar two-ply setup with high contact settings (S9-S12). The tools are modelled as discrete rigid surfaces and the applied tool stroke is implemented via a displacement boundary condition, as illustrated in Figure 3.32 (a). The tool is closed within 2 seconds at a constant velocity $u_T = 25.5$ mm/s. Furthermore, a constant gravity load

Table 3.5: Outline of the simulation setups.

Setup	Layup	Mat. state	Dataset	Contact
Single ply				
S1	[0/90]	dry	RBT	TP only
S2	[0/90]	20 mPas	RBT	TP only
S3	[0/90]	dry	cantilever	TP only
S4	[0/90]	20 mPas	cantilever	TP only
Two-plies – Low contact settings				
S5	[0/90, ±45]	dry	RBT	TP + PP low
S6	[0/90, ±45]	20 mPas	RBT	TP + PP low
S7	[0/90, ±45]	dry	cantilever	TP + PP low
S8	[0/90, ±45]	20 mPas	cantilever	TP + PP low
Two-plies – High contact settings				
S9	[0/90, ±45]	dry	RBT	TP + PP high
S10	[0/90, ±45]	20 mPas	RBT	TP + PP high
S11	[0/90, ±45]	dry	cantilever	TP + PP high
S12	[0/90, ±45]	20 mPas	cantilever	TP + PP high

is applied to the model. Each ply, with a constant thickness of 0.3 mm, is modelled using 70.000 triangular elements.

Preliminary studies using the dry material state showed that the occurring curvature rates during forming are in good agreement with the parametrised range (cf. Figure 3.32 (b)). Here, the dry parameter sets involve the highest rates because of the lowest rate-dependency (cf. Table A.6). The parametrised range is indicated by vertical lines in Figure 3.32 (b).

In the following, the modified mean curvature value originally proposed by Haanappel [24] and enhanced as part of an in-house python script [49] is applied to quantify wrinkling. Two values are of interest. The modified mean curvature κ^{el} is used for a spatial visualisation of the curvature field. It is obtained by interpolation of the nodal curvatures $\bar{\kappa}_j^{\mathrm{node}} = 0.5 \cdot (|\kappa_j^{\mathrm{I}}| +$
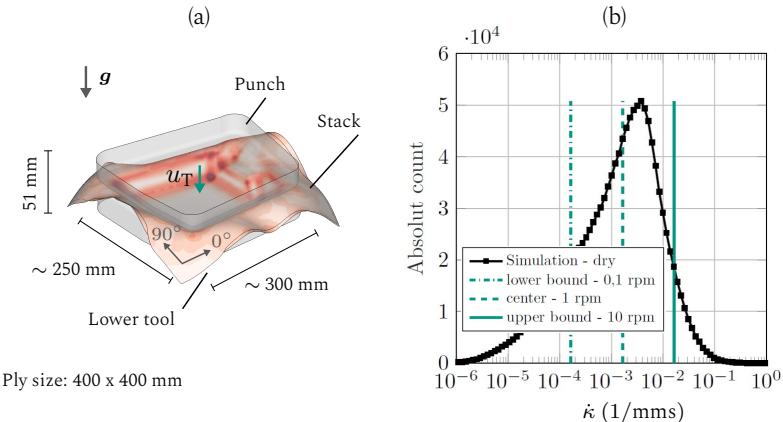
Figure 3.32: (a) Illustration of FE forming simulation setup 5 illustrating the spatial curvature distribution κ^{el} ; (b) Histogram of occurring curvature rates $\dot{\kappa}$ during forming simulation of the generic geometry [119]).

$|\kappa_j^{II}|$), which are determined using the principal curvatures κ^I, κ^{II} at the mesh nodes j, to the element centroid [49]

$$\bar{\kappa}^{el} = \frac{\sum_{i=1}^{N^{el}} (\kappa_i^{el} A_i^{el})}{\sum_{i=1}^{N^{el}} A_i^{el}} \quad \text{with} \quad \kappa_i^{el} = \frac{1}{3} \sum_{j=1}^{3} \bar{\kappa}_{ij}^{node}. \tag{3.28}$$

For quantification the predicted curvature of the whole part by a scalar value, the modified mean curvature κ_i^{el} is averaged using the total number of elements N^{el}. As elements deform, the average is calculated area-weighted using A_i^{el}. The presented curvature values are always calculated for the final tool shape as S1 in Figure 3.33 illustrates.

Results. A comparison between the predicted curvatures of the $\pm 45°$ single ply simulation setups S1 to S4 is presented in Figure 3.33. The curvature values $\bar{\kappa}_{MM}^{el}$ beneath the pictures correspond to the outlined tool shape with a remaining tool cavity of 10 mm. The overall shape and predicted curvatures are quite comparable for the two infiltration states.
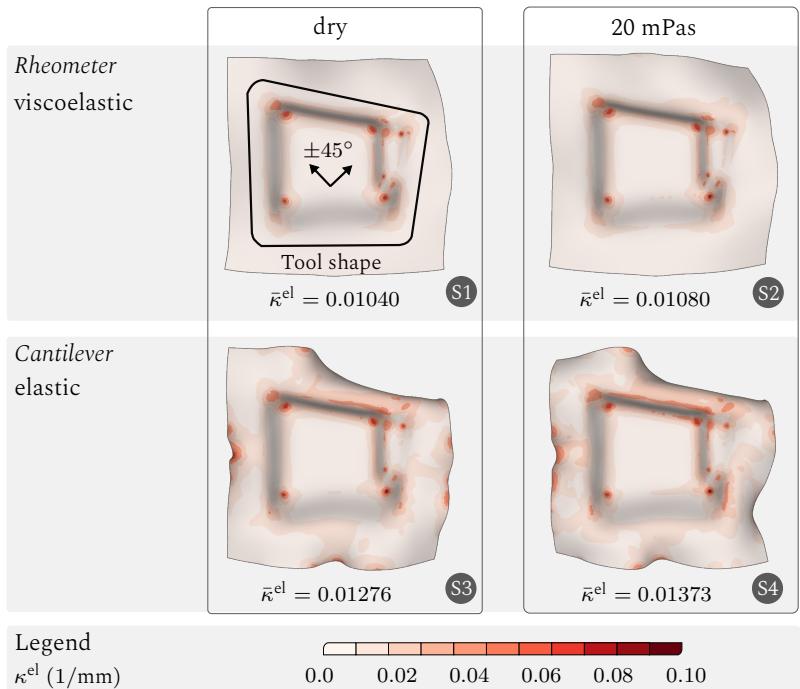
Figure 3.33: Single ply results | Curvatures κ^{el}, $\bar{\kappa}^{el}$ predicted by both bending models for a remaining tool cavity of 10 mm and two viscosities (Setups S1 to S4) [119].

The curvatures within the tool shape only slightly increase with infiltration. In contrast to the rheometer results, curvatures predicted by the cantilever model are increased inside and outside the tool shape. The differences between the results using the two viscosities are slightly more pronounced. The most noticeable difference between the two models is the predicted sag outside the tool shape.

The numerical results of the two-ply setups are displayed in Figure 3.34 for the low contact settings and for the high contact settings in Figure 3.35.
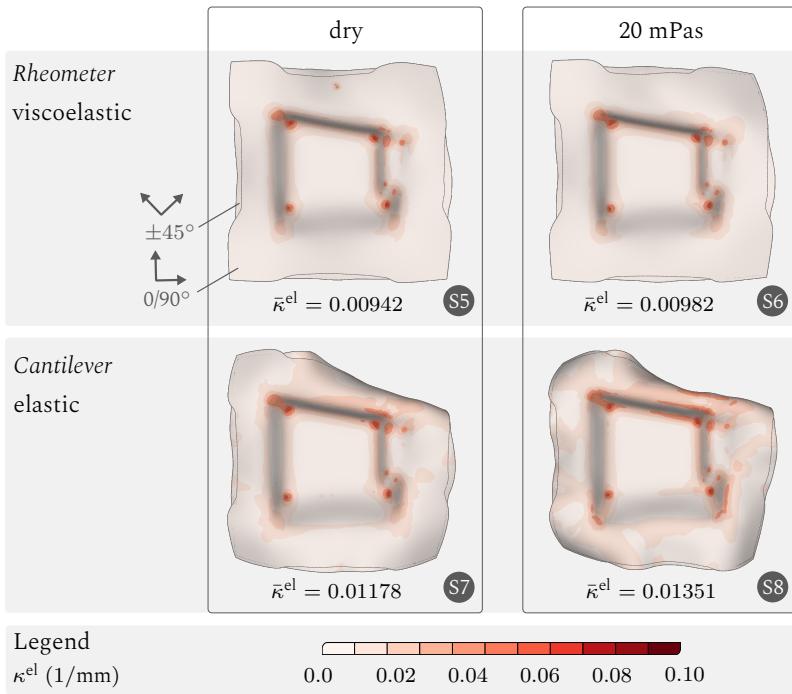
Figure 3.34: Low contact settings $\tau_{\mathrm{PP},0}^{\mathrm{low}}$ | Comparison of the numerical results and predicted curvatures $\kappa^{\mathrm{el}}, \bar{\kappa}^{\mathrm{el}}$ within the two-ply simulations for a remaining tool cavity of 10 mm (Setups S5 to S8) [119].

Almost identical results compared to the single-ply runs (cf. Figure 3.33) are obtained when the low contact settings are applied (cf. Figure 3.34). Consequently, similar tendencies, curvatures relations and shapes are predicted.

In contrast to the former, distinctive winkling is predicted when relative slip is mostly prevented (cf. Figure 3.35). The obtained curvature values are significantly higher. However, the same tendencies in terms of viscosity impact and bending model apply. The impact of viscosity is rather low and more pronounced when the cantilever model is used. Furthermore,

the cantilever bending model predicts significantly higher curvature values than the rheometer model. The position and shape of individual wrinkles vary in all configurations, but the largest difference is observed between elastic and viscoelastic bending formulation.
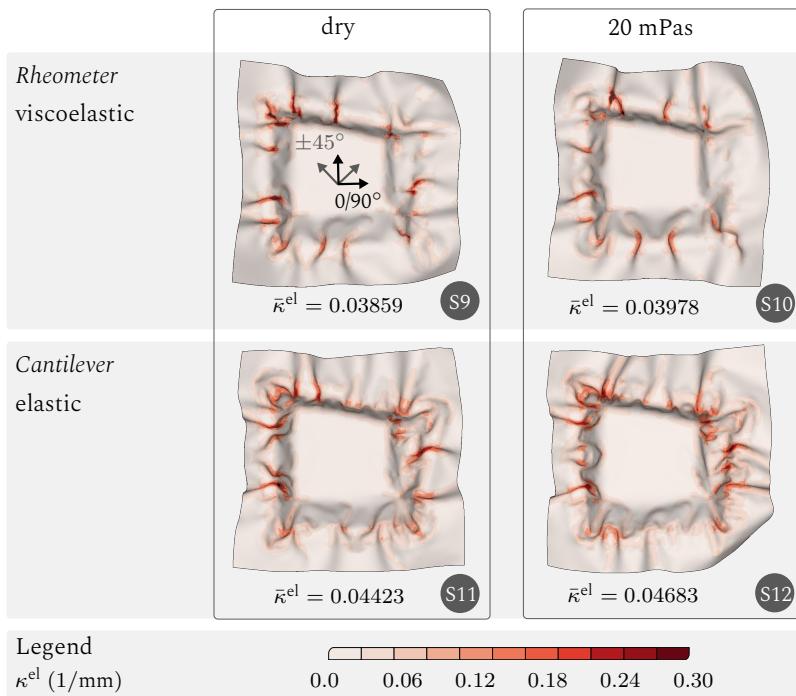
Figure 3.35: High contact settings $\tau_{\mathrm{PP},0}^{\mathrm{low}}$ | Comparison of the numerical results and predicted curvatures $\kappa^{\mathrm{el}}, \bar{\kappa}^{\mathrm{el}}$ within the two-ply simulations for a remaining tool cavity of 10 mm (Setups S9 to S12) [119].

Discussion of numerical results. The numerical results of the single-ply simulation setups (S1-S4 in Table 3.5) match the two-ply simulation setups with low contact interaction (S5-S8) because a mostly unconstrained deformation of the single plies is possible in all these simulation runs.

The obtained results directly relate to the applied bending models and their corresponding material parameters. The lower the bending stiffness, the higher the sag and predicted curvatures (cf. Figure 3.33 and Figure 3.34) as seen for the cantilever models with the lower stiffness compared to the RBT models. Recalling the identified material parameters in Figure 3.31, the bending stiffness in both models decreases along with decreasing viscosity. The values obtained by the RBT are approximately 20 - 50 % higher than the corresponding values obtained by the cantilever test. Consequently, the reduced bending stiffness and missing rate-dependency within the hypoelastic cantilever model predict, in general, higher curvatures and more sag than the rheometer model throughout all the numerical results. A rate-depended bending model is recommended as it represents the measured material behaviour more accurately.

The above-outlined reasoning also applies to the two-ply simulation setups containing the high contact interaction (S9-S12). However, the suppressed relative slip between the plies leads to increased in-plane (membrane) forces due to constrained deformation and, therefore, to the formation of wrinkles as visualised in Figure 3.35. According to literate [47, 85, 328] the initial values of the bending stiffness determine the onset of wrinkles, whereas rate-dependencies determine their progression. Since the value for the initial bending stiffness of the rheometer model is higher compared to the cantilever model, less wrinkling is predicted, which is also reflected by the averaged curvature values inside the tool shape (cf. Figure 3.35). Although the predicted averaged curvatures $\bar{\kappa}^{el}$ only increase slightly with infiltration for both bending models, the position and shape of the wrinkles differ between every configuration, at least in certain areas of the part. This is contributed to the fact that wrinkling is an instability issue, governed by the ratio of in- and out-of-plane stresses [47]. In situations with increased in-plane stresses, the model responds more sensitively to viscosity-dependent changes of the bending stiffness. Consequently, differences between the shape and size of

the predicted wrinkles are noticeable within the high contact simulation runs.

In addition, it has to be considered that, although the kinetic energies are very low compared to the total energies in the model ($< 2\%$), some degree of oscillation cannot be prevented when using a solely elastic bending model (cantilever). This may cause differences in the plies' outer shape, especially for the single plies (cf. Figure 3.33). Regarding the rheometer model, the viscous part damps such oscillations.

Collectively, the numerical results reveal that the bending models (RBT, cantilever) lead to differences in predicted shape and curvature. Moreover, the shape and size of the wrinkles are affected on part level, especially when strong contact interaction is assumed. The usage of a viscoelastic bending model is recommended as the material behaviour is shown to be rate-dependent, even for dry specimens. Furthermore, the results emphasise the relevance of accurate characterisation of the initial bending stiffness value, which is not so straightforward, as shown in Section 3.2.3.

In general, the relevance of a viscosity-dependent bending model is of minor importance within the WCM process, compared to, e.g. the thermoforming of thermoplastic UD-tapes [114, 328, 337]. This is mostly because relative slippage between the plies prevents most critical situations in WCM. Thus, localised stresses tend to be released by relative inter-ply slip and not by bending. Moreover, the process relevant viscosity range (20-250 mPas) is much lower than within, for example, the thermoforming of thermoplastic UD-tapes or prepregs.

As before the membrane behaviour, key experimental and numerical results regarding the bending behaviour of pre-infiltrated fabrics are placed in a larger context at end of this chapter in Section 3.5.

3.3   Inter-ply behaviour[1]

Inter-ply behaviour at interfaces is an important mechanism during WCM processing as large slip is observed during moulding experiments [73]. In this sense, the drapeability of the stack is normally improved under low-frictional conditions because it allows for a more unconstrained deformation of the single plies according to their current fibre orientation [47, 114, 119, 328]. To account for normal and tangential contact behaviour, different experimental techniques are required.
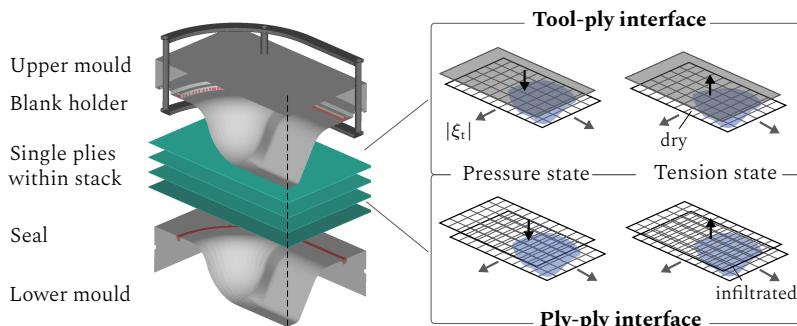
Figure 3.36: Inter-ply behaviour | Exemplary simulation setup and arising contact states.

As illustrated in Figure 3.36, contact arises at the interfaces between stack and tooling (TP), as well as within the stack (PP). Regarding contact in normal direction, pressure or tension states can arise during forming (cf. Figure 3.36). The tension state is commonly neglected for forming of dry, non-bindered textiles, as no source of significant tacking forces exists.

This no longer applies for partly or fully pre-infiltrated contact areas during WCM processing [336] as the fluid can lead to tacking forces between the contact interfaces [338]. Similar to thermoplastic UD-tapes [83, 85], the matrix's presence causes tacking in normal direction. Thus, experiments need to cover TP and PP conditions, including dry and pre-infiltrated contact states during both pressure and tension situations.

3.3.1 Experimental characterisation

3.3.1.1 Tangential behaviour

Hüttl et al. [156] show that the coefficient of friction (CoF) of the in this study investigated woven fabric is influenced by its current infiltration state. For this, they use a sledge-based setup, pulled over the surface of a clamped fabric (cf. Figure 3.37 (a)).
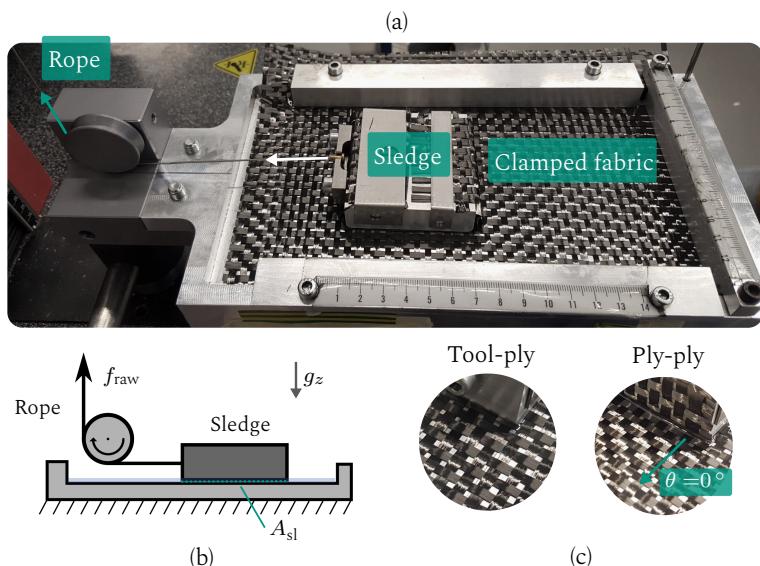
Figure 3.37: Experimental setup | (a) Test bench on tensile testing machine; (b) Schematic illustration; (c) Close-up and definition of the relative fibre orientation θ [336].

The clamped area is placed in a fluid reservoir, enabling a homogeneous infiltration of the clamped fabric. The setup is mounted on a tensile testing machine of the company Zwick GmbH & Co. KG (Germany). This setup is used for a systemic study of viscosity- and rate-dependency of frictional behaviour within both contact pairs. The relative fibre angle θ between two surfaces is shown in Figure 3.37 (c). For the latter, three different velocities are applied during the experiments (100, 350, 700 mm/min). Moreover, the previously introduced silicon oil (cf. Section 1.5) with three different but rate-independent viscosities (20, 135, 250 mPas) is applied and compared to the dry reference. To account for a potential pressure-dependency, two different sledge weights m_{sl} (718 and 1218 g) with the same contact area ($A_{sl} = 3600\,\text{mm}^2$) are used (cf. Figure 3.37 (b)). This information is used to calculate the tangential contact stress

$$\tau = \frac{f_{raw}}{A_{sl}} \quad \text{with} \quad f_{raw} = \mu\, g_z\, m_{sl}, \tag{3.29}$$

where f_{raw} provides the measured rope force. The resulting CoF is calculated using the resulting weight force of the sledge

$$\mu = \frac{f_{raw}^0}{g_z\, m_{sl}}. \tag{3.30}$$

Unless otherwise stated, all outlined configurations are repeated 3 times.

Experimental procedure. The same amount of resin is applied on top of the clamped fabric during each trial. In order to minimise drag forces of the fluid, only the amount of resin required for a homogeneous and complete infiltration of the fabrics is applied. A constant soaking time of 2 min is waited before testing. The sledge is position at a fixed starting position for each trial. Subsequently, another minute is waited to ensure contact infiltration. It has to be mentioned that arising fluid pressure around the contact area resulting from the sledge movement cannot be

measured with this setup. Therefore, it is impossible to distinguish between purely material forces in normal direction (compaction of the plies), resulting in interface friction and the fluid pressure beneath the sledge, which presumably also bears some of its weight.

Experimental results.   The experimental results for the TP contact pair with a relative contact angle of $\theta = 0°$ are presented in Figure 3.38 (a).
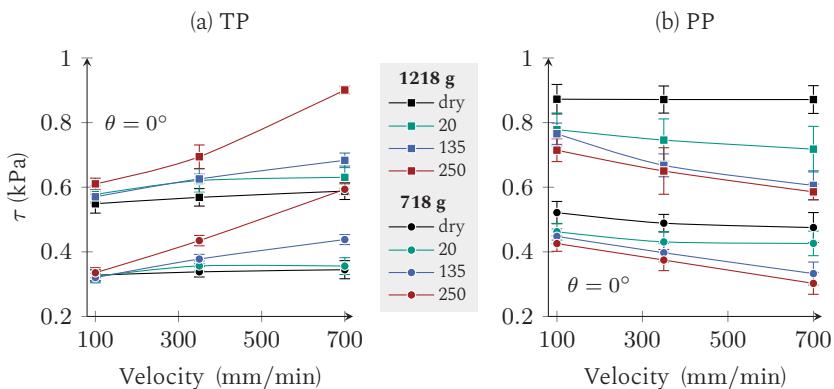
Figure 3.38: Tangential inter-ply results | (a) Dry and pre-infiltrated TP contact; (b) PP contact for a relative orientation of $\theta = 0°$ [336].

The measured tangential stress τ (cf. Equation 3.29) significantly depends on the applied slip-rate and viscosity of the resin in the contact zone. The impact of infiltration slightly increases with the sledge weight. Moreover, rate-dependency increases along with viscosity. Contrasting results are obtained for the PP results (cf. Figure 3.38 (b)). Here, increasing contact infiltration reduces the measured tangential stresses. The viscosity impact increases with increasing sledge weight.

Thus, infiltration leads to an altered tangential stress response. Regarding TP interaction (cf. Figure 3.38 (a)), the presence of the fluid increases the sliding resistance compared to the dry reference. This originates from

the smooth, rigid contact interface of the tool. The closed contact surface of the tool enables hydrodynamic friction states, which leads to a complete separation of the contact interfaces of tool and plies [161]. Optical observations could confirm this separation through slight sledge floating during experiments. Therefore, the obtained results are dominated by the fluid behaviour, which means that additional internal viscous forces within the fluid need to be overcome. A rate-dependency is introduced.

Regarding the experiments of the PP interface (cf. Figure 3.38 (b)), both contact surfaces are more uneven and deformable, which may lead to interlocking of rovings. It is assumed that a mixed contact state, e.g. combined friction on the roving crosspoints and hydrodynamic friction between them, establishes during the experiments [154, 156, 161]. This results in higher scattering of the measured tangential stresses compared to the TP trials (cf. Figure 3.38 (a)). In addition, the gaps between the rovings in conjunction with the surface structure prevents a proper separation of the contact pairs for the PP contact – a hydrodynamic friction state can only be established partly (mixed contact state). The contact infiltration leads to a lubrification of the contact areas, which reduces the tangential stress response. Moreover, the fluid homogenises the surface by accumulating in the roving gaps. Note that due to fluid displacement caused by the sledge, the formation of low-pressure zones below the sledge cannot be excluded completely.

Impact of relative fibre orientation. In addition to the above-outlined trials with a relative orientation of 0°, trials with 45° have been conducted by Hüttl et al. [156] and as part of a bachelor thesis [339]. Hüttl et al. [156] show that a reduced relative orientation within the contact decreases the tangential contact stress for dry and pre-infiltrated materials states. Additional trials in [339] show that this decrease is more pronounced for PP surfaces of the stack because of the less homogenous interfaces. Investigation with two different velocities (20 mm/min, 100 mm/min), have

found no significant impact with regard to the CoF. Given that these velocities are relativity low (cf. Figure 3.38), an impact at higher slip rates is assumed. The available data is used to calculate a scale factor $S_{\theta,\tau}$ [0-1]

$$S_{\theta,\tau}(\eta) = \frac{\tau^{45°}(\eta)}{\tau^{0°}(\eta)} \qquad (3.31)$$

between the obtained tangential stresses $\tau^{0°}$ with a relative fibre orientation of $\theta = 0°$, and $\theta = 45°$ for each infiltration state η. Using $S_{\theta,\tau}(\eta)$, the impact of the relative orientation can be estimated for each infiltration state and for the TP and PP contact pair (cf. Figure 3.39 (b)).
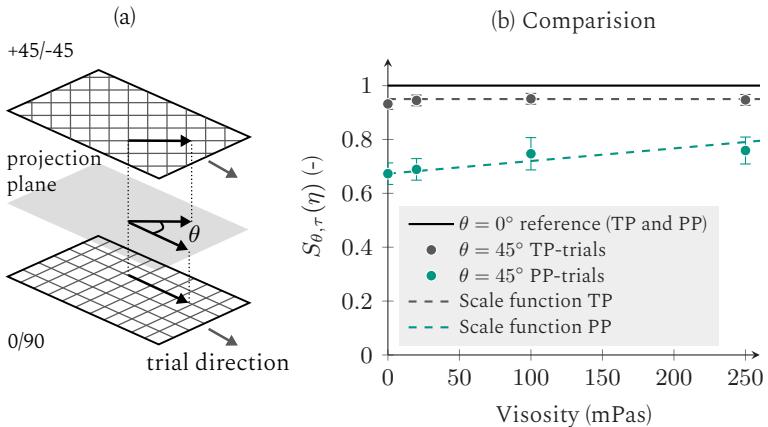
Figure 3.39: Tangential contact results | (a) Schematic illustration of inter-ply relative contact angle; (b) Scale factors for TP and PP behaviour relative to 0° reference.

For the TP trials, an almost constant and slight decrease by 5 % compared to the 0° results is observed. Consequently, relative fibre orientation is neglected for TP interaction. The PP trials revealed a linear increase towards the reference line with increasing viscosity. The constant slope can be described by

$$S_{\theta,\tau}^{\mathrm{PP}}(\eta) = 4.6961 \cdot 10^{-4}/\mathrm{Pas} \cdot \eta + 0.673. \qquad (3.32)$$

135

This linear decrease of $S_{\theta,\tau}^{\text{PP}}(\eta)$ compared to the $0\,°$ orientation is assumed to originate from an increasing impact of the fluid within the mixed contact state. Given these results, tangential stresses can be reduced by a maximal of 30 % with a smaller contact angle. It has to be noted that a possible lateral shift of the sledge might have influenced the results. Although this is not reported [156, 339], it should be considered in further experiments. This might become relevant in further investigations if the contact behaviour of the applied material shows an important impact on part level. However, the available datasets for the relative orientation of $45\,°$ are limited and not comprehensive. Consequently, further investigations in this work are solely based on the outlined results for the $0\,°$ orientation.

3.3.1.2 Normal tacking

Infiltration of the contact interfaces can lead to tacking in normal direction, as illustrated in Figure 3.36. The tacking behaviour has been investigated as part of a bachelor thesis [338]. Experimental trials according to Figure 3.40 (a) are conducted.

For these trials, the previously applied experimental setup is used for pull-off trials in normal direction (e_3). For this, the rope is fixed at the sledge's centre of gravity. As no guidance device is used, no additional frictional forces have to be taken into account, although a slight tipping during lift-off cannot be entirely excluded. The resulting tacking stress Ne_3 is calculated using the pull-off force f_{raw}^0 under consideration of the sledge m_{sl} and infiltrated specimen weight $m_{\text{sp}}(\eta)$

$$Ne_3 = \frac{f_{\text{raw}}^0}{A_{\text{sl}}} \quad \text{with} \quad f_{\text{raw}}^0 = f_{\text{raw}} - g_z \left(m_{\text{sl}} - m_{\text{sp.}}(\eta) \right). \tag{3.33}$$

As the number of stacked plies affects the resulting tacking forces, experiments with one to four plies are conducted in pre-infiltrated contact state.

(a)

(b)
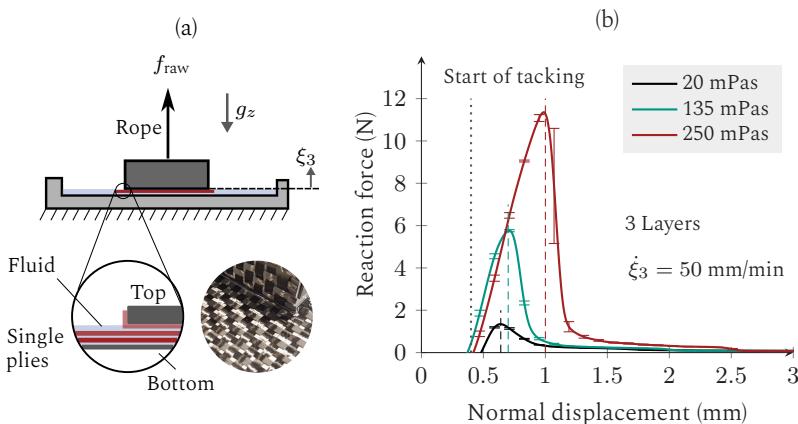
Figure 3.40: Experimental setup | (a) Schematic illustration using the rope to pull-off the sledge in normal direction; (b) Exemplary result of the tacking behaviour for three fabric layers (one attached to the sledge, two fixed at the bottom) for three different viscosities at a pull-off rate of $\dot{\xi}_3 = 50$ mm/min [338].

An exemplary result of the obtained reaction forces for a three ply configuration and a pull-off speed of $\dot{\xi}_3 = 50$ mm/min is plotted in Figure 3.40 (b). Rate-dependency is investigated via trials with three different low pull-off rates (5,20, 50 mm/min).

Experimental procedure. Only the amount of resin needed for a homogenous and complete infiltration of the contact interface is applied to minimize fluid-induced drag. For a trial, the required amount of fabric layers is stacked and clamped in the reservoir. One layer is always directly attached to the sledge itself. A soaking time of 2 min is waited before each trial.

Experimental results. The combined experimental results for the tacking behaviour are plotted in Figure 3.41 using the maximal recorded tacking force during the initial peak (cf. Figure 3.40 (b)).
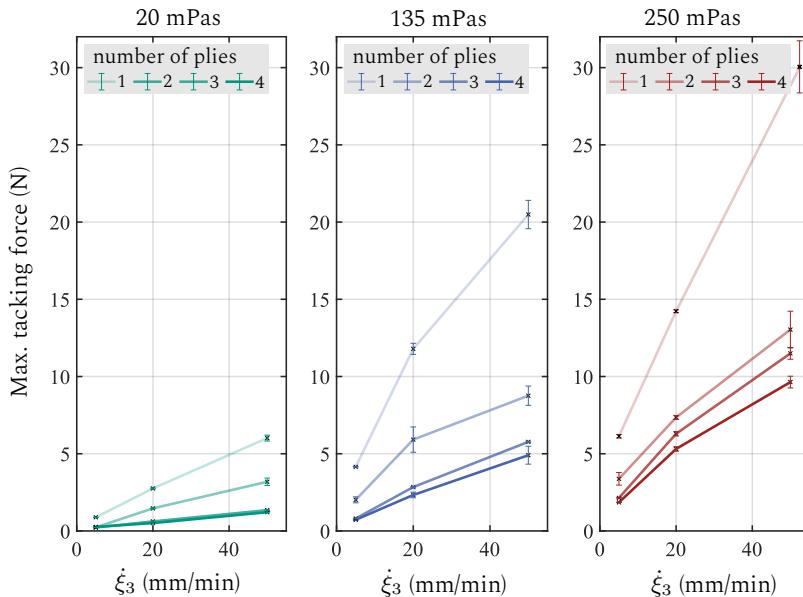
Figure 3.41: Experimental results | Normal contact tacking based on infiltration state, pull-off rate and layer number [338].

During all trials, the maximal measured tacking force is reduced by increasing the number of layers. This effect most dominant when only a few layers (1-2) are applied. Moreover, tacking forces increase with increasing viscosity and increasing pull-off rates as expected. The combined results for maximal tacking force $f_{T,3}^{max}$ and corresponding normal displacements $\xi_{T,3}^{max}$ are shown in Table A.8.

Conclusion.   The obtained results indicate a relatively strong influence of the infiltration state on the normal contact in the tacking area. However, the tacking forces are significantly below the assumed reaction forces encountered during characterisation of pre-prepregs or thermoplastic UD-tapes [24, 49, 78]. This originates from the low viscosity of

the fluid and architecture of the textile. Moreover, the formation of low-pressure zones below the sledge is assumed to be the reason for the high impact of ply numbers during trials. An overestimation for trials with only one and two plies is expected. To contribute to this, only tacking forces originating for three and four plies trials are applied during modelling and subsequent evaluation on part level.

3.3.2 Interface modelling

Contact modelling[1] is implemented using ABAQUS built-in 'General contact' [333] algorithm. As illustrated in Figure 3.42 (a), this algorithm acts on the slave nodes to identify proximal points on the corresponding master surface. A local and orthonormal coordinate system $\boldsymbol{\xi}_i$ is introduced at each of these proximity points (PP) to describes normal distance ξ_3 and tangential slip ξ_t.
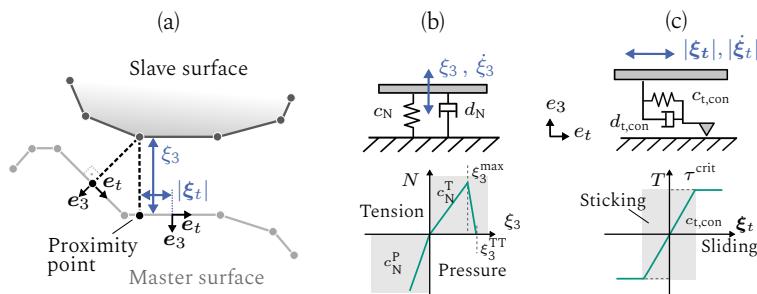
Figure 3.42: Contact formulation | (a) ABAQUS' general contact algorithm ; (b) Normal and (c) Tangential contact formulation.

The total contact stress of the current slave node is determined by averaging all currently detected PP. Detection distance is defined by a tracking thickness ξ_3^{TT}, which can be adapted manually. Commonly, values between 0.1 and 0.3 mm are applied. However, tacking results show (cf. Table A.8) that values between 0.4 and 0.8 mm are needed for the tracking

---

[1] Expansion of an existing contact subroutine for UD tapes [49, 83].

distance to be able to capture the maximum of the experimental curves. Thus, $\xi_3^{\mathrm{TT}} = 0.8$ mm is applied during all subsequent analyses. This significantly reduces computational efficiency as more contacts are identified and evaluated during analysis. To prevent false contact detection, explicit contact pairs are defined for the simulation runs.

3.3.2.1 Constitutive modelling

Regarding modelling, normal traction $\boldsymbol{N}$ and tangential traction $\boldsymbol{T}$ are naturally described separately based on the normal contact distance ξ_3 and tangential contact slip $\boldsymbol{\xi}_t$ with $t = [1, 2]$ as in-plane components. Combined ($\boldsymbol{Z} = \boldsymbol{N} + \boldsymbol{T}$) they provide the resulting contract traction $\boldsymbol{Z}$ on every slave node. For this purpose, suitable constitutive equations are introduced using the ABAQUS contact subroutine VUINTERACTION. The built-in contact functionalities (ABAQUS/explicit 2020) are not able to account for tangential slip and normal tacking simultaneously [83]. The values of numerical penalty parameters, which are not directly related to the parametrisation results, are not specified for intellectual property reasons. The implemented constitutive equations, as well as their parametrisation, are outlined in the following.

Normal traction. The non-penetration condition in normal direction is regularized by means of the Penalty method [335]. Following Equation 3.34

$$\boldsymbol{N} = N\boldsymbol{e}_3 = \begin{cases} 0 & \left[\xi_3 > \xi_3^{\mathrm{TT}}\right] & \text{(no contact)} \\ A_{\mathrm{sub}} & \left[0 \leq \xi_3 \leq \xi_3^{\mathrm{TT}}\right] & \text{(tacking)} \\ c_{\mathrm{N}}^{\mathrm{P}}\xi_3 + d_{\mathrm{N}}^{\mathrm{P}}\dot{\xi}_3 & \left[\xi_3 < 0\right] & \text{(penetration)}, \end{cases} \tag{3.34}$$

two stiffnesses are introduced to minimize penetration $c_{\mathrm{N}}^{\mathrm{P}}$ and to account for the tacking during contact tension $c_{\mathrm{N}}^{\mathrm{T}}$ (cf. Figure 3.42 (b)). Similarly, contact damping is introduced via $d_{\mathrm{N}}^{\mathrm{P}}$ and rate-dependency during tacking using $d_{\mathrm{N}}^{\mathrm{T}}$. A solely numerically motivated, linear decrease to zero

within $0.2\,\mathrm{mm}$ is implemented above $f_{\mathrm{T},3}^{\max}$ to increase numerical stability and prevent stiffness discontinuities during separation

$$A_{\mathrm{sub}} = \begin{cases} c_{\mathrm{N}}^{\mathrm{T}}\xi_3 + d_{\mathrm{N}}^{\mathrm{T}}\dot{\xi}_3 & \left[0 \leq \xi_3 \leq \xi_{\mathrm{T},3}^{\max}\right] \quad \text{(tacking)} \\ \sigma_{\mathrm{T},3}^{\max}\left(1 - \dfrac{|\xi_3| - \xi_{\mathrm{T},3}^{\max}}{\xi_3^{\mathrm{TT}} - \xi_{\mathrm{T},3}^{\max}}\right) & \left[\xi_{\mathrm{T},3}^{\max} < \xi_3 \leq \xi_3^{\mathrm{TT}}\right] \text{(linear decrease)}. \end{cases} \tag{3.35}$$

The maximal contact stress $\sigma_{\mathrm{T},3}^{\max} = f_{\mathrm{T},3}^{\max}/A_{\mathrm{sldge}}$ is calculated using the maximal tacking force and the contact area according to Equation 3.33. Corresponding contact reaction forces are computed using the current orthogonal contact orientation $\boldsymbol{N} = N\boldsymbol{e}_3$.

Tangential slip. An isotropic constitutive equation for friction is applied to account for the transition from sticking to sliding by means of an isotropic yield function Φ. In this case, Φ can be reduced from the general anisotropic case [49, 335] to

$$\Phi = \frac{\sqrt{G^{ij}T_iT_j}}{\tau_{\mathrm{crit}}} - 1, \tag{3.36}$$

where G^{ij} are the contravariant metric coefficients, T_i and T_j are the tangential traction components and τ_{crit} the isotropic yield stress [49, 336]. Hence, relative orientation between the slipping plies is not taken into account. The stick-slip-condition of the tangential traction $\boldsymbol{T}$ is regularized by

$$\boldsymbol{T} = T\boldsymbol{e}_t = \begin{cases} c_{\mathrm{t,con}}\boldsymbol{\xi}_t + d_{\mathrm{t,con}}\dot{\boldsymbol{\xi}}_t & [\Phi \leq 0] \quad \text{(sticking)} \\ \tau_{\mathrm{crit}}\dfrac{\dot{\boldsymbol{\xi}}_t}{|\dot{\boldsymbol{\xi}}_t|} & [\Phi > 0] \quad \text{(sliding)}, \end{cases} \tag{3.37}$$

where the penalty parameters $c_{t,con}$ and $d_{t,con}$ are constant. The critical tangential stress τ_{crit} is modelled by means of a Coulomb friction law superimposed with a Cross model to account for the rate- and pressure dependent inter-ply slip behaviour between the infiltrated plies according to

$$\tau_{crit} = \begin{cases} 0 & \left[\xi_3 \geq \xi_3^{TT}\right] \\ \eta_{t,con} & \left[0 \leq \xi_3 < \xi_3^{TT}\right] \text{ with } \eta_{t,con} = \dfrac{\eta_0 - \eta_\infty}{1 + m|\dot{\boldsymbol{\xi}}_t|^{(1-n)}} + \eta_\infty \\ p_N\mu_{t,con} + \eta_{t,con} & \left[\xi_3 < 0\right] \end{cases}$$

(3.38)

Here, $\mu_{t,con}$ and $\eta_{t,con}$ provide the material parameters, which depend on the in-plane tangential slip rate $\dot{\boldsymbol{\xi}}_t$ and the contact pressure p_N, respectively. The outlined model, therefore, describes the infiltration state on macro-scale in a homogenised manner. The contact stresses are calculated based on the slip rate and the infiltration state.

3.3.2.2 Parametrisation

The outlined approaches for normal and tangential direction are parametrised using an inverse parameter identification[2]. The obtained values are summarised in Appendix A.1.1 in Tables A.7 and A.8.

Normal tacking. The location (normal displacement ξ_3) and value of the maximal measured tacking force $f_{T,3}^{max}$ is used to parametrise the normal contact. By combining all pull-off rates with the same viscosity and number of layers, a function is implemented for every of the contact infiltration states. The number of layers within the stack is predefined in the subroutine. A direct comparison with the experimental results for three layers is shown in Figure 3.43.

---

[2] In-house available, python-based script originally developed by Dominik Dörr, 2018
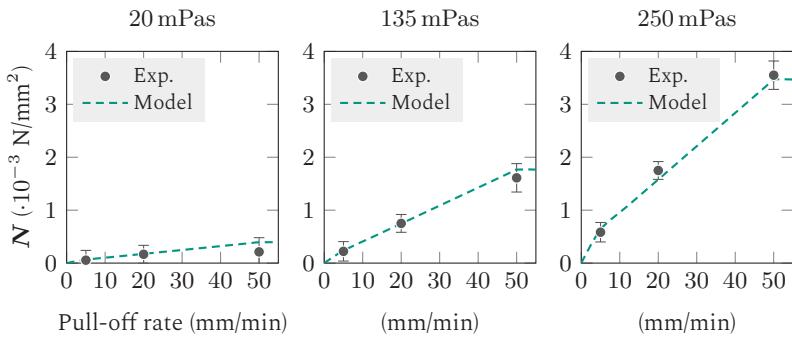
Figure 3.43: Validation of normal traction | Comparison of model prediction and experimental results for three layers.

Similar results on the four layer configurations are shown in Figure 3.44. The model captures the increasing rate-dependency for different viscosities. Moreover, extrapolation for increased velocity is prevented by prescribing the maximal value for the contact stress above $|\dot{\boldsymbol{\xi}}_t| = 50\,\text{mm/min}$. Good prediction accuracy is observed.
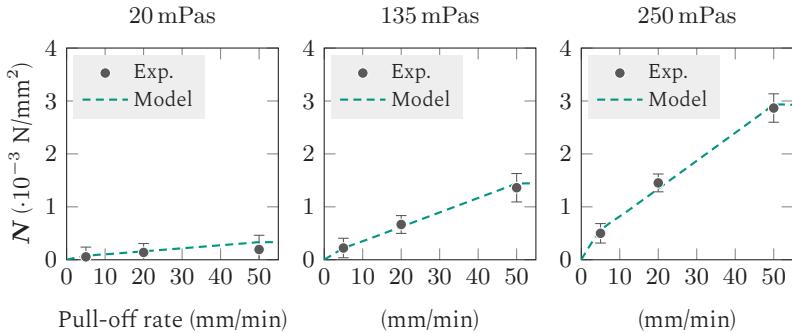
Figure 3.44: Validation of normal traction | Comparison of model prediction and experimental results for four layers.

Isotropic tangential slip. The introduced material parameters for the tangential contact behaviour are determined via reverse parameter identification. A multi-objective-based optimization accounts for the rate- and pressure dependency at different constant contact viscosities. A comparison of the experimentally determined and virtually predicted friction stress responses with different contact viscosities and contact pressures is summarized in Figure 3.45 for the TP trials and in Figure 3.46 for the PP trials.
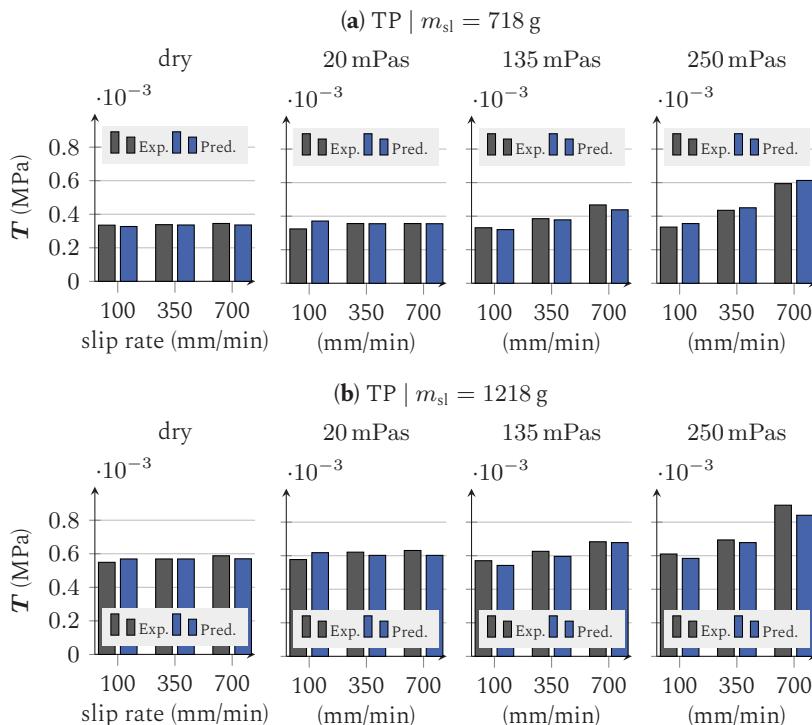
Figure 3.45: Tangential TP parametrization | Comparison of experimental results and model prediction for $\theta = 0°$ relative fibre orientation.

The overall results are in good agreement. The resulting parameters lead in most cases to a slight over-prediction for the lower contact pressures $m_{sl} = 718$ g and a corresponding under-prediction for $m_{sl} = 1218$ g (cf. Figure 3.45 (250 mPas)). The material parameters are summarized in Table A.9 and A.10.
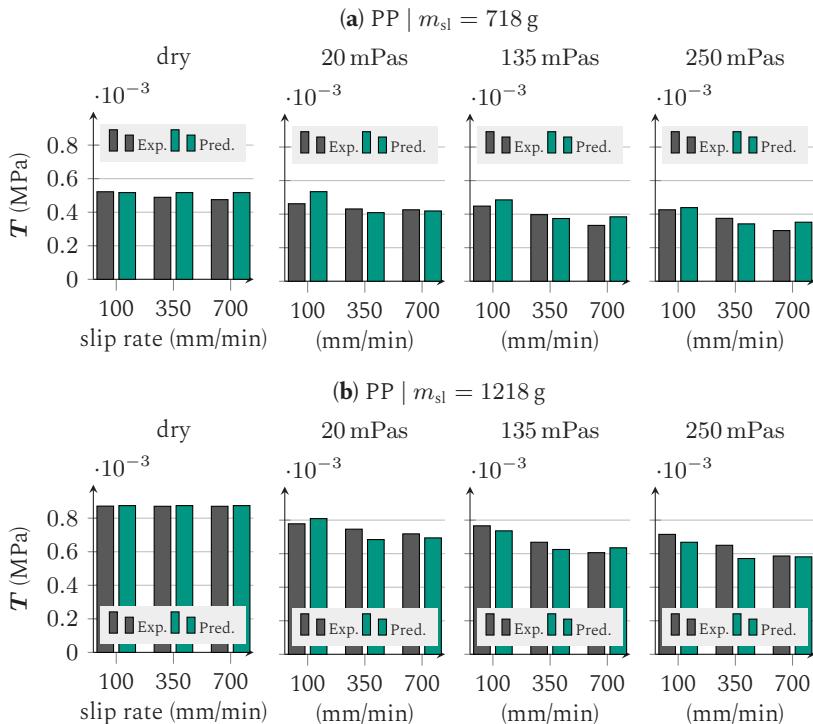
Figure 3.46: Tangential PP parametrization | Comparison of experimental results and model prediction 0° relative fibre orientation.

3.3.3 Numerical study

FE forming simulation runs are utilised to assess and evaluate the process relevance of the experimental findings. The user-defined contact formulation is investigated using two different generic geometries. Geometry 1 consists of a rather simple double dome with a circumferential blank holder (cf. Figure 3.47 (a)). Geometry 2 provides a more complex bowl-shaped geometry containing strongly curved corners end edges (cf. Figure 3.50 (a)). This geometry was already used for the numerical study of the bending behaviour in Section 3.2.5. For the bowl-shaped geometry, no blank holder is applied. The two different geometries are chosen to evaluate the impact of geometrical complexity and blank holder application on the sensitivity of the contact formulation. In this study, only the PP interfaces is investigated. The impact of the TP interface is assessed within the application to the complex demonstrator in Section 3.4. A built-in TP contact based on a Coulomb friction law is used $\mu_{\text{TP}} = 0.2$ in the following.

Geometry 1 - with blank holder. The presented numerical contact model in conjunction with the previously-outlined modelling approaches for membrane (cf. Section 3.1.2) and bending (cf. Section 3.2.4) behaviour are utilised.

For geometry 1, simulation runs containing two plies with initial fibre orientations of $0°$ and $\pm45°$ are conducted using a constant closing speed of $20\,\text{mm/s}$ for the punch. The tool surfaces are modelled via discrete rigid surfaces and gravity is considered by an additional body force (cf. Figure 3.47 (a)). An additional global blank holder with a constant pressure of $60\,\text{N}$ is used to ensure a large contact area between the plies. The resulting tangential slip rates remain within the parametrised range. The averaged curves for the dry contact setting, which provide the highest tangential slip rates are shown in Figure 3.47 (b)).
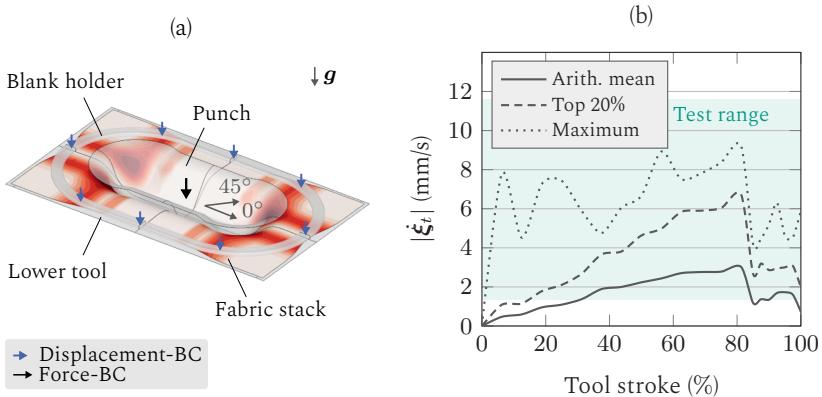
Figure 3.47: Geometry 1 | (a) Numerical setup; (b) Verification of contact slip rate $|\dot{\boldsymbol{\xi}}_t|$ [336].

Despite the tangential slip, the current contact state (tension or pressure) in normal direction is evaluated using contact state $C_s^{(n)}$. This state $C_s^{(n)}$ (-) is determined at every slave node n by averaging the contact flag $a_{\text{con},i}$ [-1,0,1] of every proximity point m_{prox} at the master surface. The contact flag $a_{\text{con},i}$ is defined based on the current contact penetration ξ_3 according to

$$C_s^{(n)} = \frac{\sum_{i=1}^{m_{\text{prox}}} a_{\text{con},i}}{m_{\text{prox}}|_{a_i \neq 0}} \quad \text{with} \quad \begin{cases} a_{\text{con},i} = -1 & [\xi_{3,i} < 0], \quad \text{pressure} \\ a_{\text{con},i} = 1 & [\xi_{3,i} > 0], \quad \text{tension} \\ a_{\text{con},i} = 0 & [\xi_{3,i} = 0], \quad \text{exclude.} \end{cases} \quad (3.39)$$

If, for example, the values of all proximity points associated with the same slave node are below zero (penetration), the corresponding contact state yields $C_s^{(n)} = -1$. Moreover, this node-based contact state is used for a global assessment of the predominate contact state $\bar{C}_s$ between the plies by averaging among all currently contacted nodes of the same element.

Individual deformation of the two plies results in relative tangential slip at the PP interface (cf. Figure 3.48 (a)). Moreover, the averaged tangential slip $|\boldsymbol{\xi}_t|$ between the two plies is plotted in Figure 3.48 (a).
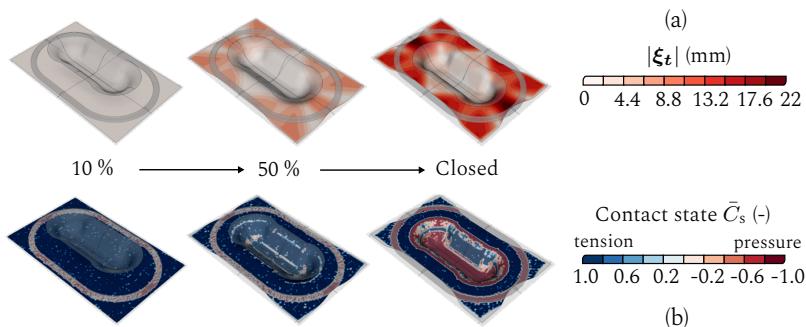
Figure 3.48: Geometry 1 | (a) Tangential slip $|\boldsymbol{\xi}_t|$ and (b) contact state during forming [336].

Only a slight impact of the assumed infiltration state is observed towards the end of the tool stroke. Additionally, Figure 3.49 (b) shows that the average contact state between the plies is predominated by tension during most of the tool stroke, except from regions below the blank holder and distinct areas beneath the punch (cf. Figure 3.48 (b)).
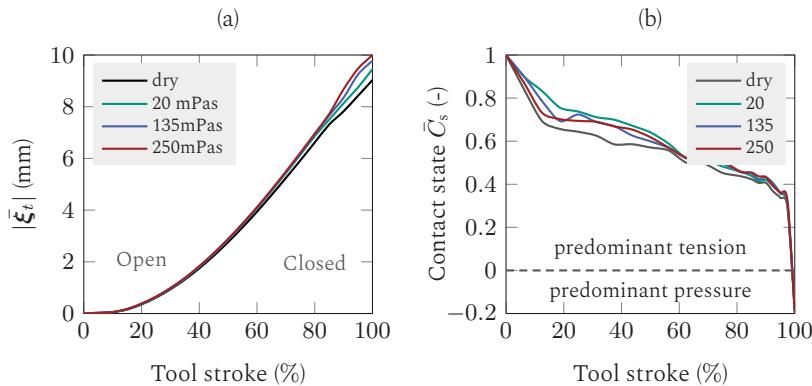
Figure 3.49: Geometry 1 | (a) Averaged interface slip $|\bar{\boldsymbol{\xi}}_t|$; (b) Predominant, averaged contact state $\bar{C}_s$ below the punch [336].

A predominated pressure state is only established within the last percent of the tool stroke. As the cavity of the tool is designed with 2 mm and

stack only measures a thickness of 0.6 mm, some regions below the punch remain in tension dominated state.

Geometry 2 - **without blank holder.**   Using a similar two-ply layup [0/90°, ±45°], the setup for geometry 2 in Figure 3.50 (a) illustrates the resulting contact slip between the two different oriented plies. The sharp corners lead to largely distributed contact slip. As the infiltration states dry, 20 mPas and 250 mPas provide the extremal values, only these three states are compared for geometry 2. A constant punch speed of 15 mm/s is applied. The resulting contact slip rates $|\dot{\boldsymbol{\xi}}_t|$ for the different infiltration states are given in (b). The arithmetic mean values are comparable,
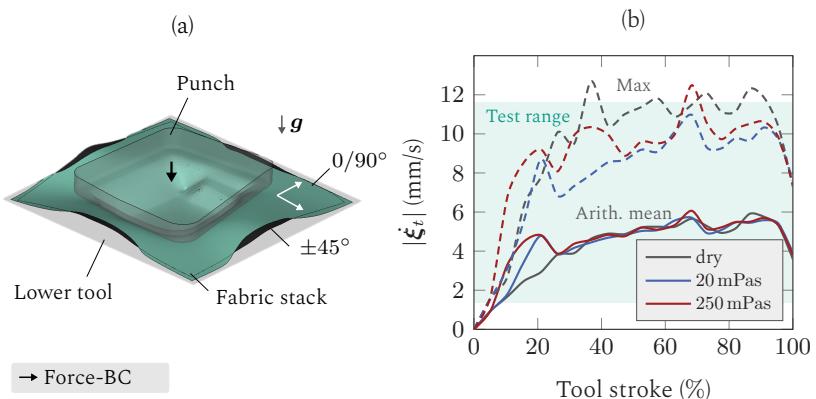
Figure 3.50: Geometry 2 | (a) Setup; (b) Verification of the occurring contact slip rates $|\dot{\boldsymbol{\xi}}_t|$ during forming using the arithmetic mean and maximal values.

whereas the maximal values slightly differ. As before, the dry state leads to the highest rates during most of the tool stroke. The values almost completely remain within the parametrised range.

For evaluation, the spatial tangential slip components ξ_1 and ξ_2 between both plies are compared for different assumed infiltration states of the PP

interface (cf. Figure 3.51). A quite comparable slip is observed for all in-filtration states. This applied to both evaluated orientations. Only minor differences are found for the extremal values.
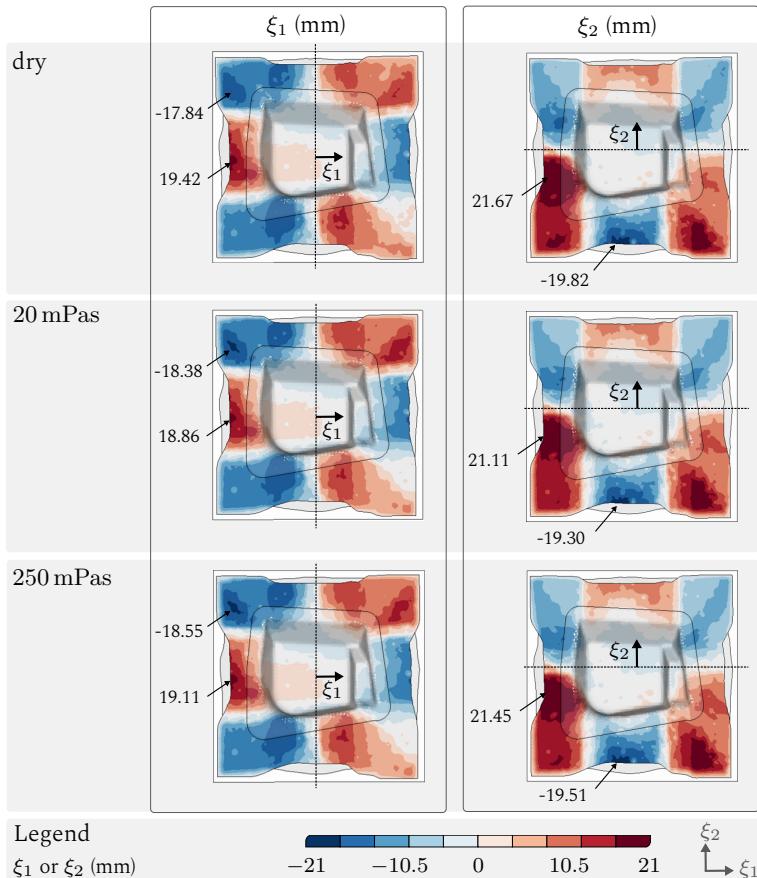
Figure 3.51: Relative slip ξ_1 and ξ_2 between the two plies in assembly COS for different infiltration viscosities of the PP contact for the fully closed mould.

Furthermore, the averaged tangential slip $|\boldsymbol{\xi}_t|$ is evaluated for two critical regions within the geometry (cf. Figure 3.52). Similar to the spatial results
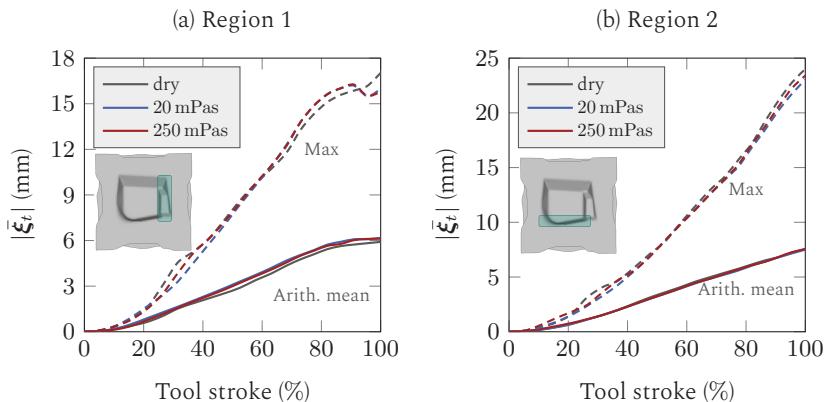
Figure 3.52: Geometry 2 | Averaged tangential slip $|\bar{\boldsymbol{\xi}}_t|$ at two critical regions 1 and 2, using arithmetic mean and maximal values.

in Figure 3.51, no significant difference is predicted for the two region. This applies to the mean displacement and the maximal values.

Discussion. Concluding the results, a two-sided picture emerges. On the one hand, experimental trials proved an impact of the contact viscosity in both tangential (cf. Figure 3.38) and normal direction (cf. Figure 3.41). The former is also affected by the local relative fibre orientation between the contacted plies in the experiments as Figure 3.39 illustrates. On the other hand, two numerical studies predict only an insignificant impact on the global draping behaviour (cf. Figures 3.49, 3.51 and 3.52).

Observed during experiments and predicted by the simulation, friction is almost always sufficiently low enough to allow for an individual deformation of each ply. This applies to dry as well as pre-infiltrated contact states from 20-250 mPas. Although the CoF decreases by almost 50 % with increasing viscosity relative to the dry one, (cf. Table A.10), the absolute viscous friction contact stresses remain low (cf. Figures 3.45 and 3.46).

Hence, the low-viscous fluid within the contact lubricates the contact interfaces but does not introduce significant viscous forces during numerical studies. Consequently, no significant impact on the predicted tangential contact slip is observed for both investigated geometries (cf. Figures 3.49 and 3.51). For comparison, the typically obtained order of magnitude for tangential stresses for a thermoplastic UD-Tape are one to two decades higher and even then, only a small effect on the overall draping results is reported [24, 49]. Given this comparison, it seems reasonable that the overall reported effect of the contact formulation is small.

In this regard, it has to be clarified whether a computational expensive user-developed contact formulation using a subroutine is necessary for a reasonable prediction accuracy on part level (process relevance). This is investigated in an additional study on a complex demonstrator part in the upcoming Section 3.4.

3.4 Complex demonstrator

3.4.1 Manufacturing

A complex sledge-shaped demonstrator (cf. Figure 3.53) has been developed and manufactured as part of the project 'Forschungsbrücke Karlsruhe-Stuttgart' and in close cooperation with the Fraunhofer ICT in Pfinztal, Germany.
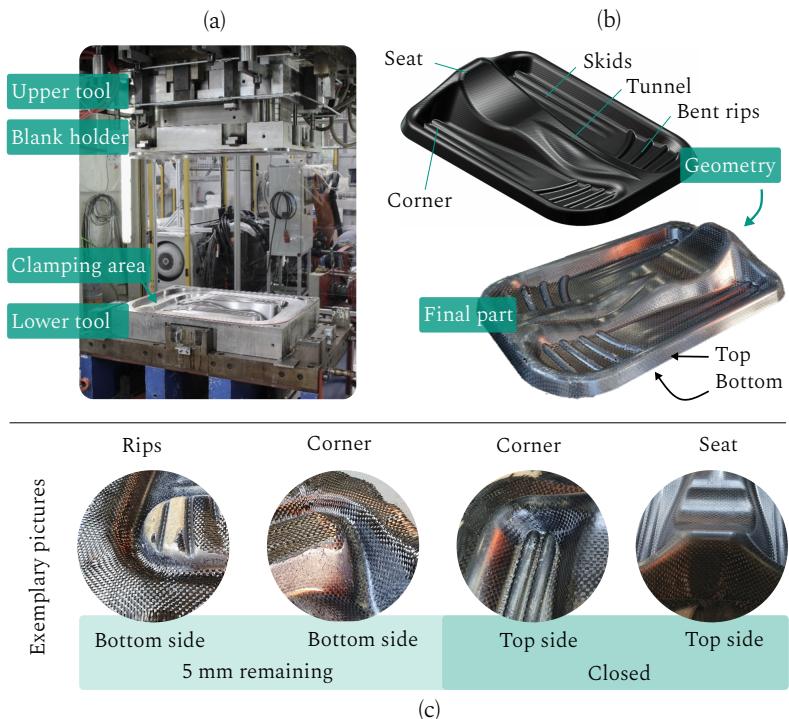
Figure 3.53: Demonstrator | (a) Tooling at Fraunhofer ICT; (b) Geometry and manufactured part; (c) Results at specific locations (rips, corners and seat) for the partly and fully closed mould.

The sledge geometry has been developed as part of a bachelor thesis [340] at the KIT-FAST under consideration of manufacturability and structural performance. As illustrated in Figure 3.53 (b), the sledge comprises several challenging geometrical features, including bent rips, skids and a sharp corner located around a double-curved tunnel. Forming simulation runs are utilised within the design phase and for the development of the tool concept using the above-introduced models for membrane, bending and inter-ply behaviour (cf. Sections 3.1 to 3.3). As shown in Figure 3.53(a), the sledge is manufactured upside down to support a superficial resin application. The tool comprises a circumferential blank holder that additionally serves as a sealing for the resin. The upper tool consists of a single stamp. Forming simulation and subsequent manufacturing proved the suitability of this tool concept.

WCM trials [73] with both introduced materials, namely woven fabric and UD-NCF, are conducted using a commercially available epoxy-based resin system VORAFORCE 5300 supplied by DOW CHEMICAL. It contains epoxy resin, hardener and internal release agent in a ratio of 100:16.2:2-weight%. The resin is preheated to $60\,°C$ before it is applied on the undeformed top side of the stack. A constant tool temperature of $110\,°C$ is prescribed during manufacturing. Six ply stacks $[0/\pm 45/0]_s$ are used for the woven fabric trials. During closing, the $\approx 400\,\mathrm{kg}$ heavy blank holder advances and clamps the outer rim of the stack before the upper tool gets into initial contact with the stack top side. Vacuum is applied within the last $20\,\mathrm{mm}$ of the tool stroke. However, some air remained trapped in the tool as the air traps in the final part indicate (cf. Figure 3.53 (b,c)). Only the woven fabric results are outlined in the following. The UD-NCF trials have been discussed in [73].

3.4.2 **Forming simulation**

Consistent with the applied FE forming models in previous sections, membrane, bending and contact behaviour are introduced via superimposed membrane and shell elements representing the single plies of the stack. The applied half-model is illustrated in Figure 3.54 (a), accompanied by an exemplary draping result (b). Due to the small radii, a fine structured mesh with a constant element size of 2 mm is required. A gravity step is applied prior to forming to account for the gravity-induced sagging of the material before clamping. The upper tool closes path-controlled, similar to the experiments and the blank holder solely moved under its self-weight.
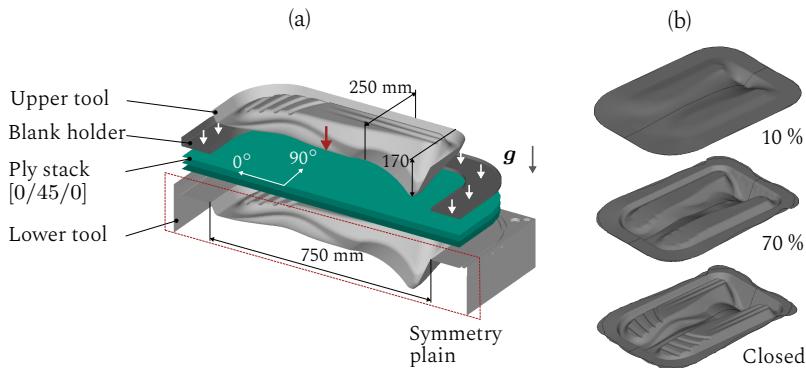
Figure 3.54: Demonstrator | (a) Forming simulation setup using a half-model and a three-ply stack; (b) Exemplary result for to 10, 70 and 100 % moulded part.

To reduce numerical effort, the closing amplitude is scaled by a factor of 2, leading to a forming within 5 s instead of 10 s. Moreover, a mass scaling of 10 is applied for the stack. Kinetic energies in the model remain below 1.5 % of the total energies. The experimentally applied symmetric six-ply stack is reduced to a symmetrical three-ply stack within the simulation runs for the stake of computational time. This still represents a similar

forming setup, as the main fibre directions are considered and the layup remains symmetric.

The model and the sledge forming setup are subsequently used to evaluate the impact of the applied contact formulation and general validation of the presented models by composition with experiments.

3.4.3 Impact of inter-ply formulation

A two-sided picture is observed for the contact behaviour in Section 3.3.3. Whereas characterisation experiments on small scale revealed an significant impact of the measured contact stresses, the numerical studies on part level predicted only a minor impact of the infiltration state on the final draping result. To ultimately evaluate the relevance of contact modelling and infiltration, a comparative study on the complex demonstrator is carried out. During this study, membrane and bending behaviour, as well as boundary conditions remain unchanged. A constant infiltration of 135 mPas is assumed for the whole stack.

Three contact configurations are compared. The *built-in* contact configuration utilises a solely tangential friction formulation based on a Coulomb friction model with $\mu_{TP} = 0.17$ for the tool-ply and $\mu_{PP} = 0.22$ for the PP interfaces. A tacking behaviour in normal direction in neglected. In contrast, the *full user* formulation combines all outlined rate- and viscosity-dependent contact properties, including tangential friction and tacking in normal direction (cf. Section 3.3.2.1). Moreover, a third *mixed* setup is investigated, where only the more sensitive PP interface is modelled with a user formulation.

The results for the in-plane shear angle distribution γ_{12} for both initial fibre orientations and the predicted outer shape for a remaining tool stroke of 5 mm are displayed in Figure 3.55.

(a)   (b)
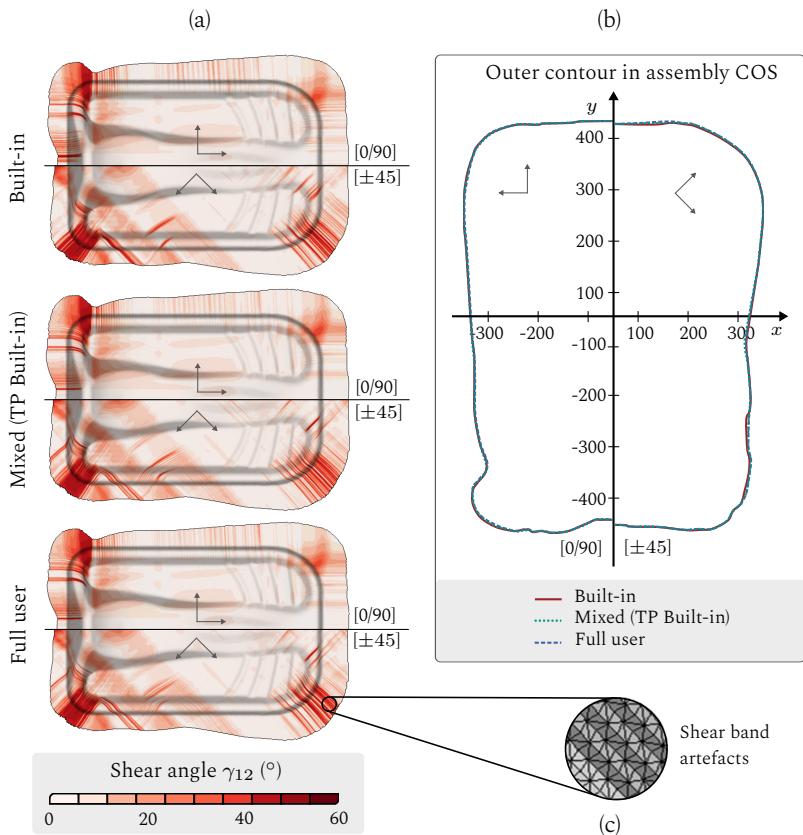
Figure 3.55: Impact of inter-ply formulation | Results in terms of (a) shear angle distribution; (b) outer shape in the global assembly coordinate system (COS) at 5 mm remaining tool stroke; Comparison of three contact formulation: Built-in – based on an already implemented coulomb friction law without tacking, Mixed – user-formulated contact model for the PP interface including tacking, Full user – TP and PP interfaces are described by the contact model introduced in Section 3.3.2; (c) Detailed view on in-plane shear band artefacts.

In general, no significant difference is observed. The spatial shear distribution is comparable for all three configurations and the predicted final

contour almost matches completely. Regarding the shear angle distribution, some artefacts are observed in all three settings. Their origin is comprehensively discussed in Section 3.4.5. The only noticeable drawback of the built-in contact originates from the missing tacking in thickness direction (cf. Example in Figure A.5 in Appendix A.2.3). Here, a local separation between the plies is predicted during simulation when tacking is neglected. This does not affect the predicted final shape, yet it is assumed that a simultaneous fluid progression would be affected by this, as transverse fluid progression would be impeded. If this also occurs during the trials could not be ascertained.

In accordance with the results obtained in Section 3.3.3, a low impact of the applied contact formulation is found. As reasoned above, the relative differences within the contact stresses are negligible compared to the high fibre tensions imposed by the heavy blank holder. It is concluded that the built-in model is sufficient for the here investigated woven fabric, especially when a circumferential blank holder is applied. Considering a computational performance advantage of 50 % for the built-in model, this is a favourable result. Moreover, experimental characterisation can be reduced to the dry material state.

3.4.4 Validation with experimental results

A direct comparison with the manufactured demonstrator is conducted to evaluate the validity of the developed macroscopic forming model. Fluid pressure is neglected and a constant viscosity of 135 mPas is assumed for all deformation mechanisms.

A comparison of the outer shape during experiment and simulation is illustrated in Figure 3.56 (a). Moreover, two critical zones (1,2) are presented where a large tangential contact slip arises between the plies. Outer contour and relative slip are predicted accurately by the simulation. Despite, the local fibre orientation within the 0/90 degree top ply is compared in

Figure 3.56 (b) for the challenging rear corner. Three distinct fibres are highlighted, showing a good agreement between experiments and simulation.
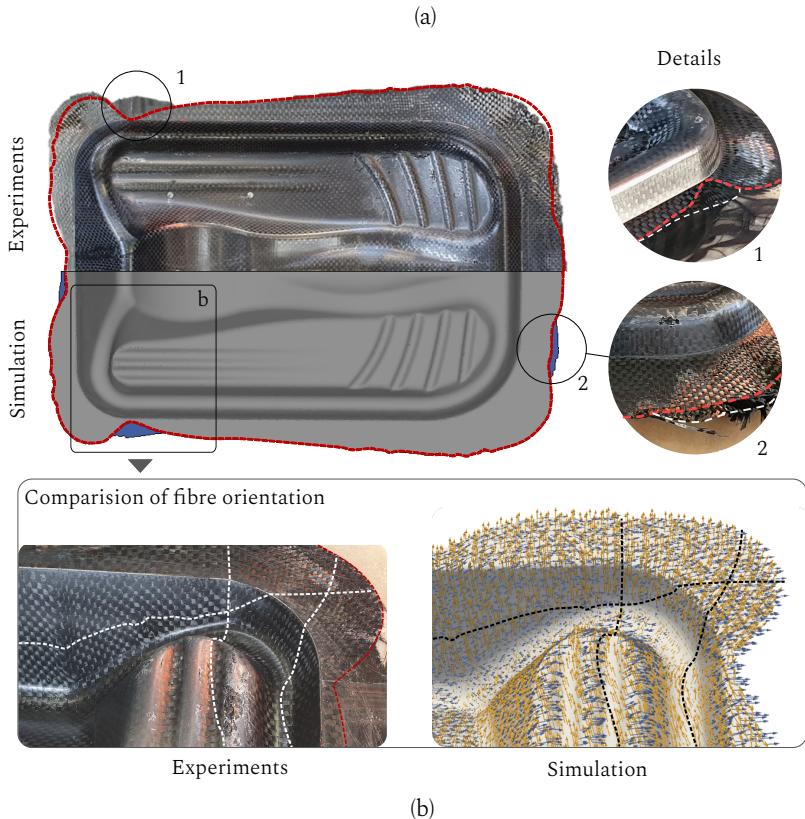
Figure 3.56: Validation | (a) Comparison of virtual prediction and experimental results for the outer shape and two critical areas (1,2); (b) Qualitative fibre orientation in the challenging rear corner.

The results show that the principal modelling approach can predict the pre-infiltrated draping behaviour of the complex demonstrator part. This supports the validity of the presented approach using a homogenised

description for the fluid via a modified viscoelastic material behaviour. However, the challenging geometry also outlines some noteworthy limitations of the applied modelling approach as discussed in the following section.

3.4.5 Limitations

In Figure 3.55, some shear band artefacts are noticeable (cf. Figure 3.55 (c)), especially in the $\pm 45\,^\circ$ plies. Although this seems not to significantly affect the final material distribution and orientation (cf. Figure 3.56), it still raises some questions. As these shear bands predict unphysical deformation modes, it is important to evaluate whether they originate from an incomplete membrane material formulation or are caused by numerical or contact issues.

Additional forming simulation runs with varied penalty contact stiffness, mesh size, scaled membrane stiffnesses and mass scaling are conducted to clarify the origin of the shear bands. A status flag based on the elastic fibre strains $\varepsilon_{\mathrm{f1,f2}}^{\mathrm{e}}$ of the membrane model (cf. Section 3.1.2) is introduced to achieve a better understanding of the material state

$$
y_{\mathrm{state}}^{\mathrm{mem}} = \begin{cases} -1 & [\varepsilon_{\mathrm{f,1}}^{\mathrm{e}}, \varepsilon_{\mathrm{f,2}}^{\mathrm{e}} < 0] \\ 0 & [\varepsilon_{\mathrm{f,1}}^{\mathrm{e}} < 0, \varepsilon_{\mathrm{f,2}}^{\mathrm{e}} > 0 \quad \text{or} \quad \varepsilon_{\mathrm{f,1}}^{\mathrm{e}} > 0, \varepsilon_{\mathrm{f,2}}^{\mathrm{e}} < 0] \\ 1 & [\varepsilon_{\mathrm{f,1}}^{\mathrm{e}}, \varepsilon_{\mathrm{f,2}}^{\mathrm{e}} > 0] \end{cases} \tag{3.40}
$$

within each membrane elements during forming (cf. Figure 3.57).

It shows that the critical areas where shear bands mostly occur are predominated by either one-sided or both sided in-plane fibre compression (mixed state). This is important, as the negative strain states are often neglected in characterisation and modelling of woven fabrics [47, 341]. Experimental setup to measure in-plane compaction of engineering textiles has been proposed in literature yet, as the inherent stability problems always introduce bending [47]. In case of the here applied circumferential

blank holder, bending is prevented by the dominating membrane tensions. In this situation, the elements can only evade by in-plane compression (pressure state), which in this case represents the energetically favourable deformation mode.
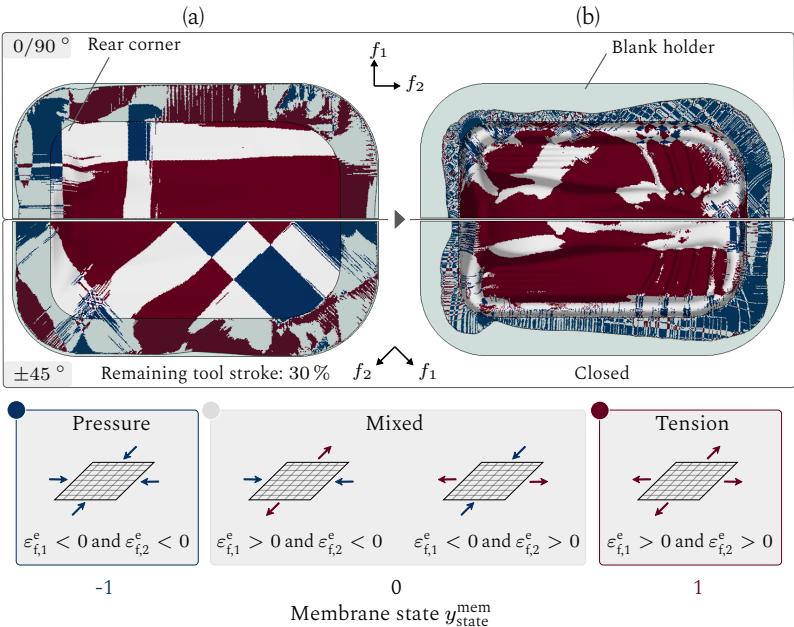
Figure 3.57: Demonstrator | Spatial membrane state $y_{\text{state}}^{\text{mem}}$ according to Equation 3.40 for the (a) 30 % and (b) complete closed tool. The colours indicate a double-sided pressure, a mixed or a bilateral tension membrane tensions state.

Therefore, the presented results strongly emphasise the importance of this material state for more complex forming setups. Moreover, shear-tension and shear-compression coupling are neglected in the presented membrane model. In both cases, the shear stiffness of the material increases significantly due to perpendicular tensions [112, 342] or out-of-plane cross-point compression [150, 153, 341]. Indeed, upscaled shear stiffnesses partly prevented or reduced the occurrence of these shear bands in some regions (cf. Figure A.6 in Appendix A.2.3). Furthermore,

out-of-plane compaction cannot be accounted for with this approach, which may influence the local contact stresses in the normal direction [325]. Consequently, the main source of the shear bands is assumed to be an incomplete material description.

Beyond that, it is found that shear bands are favoured by large areal contact and increased normal forces at the contact interfaces. This results from situations where individual nodes of the plies get stuck at the edges of the tool interfaces. This can be imaged as an external interference variable acting on the plies. Although this is a numerical issue that would matter less if the membrane behaviour would be formulated comprehensively, such situations often trigger the first shear bands. In this regard, a quite distinct clamping edge (ger: Tauchkanten) may amplify this issue even further as too large elements cannot be draped over such edges without contact penetration. Consequently, a smaller mesh size of 1 mm reduces and affects the occurrence of shear bands (cf. Figure A.7 in Appendix A.2.3).

In conclusion, the complex geometry highlights the challenges of FE forming simulations to account for small radii combined with distinct contact interfaces. This indicates that often applied shear edges (ger: Tauchkanten) and seals in WCM tools can provide a serious challenge for forming simulations. Most important, the results suggest that a 3D and more comprehensively coupled membrane model could reduce or even prevent the observed shear bands. In this regard, a comprehensive membrane model is especially recommended for complex forming setups with induced membrane forces. This is supported by the fact that no such shear bands were observed for the less challenging double-dome (cf. Section 3.1.3) and blow-shaped geometries (cf. Section 3.2.5).

Despite the discussed limitations, a good prediction could still be achieved. Thus, the observed effects did not significantly deteriorate the overall results. However, they prevent a reliable study of the infiltrated membrane

behaviour on this geometry. The results emphasise further research regarding a more comprehensive material modelling, including relevant couplings between the deformation modes.

3.5 Conclusive evaluation

This section summarises the presented experimental and numerical results of this chapter with regard to viscous draping. To evaluate the relevance for infiltration within the macroscopic deformation mechanisms, an assessment based on the experimental results and their relevance of forming simulation-related part of a comprehensive process model (cf. Figure 3.58) is conducted. A rating from low ($\star$) to high ($\star\,\star\,\star$) is introduced to compare the overall results comprehensively. The individual findings and reasons for the ratings are outlined in the following.

Membrane behaviour. The infiltrated bias-extension (IBET) test is proven to be suitable for the characterisation of shear behaviour of engineering fabrics infiltrated with low-viscous fluids. Experimental results reveal that pre-infiltration changes the internal friction at the crosspoints and within the rovings, leading to a deviation from the dry reference's shear behaviour and a shift of the locking angle. Therefore, drapeability can be either increased by low-viscous infiltration and reduced deformation rates or vice versa. In conclusion, the relevance of the infiltration state for the membrane material behaviour is high ($\star\,\star\,\star$).

Regarding modelling, both fibre stretch and viscoelastic shearing are taken into account. The model is able to predict the experimentally determined reaction forces in coupon tests, including the specimens' final shape. Finally, a numerical study on a double dome geometry demonstrated the importance to include the current infiltration state within the membrane behaviour ($\star\,\star\,\star$). Regarding future work, multi-axial

Figure 3.58: Experimental findings and impact of pre-infiltration on the obtained material behaviour (left) and relevance for detailed modelling in process simulation (right). Results are categorised by the deformation mechanisms based on Chapter 3. Additional results including strong FSI originate from Chapter 5.

stress states e.g. a 3D formulation including in-plane and out-of-plane compaction and shear-tension should be introduced to the modelling approach to achieve a more comprehensive material description. This is especially important for more complex forming task with challenging geometry features.

Bending behaviour.   A slightly modified cantilever test and a rheometer bending test (RBT) are successfully applied to investigate and characterise the bending behaviour of dry and low-viscous infiltrated woven fabrics. Experimental results reveal a rate- and viscosity-dependent material response, attributed to a combination of contact interface wetting (lubrication) and coating of the fibres. The latter could also invoke temperature dependency, which has not been investigated. Moreover, infiltration leads to rate- and viscosity-dependent hysteresis bending behaviour.

The results of both tests are directly compared for the first time, which revealed qualitative but not quantitative comparability. Three reasons are outlined and discussed to explain the systematic deviation between the experimental results (cf. Figure 3.29). The question, which bending test is more accurate and provides more reliable material parameters cannot be answered entirely based on solely one investigated material. While the cantilever approach should only be used when a fast assessment of the dry and infiltrated elastic material parameters is required, the rheometer approach is generally more recommendable because it allows for a rate- and time-depending analysis of the bending behaviour. Given the impact of infiltration on the experimentally determined material response, a high relevance is found ($\star$ $\star$ $\star$).

Based on the former, the experimental cantilever test and RBT results are used to parametrise two corresponding FE-based bending models. Application on part level of the numerical results reveals an effect of the applied infiltration-dependent bending models. However, the relevance of the bending behaviour also depends on other material- and process conditions, such as the applied contact behaviour and clamping conditions. This observation agrees with existing literature [47]. The usage of a viscoelastic bending model is recommended to account for the rate-depending material bending behaviour. Still, the viscosity-dependency of this applied viscoelastic bending model mainly matters in critical process situations e.g. sharp corners or superimposed shear deformation near the material's locking angle ($\star$ $\star$). Ultimately, the importance of a

viscosity-dependent bending model is expected to be of medium importance within process simulation models of the WCM process ($\star\ \star$). This differs from the thermoforming process of thermoplastic UD-tapes and Prepregs, where viscosity-dependent bending characterisation and modelling is recommended [47, 48, 330].

A distinction must be made for the contact evaluation. Although this is a small preview of the results from Chapter 5, it is distinguished between the 'no/weak FSI' and 'strong (both-sided) FSI' case in the following. This approach is motivated by the varying relevance of the user-contact formulation for both cases (cf. Figure 3.58).

Inter-ply behaviour (no/weak FSI). Infiltration reduces friction between the contact interfaces and introduces rate-dependency. Experimental results demonstrate an impact of a low-viscous infiltration on the normal and tangential contact behaviour. In general, the obtained contact stresses are up to 10 to 100 times below values reported for thermoplastic tapes or prepregs [24, 49, 87]. Consequently, only a medium impact is measured compared to other materials ($\star\ \star$). Moreover, a more sophisticated experimental setup is recommended for future investigations, which allows for a separated evaluation of material compaction and fluid pressure (mixed friction state).

The experimental results are modelled using a visco-elastic contact formulation with a homogenised approach for the fluid and the material. The obtained contact stresses for fully-infiltrated conditions are in good agreement with the experiments. Numerical studies on a double dome geometry and a complex demonstrator reveal only a low relevance for process modelling when FSI is neglected ($\star$). This is due to the overall low contact stresses. Collectively, a built-in contact formulation is sufficient for this material when fluid progression is neglected/unaffected by inter-ply-tacking (cf. Figure A.5) or strong FSI is not considered (weak FSI). This

is an acceptable assumption when draping simulations with constant infiltration states (cf. Demonstrator in Section 3.4.4) are used to predict the final fibre orientations for a moulded part. This implies the assumption of suitable low cavity pressures.

Inter-ply behaviour (strong FSI). Considering a strong FSI, the characterisation experiments suggest that separation between fluid pressure and material response (mixed contact state) in normal direction is required for proper evaluation. This could not be investigated with the presented setup and no comparable setup has been proposed in literature yet. A numerical study in Chapter 5 will demonstrate that a hydrodynamic friction model must be introduced for infiltrated areas and coupled with the current flow front position. Moreover, an accurate prediction of process effects such as flow-induced fibre displacement (FiFD) significantly depends on a proper contact formulation. Hence, strong FSI consideration results in high relevance of accurate infiltration-dependent contact model ($\star\,\star\,\star$). In contrast to the former case, a built-in contact formulation is not sufficient here and a more complex user-defined contact formulation is required.

167

4 Simultaneous fluid progression via weak FSI

Abstract

A reliable WCM process simulation requires a simultaneous description of draping and fluid progression. A monolithic approach based on the similarity of Fourier's and Richard's law is proposed to enable direct internal coupling between draping and fluid submodel. Utilising this similarity, a monolithic approach for combined textile forming and fluid progression is implemented in ABAQUS/explicit. A joint explicitly integrated solution of deformation and pressure field is adopted.

A feasibility study with a 2D fluid formulation based on a single-phase porous medium throughflow (user element: DPE2D) is presented following the initially proposed strategy. By superimposing the draping submodel (cf. Chapter 3), the first demonstration on a generic geometry reveals both, advantages and limitations of this 2D modelling strategy. In particular, crucial process mechanisms such as infiltration and compaction in thickness direction cannot be captured and require a 3D formulation.

Consequently, an expansion for the draping and fluid submodel is presented. Modelling of the draping submodel through user-enhanced continuum shell elements allows capturing of non-linear compaction. A superimposed user element (VUEL) is used to formulate a 3D fluid submodel (user element: DPE3D). It accounts for the local fibre volume content, the current fibre orientation and infiltration not only in in-plane, but also in thickness direction, even across multiple plies of a stack. Finally, the proposed process model is compared to the initially outlined experimental trials with in-situ flow front tracking. The results demonstrate the capabilities of this approach.

4.1 Modelling approach

A modelling approach for fluid progression during moulding is essential for a suitable process model for WCM. The experimental results in Section 2.1 demonstrate the need for a coupled approach to address forming and mould-filling simultaneously. Given the large deformations and contact areas during viscous draping, an explicit integration scheme for the FE-based draping submodel was proposed in Chapter 3.

The explicitly integrated draping submodel could be coupled with a state-of-the-art implicitly integrated and iteratively solved fluid submodel to introduce fluid progression. Doing so would require constant mutual updating and interpolation. Additionally, iteration for an unconditional stable solution of pressure and velocity field would need to be implemented. Although an implicitly integrated and iteratively solved fluid model would provide the most common way of modelling LCM processes [299, 307], it involves extremely high computational effort. Moreover, it has not yet been successfully applied for deformations comparable to draping.

Other promising approaches in literature suggest applying FE/CV-based formulations (cf. Section 1.2.5.2). They allow modelling the fluid submodel with respect to the current deformation state and fibre orientation. Still, only iterative integration schemes have been proposed so far. Although FE/CV approaches are well suited for coupling with the developed FE forming submodel, the combined process model would still be formulated half explicitly, half implicitly.

To prevent this, a monolithic approach is proposed in this thesis using an explicitly integrated FE/CV-based fluid submodel. The latter utilises that the equation for heat transfer (Fourier's law (cf. Equation 4.1)) and

fluid progression in a porous medium (Richard's law (cf. Equation 4.2)) are partial differential equations of the same order [329]

$$\int_V c_{\mathrm{p}}\rho\,\dot{T}dv = -\boldsymbol{\lambda}\int_V \left[\mathrm{div}\left(\mathrm{grad}\left(T\right)\right) + r\right]dv \tag{4.1}$$

$$\int_V C_{\mathrm{hyd}}\,\dot{p}\,dv = -\frac{\boldsymbol{K}}{\eta\,\varphi}\int_V \mathrm{div}\left(\mathrm{grad}\left(p\right) - \rho\boldsymbol{g}\right)dv\,. \tag{4.2}$$

This analogy is important since ABAQUS/explicit only provides a fully-coupled thermal-mechanical solver. By this means, the temperature degree of freedom can be reinterpreted to solve Richard's law which yields the pressure field. As highlighted, Richard's law can be expressed when replacing the heat capacity c_{p} with the hydraulic capacity $C_{\mathrm{hyd}} = \dot{V}/\dot{P}$ and the heat conduction tensor $\boldsymbol{\lambda}$ by the ratio of the permeability tensor $\boldsymbol{K}$ and the fluid viscosity η in the porous medium. The hydraulic capacity, which serves as a purely numerical parameter in this context, needs to be as small as possible to represent an incompressible fluid. Considering above introduced analogy, gravity $\rho\boldsymbol{g}$ can be taken into account for WCM modelling and replaces a potential heat source r. By this means, a fully-coupled thermo-mechanical analysis is utilized for a joint solution of deformation and fluid progression in ABAQUS/explicit. The latter uses the temperature degree of freedom to solve the pressure field. This concept can be considered a 'forming-driven' approach for process modelling, as it aims to add a suitable description for fluid progression to an existing FE forming model. This is motivated by the large draping-dominated phase during WCM (cf. Figure 2.7).

Outline. In a first step, the outlined approach is implemented in a 2D formulation to model in-plane flow progression without superimposed compaction. Moreover, two verification tests are presented, and this modelling strategy's feasibility is subsequently demonstrated on part level. Herefore, the fluid submodel is being superimposed to the draping submodel developed in Chapter 3. Afterwards, both draping and fluid

submodel are expanded to a fully-coupled 3D formulation in Section 4.3 and finally benchmarked by the double dome trials with transparent tooling.

4.2 Two-dimensional approach (DPE2D)[1]

Beginning with the modelling approach for intra-ply fluid progression, Figure 4.1 illustrates the superimposed concept (b) and the element formulation (c).
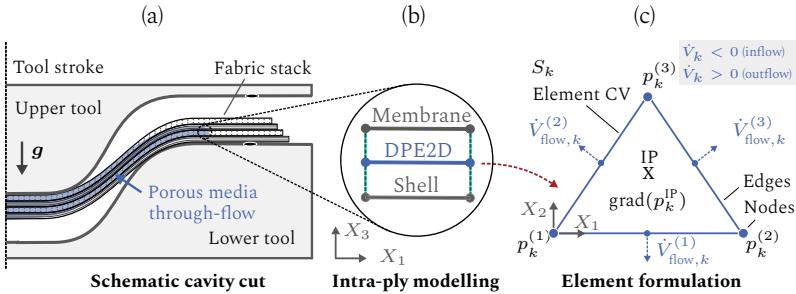
Figure 4.1: Schematic illustration of the adopted modelling concept and applied intra-ply modelling strategy (based on [329]).

A constant ply thickness t_0 is prescribed by the applied shell elements (cf. Figure 4.1 (b)). The forming submodel combines superimposed membrane and shell elements superimposed by a third element, referred to as 2D Darcy-Progression-Element (DPE2D). Whereas the former gives nodal stresses and moments, the DPE2D supplies the nodal pressure $p_k^{(N)}$ at every node $N = [1, 3]$ of every element k. The flow rate across each surface $i = [1, 3]$ of an element is given by $\dot{V}_{\text{flow},k}^{(i)}$. A structured triangular

---

mesh was applied for forming simulation in the previous chapter. Hence, a similar triangular element formulation is implemented via a user element subroutine (VUEL) in ABAQUS/explicit. The control volume (CV) of each element consists of all three edges of an element. Gravity is neglected in the DPE2D element. A moving boundary condition is implemented using element-based saturation values S_k defining the currently saturated domain according to

$$S_k = \frac{V_k^{\text{fluid}}}{V_k^{\text{fluid}} + V_k^{\text{void}}} \quad \text{with} \quad V_k^{\text{void}} = V_{1,k} - V_k^{\text{fluid}} - V_k^{\text{fibre}}. \tag{4.3}$$

Here, the current void volume of each element V_k^{void} is calculated based on the current element volume $V_{1,k}$, the already absorbed fluid volume V_k^{fluid} and the volume occupied by the fibre $V_k^{\text{fibre}} = \varphi\, V_{1,k}$. The pressure field is solely solved on the saturated domain. As this is only a first implementation test, isotropy is assumed for the permeability tensor ($K_{11} = K_{22}$). The two required key mechanisms are the solution of the pressure distribution in the currently saturated domain and the transient flow front progression, including mass conservation.

4.2.1 Numerical formulation

Saturated domain. For the implementation of Richard's law within the saturated domain, an existing triangular heat conduction element that has been developed by Dörr [49], is modified using the above outlined similarity to define a mass matrix $\boldsymbol{M}^{\text{mass}}$ based on the nodal hydraulic capacities C_{hyd}^N and a nodal diffusive flux vector $\boldsymbol{r}^{\text{diff}}$ according to:

$$\int_V C_{\text{hyd}}\, \dot{p}\, dv = -\frac{\boldsymbol{K}}{\eta\, \varphi} \int_V \text{div}\,(\text{grad}\,(p))\, dv \tag{4.4}$$

$$\underbrace{\rho C_{\text{hyd}}^N \boldsymbol{I}}_{\boldsymbol{M}^{\text{mass}}} = -\underbrace{h_0 A_1 \left(\boldsymbol{B}_1\, \boldsymbol{K}\, \boldsymbol{B}_1^\top\right) \boldsymbol{p}^{\text{vec}}}_{\boldsymbol{r}^{\text{diff}}}. \tag{4.5}$$

Here, h_0 is the constant shell thickness, A_1 is the current element area, $\boldsymbol{B}_1$ represents the operator matrix based on the triangles' linear shape functions [254], and $\boldsymbol{p}^{\mathrm{vec}} = [p_k^{(1)}, p_k^{(2)}, p_k^{(3)}]^\top$ is the nodal pressure vector of each element k. Only one centred integration point is required for a fully-integrated conduction matrix, as the gradient $\mathrm{grad}\,(p)$ is spatially constant within each element (cf. Figure 4.1 (c)). The saturated domain incorporates all elements with a saturation of $S_k = 1$. Due to the usage of an explicit time-integration scheme, complete incompressibility ($C_{\mathrm{hyd}}^N = 0$) cannot be modelled. However, the next section's verification test demonstrates that a sufficiently low value is acceptable for good prediction accuracy.

Flow front progression and mass conservation. A physical-based implementation of the flow front propagation within every single ply is required to ensure mass conservation. Therefore, a transient global CV is implemented containing all currently saturated elements. The two tasks of the CV are determining the summed propagated flow at the flow front and its partition on the filling elements. The latter is essential to ensure a mesh-independent fluid progression. Given a spatially constant pressure gradient $\mathrm{grad}\,(p)$ within each element, the flow rate $\dot{V}_{\mathrm{flow}}^{(i)}$ across each surface over the triangular element can be calculated through the scalar product

$$\dot{V}_{\mathrm{flow}}^{(i)} = \triangle t_{\mathrm{inc}}\, h_0\, A_1^{(i)} \left(\boldsymbol{n}^{(i)} \cdot \boldsymbol{v}_{\mathrm{D,IP}} \right) \quad \text{with} \quad \boldsymbol{v}_{\mathrm{D,IP}} = \frac{\boldsymbol{K}}{\eta\,\varphi}\,\mathrm{grad}\,(p)\,. \quad (4.6)$$

The element index k is omitted to increase readability. $\boldsymbol{n}^{(i)}$ is the normal outward surface vector of each element edge and $\boldsymbol{v}_{\mathrm{D,IP}}$ the fluid velocity at the elements integration point (IP). Since the summed incremental volume flow of each saturated element $\sum_{i=1}^{3} \dot{V}_{\mathrm{flow}}^{(i)} = 0$ is zero, mass conservation within every element is intrinsically captured. Still, small discrepancies could be confirmed by comparing the calculated volume flow on both sides of the same edge. Various researchers have observed

these discrepancies [304]. This discrepancy originates from the spatial interpolation of the shape function. It occurs when the flow calculation is based on the elements' pressure gradient and not the resulting gradient between two elements of the same interface (cf. Section 1.2.5.2).

An additional global CV considering all saturated and filling elements is implemented to ensure mass conservation for the whole model. This further gives the possibility to prescribe boundary conditions such as inlet, outlet, wall or flow front at certain edges (cf. Figure 4.2).
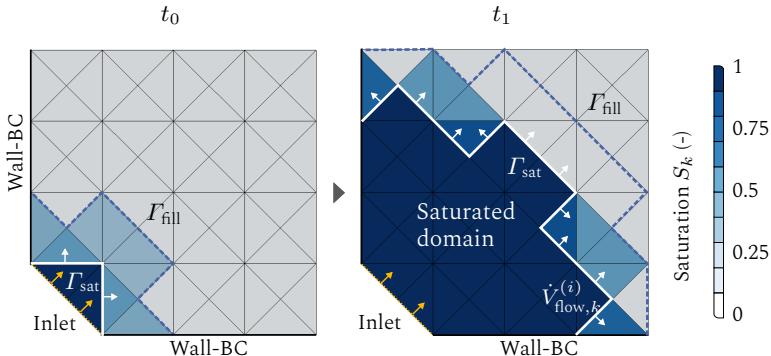
Figure 4.2: Principle flow front progression based on the transient expansion of saturated domain ($S_k = 1$) and the corresponding filling element domain $0 < S_k \leq 1$.

Furthermore, an algorithm weighting the pressure gradient and area of the currently filling elements is implemented to distribute the total flow front volume $\sum_k \sum_i \dot{V}_{\text{flow},k}^{(i)}|_{\Gamma_{\text{sat}}}$. As shown in Figure 4.2, edges are used to define the transient boundary of the currently saturated domain Γ_{sat} and the filling element domain Γ_{fill}. For mesh-independent flow distribution, elements are set to the filling state when at least one nodal pressure is above zero $p_k^{(i)} > 0$. The saturation values S_k among the filling elements are incrementally updated using Equation 4.3 until saturation is reached.

4.2.2 Verification tests

For verification, the outlined model is compared to analytical solutions for linear and radial flow scenarios. The reference solutions are outlined in [21]. Whereas the linear case proves feasibility and is used for parametric assessment of the hydraulic capacity range, the radial case demonstrates the mesh-independence of the flow front progression. In both cases, constant pressure is defined at the inlet nodes and the mesh remains undeformed.

Reference solutions. For linear case, flow front position $x_{\text{ff}}(t)$ can be calculated according to

$$x_{\text{ff}}(t) = \sqrt{\frac{2K_x p_{\text{inj}} t}{\eta \, \varphi}}, \tag{4.7}$$

where t is the injection time and K_x the permeability in linear direction. The resulting linear pressure distribution at the position x_{Loc} in the saturated domain is given by

$$p(t) = p_{\text{inj}} \left(1 - \frac{x_{\text{Loc}}}{x_{\text{ff}}(t)} \right). \tag{4.8}$$

In case of a radial flow progression, injection time t_{inj} is related with injection pressure p_{inj} and the radial flow front position r_{ff} according to:

$$t_{\text{inj}} = \frac{\phi \, \eta}{2K_r p_{\text{inj}}} \left[r_{\text{ff}}^2 \ln \left(\frac{r_{\text{ff}}}{r_{\text{inj}}} \right) - \frac{1}{2} \left(r_{\text{ff}}^2 - r_{\text{inj}}^2 \right) \right]. \tag{4.9}$$

Here, the injection radius at the inlet is given by r_{inj} and the radial permeability by K_r. The resulting non-linear pressure drop from inlet to the current flow front position $r_{ff}(t)$ can be calculated according to

$$p(t) = p_{inj} \left[\ln\left(\frac{r}{r_{ff}(t)} \right) \Big/ \ln\left(\frac{r_{inj}}{r_{ff}(t)} \right) \right].$$

(4.10)

Comparison. For the linear test case (cf. Figure 4.3 (a)), a strip comprising 1000 structured elements is infiltrated from left to right with a 1D flow under constant pressure.
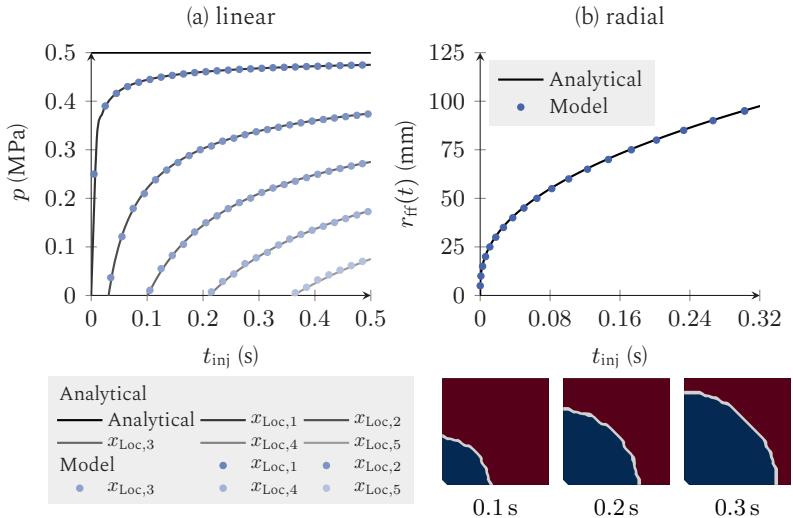
Figure 4.3: Comparison with analytical solution: (a) Pressure history during 1D scenario (injection from left to right) at distinct strip positions Loc_i – a linear pressure distribution establishes; (b) Radial flow front progression during central injection – the flow front position r_{ff} is measured from the centre [329].

The pressure of $0.5\,\mathrm{MPa}$ is predefined at the nodes of the left side of the strip, while the pressure at nodes at opposite right edge remains zero ($0\,\mathrm{MPa}$). An outlet is defined at the right edge. The strip measures

100 mm. A comparison of the pressure histories at equidistant locations $x_{\text{Loc},1} = 10$ mm to $x_{\text{Loc},5} = 90$ mm is shown in Figure 4.3 (a). A good agreement between the analytical and numerical solution is observed.

The radial setup comprises a quarter model with a mesh comprising of 6300 elements and central inlet with a radius r_{inj} of 4 mm. The total edge length of the quadratic quarter model is 100 mm. An constant pressure of $p_{\text{inj}} = 2$ MPa is prescribed. As the pressure gradient decreases during filling, the flow front slows down with increasing distance between flow front position and inlet (cf. Figure 4.3 (b)). This is consistently shown by analytical and numerical solution. For the latter, this implies a correct pressure distribution as the resulting inlet flow depends on the pressure gradient near the inlet. Moreover, three distinct pictures of the current flow front are presented. A circular progression is observed, which confirms mesh-independency. Both test cases are described in more detail in [329].

4.2.3 Feasibility study

To examine the capability of the outlined approach and to evaluate its suitability for a process simulation model, the verified DPE2D-based fluid submodel is superimposed to a draping submodel as displayed in Figure 4.1 (b). The already introduced double dome geometry is used for a feasibility study, comprising a single ply of woven fabric and a central injection port with a constant pressure of $p_{\text{inj}} = 1$ MPa infiltrating the material during moulding. As Figure 4.4 illustrates, this approach allows accounting for draping and in-plane fluid progression simultaneously. In this example, shear angle distribution (a) and resulting filling times (b) are displayed. Moreover, local permeability and FVC can directly be considered during fluid progression. The initially circular flow front becomes straighter when the edge of the stack is reached, which defines a wall in this example.
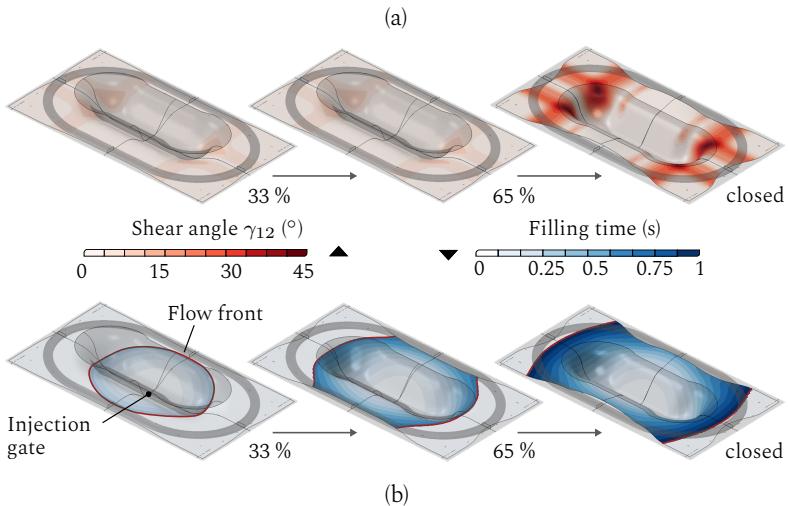
Figure 4.4: Combined forming and fluid progression simulation run of a single ply on a double dome geometry with circumferential blank holder. (a) Shear angle distribution and (b) filling times (s) (adapted from [329]).

Conclusion. An intra-ply fluid progression has been implemented by superimposing a user element with a 2D Darcy formulation (DPE2D) to an existing FE forming model. Analytical solutions are used to verify the explicitly formulated fluid submodel for porous media throughflow. By superimposing a suitable draping submodel, simultaneous modelling of draping and infiltration mechanisms of the applied woven fabric is possible. The first results on part level are promising. The monolithic approach allows for a very efficient coupling without additional external solvers.

Despite the advantages, some limitations of the presented DPE2D approach need to be discussed. First, only a single-phase flow is modelled, preventing air traps and evacuation from being considered. Moreover, superficial fluid is neglected in this approach and no fluid-interface model

179

has been presented so far, as only a single ply setup is shown. Most important, forming and fluid submodel cannot account for a variable ply thickness or compaction, which neglects key process boundary conditions of the WCM process – especially within the compression phase at the end of the tool stroke, e.g. the fluid-dominated phase (cf. Figure 2.7). For this reason, an additional injection boundary condition is necessary for the feasibility study in Section 4.2.3.

A 3D formulation of the fluid and draping model is needed to overcome these limitations, allowing for a compaction-induced fluid progression. Furthermore, such a 3D formulation for the fluid model would capture gravity-induced seeping of the superficial resin into the stack and flow progression in thickness direction. Recalling the experimental results from Section 2.1, capturing of through-thickness flows is important to predict the final infiltration state. It is concluded that only a 3D approach for the draping and fluid submodels can exploit the presented modelling strategy's potential fully.

4.3 Three-dimensional approach (DPE3D)[1,2]

Following the conclusion from the previous section, this section aims for a 3D expansion of the proposed DPE2D modelling approach. Therefore, additional material tests are required. First, compaction trials using dry and pre-infiltrated specimens are presented in Section 4.3.1. Secondly, permeability trials are used to determine the spatial permeability values of the woven fabric depending on the FVC (cf. Section 4.3.2). These results

---

[1]   Section 4.3 contains extracts of: C. Poppe, F. Albrecht, C. Krauß, L. Kärger: *A 3D Modelling Approach for Fluid Progression during Process Simulation of Wet Compression Moulding – Motivation & Approach*, Proc. Manuf., 47:85-92, 2020 [343].
[2]   Section 4.3 contains extracts of: C. Poppe, F. Albrecht, C. Krauß, L. Kärger: *A 3D process simulation model for wet compression moulding*, Composites Part A, 145:106379, 2021 [137].

are used to discuss the impact of anisotropic fluid progression caused by fibre reorientation during shearing.

On the basis of these experimental results, a modelling and implementation strategy is introduced (cf. Section 4.3.3), along with the formulations for the draping and fluid submodels (cf. Sections 4.3.4 and 4.3.5). Several verification tests are presented. Finally, the combined model is applied and validated on part level (cf. Section 4.3.6).

4.3.1 Viscous compaction trials

Compaction behaviour is analysed using a simple punch-to-plate setup mounted on a universal testing machine as shown in Figure 4.5.
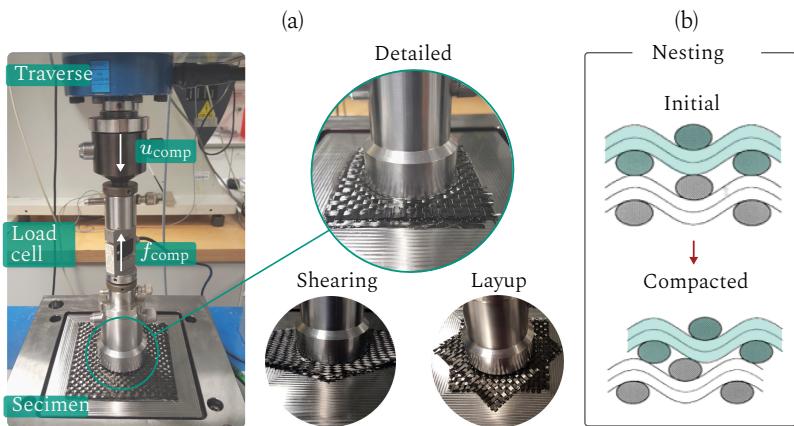
Figure 4.5: Compaction trials | (a) Setup and detailed views on the investigated configurations; (b) Interface penetrations between the uneven ply surfaces (roving crosspoints) in normal direction of the woven fabrics are referred to as 'Nesting' – it is affected by the relative orientation of the contacted plies (adapted from [137, 329, 344]).

Unsheared fabrics are investigated along with pre-sheared fabrics using shear angles of $25°$ and $50°$. The latter is close to the locking angle of

this textile. A layup of $[0]_4$ is used for the majority of the trials. A second stack $[0/45]_2$ with a relative fibre orientation of $45\,°$ is used to investigate nesting phenomena (cf. Figure 4.5).

A constant punch speed of $5\,\text{mm/s}$ is applied during all trials – rate-dependency is excluded. In addition to dry stacks, pre-impregnated stacks are investigated using a predefined amount of silicon oil with a constant viscosity of $20\,\text{mPas}$. To ensure the fluid being pushed through (porous medium flow) and not above (superficial flow) the porous fibre stack, the punch is slowly brought into contact with the top ply before the start of each trial. Each measurement is repeated three times.

The recorded reaction forces during compaction are depicted in Figure 4.6. The impact of shearing and nesting on the reaction forces is displayed in (a). Moreover, the impact of shearing and pre-infiltration is shown in Figure 4.6 (b). An expected and well-known, non-linear behaviour is observed during all trials.
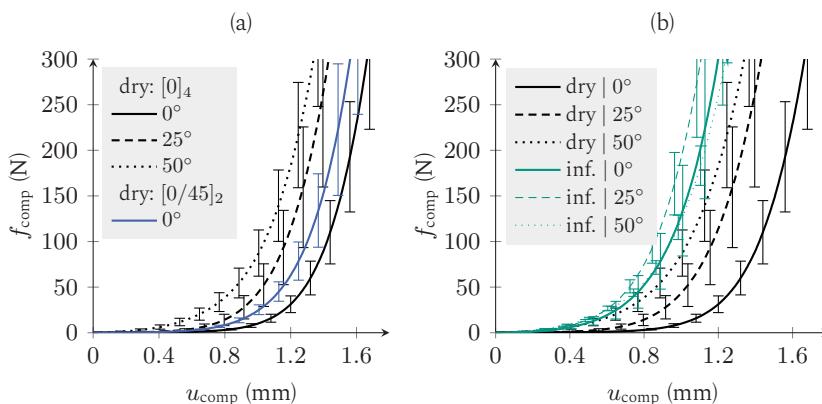
Figure 4.6: Compaction results | (a) Impact of dry shearing ($[0]_{4s}$) and dry nesting ($[0]_{4s}$ vs $[0/45]_2$); (b) Impact of pre-infiltration for different shear angle [137].

Compaction stiffness of the stacks increases along with increasing shear angle because the material density increases with shear deformation (densification). The obtained results are systematically affected by nesting (cf. Figure 4.5 (b)). In general, nesting phenomena reduce the stacks' stiffness by roving penetration at the interfaces. The amount of nesting depends on the fibre architecture of the contacted material. In accordance with existing literature [344], nesting is more pronounced when fibres are aligned in parallel ($[0]_{4s}$, cf. Figure 4.6 (a)). Consequently, a lower compaction stiffness is measured for the dry $[0]_{4s}$ configuration, compared to the $[0/45]_2$.

Furthermore, pre-infiltration during shearing further increases the measured compression forces. The superimposed fluid pressure below the punch results in a shift of the curves towards higher and earlier values. In contrast to the dry specimens, the pre-infiltrated curves for different shear angles do not differ significantly (green lines in Figure 4.6 (b)). This indicates that the presence of the incompressible fluid is more important than the increased transversal stiffness of the sheared specimens. The dry results will be used to parametrise the compaction model. The viscous compaction results will be applied to verify FSI in Chapter 5.

4.3.2 Permeability characterisation

In-plane permeability of single plies is measured using a radial test setup with circumferential clamping as illustrated in Figure 4.7 (a). The fabric stack is positioned between two plates of a mould. The upper plate is designed to provide a circumferential clamping area with constant a lamping length (cf. Figure 4.7 (b)). An additional video extensometer is used to minimize the uncertainties of the mould cavity, especially for increased FVC. A central injection port is used, pressure is measured close to the inlet.
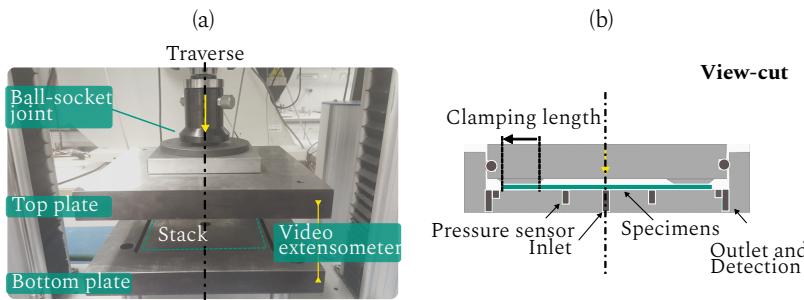
Figure 4.7: (a) Experimental setup of the used permeability test bench within a conventional tensile testing machine; (b) Schematic view cut – a 1D Darcy flow is assumed below the clamping during evaluation using the central pressure and the outflow [329].

Experimental procedure. A 1D formulation of Darcy's law is assumed to calculate the permeability based on the pressure difference between inlet and outlet in a stationary regime. For this, a constant inlet flow rate is applied and it is waited until the setup and the specimen are infiltrated completely. This procedure implies that the completely saturated and not the transient permeability is characterised [170]. In [343] this procedure has been verified via a direct comparison between a test setup measuring the transient permeability [178] and the here applied one. No significant differences for the obtained permeability values are measured for the applied woven fabric. This may be different for other materials [170]. Each trial is conducted three times with fresh material, always using a four-ply stack.

In addition to the permeability values in the undeformed state, the setup is used to measure the permeability values of four-ply stacks, which were priorly subjected to conditioned shear deformation [169]. This provides an alternative measurement method compared to the commonly applied picture frame-like clamping frames [20, 20, 153, 176, 179]. The measured areal weights ($w_A^{\gamma_{12}}$), which are needed to calculate the target gaps, corresponding to in-plane shear angle γ_{12} are summarised in Table 4.1. It

shows, that they are in good agreement with $w_{A,\gamma} = w_{A,0}/\cos(\gamma_{12})$ [20, 345].

Table 4.1: Areal weights $w_A^{\gamma_{12}}$ for different pre-sheared angles.

γ_{12} (°)	0	25	50
$w_A^{\gamma_{12}}$ (g/m^2)	318.0 ± 1.19	345.1 ± 2.52	481.0 ± 6.82

Fibre-frame permeability. Taking advantage of the forming-driven modelling strategy, the permeability tensor is also expressed in terms of the non-orthogonal material frame $\{f_i\}$. Figure 4.8 illustrates the difference between the fixed orthogonal frame $\{X_i\}$ of the test bench, a commonly applied rotated orthogonal frame $\{x_{\text{rot},i}\}$ for the ellipse and the here applied non-orthogonal material frame $\{f_i\}$ based on the principal material orientations for the 2D case with $i = 1, 2$.
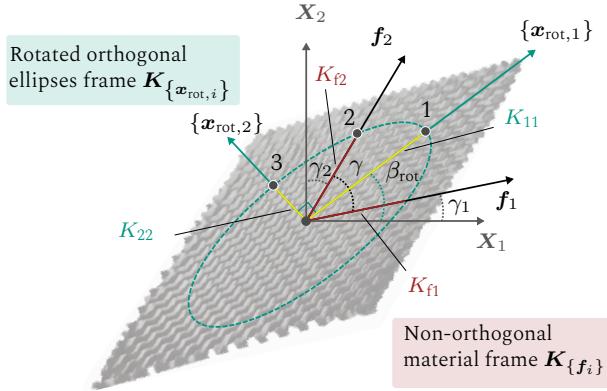
Figure 4.8: Illustration of the fixed orthogonal $\{X_i\}$, rotated orthogonal ellipse frame $\{x_{\text{rot},i}\}$ and the applied non-orthogonal $\{f_i\}$ frame during pure shear deformation of a woven fabric. Three points are needed for a unique reconstruction of the ellipse in the fixed orthogonal $\{X_i\}$ [137].

Usage of an orthogonal $\{X_i\}$ or rotated orthogonal frame $\{x_{\text{rot},i}\}$ for the permeability tensor K, which is reasonable in fluid mechanics, leads to challenges when the fabric is subjected to shear deformation [20, 173].

First, an anisotropic permeability in both ellipse directions (K_{11}, K_{22}) with non-constant ratio arises. Secondly, the orthogonal ellipse frame rotates relative to the first fibre orientation, often referred to as ellipse rotation angle (cf. β_{rot} in Figure 4.7 (b)).

Preliminary trials revealed a circular flow front progression for the undeformed balanced fabric $K_{X1}^0 = K_{X2}^0$, or $K_{f1}^0 = K_{f2}^0$, respectively. As outlined in Figure 4.8 (b) it can geometrically be shown, that the aspect ratio $a = K_{f1}/K_{f2} = \text{const.}$ between both fibre direction remains constant when the non-orthogonal material frame is subjected to shear. This is supported by the findings that have been published by Lai and Young [179] for a comparable material. In this regard, a direct calculation of the material frame permeability value K_{f1} based on the combined considerations of both fibre directions is enabled via

$$K_{f1} = K_{X1}/(\cos(\gamma_1) + \cos((\pi/2) - \gamma_2)). \tag{4.11}$$

Result. The experimental result are plotted in Figure 4.9. Every dot illustrates an investigated configuration. On the left side of Figure 4.9, the experimentally determined permeability values K_{X1} for different shear angles within the fixed orthogonal frame $\{X_i\}$ are plotted. The permeability values in the orthogonal frame K_{X1} strong decreases with increasing FVC and increase further when subjected to shearing. The same in-plane values are plotted with black dots in Figure 4.9 (b).

Furthermore, permeability in thickness direction is required to account for gravity- and inter-ply-induced flow progression (cf. Figure 4.9 (b), blue dots). For this, measurements are commissioned at the Fraunhofer IGCV in Augsburg (Germany). A test bench which has been presented by Graupner and Drechsler [185] is applied using a 12 layer stack. Similar to in-plane trials, a 1D Darcy flow in the stationary regime is assumed for evaluation. To ensure this 1D flow in thickness direction, the multiply stack is compacted between two perforated plates that distribute the inlet flow.

The permeability is evaluated at different compaction states via the resulting pressure difference within the inlet and outlet chamber.
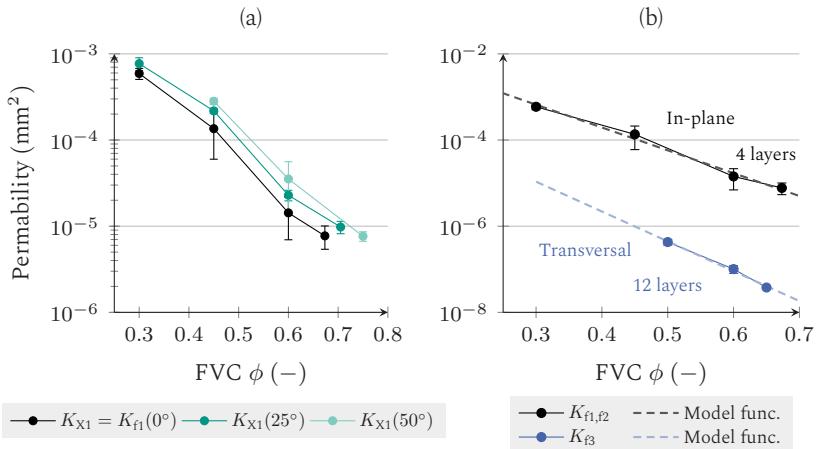
Figure 4.9: Permeability results | (a) Impact of shearing and applied frame – the enlarged plot is given in Figure A.8 in Appendix A.2.4; (b) Comparison and model functions for the material frame permeability values [137, 343].

A large number of plies is necessary due to the gaps of the 12K material and to ensure a homogenous medium. The values for transverse permeability K_{f3} are significantly lower than the values obtained for the in-plane directions. However, it is assumed that the values for the four-ply stack would be higher if they had been measured on a four-ply stack because of the increased likelihood of flow channels between the crosspoints of the woven fabric.

The values of the permeability tensor are subsequently treated via the following functions for the in-plane

$$K_{f1,f2}(\phi) = 0.0256 \cdot e^{-12.195\phi} \tag{4.12}$$

and out-of plane fibre-frame permeabilities

$$K_{\text{f3}}(\phi) = 0.001293 \cdot e^{-15.95\phi} \tag{4.13}$$

obtained through a regression.

Benefit of non-orthogonal description. To demonstrate the advantages of a non-orthogonal description of the permeability tensor, Figure 4.10 provides a comparison between measured and predicted permeability values for different shear and compaction states. Whereas the experimental values are obtained by individual measurements, the model predictions are solely based on the unsheared values. This is due to the intrinsically capturing of the underlying mechanisms by the non-orthogonal frame. Meaning, the material frame itself accounts for the fibre reorientation of the permeability values. The same advantage is used within hyperelastic material formulations (cf. Section 1.2.4.2).
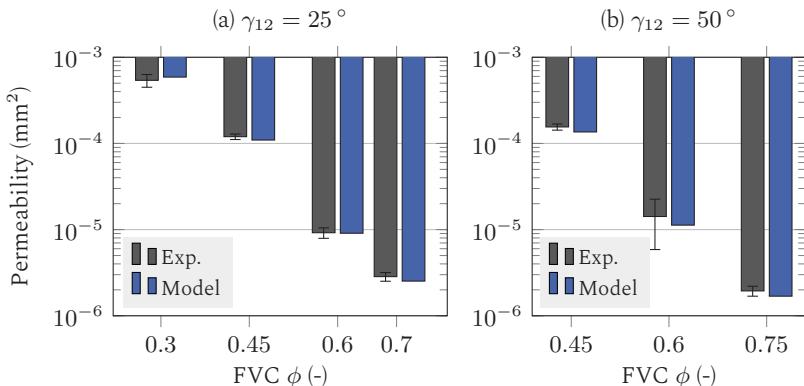
Figure 4.10: Verification of fibre-parallel description | Comparison between experimental values for sheared fabrics ((a) $\gamma_{12} = 25\,°$ and (b) $\gamma_{12} = 25\,°$) with the model predictions using the fibre-frame description for the permeability tensor $\{\boldsymbol{f}_i\}$ – which solely uses the values for the unsheared state $\{\boldsymbol{X}_i^0\}$.

Using the non-orthogonal frame to express the permeability tensor, the experimental effort can be reduced significantly, as only the values in undeformed states are required. That this is sufficient to predict the anisotropic, ellipse-shaped flow front progression during shearing will be demonstrated in Section 4.3.5.3.

4.3.3 Modelling strategy

Given the underling ideas of the chapter, a detailed illustration of the developed modelling strategy is displayed in Figure 4.11. As common in FE forming simulations, tools are modelled as rigid surfaces and individual single plies represent the stack; interconnected using a contact algorithm. Additionally, fluid progression across ply interfaces is required, which is referred to as 'Solid-Fluid-Contact'. Each single-ply is represented by two coupled submodels, a forming submodel that accounts for the displayed deformation mechanisms and a fluid submodel that addresses spatial infiltration and fluid-related contact mechanisms. Superficial fluid is not directly accounted for by explicit modelling in this work. It can only be implicitly accounted for via an increased stack thickness of the top layer.

Several user subroutines are combined during runtime for an implementation in ABAQUS' explicit solver (cf. Figure 4.11 (2)). A VUEXTERNALDB subroutine is called on several occasions and serves as a master control layer to gather and share information between subroutines, ensure thread safety and compute results fields. The two submodels are implemented within one user material routine VUMAT superimposed with a user element routine VUEL, which enhances the compaction behaviour of the forming submodel and contains the fluid submodel. Beyond that, a nodal-based subroutine VUFIELD and an integration-point-based subroutine VUSDFLD are used to access and share information during runtime (3).
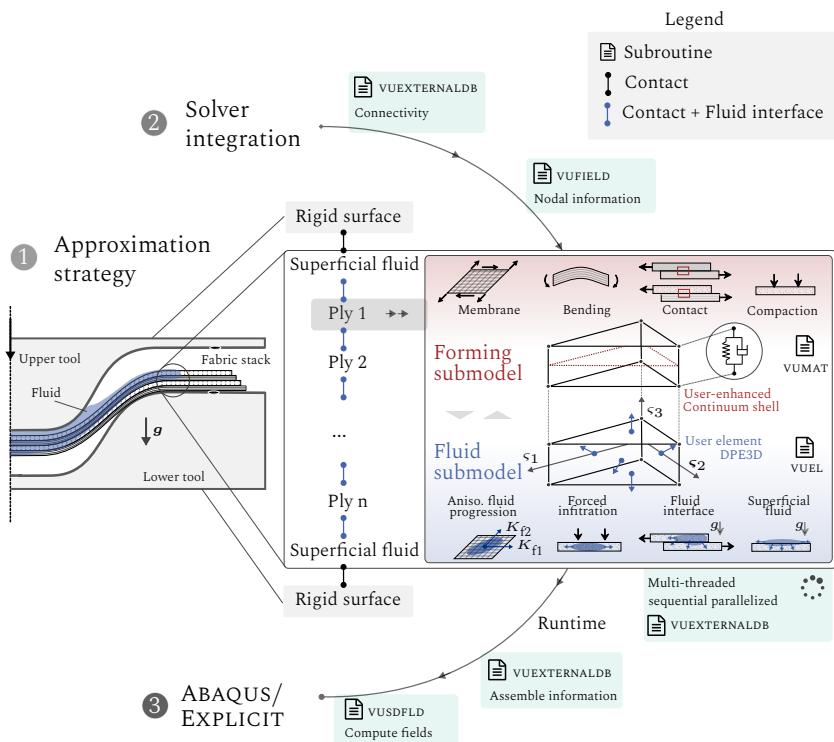
Figure 4.11: Modelling strategy, implemented key mechanisms and solver integration during runtime of the WCM model in Abaqus/explicit – solver integration bases on a combination of several subroutines [137].

The forming submodel addresses membrane, bending and compaction behaviour via built-in Continuum shell elements (SC) with user-defined membrane behaviour (cf. Section 3.1) and superimposed user-enhanced compaction behaviour. Usage of SC elements provides the advantage of a nearly locking-free 3D element, which allows for a direct application of in-plane material subroutine (VUMAT). However, using the SC element comes at the costs of coupled membrane and bending behaviour and a constant linear thickness modulus. As discussed in Section 1.2.4, assessment of compaction and its locking-free consideration within a

fully decoupled 3D formulation during forming is especially challenging [249–251].

In this work, decoupling between membrane and bending behaviour within each ply is neglected as SC elements are utilized. This does not imply that bending behaviour as a whole is neglected. Rather, the bending stiffness cannot be formulated independently from the elasticity modulus of the membrane part. In Section 4.3.4.2 it will be demonstrated that the bending stiffness of each ply can still be approximated quite accurately when the transversal shear stiffness of the SC element is adapted accordingly. This procedure is valid for minor challenging geometries and forming setups, including the later examined double dome geometry.

A constant thickness modulus proves a rather poor approximation of the material compaction behaviour as illustrated in Figure 4.12. Therefore, the compaction behaviour is enhanced by a mechanical part within the superimposed user element that supplies an additional constitutive equation in thickness direction.

The fluid submodel is embedded in a VUEL subroutine, superimposed to the SC element. The addressed key mechanisms of the fluid submodel are anisotropic permeability, compression-induced infiltration, transient interface flows and implications of gravity.

Isoparametric user element formulation. The user element is formulated in an isoparametric manner by means of linear shape functions matrix $\boldsymbol{N}_{\text{shape}}$ [254] and six integration points (cf. Table A.13, Appendix A). The operator matrix

$$\boldsymbol{B} = (\partial \boldsymbol{N}_{\text{shape}}/\partial \boldsymbol{\varsigma}) \cdot \boldsymbol{J}^{-1} \tag{4.14}$$

in the current configuration $\boldsymbol{x}$ is calculated using the spatial derivatives of these shape functions with respect to the current coordinates. The deformation gradient $\boldsymbol{F}$ within the element

$$\boldsymbol{F} = \boldsymbol{J}_1 \cdot \boldsymbol{J}_0^{-1} \quad \text{with} \quad \boldsymbol{J}_1 = (\partial \boldsymbol{N}_{\text{shape}}/\partial \boldsymbol{\varsigma}) \cdot \boldsymbol{x} \quad \text{and} \quad \boldsymbol{J}_0 = (\partial \boldsymbol{N}_{\text{shape}}/\partial \boldsymbol{\varsigma}) \cdot \boldsymbol{X},$$
(4.15)

is computed using the Jacobian matrix $\boldsymbol{J}_1$ with respect to the current configuration $\boldsymbol{x}$ and the Jacobian matrix $\boldsymbol{J}_0$ with respect to the reference configuration $\boldsymbol{X}$. For material modelling, the Green-Lagrange strain $\boldsymbol{E}$ according to Equation 3.2 is used. The Green-Lagrange strain rate $\dot{\boldsymbol{E}}$ is calculated by means of the current time increment size $\triangle t_{\text{inc}}$ and the values from the previous increment $\boldsymbol{E}^{\{\triangle t_{\text{inc}} - 1\}}$. Moreover, the rate-of-deformation tensor (cf. Equation 1.15) can also be calculated using $\boldsymbol{F}$ and $\dot{\boldsymbol{E}}$

$$\boldsymbol{D} = \frac{1}{2} \left(\dot{\boldsymbol{F}} \boldsymbol{F}^{-1} + \boldsymbol{F}^{-\top} \dot{\boldsymbol{F}}^{\top} \right) = \boldsymbol{F}^{-\top} \cdot \dot{\boldsymbol{E}} \cdot \boldsymbol{F}^{-1}.$$
(4.16)

4.3.4 Forming submodel

The SC element allows for a direct application of the membrane model presented in Section 3.1.2. Hence, modification of compaction behaviour and parametrisation of the bending behaviour remains for intra-ply modelling. Following the results of Section 3.5, inter-ply contact between the plies is implemented by a built-in general contact algorithm of ABAQUS, using friction coefficients of $\mu_{\text{TP}} = 0.29$ and $\mu_{\text{PP}} = 0.223$ [119]. The penalty contact normal stiffness c_{N}^{P} is set with the intention to reduce penetration between plies and tools as much as numerically possible by simultaneously keeping a reasonable time increment for the explicit solver.

4.3.4.1 Compaction behaviour

A hyperviscoelastic formulation is implemented within the user element to account for a non-linear compaction behaviour at finite strains. The

elastic part only affects the thickness direction. In addition, an isotropic rate-dependent numerical damping is superimposed for stability reasons. The Voigt notation is applied in the following and indicated by

$$\tilde{\boldsymbol{\sigma}} = [\sigma_{11}, \sigma_{22}, \sigma_{33}, \sigma_{23}, \sigma_{13}, \sigma_{12}]^\top. \tag{4.17}$$

For the elastic part, the Kirchhoff stress vector $\tilde{\boldsymbol{\tau}}^{\text{e}}$ is calculated by means of deformation gradient $\tilde{\boldsymbol{F}}$, Green-Lagrange strain $\tilde{\boldsymbol{E}}$ and the stiffness matrix $\boldsymbol{C}$ according to:

$$\tilde{\boldsymbol{\tau}}^{\text{e}} = \tilde{\boldsymbol{F}} \cdot \boldsymbol{C} \cdot \tilde{\boldsymbol{E}} \quad \text{with} \quad C_{33} = E_3^{\text{Mat}}(\varepsilon_3, \gamma_{12}) + E_3^{\text{Lock}}. \tag{4.18}$$

Only one component of the stiffness matrix ($C_{33} \neq 0$) is non-zero. The elastic part contains a parametrised non-linear material part E_3^{Mat} according to

$$E_3^{\text{Mat}}(\varepsilon_3, \gamma_{12}) = a_0 e^{[\varepsilon_{\text{I}}(\varepsilon_3 - \varepsilon_{\text{II}})] + \varepsilon_{\text{III}}}, \tag{4.19}$$

and an additional non-physical smooth locking part E_3^{Lock}, which only contributes for compaction states outside the experimentally acquired data range.

$$E_3^{\text{Lock}}(\varepsilon_3) = \frac{E_3^{\text{Mat}} - E_3^{\text{lim}}}{2} \left(\cos \left(\frac{\pi(\varepsilon_3 - \varepsilon_{3,\text{s}}^{\text{lim}})}{\varepsilon_{3,\text{e}}^{\text{lim}} - \varepsilon_{3,\text{s}}^{\text{lim}}} \right) + 1 \right) + E_3^{\text{lim}}. \tag{4.20}$$

Thereby, collapsing is prevented for temporarily high compressed elements. This is important, since the discrete mesh is compressed in bent and cornered regions.

The material part E_3^{Mat} is superimposed to a required base stiffness $E_0^{\text{SC}} = 7.156 \cdot 10^{-4}$ N/mm^2 of the SC element for compaction strains above $\varepsilon_{3,0}$. Parameters are obtained via reverse parameter identification with the experiments for shear angles γ_{12} of $0°, 25°$ and $50°$. The complete dataset for compaction is summarised in Table A.11. Shear-dependency is accounted for by linear interpolation between the data sets.

The viscous part of the Kirchhoff stress $\tilde{\boldsymbol{\tau}}^{\mathrm{v}} = 2\eta_0^{\mathrm{Mat}}\boldsymbol{D}$ is calculated via the rate-of-deformation tensor $\boldsymbol{D}$. A rate-dependency of the pre-infiltrated compaction trials as has been reported in literature [149]. It is neglected in this study due to a lack of experimental data.

Elastic and viscous part of the Kirchhoff stress are superimposed according to $\tilde{\boldsymbol{\tau}} = \tilde{\boldsymbol{\tau}}^{\mathrm{e}} + \tilde{\boldsymbol{\tau}}^{\mathrm{v}}$, which are subsequently used to determine the nodal reaction force matrix $\hat{\boldsymbol{f}}_{\mathrm{R}}^{\mathrm{mat}}$ with respect to ABAQUS' Green-Naghdi's frame

$$\hat{\boldsymbol{f}}_{\mathrm{R}}^{\mathrm{mat}} = \frac{1}{J} \cdot \det(\boldsymbol{J}) \cdot \boldsymbol{B}\, \tilde{\boldsymbol{\tau}}. \tag{4.21}$$

Parametrisation. Figure 4.12 shows the combined results of the shear-dependent parametrisation of the compaction behaviour.
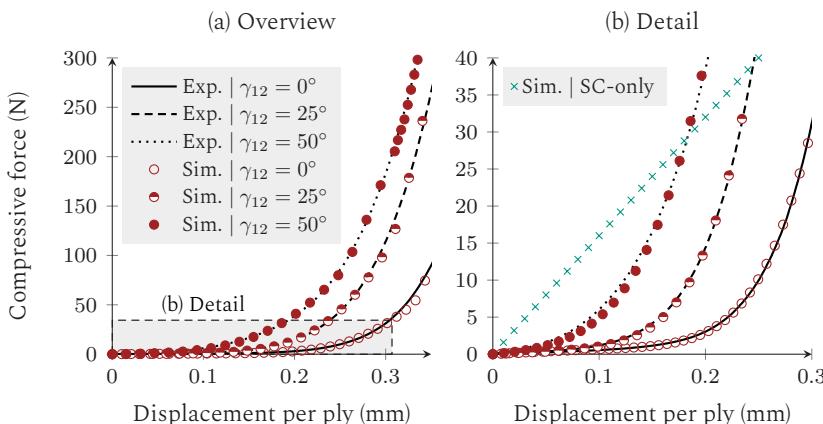
Figure 4.12: (a) Comparison between mean experimental reaction force curves and parametrised user enhanced model prediction; (b) Detailed view [137].

A good agreement is observed. The benefits of the user-enhanced compaction behaviour become particularly obvious when comparing the outlined results with a fitted built-in solution relying on a constant thickness modulus (see Figure 4.12(b)). A constant modulus would lead to an

overestimation of the initial stiffness and an underestimated locking towards higher compaction states. A constant material damping of $\eta_0^{\text{Mat}} = 5 \cdot 10^{-5}$ [Ns/mm] is using. The complete identified data set is summarised in Table A.11 in Appendix A.

4.3.4.2 Bending behaviour

The bending behaviour is supplied by the built-in continuum shell (SC) element in ABAQUS, which includes the membrane behaviour via a user material routine. As outlined, this implies a coupled membrane and bending behaviour. This leads to an overestimation of the bending stiffness when the conventional shell theory is applied because of the high prescribed in-plane fibre stiffnesses. To compensate for this, the transversal shear stiffness is reduced (see Section 4.3.4.2). Furthermore, usage of the SC element implies a purely linear-elastic, isotropic bending behaviour which neglects the anisotropy caused by the fibre orientations and rate-dependencies. This is suitable for geometries where bending is of minor importance compared to membrane or contact behaviour and where the material itself provides a comparable bending stiffness in both directions. Both apply here because the double dome geometry with a circumferential blank holder leads to a membrane dominated draping. Moreover, the applied woven fabric can be suitably described with an isotropic bending.

Parametrisation and verification. A cantilever setup (cf. Figure 4.13 (a) is used to obtain the bending parameters for the transversal shear stiffness. Target values for the cantilever bending length l_{bend} in fibre direction are obtained by the experiments outlined in Section 3.2 for the same material. Using this approach, a transverse shear stiffnesses of $\kappa_{11}^{\text{TS}} = \kappa_{22}^{\text{TS}} = 0.03 \, \text{N/mm}^2$ and $\kappa_{12}^{\text{TS}} = 0.03 \, \text{N/mm}^2$ are found using reverse parameter identification.

195

(a) Cantilever
SC6R

Encastre

$g\downarrow$

$u_3^{\max} = 114.5$ mm

(b) Reference model
M3D3 + S3R

$g\downarrow$

Forming submodel
SC6R

$g\downarrow$

Displacement u_3 (mm)

| +20 | -10 | -40 | -70 | -100 |
| +35 | +5 | -25 | -55 | -85 | -115 |
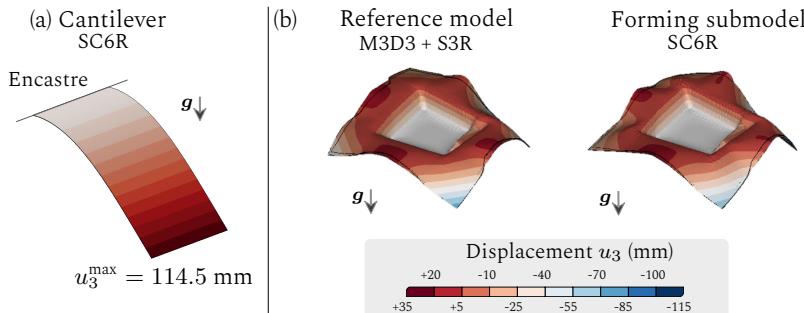
Figure 4.13: (a) Example of a cantilever result during reverse parameter identification; (b) Model compare between a properly decoupled reference model and the coupled SC-based model with reduced tangential shear stiffness [137].

To evaluate the validity of this procedure, a more complex geometry (cf. Figure 4.13 (b)) than the double dome is used to compare a properly decoupled reference model with the parametrised SC model (SC6R). The reference model consists of membrane (M3D3) and superimposed conventional shell elements (S3R) as outlined in Section 3.2.4. The bending behaviour within the reference model is reduced to a purely elastic material behaviour to ensure comparability. For the same reason, an upscaled compaction module $E_3^{SC} = 10\,\mathrm{N/mm^2}$ is used to reduce the impact of possible compaction within the SC-model.

Figure 4.13 (b) provides a direct comparison of both approaches for a two-layer forming setup exposed to gravity. Apart from minor differences in slag and shape, a comparable displacement field is predicted. Hence, it is assumed that the SC-based approach provides a suitable approximated bending behaviour. Since the later applied double dome geometry is simpler and additionally contains a circumferential blank holder that constrains the draping even further, the outlined approach is assumed to be well suited to capture the forming behaviour of the applied double dome geometry.

4.3.5 Fluid submodel

4.3.5.1 Formulation

A wedge-shape element as shown in Figure 4.14 is chosen for the fluid submodel. Therefore, the priorly presented DPE2D approach based on triangular elements is expanded to a 3D element formulation.
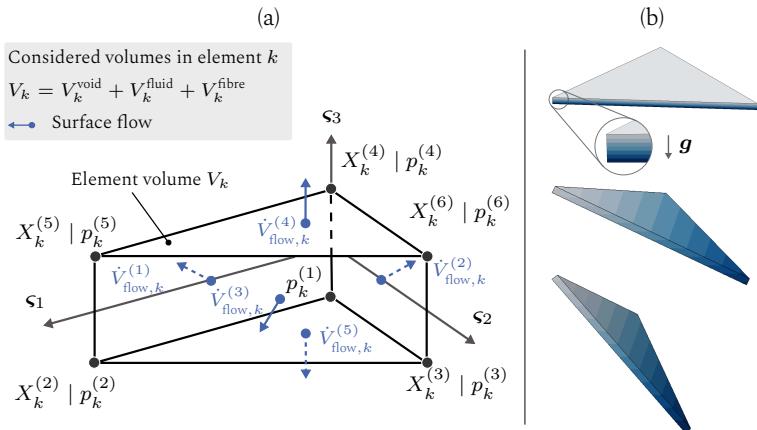
Figure 4.14: Fluid submodel | (a) Isoparametric element formulation of an element k [343]; (b) Qualitative impact of gravity $\boldsymbol{g}$ on the intra-ply pressure distribution within a rotated element [137].

The wedge element consists of six nodes and five surfaces over which the pressure-corresponding surface flows are evaluated. Every element volume V_k is occupied by a combination of fibre volume V_k^{fibre}, fluid volume V_k^{fluid} or void volume V_k^{void}. The available volume (void) is derived from the total element volume V_k. Element saturation S_k and ϕ_k (FVC) are updated accordingly in every increment. A Gaussian integration scheme in conjunction with six integration points is applied to ensure accurate integration of the system diffusion matrix $\boldsymbol{K}^{\text{diff}}$ during finite strains. Following the modelling strategy outlined in Figure 4.11, a fully coupled thermomechanical analysis within ABAQUS is utilized to model forming and fluid progression simultaneously [99,343]. Doing so enables an additional

usage of a nodal pressure degree of freedom p_N^{vec} . The implementation mainly focuses on the following three key intra-ply mechanisms:

1. Solving the pressure field within the saturated domain

2. Calculation for flow front progression and mass conservation

3. Modification of the pressure field during compaction

One and two a covered by a 3D expansion of the equations used for the DPE2D model. Only the third point provides a new mechanism.

Saturated domain. To solve the pressure field, Richard's law [21] providing a combination of mass conservation and Darcy's law is applied in a transient explicit formulation (cf. Equations 4.22-4.24). By this means, a transient single-phase fluid progression can be modelled by implicit consideration of the velocity field. This is enabled by introducing a nodal hydraulic capacity C_{hyd}^N which is used to calculate the mass matrix $\boldsymbol{M}^{\text{mass}} = \rho C_{\text{hyd}}^N \boldsymbol{I} \to 0$ of the system. As for the DPE2D model, C_{hyd} provides a purely numerical parameter, which is required to apply an explicit temporal integration scheme to solve the pressure field. This originates from the incompressibility of the fluid, which would lead to infinite pressures of the smallest numerical error during temporal integration. The latter cannot be prevented with finite precision. Hence, C_{hyd}^N introduces slight compliance $(1 >> C_{\text{hyd}} > 0)$ into the system, just enough to prevent this.

$$\int_{V_k} \rho C_{\text{hyd}}\, \dot{p}\, dv = \frac{\boldsymbol{K}(\phi)}{\eta\, \varphi} \int_{V_k} \text{div} \left(\text{grad}\,(p) - \rho \boldsymbol{g} \right)\, dv \qquad (4.22)$$

$$\approx \int_{V_k} \frac{\det\left(\boldsymbol{J}\right)}{\eta\, \varphi} \boldsymbol{B}_1 \boldsymbol{K}_{\text{f}} \left(\boldsymbol{B}_1^\top \boldsymbol{p} - \rho \boldsymbol{g} \right)\, dv, \qquad (4.23)$$

$$\boldsymbol{M}^{\text{mass}}\, \dot{\boldsymbol{p}}^{\text{e}} = \boldsymbol{K}^{\text{diff}} \left(\boldsymbol{K}_{\text{f}}, \boldsymbol{p}, \eta, \phi \right) \boldsymbol{p}^{\text{vec}} + \boldsymbol{b}_{\text{grav}}^{\text{vec}} + \boldsymbol{S}^{\text{+,vec}} \qquad (4.24)$$

Within one element and increment, viscosity η, ϕ and fibre-frame permeability $\boldsymbol{K}_\text{f}$ are constant. In equation 6, a 'vec' is superscripted as an identifier for a nodal vector representation according to $\boldsymbol{p}^\text{vec} = [p^{(1)}, p^{(2)}, ..., p^{(N)}]^\top$ with $N = [1, 6]$. The diffusion matrix $\boldsymbol{K}^\text{diff}$ is calculated based on the fibre-frame permeability tensor $\boldsymbol{K}_\text{f}$ in the current deformation state $\boldsymbol{x}_i$. Gravity is accounted for by a body force vector $\boldsymbol{b}^\text{vec}_\text{grav}$. The operator matrix $\boldsymbol{B}$ provides the spatial derivatives of the shape functions in the current configuration. The Jacobian determinate $\det(\boldsymbol{J})$ accounts for a change of element volume. Finally, a nodal source vector $\boldsymbol{S}^{+,\text{e}}$ is introduced, which is used to modify the pressure field during compaction.

Flow front progression and mass conservation. The incremental flows $\dot{V}^{(i)}_\text{flow}$ across every element surface $i = [1, 5]$ (cf. Figure 4.14 (a)) are calculated by means of a midpoint Gaussian integration of the surface integrals

$$\dot{V}^{(i)}_\text{flow} = \det (\boldsymbol{J_1}) \triangle t_\text{inc} \left(\frac{\boldsymbol{K}(\phi)}{\eta \, \varphi} \cdot \boldsymbol{B_1}^\top \cdot \boldsymbol{J_1}^{-\top} \cdot \boldsymbol{p} \right) \cdot \boldsymbol{n}^{(i)}, \qquad (4.25)$$

where $\boldsymbol{n}^{(i)}$ provides the current outward normal vector of the current surface. Similar to DPE2D triangle element, the accumulated incremental volume flow across surfaces of the same element is zero $\sum_{k=1}^{5} \dot{V}^{(k)}_\text{flow} = 0$. Only relevant surface flows (e.g. flow front, inlet, outlet) are determined permanently to reduce computational effort. As within the DPE2D formulation, the application of Richard's law prevents mass loss within the saturated domain under normal conditions. Nonetheless, the outer edges of the global CV, including the flow front edges, are used for a mass conservation check at the domain level. The individual contributions of the elements to the global CV depend on their current state (empty, filling or saturated) and their location (inlet, vent, wall or flow front). The latter is additionally used to prescribe boundary conditions. Again, a mesh-independent flow front progression is achieved via a gradient-weighted distribution of the total flow front flow [99].

Modification of the pressure field. An essential mechanism is the local response of saturated elements to change of volume during compaction or shearing. If the element volume of an already saturated element is reduced, fluid is forced out, leading to a local pressure increase until the resulting local overflow is resolved. By the same means, pressure needs to be reduced if already saturated region becomes desaturated.

The local overflow $V_{k,\text{fluid}}^+ = -V_k^{\text{void}}$ is used to modify the nodal pressures $\boldsymbol{p}^{\text{vec}}$ within each node n of every overfilled element according to the nodal source vector $\boldsymbol{S}^{+,\text{vec}} = [S^{(+,1)}, S^{(+,2)}, ..., S^{(+,N)}]^\top$ where $S^{(+,n)}$ provides the local additional flux into each nodes

$$S^{(+,n)} = \beta_0^+ V_{k,\text{fluid}}^+ + \beta_1^+ \dot{V}_{k,\text{fluid}}^+ . \qquad (4.26)$$

The two parameters $\beta_0^+ = 10.0$ and $\beta_1^+ = 0.2\,\text{s}$ can be interpreted as penalty values. The former provides a constant flux into the nodes (pressure increases), whereas the latter responds to changes of the overflow. The underlying idea of this concept is that at any point in time (increment) for which a stable pressure distribution is reached, the summarised incremental present overflow must be equal to the incremental summarised amount of fluid transpassing the flow front.

$$\underbrace{\sum_k \sum_i \dot{V}_{\text{flow},k}^{(i)}|_{\Gamma_{\text{sat}}}}_{\text{Total flow front rate}} \overset{!}{=} \underbrace{\sum_k \dot{V}_{k,\text{fluid}}^+|_{\Gamma_{\text{sat}}}}_{\text{Total overflow rate}} \qquad (4.27)$$

In this manner, overflow is only reduced when the fluid has actually crossed the flow front. This further implies that the pressure field is forced to adapt to a particular current overflow and the conduction situation as a whole. This ensures a unique solution for the pressure field. Implicit time integration methods commonly iterate until a converged solution of velocity field and pressure distribution is reached. The explicit approach uses a forward modification loop of the pressure field, which

only considers the fluid velocity field implicitly to achieve the same functionality. This provides an efficient way to consider the fluid velocity field without actually solving for it directly.

However, the presented approach only provides reliable results if the system can adapt its pressure distribution sufficiently fast. The verification tests (cf. Section 4.3.5.3) will demonstrate that this applies when temporal integration steps $\triangle t_{\text{inc}}$ are small, the hydraulic nodal capacities C_{hyd}^{N} are sufficiently low and penalty parameters β_0^+ and β_1^+ are chosen adequately. During explicit FE forming simulations, sufficiently small temporal integration steps (increments) are ensured intrinsically. However, an additional stabilisation mechanism for the fluid domain is implemented. Its functionality will be also demonstrated in Section 4.3.5.3.

4.3.5.2 Interface flow modelling

Interface flows between the single plies of the stack need to be captured. This requires the detection of the current flow front position across interfaces (cf. Figure 4.15) and pressure conduction between the nodes of different model instances (plies) within the saturated domain. Pressure conduction can be achieved via an additional gap conduction option α_{Gap} for the already presented built-in contact model. This mechanism is originally intended to describe thermal conduction in heat transfer problems.

Tracking the flow front across interfaces requires an active comparison between saturation states (saturated, filling or empty) of currently contacted neighbours. This can be complicated by large interface slip or deformations of the individual instances eminent during forming. Besides, information consistency must be ensured between interfaces that may be part of other processor threads during runtime.

An algorithm is implemented, enabling a multi-thread optimised neighbourhood search. During initialisation (cf. Figure 4.11), neighbour elements are identified within the plies but also throughout the contact

interfaces. Scanning spheres around the individual nodes r_N^{Scan} and the element midpoints $r_{i,\text{MP}}^{\text{Scan}}$ (cf. Figure 4.15) are used to achive this. A relational network of element, surface and node connectivity is created with the obtained information. During runtime, this network is updated permanently, yet only at positions where changes are possible. As constant scanning of multiple elements can require considerable computational effort, dynamic pre-partitioned lists are utilised and updated in parallel by the individual threads.
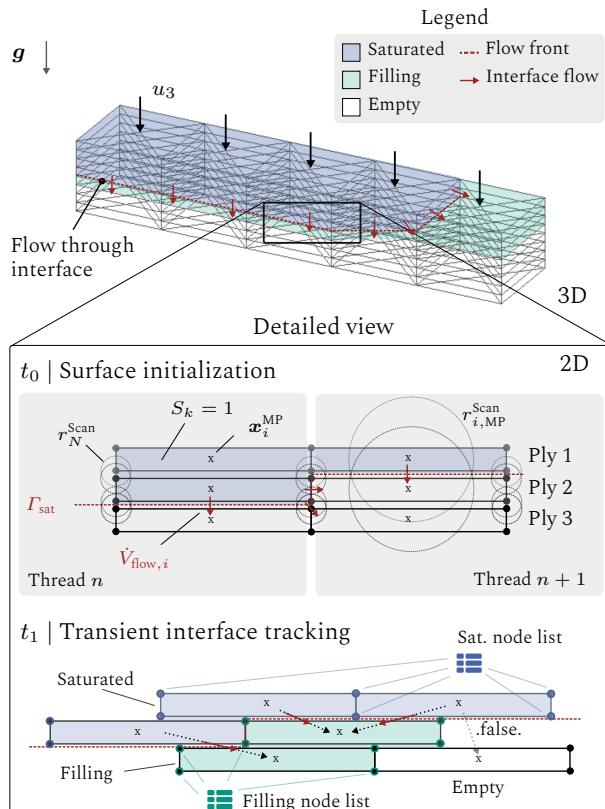
Figure 4.15: Illustration of the interface flow tracking algorithm comprising an initialisation at the start of the analysis and the tracking during runtime. Neighbour search is supported by dynamic lists and element connectivity.

Only a minor interface slip occurs between the plies for simpler geometries or forming setups with similar fibre orientations in the stack. Transient contact tracking can be neglected in these cases. Therefore, an additional 'static' contact mode is implemented, assuming constant element connectivity at the interfaces.

4.3.5.3 Verification tests

Anisotropic fluid progression.   In Section 4.3.2 it was demonstrated that a non-orthogonal description of the permeability tensor $\boldsymbol{K}_f$ is beneficial because it intrinsically accounts for shear deformation. The proposed fluid model is used to demonstrate these claims for an anisotropic flow progression within a pre-sheared fabric. An experimental result that has been published by Pierce et al. [176] is used as a reference solution. Their study characterises the permeability values of differently pre-sheared fabrics using a central injection between transparent plates. Since they later apply ANSYS FLUENT for the flow simulation, they extracted the permeability values using the ellipse method [173] as shown in Figure 4.16 (a).
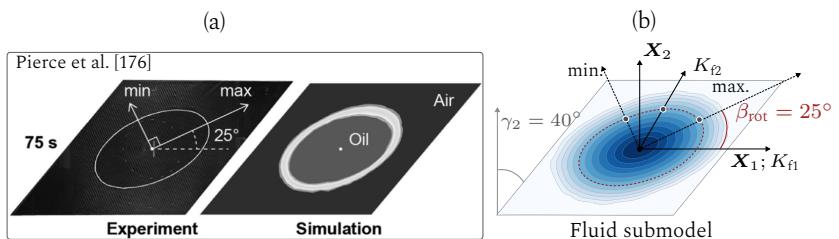
Figure 4.16: (a) Results provided by Pierce et. al. [176]; (b) Simulation result using a fibre-frame based description of the permeability tensor [137].

Figure 4.16 (b) shows that a comparable result can be reproduced with fluid submodel even though only the permeability values in the undeformed state are implemented in the model using Equation 4.12. In both

cases, an ellipse-shaped flow front progression and ellipse-shaped pressure distribution establish. A comparable rotation angle of $\beta_{\mathrm{rot}} = 25°$ between warp fibre orientation and principal ellipse axis is predicted. The results support the Demaria's work [20, 173] and verify the usage of non-orthogonal permeability description.

Radial compaction. Compaction-induced infiltration provides an important mechanism during WCM. A verification of the fluid submodel for a comparable linear case is reported in [343]. Here a radial setup with a predefined amount of centrally applied resin V_0^{fluid} is investigated. The radial flow front progression

$$r_{\mathrm{ff}}(t) = \sqrt{\frac{V_0^{\mathrm{fluid}}}{2\pi h_{\mathrm{cav}}(t) \cdot (1 - \phi(t))}} \qquad (4.28)$$

follows from mass conservation. Here, $h_{\mathrm{cav}}(t)$ is the current cavity height. Among others, Bickerton et al. [149] have published the following equation for the transient pressure distribution

$$p(r,t) = \frac{\eta \dot{h}_{\mathrm{cav}}}{4K(\phi_1)h_{\mathrm{cav}}(t)} \left[(r^2 - r_{\mathrm{ff}}^2(t)) + 2r_{\mathrm{inj}} \ln\left(\frac{r_{\mathrm{ff}}(t)}{r}\right) \right]. \qquad (4.29)$$

A constant compression rate of $\dot{h}_{\mathrm{cav}} = 0.055\,\mathrm{mm/s}$ is used. An initial resin distribution with a radius of $r_{\mathrm{ff}}^0 = 60\,\mathrm{mm}$ and a constant fibre orientation of $0°$ is assumed. Initial height of the stack is set to $h_0 = 0.4\,\mathrm{mm}$ and quarter model as a length of $100\,\mathrm{mm}$. While compaction proceeds, the resin is spread to infiltrate the dry fabric. The isotropic in-plane permeability K results in a circular propagation of the flow front (cf. Figure 4.17 (a)). $K(\phi)$ is given by the function provided by Equation 4.12 for the analytical and numerical case. A structured mesh with 6300 elements is used. The circular flow progression in the simulation demonstrated mesh-independency.
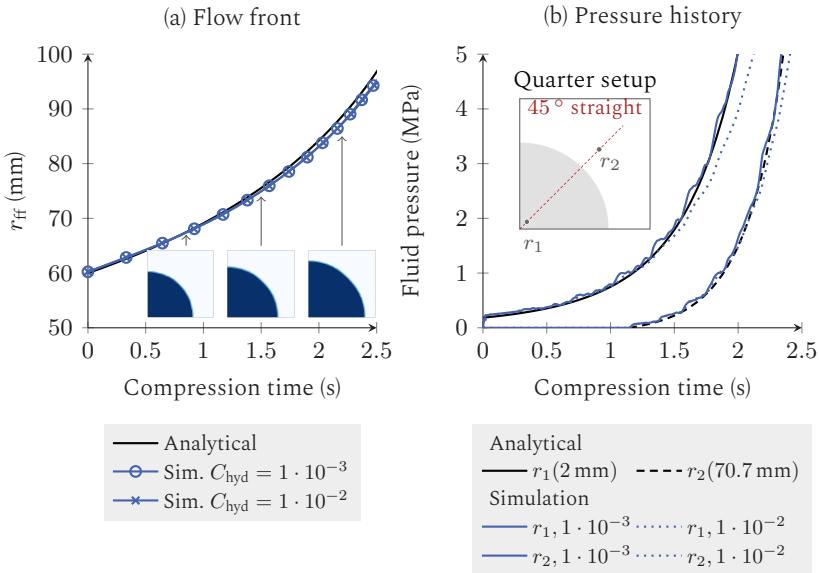
Figure 4.17: Compaction test case | Comparison with analytical solution: (a) Flow front progression; (b) Discrete pressure history at $r_1(2\,\text{mm})$ and $r_2(70.7\,\text{mm})$ for two hydraulic capacities [137].

The flow front progression in Figure 4.17 (a), evaluated along a $45\,°$ straight, seems to be in good agreement with the analytical solution. Beyond that, the pressure history (cf. Figure 4.17 (b)) at two distinct points on the $45\,°$ straight $r_0(2\,\text{mm})$ and $r_1(70.7\,\text{mm})$ is compared to the analytical solution. A good agreement is observed. Moreover, the impact of an increased hydraulic capacity of $C_{\text{hyd}} = 1 \cdot 10^{-2}$ mm^3/MPa is shown in Figure 4.17 (b). Whereas the flow front is not noticeably affected, pressures tend to lag slightly when hydraulic capacity increases. This is reasonable, as the pressure field adapts slower when the hydraulic capacity increases.

Domain stabilisation.   A local source term $\boldsymbol{S}^{+,\text{vec}}$ in combination with low nodal hydraulic capacities C_{hyd}^N lead to a oscillation-prone system. Moreover, the strong coupling between deformation and source term

makes it challenging to estimate a stable time increment in a typical manner. As a monolithic system combining both submodels is solved, a stable time increment is required, conserving both.

Therefore, an adaptive scaling based on the forming submodels' time increment estimation is implemented, using an instability criterium. Usage of the VUEXTERNALDB subroutine in ABAQUS allows to modify the time increment at the end of each increment.
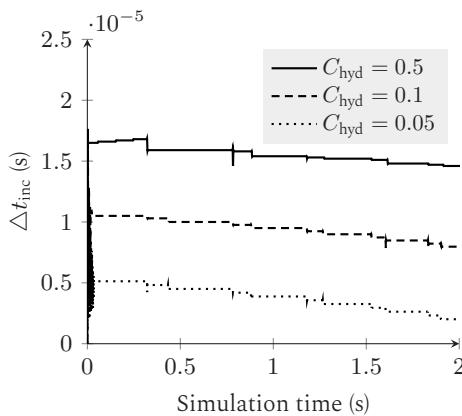
Figure 4.18: Demonstration of domain stabilisation using the radial compaction scenario with nodal hydraulic capacity C_{hyd}^N [137].

To judge stability, the occurrence of slightly negative pressure values at the current flow front has proven to be a robust indicator. If instability is detected among saturated elements, the currently estimated time increment of the forming submodel is downscaled. Under stabilised conditions, the time increment is upscaled again. The above-outlined radial test case is exposed to different stability scenarios via modification of the nodal hydraulic capacity C_{hyd}^N (cf. Figure 4.18) to demonstrate the reactions of the domain stabilisation.

While the fluid progresses, emerging instability is detected within all scenarios and the time increment is reduced accordingly, as Figure 4.18 shows. The smaller C_{hyd} is set, the stronger the time increment has to be reduced to regain stability of the pressure field. Although different hydraulic capacities slightly affect the predicted pressure history as outline in Figure 4.3, all three scenarios provide a stable, accurate solution. An error is raised if the domain cannot be stabilised within a user-defined time range.

Interface flows. A 1D test case in the through-thickness direction is used to verify the fluid flow across contact interfaces. An eight stack ply is exposed to a constant inlet flow at the top ply according to Figure 4.19 (a).
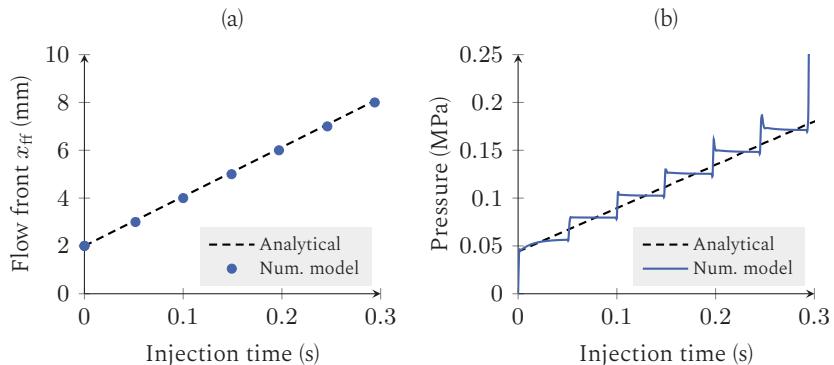
Figure 4.19: (a) Prediction of the flow front progression during injection with constant flow rate; (b) Resulting inlet pressure – complete saturation is reached at 0.29 s.

A gap conduction of 5000 W/mmK (thermo-mechanical functionality in ABAQUS) is used. In contrast to intra-ply flow progression, the flow front must now progress through the ply interfaces and not only between element surfaces of the same mesh instance (ply). Pressure history at the

top nodes is monitored and compared with the analytical solution given by Equation 4.7.

Flow front progression and pressure history seem to be in good agreement with the analytical solution (cf. Figure 4.19).
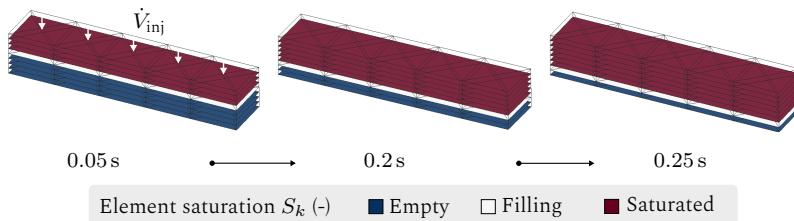
Figure 4.20: Fluid interface | Inter-ply flow front progression during injection [137].

As illustrated in Figure 4.20, volume is constantly added to the top layer elements. A local overflow is generated, which modifies the pressure distribution until a stable solution establishes. A slight peak emerges during later transitions of the flow front from one instance to the next (cf. Figure 4.19). This is due to a slight oscillation within the pressure field. This is observed when only a few elements are applied. This is not found to be an issue for increased element numbers or multi-dimensional flow cases. The pressure increases considerably beyond 0.29 s as no fluid outlet is assigned.

In summary, the implemented fluid contact enables a suitable inter-ply flow front progression between the individual plies of the stack. The correctly predicted pressure history in (b) further demonstrates that flow rate boundary conditions can also be applied to the model. Similar to the 2D approach, an application for RTM or VARI is possible.

4.3.6 Coupled application

4.3.6.1 Dry forming with variable thickness

The presented 3D forming submodel is applied to a double dome geometry as outlined in Section 2.1 to evaluate the impact of a variable thickness and to verify the dry forming submodel.
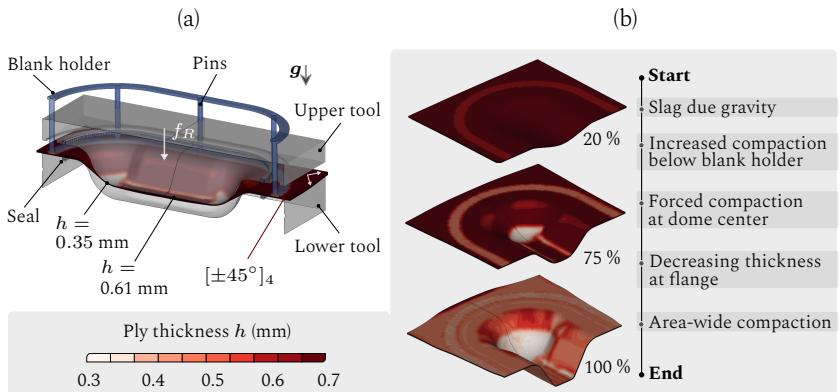
Figure 4.21: Forming submodel | (a) Model setup; (b) Exemplary forming result in terms of ply thickness h and according observations [137].

For this purpose, a simulation setup as displayed in Figure 4.21 (a) is utilized based on the modelling approach displaced in Figure 4.11. The setup comprises of rigid surfaces to account for a lower and upper tool and a blank holder and seals. The forming submodel is used within every single ply of the four-ply woven fabric stack with an initial fibre orientation of $\pm 45°$. A predefined ply thickness of $h = 0.7$ mm is used, obtained by measurements. The displacement is prescribed at the upper tool according to the closing amplitude presented in Section 4.21. Gravity is applied for the entire model, implying a closing of the blank holder under its own weight.

An exemplary forming result is displayed in Figure 4.21 (b). In the beginning, gravity leads to a central slag of the fabric, followed by slight emerging compaction below the advancing blank holder. Thereafter, forming starts by central contact of the upper tool with the slagging stack. This initial contact mainly occurs at the half dome centre and the edges, leading to localised compaction in these areas. Further forming results in a thickness decrease at the flanges. Finally, the upper tool gets into large-areal contact with the stack, leading to final part thicknesses between $h = 0.3$ and $0.55\,\text{mm}$.

Validation of shearing. A comparison with the results that have been published Boisse et al. [217] for a comparable material and double dome forming setup is given in Figure 4.22.
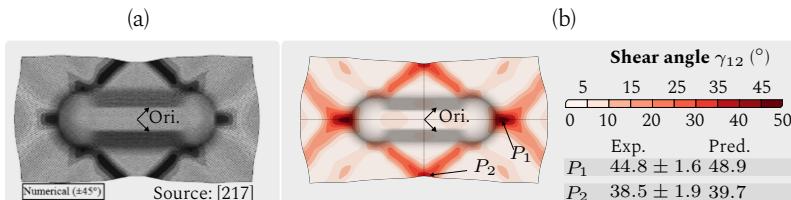
Figure 4.22: (a) Shear angle distribution published by Boise et al. [217]; (b) Shear angle distribution in the present work and direct comparison with own experiments at two critical points (P_1, P_2) [137].

Similar initial fibre orientations are used. A high qualitative agreement is observed for the predicted shear angle distribution and outer shape, even though material locking angle and compaction forces are probably not identical. In addition to the spatial comparison with the results that have been published by Boisse et al. [217], Figure 4.22 (b) provides a direct comparison between the optically evaluated and the predicted shear angle at two critical positions (P_1, P_2). The former values are obtained from the experimental trials. A slight overestimation is observed for P_1 and a good agreement is found for position P_2.

Prediction of FVC and reaction forces.   The approach can predict the thickness and corresponding FVC ϕ within every ply. Figure 4.23 gives an insight into the predicted final thickness and FVC in the top and bottom ply. A smooth transition of the quantities is observed for the middle plies.
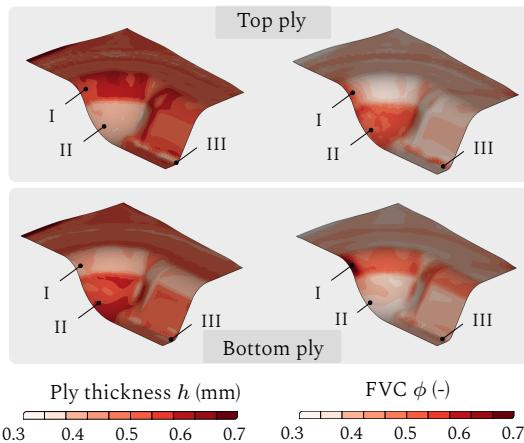
Figure 4.23: Prediction of the final ply thickness h and FVC ϕ in top and bottom ply for closed mould [137].

Strong differences are predicted for the final thickness in several important areas: the flanges (I), the half-dome centre, or the corners (II). Exemplary looking at the flange area (II), increased thickness compared to the surrounding regions is predicted for the top ply (0.55), but the opposite is predicted for the bottom ply (0.35). This contradictory relationship applies for several areas and also the FVC distribution on the right side of Figure 4.23.

In addition to the thickness information, ϕ takes the local in-plane shear deformation into account (cf. Figure 4.22). The highest FVC (0.61) is predicted for the part of the flange with the highest shear angles (close to I). In general, high FVCs are predicted for the highly compacted areas.

211

Unfortunately, elastic spring-back of the uncured stack in thickness direction prevents the experimental validation of the predicted thickness values for the completely closed tool. The predicted location of the maximum shear angle agrees with the experimental observations. It is assumed that the maximal predicted FVC in Zone I is slightly overestimated due to the slight overestimation of the maximal shear angle.

Compaction is shown to be of high importance to accurately predict the local FVC, especially in minor sheared areas. Here, pure compaction results in maximal FVC changes of 0.25 to 0.5 (100 %), whereas pure shearing from 0 to 50 ° with constant thickness increases area weight and thus FVC only by 31 % (cf. Section 4.3.2).

Consequently, the spatial distribution of the local FVC appears to be much more similar to the thickness distribution than to the shear angle distribution. It is concluded that a reasonable prediction of the local FVC should include both shearing and compaction as an interconnected source for a non-linear increase of the final local FVC.
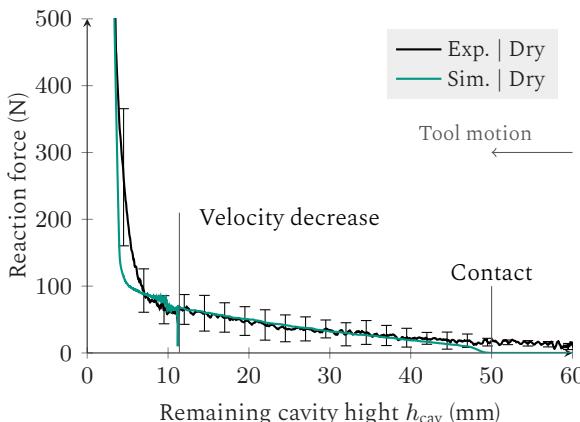
Figure 4.24: Validation of reaction forces by comparison with dry experiments – Initial contact between upper tool and stack surface is made for $h_{cav} < 50$ mm [137].

Furthermore, consideration of material compaction enables a prediction of reaction forces during forming. In Figure 4.24, reaction forces obtained by dry forming trials are compared with the numerically predicted ones.

An overall good agreement is observed for a substantial part of the tool stroke. Significant differences only arise for the first 10 mm of tool motion ($50 > h_{cav} \leq 60$) because gravity-induced slag of the stack prevents contact to the upper tool until a cavity of $h_{cav} = 50$ mm is reached. Moreover, blank holder pins (cf. Figure 4.21 (a)) are modelled frictionless in the simulation. During experiments, some slip-stick effects between the blank holder pins and upper tool are observed for the initial 15 mm of the tool stroke. For further tool displacement, the free length of the pins is short enough to prevent such effects of sticking.

Minor differences are observed for the beginning of the final compaction phase at the remaining cavity height between 5 and 3 mm. Here, the predicted reaction forces lag slightly behind. This may have several reasons:

1. The scattering within the experiments is quite high in this phase.

2. Bending forces play an important role in the overall reaction forces in this phase.

3. Some degree of contact penetrations cannot be prevented between the interfaces, leading to a slightly more compliant system.

Despite this minor differences, reasonable reaction forces are obtained by the 3D forming simulation submodel. The need for a suitable 3D locking free formulation for forming simulations is demonstrated.

4.3.6.2 Combined forming and mould-filling

For a combined application, the model is enhanced by the fluid submodel, following the modelling strategy presented in Section 4.3.3. In contrast to the 2D approach (cf. Section 4.3), where injection could only be modelled using a predefined pressure at an inlet, the 3D process model allows

using an initial fluid distribution boundary condition through element saturations. An initial fluid volume based on the experiments is added to the undeformed four-ply stack. For the 20 mPas trials, a homogenous pre-infiltration within the stack centre is used, whereas only the two top plies are set as infiltrated during the 200 mPas trials. The latter addresses the mostly superficial distribution prior to forming (cf. Figure 2.3). The initially infiltrated area within the top plies is needed to be slightly larger than measured for the experiments to achieve the required amount of fluid.

An exemplary result, predicting both forming and fluid-progression, is shown in Figure 4.25. Similar to the experiments, the fluid flow is mostly driven by gravity and local compaction, until the final compaction results in in-plane dominated infiltration and increased pressure.
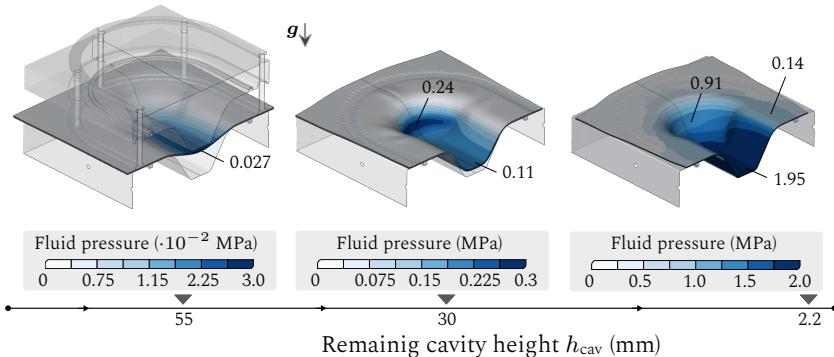
Figure 4.25: Process model | Result for cavity pressure (MPa) at a viscosity of 20 mPas [137].

A comparison of the fluid progression between the experimental results and numerical predictions is presented in Figure 4.26. When comparing the results for the low viscosity (20 mPas, top row), good prediction accuracy is observed regarding flow front progression and local resin amount. Leaked fluid prevents a proper evaluation of the bottom side at remaining cavities above 5 mm.
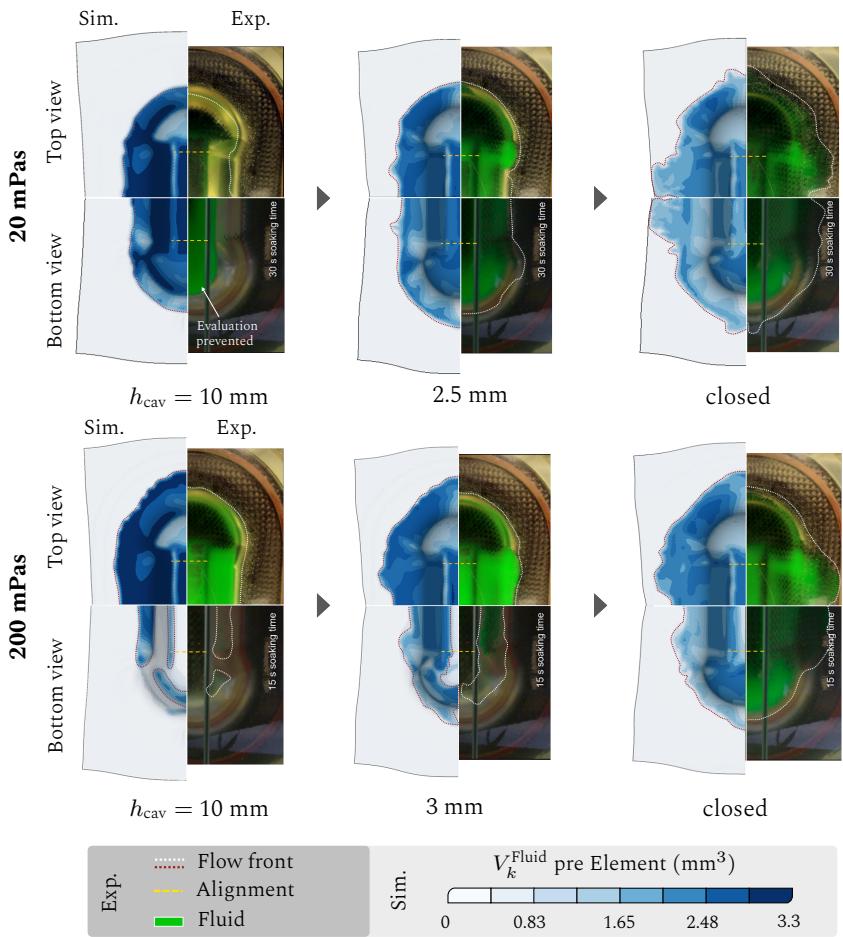
Figure 4.26: Qualitative comparison of flow front progression with experimental trials at different cavity heights h_{cav} [137].

Regarding the 200 mPas trials (bottom row), the prediction accuracy of the model is slightly lower because the flow progression is more superficial.

Still, comparable tendencies of the fluid progression can be observed, especially concerning the inhomogeneous infiltration in the thickness direction. Nevertheless, the initial resin distribution leads to an overestimated flow progression on the top side, which directly follows from the increased initial infiltration area.

Some experimentally related sources of uncertainty are to be outlined. Only four plies are used during the experiments, which leads to some scatter in terms of fluid progression because the transversal permeability can differ in some areas due to gaps. Moreover, video analysis of the transparent tools is hindered by curvature-induced optical distortions,that are reduced where possible with calibrations. In addition, some scattering must be anticipated in the initial fluid distribution during the experiments.

4.4   Discussion and conclusion[1]

A reliable WCM process simulation requires a simultaneous description of draping and fluid progression. A monolithic approach based on the similarity of Fourier's and Richard's law was proposed in Section 4.1 to enable direct internal coupling between draping and fluid submodel.

Expending the draping model from Section 3, a 2D fluid formulation based on a single-phase porous medium throughflow (user element) was presented and verified in Section 4.2. A feasibility study on a generic geometry revealed both, advantages and limitations of this 2D modelling strategy. In particular, crucial process mechanisms such as infiltration and compaction in thickness direction could not be captured and require a 3D formulation.

---

[1]   Section 4.4 contains extracts of: C. Poppe, F. Albrecht, C. Krauß, L. Kärger: *A 3D Modelling Approach for Fluid Progression during Process Simulation of Wet Compression Moulding – Motivation & Approach*, Procedia Manuf. 2020; 47:85-92, 2020 [343].

In this regard, an expansion for both draping and fluid submodels was presented in Section 4.3. Modelling of the draping submodel through user-enhanced continuum shell elements allowed capturing of non-linear compaction. A superimposed user element (VUEL) was used to formulate a 3D fluid submodel (user element: DPE3D). It accounts for the local fibre volume content, the current fibre orientation and infiltration not only in in-plane but also in thickness direction, even across multiple plies of a stack. Finally, the 3D process model was compared to the initially outlined experimental trials with in-situ flow front tracking (cf. Section 2.1).

The combined application of 3D process model gives important information about the achievements (+) and limitations (-) of the forming-driven modelling strategy:

- + Successful coupling the models for forming and infiltration is essential for an accurate WCM process model.

- + Initial results are promising and confirm the general suitability of the approach and the need for a 3D formulation for both submodels.

- + The monolithic approach allows an explicit and efficient solving of the involved equations of the model without iteratively coupled algorithms.

- + Gravity can be considered in both submodels and proved to be important for an accurate prediction.

- - A suitable approach to consider the superficial flow (squeeze flow) is crucial to exploit the capabilities of this approach, especially when applied to more complex geometries or unfavourable process parameter settings.

- - Heat transfer and curing need to be implemented in forthcoming steps to account for changing viscosities and related thermal-induced strains.

- - The macroscopic, single-phase approach assumes a prefect vacuum inside the mould and within the microstructure of the reinforcements. This currently prevents a prediction of air traps and micro-saturation.

Compared to the aforementioned 2D approach (DPE2D), several improvements and new capabilities are capture by the 3D formulation (DPE3D). Most important, the DPE3D approach allows the inclusion of key WCM effects and boundary conditions, such as initial resin application, fluid progression in thickness direction and compaction in a single simulation run. This can already enable reliable support for virtual process and part development.

5 Simultaneous fluid progression via strong FSI [1]

Abstract

The inherent Fluid-Structure-Interaction (FSI) of LCM processes, including the WCM process, can cause undesired process defects, such as flow-induced fibre displacement (FiFD). More severe cases can complicate mould-filling and reduce final parts' structural performance. Given that simplified, existing analytical predictions are not directly applicable for WCM parts, a numerical prediction using process modelling is desired. Unlike woven fabric, which incorporates two fibre orientations, UD-NCF is particularly vulnerable to FiFD. Hence, the 3D macroscopic process model is adapted to a UD-NCF, which further demonstrates the modular approach of the proposed modelling strategy. Using Terzaghi's effective stress approach, a strong interaction between material deformation and fluid pressure is implemented. The resulting process model is successfully validated with additional viscous compaction trials. Beyond that, a parametric study reveals principal relationships and conditions for a global or localised FiFD. The results emphasise the high impact of a suitable hydrodynamic tangential contact formulation. Finally, a feasibility study demonstrates the model's suitability to predict planar FiFD by comparison to experimental results from literature. Some important limitations are identified, e.g. hydrodynamic contact modelling, which motivates further research.

5.1   Flow-induced fibre displacement (FiFD)

FSI leads to mutual couplings between the material stress and fluid pressure during moulding. This complicates liquid moulding processes since defects such as fibre-washout [57] or FiFD [59, 147, 346] can significantly alter the local fibre architecture during processing. This affects mould-filling behaviour and structural performance [9, 76, 345]. Whereas fibre-washout during RTM usually addresses the local dissolution of the fibre structure due to locally increased pressure, FiFD describes a local or global macroscopic shift or reorientation of fibres during viscous compaction. FiFD is of minor importance for engineering textiles with two fibre orientations, such as weaved woven fabrics, as the high fibre stiffnesses mostly prevent a deformation within the occurring cavity pressure range. Yet it can lead to in-plane fibre undulations. In contrast, unidirectional reinforced materials such as UD-NCF are particularly vulnerable to such effects as these materials show a high anisotropy between the fibre and perpendicular direction in terms of stiffness and permeability.

5.1.1   Process example

A exemplarily result caused by FiFD is demonstrated in Figure 5.1. The planar WCM compression trials[1] were carried out at the Fraunhofer ICT in Pfinztal (Germany). A six-ply stack $[0/90/0]_s$ of UD-NCF material is used. FiFD is provoked by a central resin application and a relatively fast closing velocity of $v_{tool} = 1.4\,\text{mm/s}$ within the final compression phase of the tool stroke. A constant tool temperature of $120\,°C$ and a prior infiltration time of $30\,\text{s}$ is used. The spatial evaluation of superficial FiFD using MATLAB has been developed as part of a cooperative master thesis [346] between KIT-FAST and Fraunhofer ICT.

---

[1]   Part of a cooperative master thesis [346] between KIT-FAST and Fraunhofer ICT, 2019.
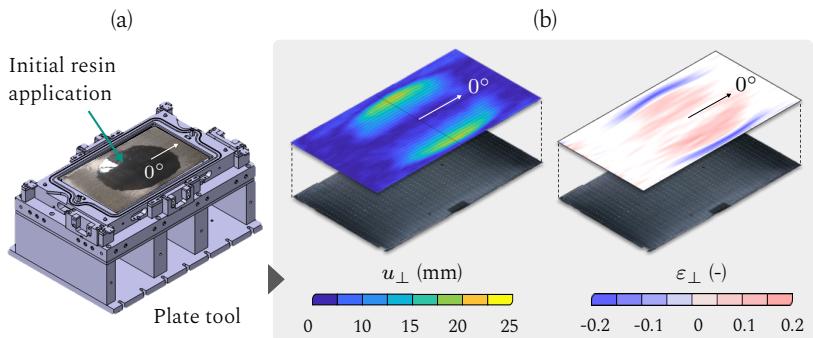
Figure 5.1: Process observation | Superficial FiFD during manufacturing of UD-NCF; (a) Plate tool and trial setup at Fraunhofer ICT; (b) Calculated displacement and strain fields of the top side of the stack (based on [325, 346]).

As Figure 5.1 (b) shows, a macroscopic fibre-displacement $u_\perp$ of up to 25 mm is observed perpendicular to the initial fibre orientation at the top side of the stack. The bottom side of the stack showed no such displacements. Responsible for this is the initial infiltration state of the stack, which leads to much higher drag forces at the top side. Moreover, it is assumed that the bottom side of the stack is additionally constrained by friction with the tool surface. The superficial FiFD leads to a centrally localised positive material strain ($\varepsilon_\perp > 0$) and in-plane compaction of the material towards the outer fibre clamping ($\varepsilon_\perp < 0$). Consequently, the initially homogeneously distributed FVC is reduced within the plate centre and increases towards the outer clamping. This affects the manufactured plate's structural properties. Preventing such undesired effects during WCM is important for process robustness. This section aims to expand the presented simulation approach based on a weak FSI (cf. Section 4) by a strong interaction to predict such defects.

Outline. First, additional experimental permeability and compaction tests are conducted to adapt the process model to UD-NCF (Section 5.2).

Subsequently, a strong FSI is implemented and verified with dry and viscous compaction trials (cf. Section 5.3.3). In Section 5.3.4, a parametric study demonstrates the interaction between deformation, pressure field and the applied contact conditions. Finally, the model's capability is evaluated via a qualitative comparison with the results that have been reported by Hautefeuille et al. [59] for a comparable uni-directional material.

Delimitation. Superficial fluid flows are neglected in this chapter. The presented results are purely based on strong FSI within the porous medium.

5.2 Experimental assessment of UD-NCF

The UD-NCF material (cf. Section 1.5) provides a distinctly different fabric architecture compared to woven fabrics. Consequently, differences regarding draping and infiltration behaviour are expected. However, the draping behaviour of the dry UD-NCF has already been investigated within a DFG Project[1] [248, 345, 347]. Consequently, the anisotropic permeability and the non-linear compaction behaviour need to be characterised.

5.2.1 Permeability characterisation

For the permeability tensor $\boldsymbol{K}$, values in fibre direction, perpendicular and in thickness direction are required (K_f, $K_\perp$, K_3). Similar trials to the ones presented in Section 4.3.2 are conducted with UD-NCF.

---

[1] 'Experimental and virtual analysis of draping effects and their impact on the mechanical behaviour of composite components' (KA4224/1-1).
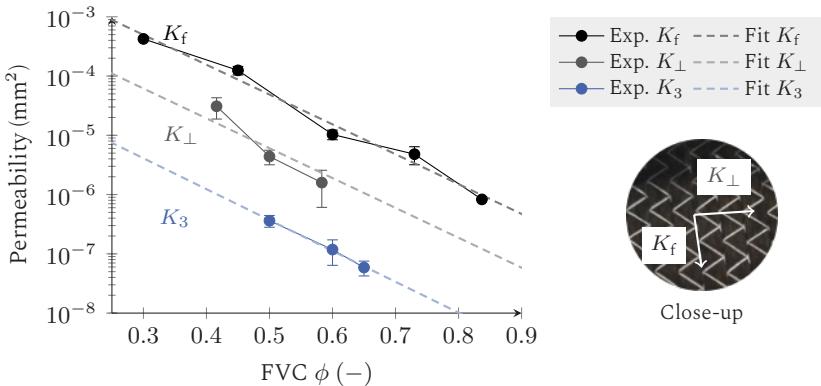
Figure 5.2: Principal permeability values for UD-NCF. K_f is measured with the radial setup presented in Section 4.3.2, $K_\perp$ with the linear setup proposed by [178] and K_3 at the Fraunhofer IGCV in Augsburg.

The in-plane components (K_f, $K_\perp$) are measured with the already outlined radial setup (cf. Figure 4.7) and an additional linear setup that has been proposed by Magagnato et al. [178]. As in Section 4.3.2, transverse permeability in thickness direction was determined at the Fraunhofer IGCV in Augsburg. The experimental results for different compaction states are summarised in Figure 5.2. Analogous to other experimental results that have been published for uni-directional reinforcements [180, 181], permeability decreases strongly with increasing FVC. Moreover, permeability in fibre direction is approximately 10 times higher than in perpendicular direction for the same deformation state [181]. The lowest permeability values are obtained in thickness direction.

The measured permeability values are formalised within function 5.1 to 5.3 based on the current FVC ϕ

$$K_f(\phi) = 0.0161 \cdot e^{-11.6\phi} \tag{5.1}$$

$$K_\perp(\phi) = 0.002 \cdot e^{-11.6\phi} \tag{5.2}$$

$$K_3(\phi) = 0.00015 \cdot e^{-12.0\phi}. \tag{5.3}$$

223

They are obtained by regression with the experimental results. In Sections 4.3.2 and 4.3.5.3 it was demonstrated that the fibre-frame based description of the permeability tensor allows to intrinsically capture fibre-reorientation due to shearing. For this reason, a permeability characterisation in the undeformed state is sufficient for further modelling.

5.2.2 Viscous compaction

Dry and pre-infiltrated compaction trials with a six-ply stack $[0]_6$ are carried out to parametrise the transverse compaction behaviour. The same punch-to-plate setup outlined in Section 4.3.1 is used.

In Figure 5.3 (a), dry and viscous compaction forces are compared, revealing a non-linear increase towards high compaction states and a further increase for pre-infiltrated specimens. Comparable results were found for the woven fabric (cf. Figure 5.3).

The impact of nesting phenomena, e.g. overlapping at the PP interfaces, is shown in Figure 5.3 (b). In contrast to woven fabric, no significant impact of nesting is observed for the UD-NCF.

Discussion. An expected non-linear reaction force is obtained for the UD-NCF. The reaction forces are for example five times higher (≈ 80 N vs ≈ 400 N at $u_{\text{com}} = 2$ mm) when the UD-NCF is compared in the wet state. The insignificance of the nesting phenomena is attributed to the more homogenous material interface. This favours minimal interlocking between the stack interfaces, even for relative orientations of 0 and $90°$. Minor nesting within the UD-NCF stack is also assumed to be responsible for the less pronounced effect of infiltration on the measured reaction force (cf. Figure 5.3 (a)). In contrast to the five times higher values of the UD-NCF, the infiltrated compaction forces for the woven fabric in Section 4.3.1 were about ten times higher (≈ 30 N vs ≈ 300 N at
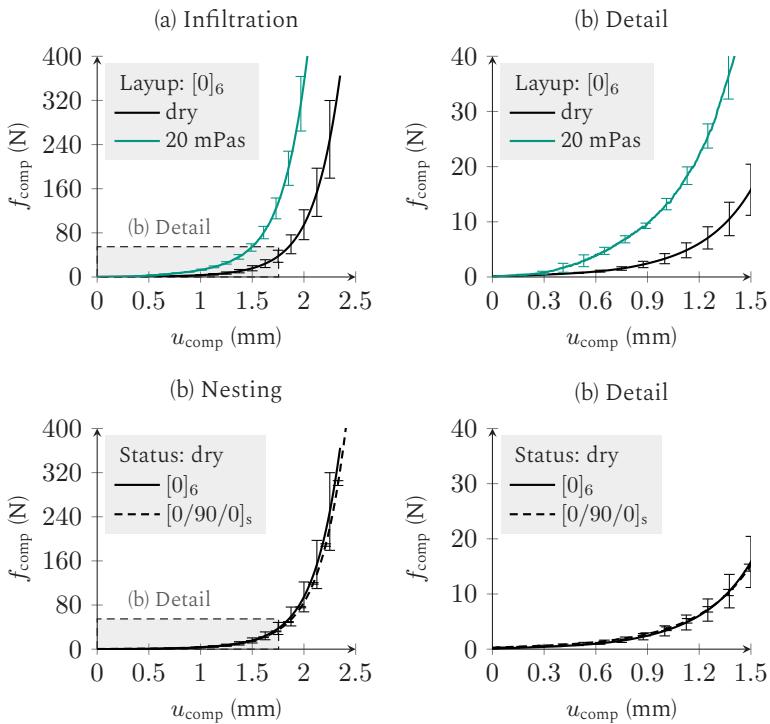
Figure 5.3: Compaction results UD-NCF | (a) Impact of infiltration and (b) nesting phenomena on the compaction behaviour of UD-NCF.

$u_{\text{com}} = 1.2$ mm). It is assumed that this difference originates from the woven architecture, which allows for a distinct interlocking of the rovings, sealing potential flow channels during compaction. For UD-NCF, the increased permeability in fibre direction persists even for higher compaction states. Due to minimal interlocking of the layers, potential flow channels are less likely to be sealed, leading to lower fluid pressures below the punch (cf. Table A.1).

5.3 Numerical modelling

For the numerical implementation on the macro-scale, the fully-coupled 3D modelling approach (DPE3D) introduced in the previous chapter is adapted to the UD-NCF material. Given the outlined additional experiments, an adaption of the fluid submodel is straightforward using the permeability functions 5.1 to 5.3. The draping behaviour, especially the membrane behaviour, is significantly different due to the unidirectional fibre architecture. In contrast to the interwoven fibre yarns of the woven fabric, the UD-NCF contains uni-directional aligned fibres that are interconnected by a polymer yarn. A macroscopic membrane model that has been proposed by Schirmaier et al. [248] is used for modelling, replacing the membrane model within the CS element (cf. Figure 4.11). Moreover, a parametrisation of the user-enhanced compaction behaviour is required (cf. Figure 5.3).

The constitutive equations of the UD-NCF draping submodel are outlined in the following, followed by the implementation of the strong FSI in Section 5.3.2. The latter will be verified in Section 5.3.3 using the outlined viscous compaction trials.

5.3.1 Adaption of the draping submodel to UD-NCF

Membrane model. In contrast to woven fabric, where pure shear is the dominant deformation mode, macroscopic modelling of UD-NCF requires capturing large tensile deformations in the stitching direction ε_2 in combination with compressive in-plane strains perpendicular to carbon fibre direction $\varepsilon_\perp$ [105]. Schirmaier et al. [51] propose off-axis-tension (OAT) tests (cf. Figure 1.7) to analyse and characterise the multiaxial deformations at macro-scale [347].

The underlying concept proposed by Schirmaier et al. is to formulate a non-orthogonal elastic-plastic material model based on linear strain

measures and especially the perpendicular strain component $\varepsilon_\perp$ (cf. Figure 5.4).
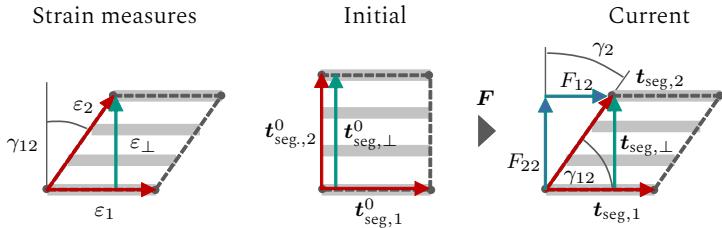
Figure 5.4: Schematic illustration of the UD-NCF material model based on linear strain measures in initial and current deformation state (based on [248, 325, 347]).

This enables a material formulation using the principal material strain ε_1 in fibre direction, the non-orthogonal transverse tensile yarn strain ε_2, which only contributes under tensile load, the shear angle γ_{12} and the perpendicular strain $\varepsilon_\perp$, which is used to model in-plane roving compression. The latter enables homogenised modelling and prediction of in-plane gapping ($\varepsilon_\perp > 0$) or compression ($\varepsilon_\perp < 0$) in stitching yarn direction. The linear strains ε_1 and ε_2 are obtained by the stretch of the respective line segments of the unit cell according to

$$\varepsilon_i = \frac{|\boldsymbol{t}_{\text{seg},i}|}{|\boldsymbol{t}^0_{\text{seg},i}|} - 1 = \sqrt{\sum_j F_{ji}^2} - 1, \quad \text{with} \quad i,j = 1,2. \tag{5.4}$$

Here, the deformed line segment is calculated by $\boldsymbol{t}_{\text{seg},i} = \boldsymbol{F} \cdot \boldsymbol{t}^0_{\text{seg},i}$. The corresponding shear angle γ_{12} in the current configuration is given geometrically by

$$\gamma_{12} = \frac{\pi}{2} - \gamma_2 = \frac{\pi}{2} - \cos^{-1}\left(\frac{\boldsymbol{t}_{\text{seg},1} \cdot \boldsymbol{t}_{\text{seg},2}}{|\boldsymbol{t}_{\text{seg},1}||\boldsymbol{t}_{\text{seg},2}|}\right). \tag{5.5}$$

227

Finally, the linear perpendicular strain component $\varepsilon_\perp$ is introduced by the stretch of an orthogonal line segment $\boldsymbol{t}_{\mathrm{seg},\perp}$ with yields

$$\varepsilon_\perp = \frac{\boldsymbol{t}_{\mathrm{seg},\perp}}{\boldsymbol{t}_{\mathrm{seg},\perp}^0} - 1 = \frac{|\boldsymbol{t}_{\mathrm{seg},1}|\sin(\gamma_{12})}{\boldsymbol{t}_{\mathrm{seg},2}^0} - 1 = \sqrt{F_{12}^2 + F_{22}^2}\sin(\gamma_{12}) - 1. \quad (5.6)$$

These strains correspond to the nominal stress tensor $\boldsymbol{P}^*$ and the scalar nominal transverse stress $P_\perp$ obtained by an alternative decomposition of the deformation gradient $\boldsymbol{F}$ [248]. Pushing $\boldsymbol{P}^*$ and $P_\perp$ to the current configuration $\mathscr{B}_1$ ultimately yields the Cauchy stress $\hat{\boldsymbol{\sigma}}$ by combining the Cauchy stress $\hat{\boldsymbol{\sigma}}_{\mathrm{Ph}}$ in principal material direction and perpendicular to the fibre orientation $\hat{\boldsymbol{\sigma}}_\perp$ according to

$$\hat{\boldsymbol{\sigma}} = \hat{\boldsymbol{\sigma}}_{\mathrm{Ph}}\left(\varepsilon_1, \varepsilon_2, \gamma_{12}\right) + \hat{\boldsymbol{\sigma}}_\perp(\varepsilon_\perp). \quad (5.7)$$

Elastic-plastic behaviour is introduced by superimposed elastic $\varepsilon_2^{\mathrm{e}}$ and plastic parts $\varepsilon_2^{\mathrm{p}}$ of the strain components and the elastic γ_{12}^{e} and plastic γ_{12}^{p} part of the shear angle. A yield surface $R_{2,\Gamma}(\varepsilon_2^{\mathrm{p}}, \gamma_{12})$ and a yield curve $R_{12,\Gamma}(\gamma_{12}^{\mathrm{p}})$ are introduced based on plastic strain $\varepsilon_2^{\mathrm{p}}$, shear angle γ_{12} and the plastic part of the shear angle γ_{12}^{p}, respectively. Moreover, compressive stresses $P_\perp^*$ are modelled with a superimposed non-linear elastic material law based on the perpendicular yarn strain $\varepsilon_\perp$ and the shear angle. The model is comprehensively described in [51].

OAT trials (cf. Figure 5.5) were used to parametrise the outlined model for the applied UD-NCF material in the dry state as part of a DFG project[1].

Figure 5.5 shows the experimentally obtained reaction forces for different shear angles following the setup illustrated in Figure 1.7 (c). Moreover, a comparison with the UD-NCF model is given – a good agreement is

---

[1] 'Experimental and virtual analysis of draping effects and their impact on the mechanical behaviour of composite components' (KA4224/1-1).

observed. The obtained dataset (cf. Table A.14 in Appendix A) accounts for all three fibre orientations simultaneously.
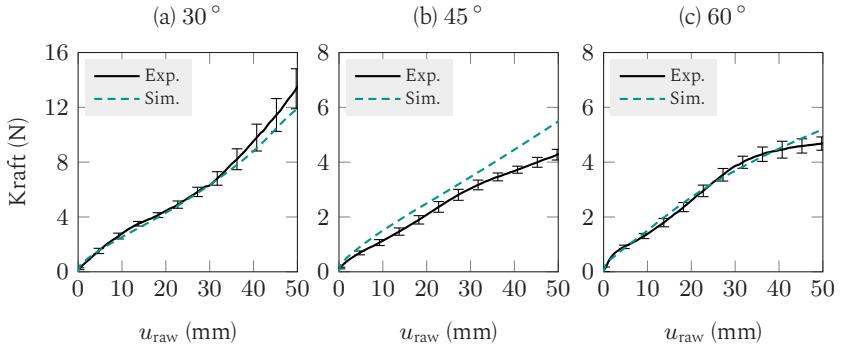
Figure 5.5: Results of the experimental OAT trials with fibre orientations of (a) 30 °, (b) 45 ° and (c) 60 ° using a specimen size of 320 x 160 mm and a constant traverse velocity of $\dot{u}_{\text{raw}} = 100$ mm/min; The results are compared with the identified parameter set for the applied UD-NCF.

Compaction. Compaction behaviour is modelled within the mechanical part of the superimposed user element similar to the equations outlined in Section 4.3.4. The non-linear stiffness in thickness direction C_{33} is given by

$$C_{33} = E_0^{\text{SC}} + \underbrace{a_0 e^{[\varepsilon_{\text{I}}(\varepsilon_3 - \varepsilon_{\text{II}})] + \varepsilon_{\text{III}}}}_{\text{if } \varepsilon_3 > \varepsilon_3^0}, \tag{5.8}$$

where ε_3 provides the compressive strain in thickness direction and E_0^{SC} the base stiffness of the CS element. Similar to the previous Chapter, the model is parametrised using reverse parameter identification with virtual compaction trials (cf. Figure 5.3). The final dataset is given in Table A.12 in Appendix A. A verification will be given in Section 5.3.3.

Tool-ply contact. The term 'in-mould stiffness' of the material is often used in the context of fibre-washout and FiFD [57,58,60]. The term recognises that the current material stiffness inside the mould depends on its local deformation state and imposed contact boundary conditions. FiFD arises when the fluid-induced drag forces exceed the material's tangential contact stresses and/or in-plane stiffness. Consequently, local contact conditions strongly affect the results [57, 60].

Regarding modelling, the implementation of a strong FSI in Section 5.3.2 introduces pressure-related forces to the nodes of the saturated elements. This fluid pressure must be considered at the contact interface to predict viscous compaction forces. However, these superimposed normal contact stresses cannot be directly combined with a Coulomb friction law. An interpretation of the pressure as a normal contact force for the coulomb model would lead to overestimated tangential forces in the contact. This would imply a distinct, impenetrable interface between fluid pressure inside the porous medium. In reality however, the fluid encloses the stack. Therefore, a hydrodynamic contact formulation is required for the infiltrated part.

To contribute to this without an extensive expansion of the contact model and additional experiments, a maximal tangential stress τ^{max} is introduced, limiting the predicted tangential stresses for the infiltrated contact zone. A shear flow for an incompressible Newtonian fluid is assumed for an estimation of τ_0^{max} according to

$$\tau_0^{\mathrm{max}} = \eta \frac{\partial v_{\mathrm{Fluid}}}{\partial y} \approx \eta \frac{v_{\mathrm{Fluid}} - \overset{0}{\cancel{v_{\mathrm{Fluid}}^{\mathrm{wall}}}}}{h_{\mathrm{rim}}}. \tag{5.9}$$

Assuming a viscosity of $100\,\mathrm{mPas}$, a channel height of $h_{\mathrm{rim}} = 0.01\,\mathrm{mm}$ for the fluid boundary layer and an average fluid velocity of $v_{\mathrm{Fluid}} = 10\,\mathrm{mm/s}$ this yields $\tau_0^{\mathrm{max}} = 1 \cdot 10^{-4}\,\mathrm{N/mm^2}$. This is an interim solution and the impact of the applied maximal tangential stress will be investigated in Section 5.3.4.

5.3.2 Implementation of strong FSI

Terzaghi's effective stress as described by MacMinn et al. [321] is used for a strong coupling between fluid pressure and deformation. Two additional sources for nodal reaction forces within ABAQUS' Green-Naghdi frame $[e_i]$ are introduced to the user element. The first one represents the reaction forces caused by the fluid pressure $\hat{f}_R^p$ within the skeleton structure of deformable porous medium and the second one gives the fluid drag $\hat{f}_R^d$ between flow and fabric. The pressure itself cannot lead to deformation of the element cell, since the fluid is assumed to be incompressible [61]. Superimposed to the dry material response in thickness direction $\hat{f}_R^{mat}$, the entire material reaction yields

$$\hat{f}_R^{FSI} = \underbrace{\hat{f}_R^{mat}}_{\text{Eq. 4.21}} + \underbrace{\hat{f}_R^p + \hat{f}_R^d}_{\text{strong FSI}} \tag{5.10}$$

$$= \det(\boldsymbol{J}) \left[\frac{1}{J} \boldsymbol{B}_1 \cdot \tilde{\boldsymbol{\tau}} - p\tilde{\boldsymbol{I}} + \phi \, \boldsymbol{N}_{\text{shape}} \, \tilde{\text{grad}}(p) \right]. \tag{5.11}$$

Here, $\boldsymbol{B}_1$ provides the operator matrix of the user element, $\det(\boldsymbol{J})$ the Jacobean determinant, $\tilde{\boldsymbol{\tau}}$ the Kirchhoff stress tensor in Voigt Notation and $\boldsymbol{N}_{\text{shape}}$ the shape function matrix. Gravity within the fluid submodel is implemented through an additional body force (cf. Section 4.3.5.1).

5.3.3 Validation of viscous compaction

The dry and viscous compaction trials (cf. Figure 5.3) are used for validation of the dry material response of a multi-ply stack (cf. Figure 5.6 (b)) and the implemented FSI in Sub Figure 5.3 (c). A half model of the compaction setup containing 2000 elements per single ply is used. The contact normal stiffness c_p^N is set significantly higher than the maximal material compaction stiffness. The stack size from the experiments is

used for the simulation of the dry trials (cf. Figure 5.3 (b)). For the simulation of the viscous compaction trials, the stack size is matched with the punch size to ensure suitable outlet condition and ambient pressure.

(a)

Setup

Dry state

Ply thickness h (mm)

20 mPas

Pressure p (MPa)

(b)
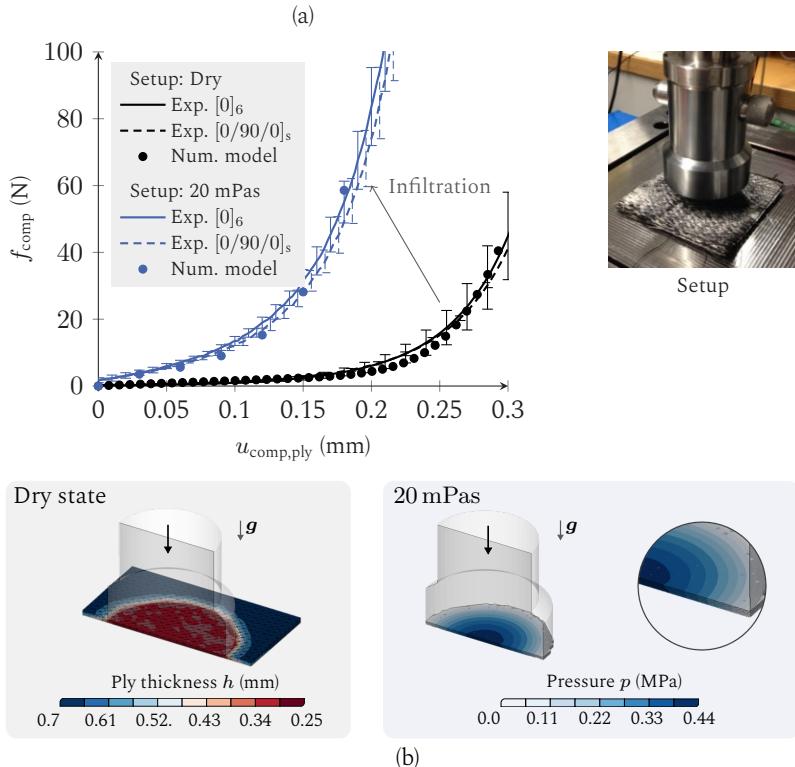
Figure 5.6: (a) Measured and predicted reaction forces during dry and viscous compaction; (b) Exemplary dry simulation results; (c) Setup and predicted pressure distribution below the punch [325].

As shown in Figure 5.6, a good agreement between experimental results and model predictions is observed. As nesting is of minor importance, one parameter set is able to capture both investigated layups

($[0]_6$, $[0/90/0]_s$). The only difference between the dry and infiltrated setup is the presence of the fluid. It is concluded that the implemented strong FSI allows for a prediction of the viscous reaction forces during compression. This confirms that the entire fluid pressure needs to be considered at the interface for a reasonable prediction of the normal reaction forces at the tool-ply interface.

5.3.4 Parametric study

Seong et al. [60] have experimentally studied flow-induced process effects on UD-NCF. They separate between two types of flow-induced displacements - rigid body slip and local deformation such as fibre-displacement, ondulation or wrinkling. Rigid body slip occurs when the flow-induced drag exceeds the frictional tangential forces. In contrast, local deformation occurs when the flow-induced drag forces exceed the local material stiffness of the stack. Consequently, the ratio of in-mould stiffness and frictional conditions determines which deformation is most likely triggered. Similar observations for WCM have been made in literature [147] and during own trials [346].

In the following, a comparable numerical study on a partly and completely infiltrated strip is carried out to evaluate the models' response to different frictional conditions. This allows a comparison between the above introduced experimental observations and the predicted deformations.

Setup. A pre-infiltrated strip (100 x 10 x 0.5 mm) containing the model is compacted with a constant rate of $\dot{h} = 0.05\,\text{mm/s}$ between two parallel rigid planar surfaces (cf. Figure 5.7 (a)). The left strip side is pinned and an outlet is defined at the opposite nodes at the right side. All remaining nodes are unconstrained. A fibre orientation of $90\,°$ is used to maximize the effect of FiFD. Due to compaction, a 1D flow from left to right establishes, leading to a similarly directed drag. A constant viscosity

of 100 mPas is assumed. Contact is implemented with a coulomb friction coefficient of $\mu_{\text{TP}} = 0.2$.
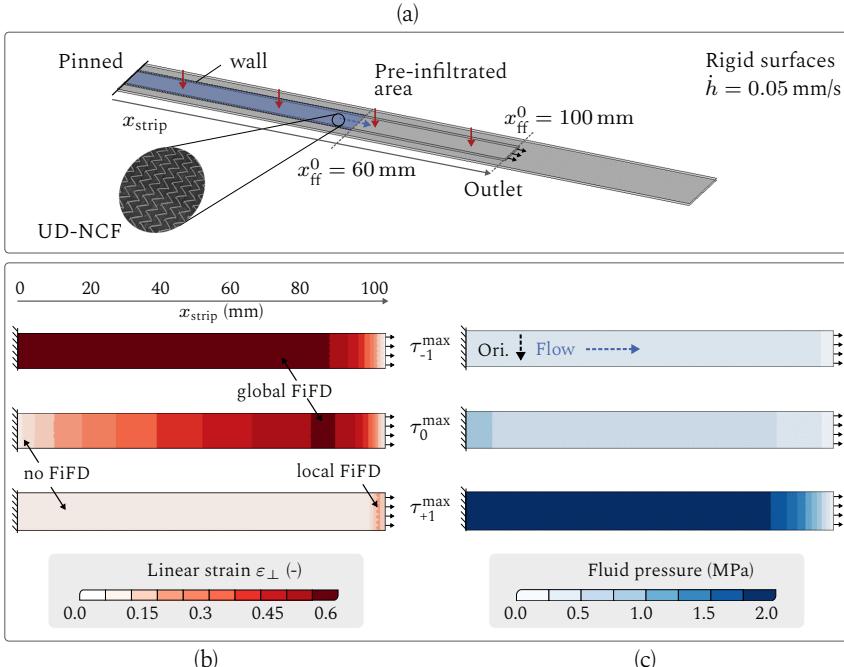
Figure 5.7: Parametric study | (a) Setup illustration; Impact of contact formulation on predicted flow-induced strains [325] (b) and pressure distribution (c) for a fully pre-infiltrated specimen. Results are plotted with respect to the initial the configuration for the final deformation state (time point $t_1 = 0.6\,\text{s}$).

For the study, the maximal tangential stress is varied using the above estimated maximal stress centre value $\tau_0^{\text{max}} = 1 \cdot 10^{-4}\,\text{N/mm}^2$ by a factor of 10 ($\tau_{-1}^{\text{max}} = 1 \cdot 10^{-5}\,\text{N/mm}^2$, $\tau_{+1}^{\text{max}} = 1 \cdot 10^{-3}\,\text{N/mm}^2$). The average predicted FVC ranges between 42 and 50 % for the final deformation state. The ambient pressure is set to zero. Gravity is neglected. x_{ff}^0 is the initial flow front position, $x_{\text{ff}}^{t_1}$ gives the current position for the final deformation state t_1.

Results. The results of the fully-infiltrated strip ($x_{ff}^0 = 100$ mm) and different contact conditions are displayed in Figure 5.7 (b,c). The spatial distributions of linear perpendicular strain $\varepsilon_\perp$ and the related pressure distribution along the strip are compared for the final deformation state $t_1 = 0.6$ s. Rigid body slip cannot occur as the left side of the strip is pinned. Looking at the centre configuration $\tau_0^{\max}$, an interesting strains transition is observed (b). The strain increases from the left to right until a maximum at approximately 80 mm is reached. As in-plane strains occur, increased pressure is prevented (cf. Figure 5.7 (c), $\tau_0^{\max}$). Reducing the tangential friction stress $\tau_{-1}^{\max}$ increases the FiFD along the strip.

(a) Fully-infiltrated   (b) Partly-infiltrated
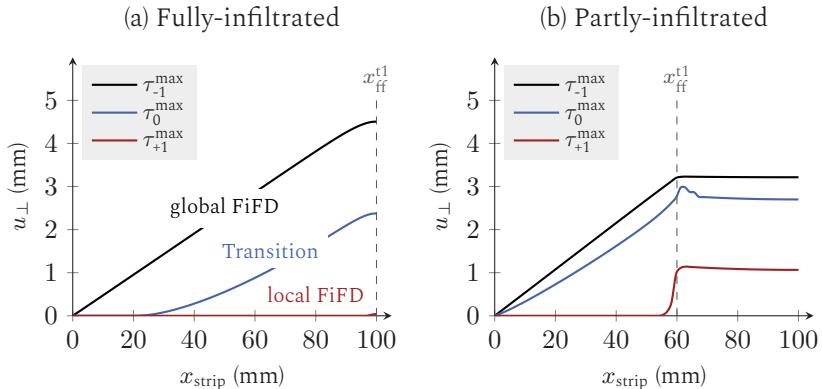
Figure 5.8: Parametric study | Nodal displacement along the (a) fully-infiltrated and (b) partly infiltrated strip for the final deformation state, time point $t_1 = 0.6$ s. A transition between global and local FiFD is predicted, depending on the assumed contact conditions.

Consequently, the pressure reduces compared to the central configuration. In contrast, high friction between ply and tool prevents FiFD almost completely (cf. Figure 5.7 (b,$\tau_{+1}^{\max}$)). Only minor local FiFD is predicted near the outlet. As the contact stress prevents in-plane strains, more fluid is forced out, FVC increases and more than twice as high pressures values are observed. The presented time point t_1 represents the

entire observed behaviour for the complete simulation run and the final deformation state.

The predicted perpendicular strains in Figure 5.7 imply nodal displacements, e.g. FiFD, along the strip (cf. Figure 5.8). Whereas no significant FiFD is observed for $\tau_{+1}^{\max}$, displacements up to 5 mm are predicted towards the outlet under low frictional condition $\tau_{-1}^{\max}$ (cf. Figure 5.8 (a)).
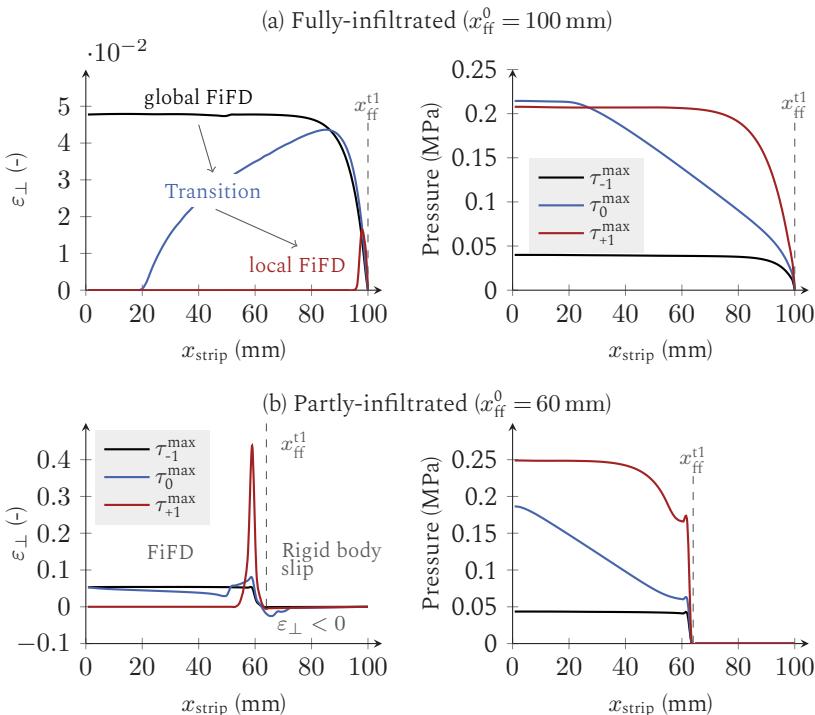
Figure 5.9: Parametric study | (a) Perpendicular strain and pressure distribution along the fully-impregnated strip ($x_{\text{ff}}^0 = 100$ mm); (b) Similar for the partly-saturated strip.

Since drag forces only act on the saturated part of the strip, a similar displacement profile is predicted within the infiltrated area of the partly infiltrated strip in Figure 5.8 (b). The remaining dry part is pushed to the

right side since the remaining contact forces are not sufficiently high. Only the high frictional conditions slightly reduce the slip behind the flow front.

Moreover, the spatial distribution of the perpendicular strain $\varepsilon_\perp$ along the strip is given by Figure 5.9 (a). Similar to the observations for the displacement field, the occurrence of FiFD changes from globally distributed ($\tau_{-1}^{\max}$), to localised at the outlet ($\tau_{+1}^{\max}$), solely by changing the interface behaviour.

Beyond that, a similar results for a partly saturated strip ($x_{\mathrm{ff}}^0 = 60$ mm) are shown in Figure 5.8 (b) and Figure 5.9 (b) for the final compation state $t_1 = 0.6$ s. As mentioned above, drag forces act solely on the saturated part of the strip, which leads to a rigid body slip of the dry unconstrained part of the strip (cf. Figure 5.8 (b)). The predicted perpendicular strains are significantly higher than for the fully impregnated case. Moreover, the positive strain in the saturated domain can lead to slight in-plane compression ($\varepsilon_\perp < 0$) behind the flow front ($x_{\mathrm{ff}}^{\mathrm{t1}}$) (cf. Figure 5.9 (b), τ_{mid}).

Discussion. The results agree with observations that have been published in literature [57, 60, 147]. In this regard, increased fluid drag can lead to local or global FiFD, depending on the material behaviour and contact conditions. In agreement with the results that have been published by Seong et al. [60], FiFD is favoured by low frictional conditions ($\tau_{-1}^{\max}$), resulting to a deformation which solely depends on the ratio between in-mould stiffness and fluid drag. The obtained distribution of the linear strains along the strip (cf. Figures 5.7 (b) and 5.9 (a, left)) is assumed to result from the plastic part in yarn direction [248]. Although the pressure slightly decreases towards the flow front (cf Figure 5.9 (a, right)), increasing yarn stiffness and accumulated tangential friction towards the outlet lead to an almost linear strain state along the strip (cf. Figure 5.9 (a, left)). This results in a linear slope for the displacement in the drag direction. This has been experimentally confirmed by a master thesis [346].

In all cases, the pressure at the flow front drops to ambient pressure zero, which increases the gradient-related drag towards the outlet. For low frictional conditions ($\tau_{-1}^{\max}$) the resulting local drag is not high enough to affect the strain distribution. This changes when an increased friction is assumed ($\tau_0^{\max}$,$\tau_{+1}^{\max}$). Then, FiFD increasingly localises at the outlet. This originates from high drag forces resulting from the increased fluid pressure within the strip.

Similar correlations are observed for the partly infiltrated strip. The frictional conditions are more complex, which results in more pronounced strain localisation along the strip (cf. Figure 5.9 (b)). Beyond that, additional tangential friction forces within the clamped dry part of the strip can lead to positive strain within the saturated and a corresponding in-plane compression $\varepsilon_\perp < 0$ within the dry part. This occurs when the fluid drag locally exceeds the frictional forces and in-mould stiffness of the UD-NCF, but rigid body slip at least partly prevents this deformation in the remaining dry part (cf. Figure 5.9 (b, $\tau_0^{\max}$). Seals and blank holders can have similar effects on the part manufactured by WCM. A similar situation is assumed to be responsible for the initially motivated process results (cf. Figure 5.1).

5.3.5 Comparison with literature

This section aims to quantitatively compare the introduced model's response with experimental results from literature. The presented comparison is therefore not a validation of the modelling approach. Yet, it allows investigation of whether the modelling approach can predict comparable qualitative results by addressing the same underlying mechanisms leading to FiFD. Moreover, an experimental reference without superficial flow is required since they are neglected in the current model. The same

reason prevents a direct comparison with the above-introduced plate experiments (cf. Figure 5.1), as current research suggest that superficial flows play an important role during mould closure.

5.3.5.1 Experimental results

In their experimental study on viscous compaction of a quasi UD 'weft glass fabric' (UDT[1] 400P), Hautefeuille et al. [59, 147] have measured FiFD via video tracing of markers. Instead of a strip-shaped geometry, they used a 2D plate setup for compaction, which results in anisotropic FiFD as shown in Figure 5.10.
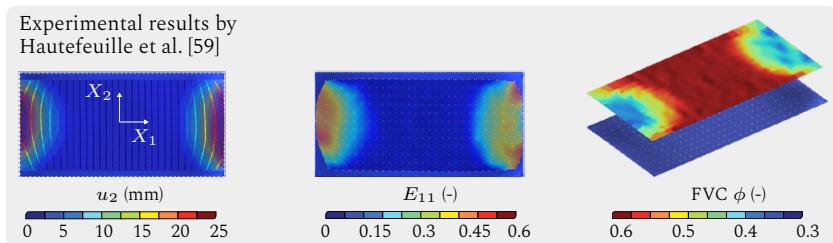
Figure 5.10: Experimental results published by Hautefeuille et al. [59] for in-plane FiFD during viscous compaction for an unidirectional reinforced composite (glass fibre UDT) – the fabric is oriented in X_2 direction [325].

For one of their trial sets, they compact pre-infiltrated stacks with a very low compression rate of $\dot{h} = 0.025$ mm/s, using a constant, relatively high viscosity of 4580 mPas, provoking FiFD. The low compression rate further prevents a potential superficial fluid flow as it is being squeezed out before relevant forces, pressure or displacements occur [59]. Due to the low compaction rate, one trial took around 92 s.

---

[1]   Supplied by CHOMARAT, 400 g/m^2 weft, 20 g/m^2 wrap.

Moreover, compression forces up to 150 kN are applied to the material, resulting in FiFD of the stack. The high compaction force and low compaction rate favours localised FiFD towards the outlet (cf. Figure 5.10). The anisotropy of the unidirectional reinforcement leads to pronounced FiFD ($u_\perp$) perpendicular to the fibre orientation. In their work, Hautefeuille et al. use optically tracked markers to calculate the spatial displacement field $u_\perp$ and the perpendicular Green strain E_{11} (cf. Equation 3.2). The FVC ϕ is estimated using $\varepsilon_\perp$ and the cavity height h_{cav}.

5.3.5.2 Prediction of the process model

A similar 2D pre-infiltrated compression setup is simulated with the 3D process model. As a relatively low compaction rate was used for the experimental trials, high contact forces are assumed for the simulation $\tau_{+1}^{\max}$. In contrast to Hautefeuille et al., more realistic process conditions for a WCM process are assumed for the simulation, as FiFD was already observed at these conditions for the UD-NCF (cf. Figure 5.1). Moreover, a simulation time of 92 s exceeds the available computational resources. A compaction rate of $\dot{h} = 0.3$ mm/s and a constant viscosity of 100 mPas is used.
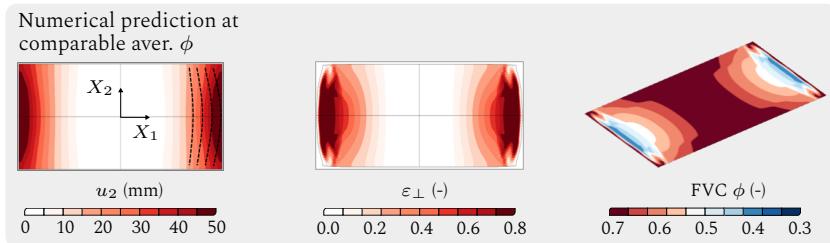
Figure 5.11: Qualitative comparison with literature | Numerical prediction with process model for the UD-NCF material [325].

A good qualitative agreement for the in-plane displacement, strain and FVC field is observed (cf. Figure 5.11). Even though two slightly different kinds of unidirectional fabrics are compared (glass fibre UDT ($400\,g/m^2$)) vs UD-NCF ($330\,g/m^2$), similar mechanisms favour FiFD during compression. These mechanisms arise during the experiments and are captured by the model.

5.4 Discussion and conclusion

FiFD is an undesired process defect that may significantly affect mould-filling behaviour during the processing and structural performance of the manufactured part.

The macroscopic process model is adapted to a UD-NCF via an additional characterisation of permeability and compaction behaviour (cf. Section 5.2). For modelling of the membrane behaviour, an existing model that has been proposed by Schirmaier et al. [248] is used and parametrised via OATs. Using Terzaghi's effective stress approach, a strong interaction between material deformation and fluid pressure is implemented. Additional viscous compaction trials are used to verify the introduced strong FSI (cf. Section 5.3.3).

A parametric study reveals key relationships and conditions for global or localised FiFD and the overall high importance of the frictional conditions. The predicted results agree with experimental results that have been published and discussed in literature [57,59–61]. Moreover, the suitability of the numerical model is demonstrated via a comparison with an experimental study that has been presented by Hautefeuille et al. [59] for a comparable material. The results emphasise the substantial impact of anisotropic material behaviour.

Beyond that, some important limitations of the current modelling approach have become apparent, thus motivating further research. As discussed in Section 5.3.1, the contact formulation needs further improvement. A comprehensive investigation of the contact formulation is required to distinguish between a hydrodynamic and a dry material state in a homogenised manner. Moreover, only a single phase flow is investigated. Thus air traps are neither predictable nor investigated. Furthermore, a suitable cavity representation approach and superficial flow are needed to account for more complex process conditions.

Finally, a deeper look into the applied UD-NCF membrane model is recommended. The membrane model invokes a complex material formulation which is challenging to parametrise. Although the complex yarn behaviour requires capturing, it remains debatable if the implemented complex plasticity formulation is necessary for the obtained results.

6 Conclusion and recommendations

A systematic analysis of woven fabrics' forming and mould-filling behaviour under wet compression moulding (WCM) process conditions has been conducted. The physical mechanisms have been identified and structured into four areas during simulation model development: (1) Viscous draping, (2) Simultaneous fluid progression, (3) Fluid-Structure-Interaction and (4) Non-isothermal curing. A macroscopic simulation strategy was presented that can account for simultaneous draping and fluid progression during moulding. The process model predicts crucial interactions between material behaviour and process boundary conditions. A good agreement with experimental results is achieved. Moreover, it was demonstrated that the modelling approach could be adapted to other textile architectures, as shown for UD-NCF. An enhanced version of the process model can predict crucial process defects such as flow-induced fibre-displacement (FiFD). This was achieved by introducing a strong Fluid-Structure-Interaction (FSI) between material stresses and fluid pressure. These results contribute to a virtual process and component development for WCM processes.

Major conclusions and recommendations are summarised in the following, categorised by the initially proposed objectives (cf. Section 1.3). The first objective was to empirically determine the relevant physical mechanism during WCM processing.

Results and conclusions for Objective 1
Systematic analysis of the interrelated material behaviour of textile and fluid during WCM processing with special emphasis on a comprehensive, physics-based understanding of significant mechanisms and their interdependencies to ultimately enable process modelling.

WCM processes analyis (Sec. 2)
- The trials allowed for an in-situ visualisation of the flow progression during moulding.
- The mutual dependencies between draping and mould-filling are demonstrated.
- A comparison between a woven fabric and UD-NCF material highlights the impact of transversal permeability on the final resin distribution.
- Material behaviour and process control ($\dot{u}_\mathrm{T}$, K_3, t_soak) are decisive for the relevance of superficial flows.
  ▶ Process simulation requires coupled modelling of draping and infiltration

Membrane behaviour (Sec. 3.1)
- An infiltrated bias-extension test for shear characterisation of low-viscous infiltrated fabrics is developed.
- Rate- and viscosity-dependent shear behaviour is observed.
  ▶ Shear resistance can be increased or decreased by the infiltration state.

Bending behaviour (Sec. 3.2)
- A modified cantilever test and a rheometer bending test are applied for bending characterisation of low-viscous infiltrated fabrics.
- The results are qualitatively but not quantitatively comparable.
- Low-viscous infiltration reduces the bending stiffness significantly.
- Viscosity-, rate-dependency and hysteresis behaviour is observed.
  ▶ Infiltration significantly affects bending stiffness.

Inter-ply behaviour (Sec. 3.3)
- Infiltration reduces interface friction but introduces rate-dependency
- Due to the low viscosity, tangential stresses remain comparably low.
- Infiltration affects normal behaviour but is difficult to measure.
  ▶ Low inter-ply stresses prevent a relevant impact of infiltration.

Compaction & permeability (Sec. 4.3.1, 4.3.2, 5.2)
- Non-linear compaction behaviour with shear-dependency is observed
- Anisotropic permeability with shear-dependency is measured.
- Viscous reaction forces depend on both the material's and fluid's response.
  ▶ Process simulation requires compaction and anisotropic permeability.

WCM process for a complex demonstrator (Sec. 3.4)
- Tool and part concept were designed virtually using the CAE-Chain.
- The direct WCM process route is analysed.
- Exp. findings confirm the results obtained at the test bench level.
  ▶ A complex demonstrator could be manufactured using direct WCM.

Woven fabric   UD-NCF

Figure 6.1: Objective 1 | Experimental results and conclusions.

Results and conclusions for Objective 2
Development and validation of a macroscopic WCM process simulation model, allowing for a simultaneous description of draping and fluid progression under consideration of process boundary conditions.

Membrane behaviour (Sec. 3.1)
- A non-orthogonal, hyperviscoelastic material model is developed.
- Infiltration states of 20-250 mPas are modelled homogeneously.
- A significant impact on part level is observed.

▶ Infiltrated membrane behaviour is relevant for process modelling.
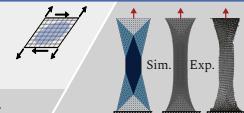
Bending behaviour (Sec. 3.2)
- A non-orthogonal, hypoviscoelastic bending model is modified.
- Infiltration is modelled in a homogenised manner.
- Contact slip prevents a higher significance on part level.

▶ A viscoelastic model, parametrised in a dry state, is sufficient.
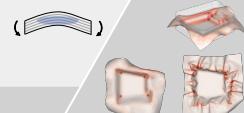
Inter-ply behaviour (Sec. 3.3)
- A penalty-based tangential and normal contact model is developed.
- Infiltration is modelled in a homogenised manner.
- Numerical studies showed an only minor significance on part level.

▶ A dry, built-in contact modelling seems to be sufficient (weak FSI).
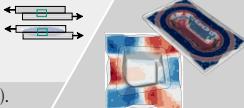
Viscous draping of a complex demonstrator (Sec. 3.4)
- A combined viscous draping simulation based on the submodels is conducted.
- The outer shape and fibre orientations in critical regions are predicted accurately.
- The study supports the lower significance of the contact formulation.
- Limitions (multi-axial stress states, constant thickness) of current 2D macroscopic forming simulations are outlined.

▶ Virtual process development is enabled with the developed models.

3D process model (weak FSI, Sec. 4.3)
- A 2D approach demonstrates the feasibility of an explicitly formulated, fully-coupled process simulation model based on draping- and fluid-submodels.
- A 3D formulation enables the prediction of transverse fluid progression and consideration of key process boundary conditions such as compaction, initial fluid distribution and sealing edges.
- Verification tests and experimental validation on part level demonstrates the suitability of the proposed strategy for a multi-ply stack.

▶ Promising results on part level motivate further research.
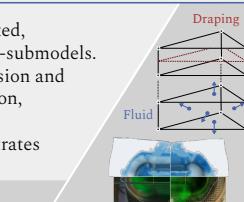
3D process model (strong FSI, Sec. 5.3)
- Terzaghi's effective stress approach is used to implement a strong FSI.
- Numerical studies show the relevance of the contact formulation.
- Superficial fluid and curing is requried for further enhancement.
- The modular concept allows for fast adaption to other textiles.

▶ Coupled process effects (reaction forces, FiFD) become predictable.
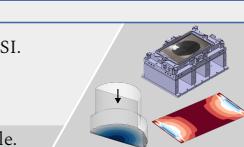
 Woven fabric   UD-NCF

Figure 6.2: Objective 2 | Numerical results and conclusions.

245

The according experimental results and conclusions are summarised in Figure 6.1. Based on the derived requirements, the second objective was the development and validation of a macroscopic process simulation strategy (cf. Figure 6.2). For this purpose, material models as well as numerical solid- and fluid-mechanics approaches were developed to capture the observed physical mechanisms. Moreover, numerical studies were conducted to assess the relevance of individual mechanisms on component scale and give recommendations for WCM modelling.

Outlook. Throughout this thesis, comprehensive knowledge regarding the WCM process and a suitable process simulation model is presented. Although the model shows already good agreement with experiments, further development is still envisaged towards elimination of simplifying assumptions. These assumptions limit the area of application in some cases. In this regard, the following recommendations for improvements motivate further research:

- Viscous draping submodel (Quarter 1 in Figure 2.8)

    - A 3D formulation for FE-draping models (e.g. a solid-shell element) is required to account for compaction during challenging geometries.

    - Implementation of relevant couplings for multi-axial stress states such as shear-tension or shear-compaction is recommended for the woven fabrics, especially for complex geometries. Moreover, in-plane compression states should be addressed with suitable experiments and constitutive equations as illustrated by the application on the demonstrator.

- Fluid submodel (Quarter 2 in Figure 2.8)

    - A suitable approach to model the superficial flow (squeeze flow) is important to further exploit this approach's capabilities, especially concerning complex geometries or unfavourable process parameter settings.

- Fluid-Structure-Interaction (Quarter 3 in Figure 2.8)

  - Comprehensive experiments are needed to further investigate the partly-infiltrated contact behaviour in the case of strong FSI.

  - Implementation of a hydrodynamic contact formulation coupled with the current flow front position is recommended.

- Non-isothermal curing (Quarter 4 in Figure 2.8)

  - Heat conduction needs to be implemented within the user element and coupled with the convective part of the fluid submodel. The thermo-mechanical analysis in ABAQUS/EXPLICIT provides this degree of freedom, which allows for such an implementation.

  - A suitable curing submodel should be implemented in the user element to predict the degree of cure. Combined with a rheology model and linked with the heat transfer equation, this would enable a local prediction of viscosity during moulding. This would allow the optimisation of processing temperatures and timings.

- The macroscopic, single-phase approach neglects air inside the mould and within the microstructure of the reinforcements. This currently prevents a prediction of air traps and micro-saturation. Further work may find approximative approaches or numerical formulation to overcome this limitation.

- The modular modelling strategy allows for a fast adaptation to other reinforcements on the macroscale. As material compaction can be considered, additional reinforcements such as different engineering textiles or recycled nonwovens could be addressed in future simulations.

A Appendix

A.1 Material parameters

Table A.1: Comparison of permeability values in principal material orientation [137, 325].

	Woven fabric			UD-NCF		
φ (-)	K_{11}^0 (mm^2)	K_{22}^0 (mm^2)	K_{33}^0 (mm^2)	K_{11}^0 (mm^2)	K_{22}^0 (mm^2)	K_{33}^0 (mm^2)
0.3	$6.62 \cdot 10^{-4}$	$6.62 \cdot 10^{-4}$	$1.08 \cdot 10^{-5}$	$4.96 \cdot 10^{-4}$	$6.16 \cdot 10^{-5}$	$4.10 \cdot 10^{-6}$
0.45	$1.05 \cdot 10^{-4}$	$1.05 \cdot 10^{-4}$	$9.87 \cdot 10^{-7}$	$8.71 \cdot 10^{-5}$	$1.08 \cdot 10^{-5}$	$6.77 \cdot 10^{-7}$
0.6	$1.71 \cdot 10^{-5}$	$1.71 \cdot 10^{-5}$	$9.03 \cdot 10^{-8}$	$1.53 \cdot 10^{-5}$	$1.90 \cdot 10^{-6}$	$1.12 \cdot 10^{-7}$

A.1.1 Membrane model – Woven fabric

Table A.2: Membrane model | Dry fiber elongation dataset.

$E_{f,i}^{\text{init}}$ (N/mm^2)	$E_{f,i}^{\text{end}}$ (N/mm^2)	$\varepsilon_{f,i}^{\text{init}}$ (-)	$\varepsilon_{f,i}^{\text{end}}$ (-)
844.53	7248.36	$1.37 \cdot 10^{-3}$	$3.21 \cdot 10^{-3}$

k_1^{P1} (-)	k_2^{P1} (-)	k_3^{P1} (-)	
$4.22 \cdot 10^8$	$-1.15 \cdot 10^6$	1.63^3	

Table A.3: Membrane model | Elastic shear dataset.

η_{Fluid}	k_1^{P2}	k_2^{P2}	k_3^{P2}	k_4^{P2}	
dry	0.986	-0.551	0.099	6.400	
20	0.846	-0.390	0.052	4.565	
135	1.189	-0.547	0.072	4.300	
250	1.634	-0.844	0.123	4.427	
	G_1 (N/mm^2)	G_2 (N/mm^2)	$\gamma_{12}^{\text{init}}$ (rad)	γ_{12}^{mid} (rad)	$\gamma_{12}^{\text{lock}}$ (rad)
dry	0.097	0.023	0.005	0.280	0.545
20	0.039	0.007	0.036	0.231	0.571
135	0.050	0.009	0.044	0.230	0.558
250	0.084	0.014	0.053	0.258	0.550

Table A.4: Membrane model | Viscous shear parameters.

	20 mPas	135 mPas	250 mPas
$d_{\text{s}}(\eta)$	0.0120	0.0121	0.0247

A.1.2 Bending models

Table A.5: Bending model | Ply-Ply contact parameter settings.

Setting	μ_{PP} (-)	η_{PP} (Ns/mm)	$\tau_{PP,0}$ (N)
low	0.28	0.0	$2.5 \cdot 10^{-5}$
high	0.28	0.0	$2.5 \cdot 10^{-2}$

Table A.6: Bending model | Material parameter of rheometer model.

Viscosity η_{Fluid} (mPa s)	Parameter E_i^{rheo} E_0 (MPa)	E_∞ (MPa)	m_1 (-)	n_1 (-)
dry	987.079	3381.037	72.917	0.299
20	628.903	1980.352	77.302	0.252
135	645.101	2161.137	76.402	0.248
250	669.672	2278.262	62.484	0.283
Viscosity η_{Fluid} (mPa s)	Parameter η_D η_0 (MPa s)	η_∞ (MPa s)	m_2 (-)	n_2 (-)
dry	45301.348	5.410	248515.843	-0.0001
20	39127.217	172.315	474982.425	-0.007
135	42021.124	207.418	351671.347	-0.016
250	42932.570	210.495	401156.578	-0.025

A.1.3 Contact model

Table A.7: Contact model | Traction parameters ($\cdot 10^{-3}$).

Viscosity (mPas)	1 Layer		2 Layer		3 Layer		4 Layer	
	c_N^T $\left(\dfrac{MPa}{mm}\right)$	d_N^T $\left(\dfrac{MPa}{s\,mm}\right)$	c_N^T $\left(\dfrac{MPa}{mm}\right)$	d_N^T $\left(\dfrac{MPa}{s\,mm}\right)$	c_N^T $\left(\dfrac{MPa}{mm}\right)$	d_N^T $\left(\dfrac{MPa}{s\,mm}\right)$	c_N^T $\left(\dfrac{MPa}{mm}\right)$	d_N^T $\left(\dfrac{MPa}{s\,mm}\right)$
20	0.088	2.029	0.033	1.204	0.029	0.439	0.045	0.345
135	0.681	6.687	0.358	2.931	0.066	2.040	0.077	1.640
250	1.008	9.180	0.640	3.893	0.321	3.750	0.285	3.171

Table A.8: Contact model | Traction results.

Viscosity (mPas)	1 Layer		2 Layer		3 Layer		4 Layer	
	$f_{T,3}^{max}$ (N)	$\xi_{T,3}^{max}$ (mm)	$f_{T,3}^{max}$ (N)	$\xi_{T,3}^{max}$ (mm)	$f_{T,3}^{max}$ (N)	$\xi_{T,3}^{max}$ (mm)	$f_{T,3}^{max}$ (N)	$\xi_{T,3}^{max}$ (mm)
Pull-off rate: $\dot{\xi}_3 = 5.0$ (mm/min)								
20	0.925	0.154	0.479	0.096	0.233	0.082	0.264	0.180
135	4.461	0.337	2.167	0.201	0.850	0.136	0.767	0.161
250	6.402	0.513	3.471	0.265	2.290	0.233	1.980	0.233
Pull-off rate: $\dot{\xi}_3 = 20.0$ (mm/min)								
20	2.751	0.237	1.563	0.136	0.628	0.099	0.574	0.170
135	10.49	0.469	4.804	0.277	2.685	0.208	2.240	0.196
250	14.64	0.648	6.974	0.362	5.687	0.350	4.831	0.317
Pull-off rate: $\dot{\xi}_3 = 50.0$ (mm/min)								
20	6.403	0.402	3.720	0.217	1.418	0.134	1.195	0.150
135	22.51	0.733	10.08	0.427	6.358	0.353	5.184	0.267
250	31.17	0.918	13.98	0.557	12.48	0.582	10.54	0.484

Table A.9: Contact model | Tool-ply parameter | $\theta = 0°$ relative fiber orientation.

Tool-ply (TP)

Viscosity (mPas)	μ_{TP} (-)	η_0 (MPas/mm)	η_∞ (MPas/mm)	m (-)	n (-)
dry	0.189	$1.0 \cdot 10^{-7}$	$1.0 \cdot 10^{-7}$	1	1
20	0.200	$1.2 \cdot 10^{-5}$	0.0	0.01	-5.0
135	0.171	$1.7 \cdot 10^{-5}$	$1.4 \cdot 10^{-5}$	0.01	-5.0
250	0.185	$1.7 \cdot 10^{-5}$	$2.6 \cdot 10^{-5}$	0.01	-1.589

Table A.10: Contact model | Ply-ply parameter | $\theta = 0°$ relative fiber orientation.

Ply-ply (PP)

Viscosity (mPas)	μ_{PP} (-)	η_0 (MPas/mm)	η_∞ (MPas/mm)	m (-)	n (-)
dry	0.290	$2.0 \cdot 10^{-6}$	0.0	1	1
20	0.223	$1 \cdot 10^{-4}$	$2.0 \cdot 10^{-6}$	0.01	-5.0
135	0.203	$9.0 \cdot 10^{-5}$	$2.0 \cdot 10^{-6}$	0.01	-5.0
250	0.185	$8.0 \cdot 10^{-5}$	$2.0 \cdot 10^{-5}$	0.01	-5.0

A.1.4 Compaction model and user element

Table A.11: Datasets for compaction | Woven fabric.

γ_{12} ($^\circ$)	$\varepsilon_{3,0}$ (-)	a_0 (N/mm^2)	ε_{I} (-)	$\varepsilon_{\mathrm{II}}$ (-)	$\varepsilon_{\mathrm{III}}$ (-)	$\varepsilon_{3,s}^{\mathrm{lim}}$ (-)	$\varepsilon_{3,e}^{\mathrm{lim}}$ (-)	E_3^{lim} (N/mm^2)
0	0.137	1.0	46.535	0.810	0.317	0.432	1.139	39.725
25	0.098	1.0	27.735	0.603	0.126	0.406	1.122	39.569
50	0.011	1.0	17.122	0.787	0.296	0.343	1.300	14.837

Table A.12: Datasets for compaction | UD-NCF.

E_0^{SC} (N/mm^2)	$\varepsilon_{3,0}$ (-)	a_0 (N/mm^2)	ε_{I} (-)	$\varepsilon_{\mathrm{II}}$ (-)	$\varepsilon_{\mathrm{III}}$ (-)	η_0^{Mat} (Ns/mm^2)
0.001	0.133	1.0	36.758	0.709	0.214	$5 \cdot 10^{-6}$

Table A.13: Element integration points in isoparametric configuration ς_i.

	IP$_1$	IP$_2$	IP$_3$	IP$_4$	IP$_5$	IP$_6$
ς_1	$\dfrac{1}{6}$	$\dfrac{2}{3}$	$\dfrac{1}{6}$	$\dfrac{1}{6}$	$\dfrac{2}{3}$	$\dfrac{1}{6}$
ς_2	$\dfrac{1}{6}$	$\dfrac{1}{6}$	$\dfrac{2}{3}$	$\dfrac{1}{6}$	$\dfrac{1}{6}$	$\dfrac{2}{3}$
ς_3	$-\dfrac{1}{\sqrt{3}}$	$-\dfrac{1}{\sqrt{3}}$	$-\dfrac{1}{\sqrt{3}}$	$\dfrac{1}{\sqrt{3}}$	$\dfrac{1}{\sqrt{3}}$	$\dfrac{1}{\sqrt{3}}$

A.1.5 Membrane model – UD-NCF

Table A.14: Datasets for UD-NCF membrane model – the parameters and their nomenclature is comprehensibly outlined in [51] .

$E_{1,t}$	$E_{1,c}$	$E_{2,t}$	$E_{2,t}$	γ_{12}^0	γ_{12}^c	$R_{2\mathrm{fmax},0,\gamma_{12}^0}$
(N/mm^2)	(N/mm^2)	(N/mm^2)	(N/mm^2)	(rad)	(rad)	(N/mm^2)
1000	1000	3	0	0.05	0.15	0.1

$R_{2\mathrm{fmax},0,\gamma_{12}^c}$	$H_{2\mathrm{p},\gamma_{12}^0}$	$H_{2\mathrm{p},\gamma_{12}^c}$	$R_{2\mathrm{f},0,\gamma_{12}^0}$	$R_{2\mathrm{f},0,\gamma_{12}^0}$	$k_{2\mathrm{p},\gamma_{12}^0}$	$k_{2\mathrm{p},\gamma_{12}^c}$
(N/mm^2)	(N/mm^2)	(N/mm^2)	(N/mm^2)	(N/mm^2)	($-$)	($-$)
0.05	0.25	0.1	0.005	0.005	30	40

$H_{2\mathrm{p,lock},\gamma_{12}^0}$	$H_{2\mathrm{p,lock},\gamma_{12}^c}$	$\lvert\varepsilon_{2\mathrm{p,lock},\gamma_{12}^0}\rvert$	$\lvert\varepsilon_{2\mathrm{p,lock},\gamma_{12}^c}\rvert$	$\triangle\varepsilon_{2\mathrm{p,lock}}$	$E_\perp$	$\gamma_{12,P_\perp,\mathrm{off}}^0$
(N/mm^2)	(N/mm^2)	($-$)	($-$)	(1/s)	(N/mm^2)	(rad)
0.02	0.012	0.1	0.2	0.4	1	0.2

$\gamma_{12,P_\perp,\mathrm{off}}^c$	$E_{\perp,\mathrm{off}}^0$	$E_{\perp,\mathrm{off}}^c$	$\lvert P_{\perp,\mathrm{off}}^0\rvert$	$\lvert P_{\perp,\mathrm{off}}^c\rvert$	$E_{\perp,\mathrm{lock}}^0$	$E_{\perp,\mathrm{lock}}^c$
(rad)	(N/mm^2)	(N/mm^2)	(N/mm^2)	(N/mm^2)	(N/mm^2)	(N/mm^2)
1	0.08	0.01	0.008	0.004	10	5

$\lvert\varepsilon_{\perp,\mathrm{lock}}^0\rvert$	$\lvert\varepsilon_{\perp,\mathrm{lock}}^0\rvert$	$\triangle\varepsilon_{\perp,\mathrm{lock}}$	G_{12}	$R_{12f,0}$	$H_{12,\mathrm{plast}}$	$a_{\gamma_{12p}}$
($-$)	($-$)	(1/s)	(N/mm^2)	(N/mm^2)	(N/mm^2)	($-$)
0.2	0.5	0.2	3	0.002	0.6	10

$b_{\gamma_{12p}}$	$c_{\gamma_{12p}}$	$d_{\gamma_{12p}}$	$\gamma_{12,\mathrm{p,lock}}$	$H_{12\mathrm{p,lock}}$	$\lvert\gamma_{12\mathrm{p,lock}}\rvert$	$\triangle\gamma_{12\mathrm{p,lock}}$
($-$)	($-$)	($-$)	(rad)	(N/mm^2)	(rad)	(rad/s)
0.028	10	0.018	-2	0.02	1	0.3

| $v_{12,\mathrm{e}}$	$v_{12,\mathrm{p}}$	$v_{21,\mathrm{e}}$	$v_{21,\mathrm{p}}$	$\varepsilon_{2\mathrm{p,QK}}$	η	$\eta_\perp$
($-$)	($-$)	($-$)	($-$)	($-$)	(MPas/mm)	(MPas/mm)
0	0	0	0	0	0.001	0.001

A.2 Complementary plots

A.2.1 Membrane behaviour
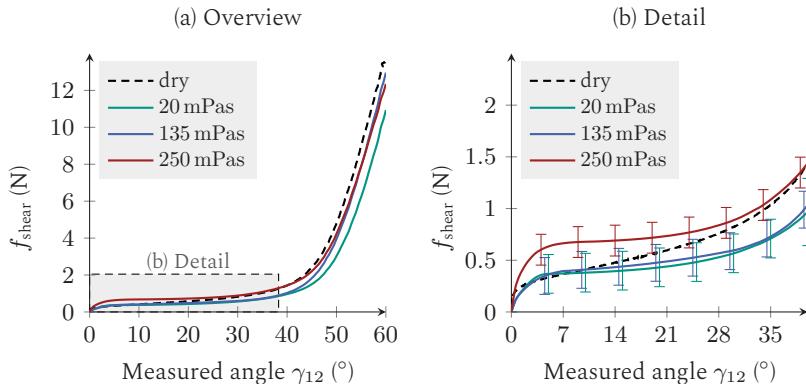
Figure A.1: Additional experimental results for the membrane trials using the IBET | Comparison at constant velocity of $v_{tool} = 350\,\text{mm/min}$.
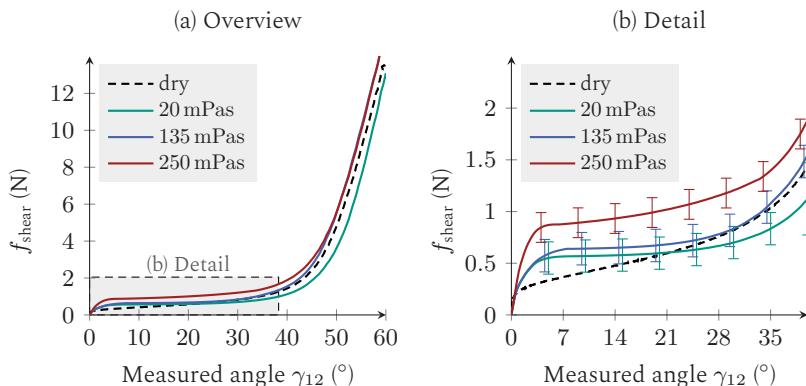

Figure A.2: Additional experimental results for the membrane trials using the IBET | Comparison at constant velocity of $v_{tool} = 700\,\text{mm/min}$.

A.2.2 Bending behaviour
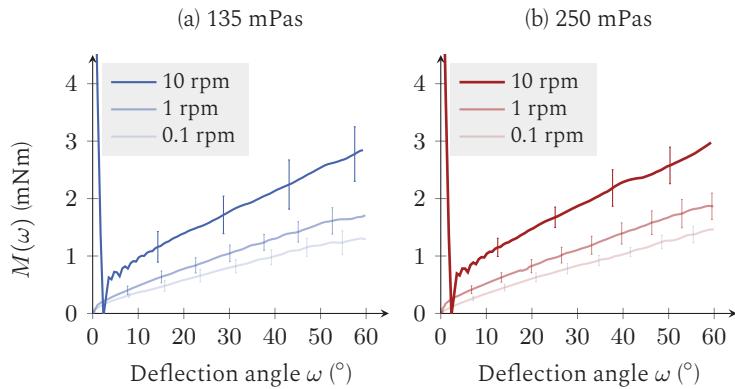
(a) 135 mPas

(b) 250 mPas

Figure A.3: Additional experimental results of RBT | Rate-dependency for specimens with a infiltration viscosity of (a) 135 mPas and (b) 250 mPas [348].
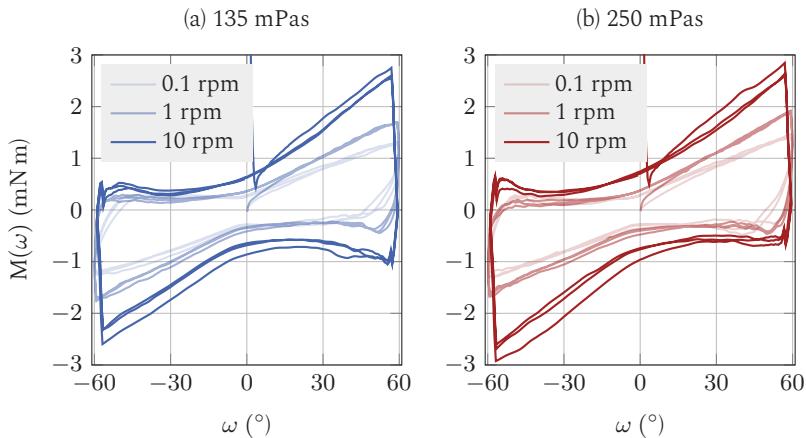
(a) 135 mPas

(b) 250 mPas

Figure A.4: Additional experimental results of RBT | Hysteresis behaviour during 3 load cycles with a infiltration viscosity of (a) 135 mPas and (b) 250 mPas [348].

A.2.3 Complex demonstrator

(a)
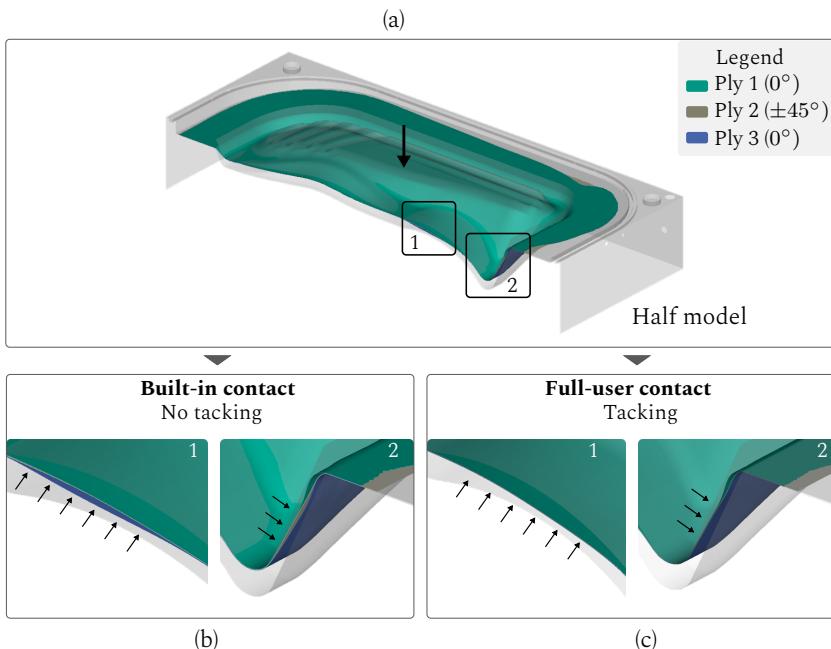
Figure A.5: Demonstrator | Impact of tacking in thickness direction within the contact formulation; (a) Forming at a remaining tool stroke of 30 %; (b) Detailed zones using the built-in contact model without tacking; (c) Detailed zones using the user-contact formulation including tacking. Without tacking, large gapping of 3-8 mm is observed in thickness direction for some region (black arrows). This could impede transverse fluid progression.

(a)   (b)
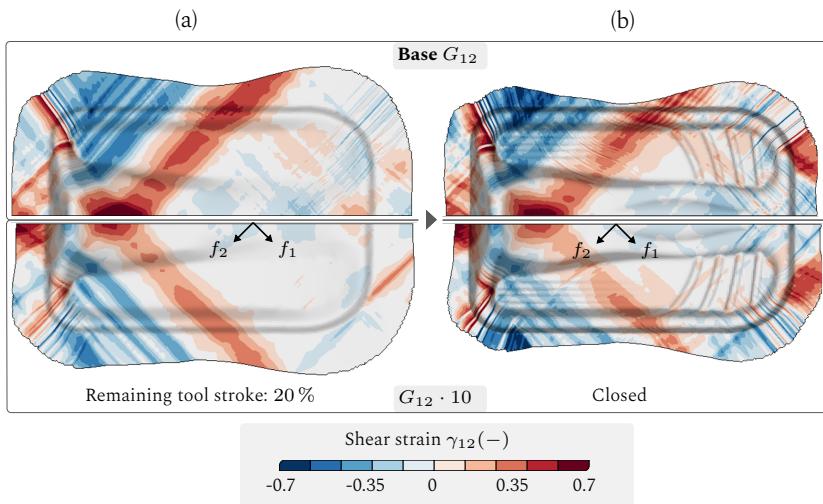
Figure A.6: Demonstrator | Impact of shear modus for (a) a remaining tool stroke of 25 % and (b) the complete closed tool for an initial fibre orientation of $\pm 45\,^\circ$.

(a)   (b)
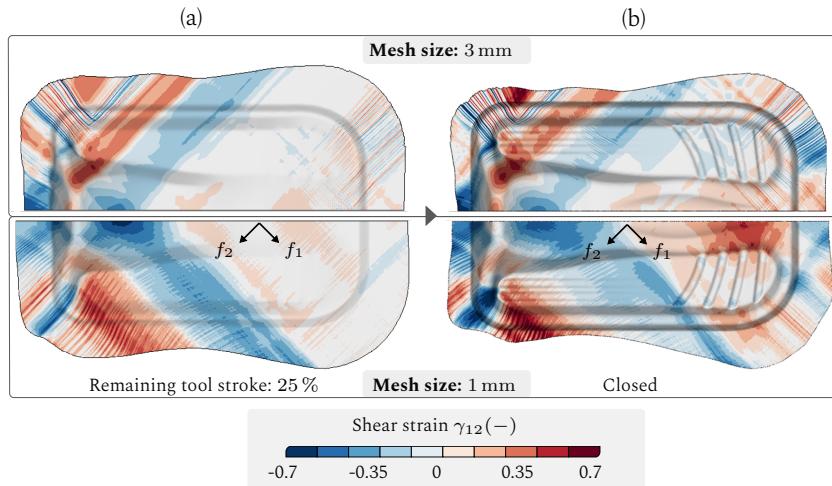
Figure A.7: Demonstrator | Impact of mesh size for (a) a remaining tool stroke of 25 % and (b) the complete closed tool for an initial fibre orientation of $\pm 45\,^\circ$.

259
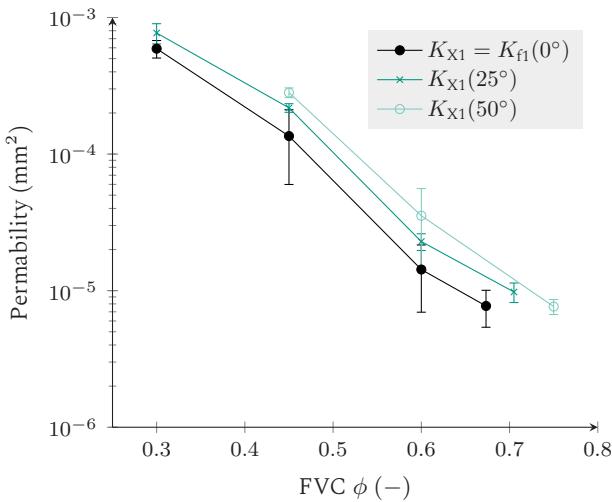
A.2.4 Permeability

Figure A.8: Permeability results | Impact of shearing with standard deviation [137, 343].

A.3 Bibliography

[1] Frank Henning and Elvira Moeller. *Handbuch Leichtbau: Methoden, Werkstoffe, Fertigung*. Hanser Verlag (in german), München, 2011.

[2] Frank Henning, Luise Kärger, Dominik Dörr, Fabian J. Schirmaier, Julian Seuffert, and Alexander Bernath. Fast processing and continuous simulation of automotive structural composite components. *Composites Science and Technology*, 171:261–279, 2019.

[3] Klaus Friedrich and Abdulhakim A. Almajid. Manufacturing aspects of advanced polymer composites for automotive applications. *Applied Composite Materials*, 20(2):107–128, 2013.

[4] L. Zhu, N. Li, and P.R.N. Childs. Light-weighting in aerospace component and system design. *Propulsion and Power Research*, 7(2):103–119, 2018.

[5] P. Beardmore and C. F. Johnson. The potential for composites in structural automotive applications. *Composites Science and Technology*, 26(4):251–281, 1986.

[6] Christian-Simon Ernst, Lutz Eckstein, and Ingo Olschewski. Abschlussbericht: C02 Reduktionspotentiale bei Pkw bis 2020 (in german). *German Federal Ministry of Economics and Technology (BMWi)*, 2012.

[7] Heinz Voggenreiter. Werkstoffinnovationen für nachhaltige Mobilität und Energieversorgung. *VDI-Society: Materials Engineering, VDI-GME-Study (in german), https://www.vdi.de/ueber-uns/presse/publikationen/details/werkstoffinnovationen-fuer-nachhaltige-mobilitaet-und-energieversorgung*, 2014.

[8] Yongxiang Yang, Rob Boom, Brijan Irion, Derk-Jan van Heerden, Pieter Kuiper, and Hans de Wit. Recycling of composite materials. *Chemical Engineering and Processing: Process Intensification*, 51:53–68, 2012.

[9] P. Bockelmann. *Process Control in Compression Molding of Composites*. Doctoral thesis, Fakultät für Maschinenwesen, Technische Universität München, München, 2017.

[10] Uday Vaidya. *Composites for Automotive, Truck and Mass Transit: Materials, design, manufacturing*. DEStech Publications, Lancaster, England, 2010.

[11] J. Bergmann, H. Dörmann, and R. Lange. Interpreting process data of wet pressing process. Part 2: Verification with real values. *Journal of Composite Materials*, 50(17):2409–2419, 2016.

[12] M. F. Ashby. *Materials selection in mechanical design*. Butterworth-Heinemann, Oxford, 2nd edition, 2010.

[13] Luise Kärger, Siegfried Galkin, Clemens Zimmerling, Dominik Dörr, Johannes Linden, André Oeckerath, and Klaus Wolf. Forming optimisation embedded in a CAE chain to assess and enhance the structural performance of composite components. *Composite Structures*, 192:143–152, 2018.

[14] Clemens Zimmerling, Christian Poppe, and Luise Kärger. Virtual product development using simulation methods and AI. *Lightweight Design worldwide*, 12(6):12–19, 2019.

[15] Luise Kärger, Alexander Bernath, Florian Fritz, Siegfried Galkin, Dino Magagnato, André Oeckerath, Alexander Schön, and Frank Henning. Development and validation of a CAE chain for unidirectional fibre reinforced composite components. *Composite Structures*, 132:350–358, 2015.

[16] Helmut Schürmann. *Konstruieren mit Faser-Kunststoff-Verbunden (in german)*. Springer, Berlin, 2005.

[17] Philippe Boisse, editor. *Advances in composites manufacturing and process design*, volume number 56 of *Woodhead publishing series in composites science and engineering*. Woodhead Publishing, Cambridge, UK, 2015.

[18] Alexander Bernath. *Numerical prediction of curing and process-induced distortion of composite structures*. Doctoral thesis, Karlsruhe Institute of Technology (KIT), 2020.

[19] F. Trochu, R. Gauvin, and D.-M. Gao. Numerical analysis of the resin transfer molding process by the finite element method. *Advances in Polymer Technology*, 12(4):329–342, 1993.

[20] C. Demaría, Edu Ruiz, and F. Trochu. In-plane anisotropic permeability characterization of deformed woven fabrics by unidirectional injection. part i: Experimental results. *Polymer Composites*, 28(6):797–811, 2007.

[21] Rudd, Long, Kendall, Mangin. *Liquid moulding technologies: Resin transfer moulding, structural reaction injection moulding and related processing techniques*. Woodhead, Cambridge, 1997.

[22] A. C. Long. *Design and manufacture of textile composites*. Woodhead publishing in textiles. Woodhead in association with the Textile Institute, Cambridge, 2005.

[23] Thomas Gereke, Oliver Döbrich, Matthias Hübner, and Chokri Cherif. Experimental and computational composite textile reinforcement forming: A review. *Composites Part A*, 46:1–10, 2013.

[24] Sebastiaan Haanappel. *Forming of UD fibre reinforced thermoplastics: A critical evaluation of intra-ply shear*. Doctoral thesis, University of Tewente, 2013.

[25] Géraldine Oliveux, Luke O. Dandy, and Gary A. Leeke. Current status of recycling of fibre reinforced polymers: Review of technologies, reuse and resulting properties. *Progress in Materials Science*, 72:61–99, 2015.

[26] Paolo Ermanni, Claudio Di Fratta, and François Trochu. Molding: Liquid Composite Molding (LCM). In *Wiley Encyclopedia of Composites*, pages 1–10. American Cancer Society, 2012.

[27] Alexander Bernath, Luise Kärger, and Frank Henning. Accurate cure modeling for isothermal processing of fast curing epoxy resins. *Polymers*, 8(11):390, 2016.

[28] E. Guzman-Maldonado, N. Hamila, N. Naouar, G. Moulin, and P. Boisse. Simulation of thermoplastic prepreg thermoforming based on a visco-hyperelastic model and a thermal homogenization. *Materials & Design*, 93:431–442, 2016.

[29] Daniel Kugele. *Experimentelle und numerische Untersuchung des Abkühlverhaltens thermoplastischer Gelegelaminate in der Prozesskette*. Doctoral thesis (in german), Karlsruhe Institute of Technology (KIT), 2020.

[30] Dominik Dörr, Ryan Gergely, Stanislav Ivanov, Luise Kärger, Frank Henning, and Andrew Hrymak. On the applicability of thermoforming characterization and simulation approaches to glass mat thermoplastic composites. *Procedia Manufacturing*, 47:118–125, 2020.

[31] Philipp Rosenberg. *Entwicklung einer RTM Prozessvariante zur kavitätsdruckgeregelten Herstellung von Faserverbundstrukturbauteilen*. Doctoral thesis (in german), Karlsruhe Institute of Technology (KIT) in cooperation with Fraunhofer ICT, 2018.

[32] Julian Seuffert, Philipp Rosenberg, Luise Kärger, Frank Henning, Martin Heinz Kothmann, and Günter Deinzer. Experimental and numerical investigations of pressure-controlled resin transfer molding (PC-RTM). *Advanced Manufacturing: Polymer & Composites Science*, 6(3):154–163, 2020.

[33] M. Deléglise, P. Le Grognec, C. Binetruy, P. Krawczak, and B. Claude. Modeling of high speed rtm injection with highly reactive resin with on-line mixing. *Composites Part A*, 42(10):1390–1397, 2011.

[34] François Trochu, Edu Ruiz, Vincent Achim, and Sofiane Soukane. Advanced numerical simulation of liquid composite molding for process analysis and optimization. *Composites Part A*, 37(6):890–902, 2006.

[35] Christian Fais. Lightweight automotive design with HP-RTM. *Reinforced Plastics*, 55(5):29–31, 2011.

[36] Prashant Sharad Shembekar, Muhammad Ali Siddiqui, and Hein Koelman. High Pressure RTM Process Modeling for Automotive Composite Product Development. In *Symposium on International Automotive Technology 2017*. SAE International, 2017.

[37] Pavel Simacek, Suresh G. Advani, and Stanley A. Iobst. Modeling flow in compression resin transfer molding for manufacturing of complex lightweight high-performance automotive parts. *Journal of Composite Materials*, 42(23):2523–2545, 2008.

[38] Justin Merotte, Pavel Simacek, and Suresh G. Advani. Resin flow analysis with fiber preform deformation in through thickness direction during compression resin transfer molding. *Composites Part A*, 41(7):881–887, 2010.

[39] Julian Seuffert, Luise Kärger, and Frank Henning. Simulating Mold Filling in Compression Resin Transfer Molding (CRTM) Using a Three-Dimensional Finite-Volume Formulation. *Journal of Composites Science*, 2(2):23, 2018.

[40] Da Wu, Ragnar Larsson, and Mohammad S. Rouhi. Modeling and experimental validation of the VARTM process for thin-walled preforms. *Polymers*, 11(12), 2019.

[41] P. Ouagne, D. Soulat, J. Moothoo, E. Capelle, and S. Gueret. Complex shape forming of a flax woven fabric; analysis of the tow buckling and misalignment defect. *Composites Part A*, 51:1–10, 2013.

[42] Farbod Nosrat-Nezami, Thomas Gereke, Christian Eberdt, and Chokri Cherif. Characterisation of the shear–tension coupling of carbon-fibre fabric under controlled membrane tensions for precise simulative predictions of industrial preforming processes. *Composites Part A*, 67:131–139, 2014.

[43] S. Chen, L. T. Harper, A. Endruweit, and N. A. Warrior. Formability optimisation of fabric preforms by controlling material draw-in through in-plane constraints. *Composites Part A*, 76:10–19, 2015.

[44] M. Haghi Kashani, A. Rashidi, B. J. Crawford, and A. S. Milani. Analysis of a two-way tension-shear coupling in woven fabrics under combined loading tests: Global to local transformation of non-orthogonal normalized forces and displacements. *Composites Part A*, 88:272–285, 2016.

[45] Farbod Nosrat Nezami, Thomas Gereke, and Chokri Cherif. Active forming manipulation of composite reinforcements for the suppression of forming defects. *Composites Part A*, 99:94–101, 2017.

[46] P. Hallander, M. Akermo, C. Mattei, M. Petersson, and T. Nyman. An experimental study of mechanisms behind wrinkle development during forming of composite laminates. *Composites Part A*, 50:54–64, 2013.

[47] P. Boisse, J. Colmars, N. Hamila, N. Naouar, and Q. Steer. Bending and wrinkling of composite fiber preforms and prepregs. a review and new developments in the draping simulations. *Composites Part B: Engineering*, 141:234–249, 2018.

[48] Dominik Dörr, Fabian J. Schirmaier, Frank Henning, and Luise Kärger. A viscoelastic approach for modeling bending behavior in finite element forming simulation of continuously fiber reinforced composites. *Composites Part A*, 94:113–123, 2017.

[49] Dominik Dörr. *Simulation of the thermoforming process of UD fiber-reinforced thermoplastic tape laminates.* Doctoral thesis, Karlsruhe Institute of Technology (KIT), 2019.

[50] C. Tephany, J. Gillibert, P. Ouagne, G. Hivet, S. Allaoui, and D. Soulat. Development of an experimental bench to reproduce the tow buckling defect appearing during the complex shape forming of structural flax based woven composite reinforcements. *Composites Part A*, 81:22–33, 2016.

[51] Fabian Schirmaier. *Experimentelle Untersuchung und Simulation des Umformverhaltens nähgewirkter unidirektionaler Kohlenstofffasergelege.* Doctoral thesis (in german), Karlsruhe Institute of Technology (KIT), Karlsruhe, 2016.

[52] Christian Krogh, Jens A Glud, and Johnny Jakobsen. Modeling the robotic manipulation of woven carbon fiber prepreg plies onto double curved molds: A path-dependent problem. *Journal of Composite Materials*, 53(15):2149–2164, 2019.

[53] S. Chen, A. Endruweit, L. T. Harper, and N. A. Warrior. Inter-ply stitching optimisation of highly drapeable multi-ply preforms. *Composites Part A*, 71:144–156, 2015.

[54] Helga Krieger, Thomas Gries, and Scott E. Stapleton. Design of tailored non-crimp fabrics based on stitching geometry. *Applied Composite Materials*, 25(1):113–127, 2018.

[55] M. Hübner, O. Diestel, C. Sennewald, T. Gereke, and C. Cherif. Simulation of the drapability of textile semi- finished products with gradient-drapability characteristics by varying the fabric weave. *Fibres and Textiles in Eastern Europe*, 20(5):88–93, 2012.

[56] Tobias Fürst. *Experimentelle Charakterisierung von Designvarianten überlappend gefügter Kohlenstofffaserverbundstrukturen im Kontext der Entwicklung neuartiger Drapiertechnologien.* Doctoral thesis (in german), Karlsruhe Institute of Technology in cooperation with Fraunhofer ICT, Stuttgart, 2017.

[57] Masoud Bodaghi, Pavel Simacek, Suresh G. Advani, and Nuno C. Correia. A model for fibre washout during high injection pressure resin transfer moulding. *Journal of Reinforced Plastics and Composites*, 37(13):865–876, 2018.

[58] Masoud Bodaghi, Pavel Simacek, Nuno Correia, and Suresh G. Advani. Experimental parametric study of flow–induced fiber washout during high–injection–pressure resin transfer molding. *Polymer Composites*, 41(3):1053–1065, 2020.

[59] A. Hautefeuille, S. Comas-Cardona, and C. Binetruy. Consolidation and compression of deformable impregnated fibrous reinforcements: Experimental study and modeling of flow-induced deformations. *Composites Part A*, 131:105768, 2020.

[60] Dong Gi Seong, Shino Kim, Moon Kwang Um, and Young Seok Song. Flow-induced deformation of unidirectional carbon fiber preform during the mold filling stage in liquid composite molding process. *Journal of Composite Materials*, 52(9):1265–1277, 2018.

[61] Véronique Michaud. A review of non-saturated resin flow in liquid composite moulding processes. *Transport in Porous Media*, 115(3):581–601, 2016.

[62] E. Ruiz, V. Achim, S. Soukane, F. Trochu, and J. Breard. Optimization of injection flow rate to minimize micro/macro-voids formation in resin transfer molded composites. *Composites Science and Technology*, 66(3-4):475–486, 2006.

[63] Doh Hoon Lee, Woo Il Lee, and Moon Koo Kang. Analysis and minimization of void formation during resin transfer molding process. *Composites Science and Technology*, 66(16):3281–3289, 2006.

[64] J.S.U. Schell, M. Deleglise, C. Binetruy, P. Krawczak, and P. Ermanni. Numerical prediction and experimental characterisation of meso-scale-voids in liquid composite moulding. *Composites Part A*, 38(12):2460–2470, 2007.

[65] Hua Tan and Krishna M. Pillai. Numerical simulation of reactive flow in liquid composite molding using flux-corrected transport (FCT) based finite element/control volume (FE/CV) method. *International Journal of Heat and Mass Transfer*, 53(9):2256–2271, 2010.

[66] Hua Tan and Krishna M. Pillai. Multiscale modeling of unsaturated flow in dual-scale fiber preforms of liquid composite molding III: Reactive flows. *Composites Part A*, 43(1):29–44, 2012.

[67] A. Hammami, R. Gauvin, F. Trochu, O. Touret, and P. Ferland. Analysis of the edge effect on flow patterns in liquid composites molding. *Applied Composite Materials*, 5(3):161–173, 1998.

[68] Luise Kärger, Siegfried Galkin, Dominik Dörr, and Christian Poppe. Capabilities of macroscopic forming simulation for large-scale forming processes of dry and impregnated textiles. *Procedia Manufacturing*, 47:140–147, 2020.

[69] Thomas Senner. *Methodik zur virtuellen Absicherung der formgebenden Operation des Nasspressprozesses von Gelege-Mehrschichtverbunden*. Doctoral thesis (in german), Friedrich-Alexander-Universität Erlangen-Nürnberg, 2016.

[70] Stefan Josef Stanglmaier. *Empirische Charakterisierung und Modellierung des Imprägnierprozesses lokal verstärkter Kohlenstofffaserhalbzeuge im RTM- und Nasspress-Verfahren für die Großserie*. Doctoral thesis (in german), Karlsruhe Institute of Technology (KIT), 2017.

[71] Kerang Han, Jun Ni, James Toth, L. James Lee, and Joseph P. Greene. Analysis of an injection/compression liquid composite molding process. *Polymer Composites*, 19(4):487–496, 1998.

[72] Jana Bergmann. *Analyse und anlagentechnische Verbesserung des Nasspressverfahrens*. Doctoral thesis (in german), Technische Universität Dresden, Dresden, 2015.

[73] Fabian Albrecht, Christian Poppe, Julian Fial, Philipp Rosenberg, Peter Middendorf, and Frank Henning. Impact of process routing on part infiltration during wet compression moulding (WCM). In *Proceedings of SAMPE Europe, Amsterdam*, 2020.

[74] J. Bergmann, H. Dörmann, and R. Lange. Interpreting process data of wet pressing process. Part 1: Theoretical approach. *Journal of Composite Materials*, 50(17):2399–2407, 2016.

[75] Balaji Muthuvel, Debes Bhattacharyya, and Simon Bickerton. Development of innovative flow visualisation methods to investigate the stages of Wet Compression Moulding (WCM) process. *IOP Conference Series: Materials Science and Engineering*, 912(5):052013, 2020.

[76] Heudorfer, K., Carosella, C., Middendorf, P,. Compression wet moulding as alternative to RTM. In *Proceedings of 25. Stuttgarter Kunststoffkolloquium*, Stuttgart, 22./23. März 2017.

[77] Sooyoung Lee, Chaeyoung Hong, Taeseong Choi, Hye-gyu Kim, Seong-Woo Im, Soo-Chang Kang, Young-Bin Park, and Wooseok Ji. CSAI analysis of non-crimp fabric cross-ply laminate manufactured through wet compression molding process. *Composite Structures*, 255:113056, 2021.

[78] U. Sachs. *Friction and bending in thermoplastic composites forming processes*. Doctoral thesis, University of Twente, Enschede, 2014.

[79] Tobias Dominik Joppich. *Beitrag zum Umformverhalten von PA6/CF Gelegelaminaten im nicht-isothermen Stempelumformprozess*. Doctoral thesis (in german), Karlsruhe Institute of Technology (KIT), 2019.

[80] T. K. Slange, L. L. Warnet, W.J.B. Grouve, and R. Akkerman. Deconsolidation of c/peek blanks: on the role of prepreg, blank manufacturing method and conditioning. *Composites Part A*, 113:189–199, 2018.

[81] P. Harrison, R. Gomes, and N. Curado-Correia. Press forming a 0/90 cross-ply advanced thermoplastic composite using the double-dome benchmark geometry. *Composites Part A*, 54:56–69, 2013.

[82] E. Guzman-Maldonado, N. Hamila, P. Boisse, and J. Bikard. Thermomechanical analysis, modelling and simulation of the forming of pre-impregnated thermoplastics composites. *Composites Part A*, 78:211–222, 2015.

[83] Dominik Dörr, Markus Faisst, Tobias Joppich, Christian Poppe, Frank Henning, and Luise Kärger. Modelling approach for anisotropic inter-ply slippage in finite element forming simulation of thermoplastic UD-tapes. In *AIP Conference Proceedings 1960:020005*. 22nd ESAFORM, 2018.

[84] Kristof Vanclooster. *Forming of multilayered fabric reinforced thermoplastic composites*. Doctoral thesis, KU Leuven, 2009.

[85] S. P. Haanappel, R.H.W. ten Thije, U. Sachs, B. Rietman, and R. Akkerman. Formability analyses of uni-directional and textile reinforced thermoplastics. *Composites Part A*, 56:80–92, 2014.

[86] Martín Machado, Michael Fischlschweiger, and Zoltan Major. A rate-dependent non-orthogonal constitutive model for describing shear behaviour of woven reinforced thermoplastic composites. *Composites Part A*, 80:194–203, 2016.

[87] U. Sachs, R. Akkerman, K. Fetfatsidis, E. Vidal-Sallé, J. Schumacher, G. Ziegmann, S. Allaoui, G. Hivet, B. Maron, K. Vanclooster, and S. V. Lomov. Characterization of the dynamic friction of woven fabrics: Experimental methods and benchmark results. *Composites Part A*, 67:289–298, 2014.

[88] Philippe Bussetta and Nuno Correia. Numerical forming of continuous fibre reinforced composite material: A review. *Composites Part A*, 113:12–31, 2018.

[89] P. Boisse, N. Naouar, and A. Charmetant. Finite element analysis of composite forming at macroscopic and mesoscopic scale. In Philippe Boisse, editor, *Advances in composites manufacturing and process design*, Woodhead publishing series in composites science and engineering, pages 297–315. Woodhead Publishing, Cambridge, UK, 2015.

[90] P. Badel, S. Gauthier, E. Vidal-Sallé, and P. Boisse. Rate constitutive equations for computational analyses of textile composite reinforcement mechanical behaviour during forming. *Composites Part A*, 40(8):997–1007, 2009.

[91] Michel Tourlonias, Marie-Ange Bueno, and Dominique Poquillon. Friction of carbon tows and fine single fibres. *Composites Part A*, 98:116–123, 2017.

[92] Mathias Engelfried, Benedikt Aichele, and Peter Middendorf. Investigation of the friction between dry and wetted carbon filaments. *Procedia Manufacturing*, 47:60–64, 2020.

[93] G. Creech and A. K. Pickett. Meso-modelling of non-crimp fabric composites for coupled drape and failure analysis. *Journal of Materials Science*, 41(20):6725–6736, 2006.

[94] M. Duhovic and D. Bhattacharyya. Simulating the deformation mechanisms of knitted fabric composites. *Composites Part A*, 37(11):1897–1915, 2006.

[95] Long Li, Yan Zhao, Ha-gia-nam Vuong, Yuan Chen, Jin Yang, and Yuexin Duan. In-plane shear investigation of biaxial carbon non-crimp fabrics with experimental tests and finite element modeling. *Materials & Design*, 63:757–765, 2014.

[96] S. Lomov, D. Ivanov, I. Verpoest, M. Zako, T. Kurashiki, H. Nakai, and S. Hirosawa. Meso-FE modelling of textile composites: Road map, data flow and algorithms. *Composites Science and Technology*, 67(9):1870–1891, 2007.

[97] F. N. Cogswell. The experience of thermoplastic structural composites during processing. *Composites Manufacturing*, 2(3-4):208–216, 1991.

[98] P. Boisse, N. Hamila, and A. Madeo. The difficulties in modeling the mechanical behavior of textile composite reinforcements with standard continuum mechanics of cauchy. some possible remedies. *International Journal of Solids and Structures*, 154:55–65, 2016.

[99] Christian Poppe, Dominik Dörr, Frank Henning, and Luise Kärger. Experimental and numerical investigation of the shear behaviour of infiltrated woven fabrics. *Composites Part A*, 114:327–337, 2018.

[100] J. Cao, R. Akkerman, P. Boisse, J. Chen, H. S. Cheng, E. F. de Graaf, J. L. Gorczyca, P. Harrison, G. Hivet, J. Launay, W. Lee, L. Liu, S. V. Lomov, A. Long, E. de Luycker, F. Morestin, J. Padvoiskis, X. Q. Peng, J. Sherwood, Tz. Stoilova, X. M. Tao, I. Verpoest, A. Willems, J. Wiggers, T. X. Yu, and B. Zhu. Characterization of mechanical behavior of woven fabrics: Experimental methods and benchmark results. *Composites Part A*, 39(6):1037–1053, 2008.

[101] B. Zhu, T. YU, and X. TAO. An experimental study of in-plane large shear deformation of woven fabric composite. *Composites Science and Technology*, 67(2):252–261, 2007.

[102] P. Boisse, N. Hamila, E. Vidal-Sallé, and F. Dumont. Simulation of wrinkling during textile composite reinforcement forming. influence of tensile, in-plane shear and bending stiffnesses. *Composites Science and Technology*, 71(5):683–692, 2011.

269

[103] A. Willems. *Forming simulations of textile reinforced composite shell structures*. Doctoral thesis, Katholieke Universiteit Leuven, Herverlee, Belgium, 2008.

[104] A. G. Colman, B. N. Bridgens, P. D. Gosling, G.-T. Jou, and X.-Y. Hsu. Shear behaviour of architectural fabrics subjected to biaxial tensile loads. *Composites Part A*, 66:163–174, 2014.

[105] F. J. Schirmaier, K. A. Weidenmann, L. Kärger, and F. Henning. Characterisation of the draping behaviour of unidirectional non-crimp fabrics (UD-NCF). *Composites Part A*, 80:28–38, 2016.

[106] P. Harrison, M. J. Clifford, A. C. Long, and C. D. Rudd. A constituent-based predictive approach to modelling the rheology of viscous textile composites. *Composites Part A*, 35(7-8):915–931, 2004.

[107] Gilbert Lebrun, Martin N. Bureau, and Johanne Denault. Evaluation of bias-extension and picture-frame test methods for the measurement of intraply shear properties of pp/glass commingled fabrics. *Composite Structures*, 61(4):341–352, 2003.

[108] P. Harrison, M. J. Clifford, and A. C. Long. Shear characterisation of viscous woven textile composites: A comparison between picture frame and bias extension experiments. *Composites Science and Technology*, 64(10-11):1453–1465, 2004.

[109] Sylvain Bel, Philippe Boisse, and François Dumont. Analyses of the deformation mechanisms of non-crimp fabric composite reinforcements during preforming. *Applied Composite Materials*, 19(3-4):513–528, 2012.

[110] Philip Harrison. Normalisation of biaxial bias extension test results considering shear tension coupling. *Composites Part A*, 43(9):1546–1554, 2012.

[111] P. Harrison, F. Abdiwi, Z. Guo, P. Potluri, and W. R. Yu. Characterising the shear–tension coupling and wrinkling behaviour of woven engineering fabrics. *Composites Part A*, 43(6):903–914, 2012.

[112] Yuan Yao, Xiongqi Peng, and Youkun Gong. Influence of tension–shear coupling on draping of plain weave fabrics. *Journal of Materials Science*, 54(8):6310–6322, 2019.

[113] C. Galliot and R. H. Luchsinger. The shear ramp: A new test method for the investigation of coated fabric shear behaviour – part i: Theory. *Composites Part A*, 41(12):1743–1749, 2010.

[114] Dominik Dörr, Frank Henning, and Luise Kärger. Nonlinear hyperviscoelastic modelling of intra-ply deformation behaviour in finite element forming simulation of continuously fibre-reinforced thermoplastics. *Composites Part A*, 109:585–596, 2018.

[115] K. Buet-Gautier and P. Boisse. Experimental analysis and modeling of biaxial mechanical behavior of woven composite reinforcements. *Experimental Mechanics*, 41(3):260–269, 2001.

[116] Ozan Erol, Brian Powers, and Michael Keefe. Development of a non-orthogonal macroscale material model for advanced woven fabrics based on mesoscale structure. *Composites Part B: Engineering*, 110:497–510, 2017.

[117] P. Boisse, A. Gasser, and G. Hivet. Analyses of fabric tensile behaviour: Determination of the biaxial tension–strain surfaces and their use in forming simulations. *Composites Part A*, 32:1395–1414, 2001.

[118] S. V. Lomov, M. Barburski, Tz. Stoilova, I. Verpoest, R. Akkerman, R. Loendersloot, and R.H.W.ten Thije. Carbon composites based on multiaxial multiply stitched preforms. part 3: Biaxial tension, picture frame and compression tests of the preforms. *Composites Part A*, 36(9):1188–1206, 2005.

[119] Christian Poppe, Tobias Rosenkranz, Dominik Dörr, and Luise Kärger. Comparative experimental and numerical analysis of bending behaviour of dry and low viscous infiltrated woven fabrics. *Composites Part A*, 124:105466, 2019.

[120] F. T. Peirce. 26—the "handle" of cloth as a measurable quantity. *Journal of the Textile Institute Transactions*, 21(9):T377–T416, 1930.

[121] Testing of plastics films and textile fabrics (excluding nonwovens), coated or not coated fabrics - Determination of stiffness in bending - Method according to Cantilever. Beuth publishing DIN 53362:2003-10, 59.080.40; 83.140.10, 2003-10.

[122] E. de Bilbao, D. Soulat, G. Hivet, and A. Gasser. Experimental study of bending behaviour of reinforcements. *Experimental Mechanics*, 50(3):333–351, 2010.

[123] Biao Liang, Nahiene Hamila, Mickaël Peillon, and Philippe Boisse. Analysis of thermoplastic prepreg bending stiffness during manufacturing and of its influence on wrinkling simulations. *Composites Part A*, 67:111–122, 2014.

[124] B. Liang, P. Chaudet, and P. Boisse. Curvature determination in the bending test of continuous fibre reinforcements. *Strain*, 53(1):12213, 2016.

[125] Nicolas Lammens, Mathias Kersemans, Geert Luyckx, Wim van Paepegem, and Joris Degrieck. Improved accuracy in the determination of flexural rigidity of textile fabrics by the peirce cantilever test (astm d1388). *Textile Research Journal*, 84(12):1307–1314, 2014.

[126] Lisa M. Dangora, Cynthia J. Mitchell, and James A. Sherwood. Predictive model for the detection of out-of-plane defects formed during textile-composite manufacture. *Composites Part A*, 78:102–112, 2015.

271

[127] E. de Bilbao, D. Soulat, G. Hivet, J. Launay, and A. Gasser. Bending test of composite reinforcements. *International Journal of Material Forming*, 1(S1):835–838, 2008.

[128] Bernd Thoma. *Methodische Umsetzung und Bewertung eines neuartigen Prozesses zur lokalen und automatisierten Fixierung von textilen Preformlingen*. Doctoral thesis at Karlsruhe University of Technology (in german), Fraunhofer Verlag, Stuttgart, 2015.

[129] U. Sachs and R. Akkerman. Viscoelastic bending model for continuous fiber-reinforced thermoplastic composites in melt. *Composites Part A*, 100:333–341, 2017.

[130] Sueo Kawabata. The standardization and analysis of hand evaluation: 2nd ed. *Textile Machinery Society of Japan - Osaka*, 1980.

[131] Timothy John Lahey. *Modelling Hysteresis in the Bending of Fabrics*. Doctoral thesis, University of Waterloo, Waterloo, Ontario, Canada, 2002.

[132] S.V Lomov, I. Verpoest, M. Barburski, and J. Laperre. Carbon composites based on multiaxial multiply stitched preforms. part 2. kes-f characterisation of the deformability of the preforms at low loads. *Composites Part A*, 34(4):359–370, 2003.

[133] Philip R. Dahl. Solid friction damping of mechanical vibrations. *AIAA Journal*, 14(12):1675–1682, 1976.

[134] P. Grosberg. The Mechanical Properties of Woven Fabrics Part II: The Bending of Woven Fabrics. *Textile Research Journal*, 36(3):205–211, 1966.

[135] A. Margossian, S. Bel, and R. Hinterhoelzl. Bending characterisation of a molten unidirectional carbon fibre reinforced thermoplastic composite using a dynamic mechanical analysis system. *Composites Part A*, 77:154–163, 2016.

[136] Fengxin Sun, Chaoyu Chen, Sai Liu, Huanhuan Jin, Linge He, Du Zhaoqun, and Weidong Yu. Simulative analysis of the bending property of woven fabric by the comprehensive handle evaluation system for fabrics and yarns. *Textile Research Journal*, 87(16):1977–1990, 2016.

[137] Christian T. Poppe, Constantin Krauß, Fabian Albrecht, and Luise Kärger. A 3D process simulation model for wet compression moulding. *Composites Part A*, 145:106379, 2021.

[138] T. G. Gutowski, Z. Cai, S. Bauer, D. Boucher, J. Kingery, and S. Wineman. Consolidation experiments for laminate composites. *Journal of Composite Materials*, 21(7):650–669, 1987.

[139] R. A. Saunders, C. Lekakou, and M. G. Bader. Compression in the processing of poly-mer composites 2. modelling of the viscoelastic compression of resin-impregnated fibre networks. *Composites Science and Technology*, 59(10):1483–1494, 1999.

[140] Franois Robitaille and Raymond Gauvin. Compaction of textile reinforcements for composites manufacturing. II: Compaction and relaxation of dry and H2O-saturated woven reinforcements. *Polymer Composites*, 19(5):543–557, 1998.

[141] Moon Koo Kang and Woo Il Lee. Analysis of resin transfer/compression molding process. *Polymer Composites*, 20(2):293–304, 1999.

[142] Baoxing Chen, Eric J. Lang, and Tsu-Wei Chou. Experimental and theoretical studies of fabric compaction behavior in resin transfer molding. *Materials Science and Engineering: A*, 317(1):188–196, 2001.

[143] P. A. Kelly, R. Umer, and S. Bickerton. Viscoelastic response of dry and wet fibrous materials during infusion processes. *Composites Part A*, 37(6):868–873, 2006.

[144] P. A. Kelly and S. Bickerton. A comprehensive filling and tooling force analysis for rigid mould lcm processes. *Composites Part A*, 40(11):1685–1697, 2009.

[145] Sang-Jae Yoon, Kazuo Arakawa, Seung-Wook Han, Dingding Chen, and Nak-Sam Choi. Effect of compaction treatment on laminated cfrp composites fabricated by vacuum-assisted resin-transfer molding. *Polymer Composites*, 38(2):217–226, 2017.

[146] S. Bickerton and M. Z. Abdullah. Modeling and evaluation of the filling stage of injec-tion/compression moulding. *Composites Science and Technology*, 63(10):1359–1375, 2003.

[147] A. Hautefeuille, S. Comas-Cardona, and C. Binetruy. Mechanical signature and full-field measurement of flow-induced large in-plane deformation of fibrous reinforce-ments in composite processing. *Composites Part A*, 118:213–222, 2019.

[148] Hu Xiong, Nahiène Hamila, and Philippe Boisse. Consolidation modeling during thermoforming of thermoplastic composite prepregs. *Materials*, 12(18):PMC6766047, 2019.

[149] S. Bickerton, M. J. Buntain, and A. A. Somashekar. The viscoelastic compression be-havior of liquid composite molding preforms. *Composites Part A*, 34(5):431–444, 2003.

[150] Jonathan P.-H. Belnoue, Mario A. Valverde, Maria Onoufriou, Xiaochuan Sun, Dmitry S. Ivanov, and Stephen R. Hallett. On the physical relevance of power law-based equations to describe the compaction behaviour of resin infused fibrous materials. *International Journal of Mechanical Sciences*, 199:106425, 2021.

[151] P. Potluri and T. V. Sagar. Compaction modelling of textile preforms for composite structures. *Composite Structures*, 86(1):177–185, 2008.

[152] Mario Danzi, Christoph Schneeberger, and Paolo Ermanni. A model for the time-dependent compaction response of woven fiber textiles. *Composites Part A*, 105:180–188, 2018.

[153] Dmitry S. Ivanov and Stepan V. Lomov. Compaction behaviour of dense sheared woven preforms: Experimental observations and analytical predictions. *Composites Part A*, 64:167–176, 2014.

[154] S. Allaoui, G. Hivet, A. Wendling, P. Ouagne, and D. Soulat. Influence of the dry woven fabrics meso-structure on fabric/fabric contact behavior. *Journal of Composite Materials*, 46(6):627–639, 2012.

[155] S. Allaoui, C. Cellard, and G. Hivet. Effect of inter-ply sliding on the quality of multilayer interlock dry fabric preforms. *Composites Part A*, 68:336–345, 2015.

[156] J. Hüttl, F. Albrecht, C. Poppe, F. Lorenz, B. Thoma, L. Kärger, P. Middendorf and F. Henning. Investigations on friction behaviour and forming simulation of plain woven fabrics for wet compression moulding. *Proceedings of SAMPE Europa, Stuttgart*, 2017.

[157] B. Cornelissen, B. Rietman, and R. Akkerman. Frictional behaviour of high performance fibrous tows: Friction experiments. *Composites Part A*, 44:95–104, 2013.

[158] B. Cornelissen, U. Sachs, B. Rietman, and R. Akkerman. Dry friction characterisation of carbon fibre tow and satin weave fabric for composite applications. *Composites Part A*, 56:127–135, 2014.

[159] Konstantine A. Fetfatsidis, James A. Sherwood, Julie Chen, and David Jauffres. Characterization of the fabric/tool and fabric/fabric friction during the thermostamping process. *International Journal of Material Forming*, 2(1):165, 2009.

[160] Farbod Nosrat Nezami, Thomas Gereke, and Chokri Cherif. Analyses of interaction mechanisms during forming of multilayer carbon woven fabrics for composite applications. *Composites Part A*, 84:406–416, 2016.

[161] Jennifer L. Gorczyca-Cole, James A. Sherwood, and Julie Chen. A friction model for thermostamping commingled glass–polypropylene woven fabrics. *Composites Part A*, 38(2):393–406, 2007.

[162] R. H. W. ten Thije, R. Akkerman, L. van der Meer, and M. P. Ubbink. Tool-ply friction in thermoplastic composite forming. *International Journal of Material Forming*, 1(1):953–956, 2008.

[163] Adrian M. Murtagh, John J. Lennon, and Patrick J. Mallon. Surface friction effects related to pressforming of continuous fibre thermoplastic composites. *Composites Manufacturing*, 6(3-4):169–175, 1995.

[164] Dennis Budelmann, Carsten Schmidt, and Dieter Meiners. Prepreg tack: A review of mechanisms, measurement, and manufacturing implication. *Polymer Composites*, 41(9):3440–3458, 2020.

[165] N. Patel and L. James Lee. Effects of fiber mat architecture on void formation and removal in liquid composite molding. *Polymer Composites*, 16(5):386–399, 1995.

[166] Edu Ruiz and F. Trochu. Multi-criteria thermal optimization in liquid composite molding to reduce processing stresses and cycle time. *Composites Part A*, 37(6):913–924, 2006.

[167] H. Darcy. Les fontaines publiques de la ville de dijon: Exposition et application des principes a suivre et des formulesa employer dans les questions de distribution d'eau. *Dalmant Paris (in french)*, 1856.

[168] R. Arbter, J. M. Beraud, C. Binetruy, L. Bizet, J. Bréard, S. Comas-Cardona, C. Demaria, A. Endruweit, P. Ermanni, F. Gommer, S. Hasanovic, P. Henrat, F. Klunker, B. Laine, S. Lavanchy, S. V. Lomov, A. Long, V. Michaud, G. Morren, E. Ruiz, H. Sol, F. Trochu, B. Verleye, M. Wietgrefe, W. Wu, and G. Ziegmann. Experimental determination of the permeability of textiles: A benchmark exercise. *Composites Part A*, 42(9):1157–1168, 2011.

[169] N. Vernet, E. Ruiz, S. Advani, J. B. Alms, M. Aubert, M. Barburski, B. Barari, J. M. Beraud, D. C. Berg, N. Correia, M. Danzi, T. Delavière, M. Dickert, C. Di Fratta, A. Endruweit, P. Ermanni, G. Francucci, J. A. Garcia, A. George, C. Hahn, F. Klunker, S. V. Lomov, A. Long, B. Louis, J. Maldonado, R. Meier, V. Michaud, H. Perrin, K. Pillai, E. Rodriguez, F. Trochu, S. Verheyden, M. Wietgrefe, W. Xiong, S. Zaremba, and G. Ziegmann. Experimental determination of the permeability of engineering textiles: Benchmark II. *Composites Part A*, 61:172–184, 2014.

[170] Gastón Francucci, Exequiel S. Rodríguez, and Analía Vázquez. Study of saturated and unsaturated permeability in natural fiber fabrics. *Composites Part A*, 41(1):16–21, 2010.

[171] Chung Hae Park and Patricia Krawczak. Unsaturated and saturated permeabilities of fiber reinforcement: Critics and suggestions. *Frontiers in Materials*, 2:38–44, 2015.

[172] T. James Wang, C. H. Wu, and L. James Lee. In-plane permeability measurement and analysis in liquid composite molding. *Polymer Composites*, 15(4):278–288, 1994.

[173] C. Demaría, Edu Ruiz, and F. Trochu. In-plane anisotropic permeability characterization of deformed woven fabrics by unidirectional injection. part ii: Prediction model and numerical simulations. *Polymer Composites*, 28(6):812–827, 2007.

275

[174] Pierre-Jacques Liotier, Quentin Govignon, Elinor Swery, Sylvain Drapier, and Simon Bickerton. Characterisation of woven flax fibres reinforcements: Effect of the shear on the in-plane permeability. *Journal of Composite Materials*, 49(27):3415–3430, 2015.

[175] Robert S. Pierce, Brian G. Falzon, and Mark C. Thompson. Permeability characterization of sheared carbon fiber textile preform. *Polymer Composites*, 39(7):2287–2298, 2016.

[176] Robert S. Pierce, Brian G. Falzon, and Mark C. Thompson. A multi-physics process model for simulating the manufacture of resin-infused composite aerostructures. *Composites Science and Technology*, 149:269–279, 2017.

[177] Kris Hoes, Daniela Dinescu, Hugo Sol, Marleen Vanheule, Richard S. Parnas, Yiwen Luo, and Ignaas Verpoest. New set-up for measurement of permeability properties of fibrous reinforcements for RTM. *Composites Part A*, 33(7):959–969, 2002.

[178] Dino Magagnato and Frank Henning. Process-oriented determination of preform permeability and matrix viscosity during mold filling in resin transfer molding. *Materials Science Forum*, 825-826:822–829, 2015.

[179] Chyi-Lang Lai and Wen-Bin Young. Model resin permeation of fiber reinforcements after shear deformation. *Polymer Composites*, 18(5):642–648, 1997.

[180] B. R. Gebart. Permeability of unidirectional reinforcements for RTM. *Journal of Composite Materials*, 26(8):1100–1133, 1992.

[181] David Becker, Harald Grössing, Spiridon Konstantopoulos, Ewald Fauster, Peter Mitschang, and Ralf Schledjewski. An evaluation of the reproducibility of ultrasonic sensor-based out-of-plane permeability measurements: A benchmarking study. *Advanced Manufacturing: Polymer & Composites Science*, 2(1):34–45, 2016.

[182] Jeferson Avila Souza, Marcelo José Anghinoni Nava, Luiz Alberto Oliveira Rocha, and Sandro Campos Amico. Two-dimensional control volume modeling of the resin infiltration of a porous medium with a heterogeneous permeability tensor. *Materials Research*, 11(3):261–268, 2008.

[183] J. R. Weitzenböck, R. A. Shenoi, and P. A. Wilson. Measurement of three-dimensional permeability. *Composites Part A*, 29(1-2):159–169, 1998.

[184] Pierre Ouagne, Tariq Ouahbi, Chung Hae Park, Joël Bréard, and Abdelghani Saouab. Continuous measurement of fiber reinforcement permeability in the thickness direction: Experimental technique and validation. *Composites Part B: Engineering*, 45(1):609–618, 2013.

[185] Robert Graupner and K. Drechsler. Quantitative transversal permeability testing - challenges and enhancements. In *Proceedings of 14th International Conference on Flow Processes in Composite Materials (FPCM 14)*, Lulea, Sweden, 2018.

[186] Julia Studer, Clemens Dransfeld, Jon Jauregui Cano, Andre Keller, Marianne Wink, Kunal Masania, and Bodo Fiedler. Effect of fabric architecture, compaction and permeability on through thickness thermoplastic melt impregnation. *Composites Part A*, 122:45–53, 2019.

[187] Krishna M. Pillai. Governing equations for unsaturated flow through woven fiber mats. part 1. isothermal flows. *Composites Part A*, 33(7):1007–1019, 2002.

[188] A. Endruweit and P. Ermanni. The in-plane permeability of sheared textiles. experimental observations and a predictive conversion model. *Composites Part A*, 35(4):439–451, 2004.

[189] Pavel Simacek and Suresh G. Advani. Permeability model for a woven fabric. *Polymer Composites*, 17(6):887–899, 1996.

[190] Xuesen Zeng, Andreas Endruweit, Louise P. Brown, and Andrew C. Long. Numerical prediction of in-plane permeability for multilayer woven fabrics with manufacture-induced deformation. *Composites Part A*, 77:266–274, 2015.

[191] M. Bodaghi, A. Vanaerschot, S. V. Lomov, and N. C. Correia. On the variability of mesoscale permeability of a 2/2 twill carbon fabric induced by variability of the internal geometry. *Composites Part A*, 101:394–407, 2017.

[192] A. Endruweit, X. Zeng, M. Matveev, and A. C. Long. Effect of yarn cross-sectional shape on resin flow through inter-yarn gaps in textile reinforcements. *Composites Part A*, 104:139–150, 2018.

[193] Hai Long Liu and Wook Ryol Hwang. Permeability prediction of fibrous porous media with complex 3D architectures. *Composites Part A*, 43(11):2030–2038, 2012.

[194] F. Zhang, S. Comas-Cardona, and C. Binetruy. Statistical modeling of in-plane permeability of non-woven random fibrous reinforcement. *Composites Science and Technology*, 72(12):1368–1379, 2012.

[195] Zhaofei Xiao, Xiaoling Liu, Lee T. Harper, Andreas Endruweit, and Nicholas A. Warrior. Modelling the permeability of random discontinuous carbon fibre preforms. *Journal of Composite Materials*, 54(20):2739–2751, 2020.

[196] Francisco J. Valdes-Parada, J. Alberto Ochoa-Tapia, and Jose Alvarez-Ramirez. Validity of the permeability carman–kozeny equation: A volume averaging approach. *Physica A: Statistical Mechanics and its Applications*, 388(6):789–798, 2009.

[197] A. Yousefi, P. G. Lafleur, and R. Gauvin. Kinetic studies of thermoset cure reactions: A review. *Polymer Composites*, 18(2):157–168, 1997.

[198] S. L. Simon and J. K. Gillham. Cure kinetics of a thermosetting liquid dicyanate ester monomer/high-tg polycyanurate material. *Journal of Applied Polymer Science*, 47(3):461–485, 1993.

[199] Peter J. Halley and Michael E. Mackay. Chemorheology of thermosets—an overview. *Polymer Engineering & Science*, 36(5):593–609, 1996.

[200] L. F. Yang, K. D. Yao, and W. Koh. Kinetics analysis of the curing reaction of fast cure epoxy prepregs. *Journal of Applied Polymer Science*, 73(8):1501–1508, 1999.

[201] J. Lange, N. Altmann, C.T Kelly, and P.J Halley. Understanding vitrification during cure of epoxy resins using dynamic scanning calorimetry and rheological techniques. *Polymer*, 41(15):5949–5955, 2000.

[202] Daniel J. O'Brien, Patrick T. Mather, and Scott R. White. Viscoelastic properties of an epoxy resin during cure. *Journal of Composite Materials*, 35(10):883–904, 2001.

[203] V. M. González-Romero and N. Casillas. Isothermal and temperature programmed kinetic studies of thermosets. *Polymer Engineering & Science*, 29(5):295–301, 1989.

[204] Alexander Bernath, Maximilian Grulich, Luise Kärger, and Frank Henning. Enhanced viscosity characterization for fast curing epoxy resins at process relevant temperatures. In *Proceedings of 14th International Conference on Flow Processes in Composite Materials (FPCM 14)*, Lulea, Sweden, 2018.

[205] Markus Muth, Jan Schwennen, Alexander Bernath, Julian Seuffert, Kay André Weidenmann, Jürgen Fleischer, and Frank Henning. Numerical and experimental investigation of manufacturing and performance of metal inserts embedded in CFRP. *Production Engineering*, 12(2):141–152, 2018.

[206] Teik-Cheng Lim and S. Ramakrishna. Modelling of composite sheet forming: A review. *Composites Part A*, 33(4):515–537, 2002.

[207] M. Aono, D. E. Breen, and M. J. Wozny. Fitting a woven-cloth model to a curved surface: mapping algorithms. *Computer-Aided Design*, 26(4):278–292, 1994.

[208] F. Trochu, A. Hammami, and Y. Benoit. Prediction of fibre orientation and net shape definition of complex composite parts. *Composites Part A*, 27(4):319–328, 1996.

[209] C. Mack and H. M. Taylor. The fitting of woven cloth to surfaces. *Journal of the Textile Institute Transactions*, 47(9):477–488, 1956.

[210] Francesann L. Heisey and K. D. Haller. Fitting woven fabric to surfaces in three dimensions. *Journal of the Textile Institute*, 79(2):250–263, 1988.

[211] F. van der Weeën. Algorithms for draping fabrics on doubly-curved surfaces. *International Journal for Numerical Methods in Engineering*, 31(7):1415–1426, 1991.

[212] Abdelhakim Cherouat, Houman Borouchaki, and Jean-Louis Billoët. Geometrical and mechanical draping of composite fabric. *Revue Européenne des Éléments Finis*, 14(6-7):693–707, 2012.

[213] Dennis Zink, Maximilian Huber, and Peter Middendorf. Formpatch - forming of complex composite structures using patching technologies. *Procedia Manufacturing*, 47:100–106, 2020.

[214] M. Aono, P. Denti, D. E. Breen, and M. J. Wozny. Fitting a woven cloth model to a curved surface: dart insertion. *IEEE Computer Graphics and Applications*, 16(5):60–70, 1996.

[215] S. G. Hancock and K. D. Potter. Inverse drape modelling—an investigation of the set of shapes that can be formed from continuous aligned woven fibre reinforcements. *Composites Part A*, 36(7):947–953, 2005.

[216] S. G. Hancock and K. D. Potter. The use of kinematic drape modelling to inform the hand lay-up of complex composite components using woven reinforcements. *Composites Part A*, 37(3):413–422, 2006.

[217] Philippe Boisse, Yamina Aimène, Abdelwaheb Dogui, Samia Dridi, Sébastien Gatouillat, Nahiene Hamila, Muhammad Aurangzeb Khan, Tarek Mabrouki, Fabrice Morestin, and Emmanuelle Vidal-Sallé. Hypoelastic, hyperelastic, discrete and semi-discrete approaches for textile composite reinforcement forming. *International Journal of Material Forming*, 3(2):1229–1240, 2010.

[218] Elena Syerko, Sébastien Comas-Cardona, and Christophe Binetruy. Models for shear properties/behavior of dry fibrous materials at various scales: a review. *International Journal of Material Forming*, 8(1):1–23, 2015.

[219] Pier Paolo Valentini, Michele Falcone, Emanule Marotta, Ettore Pennestrì, and Pietro Salvini. Theoretical and experimental characterization of a FEM element assembly for the simulation of very compliant knitted mesh. *International Journal for Numerical Methods in Engineering*, 107(5):419–429, 2016.

[220] Damien Durville. Simulation of the mechanical behaviour of woven fabrics at the scale of fibers. *International Journal of Material Forming*, 3(S2):1241–1251, 2010.

[221] K. Y. Sze and X. H. Liu. A new skeletal model for fabric drapes. *International Journal of Mechanics and Materials in Design*, 2(3-4):225–243, 2005.

[222] B. Ben Boubaker, B. Haussy, and J. F. Ganghoffer. Discrete models of woven structures. macroscopic approach. *Composites Part B: Engineering*, 38(4):498–505, 2007.

[223] Abdelhakim Cherouat and Jean Louis Billoët. Mechanical and numerical modelling of composite manufacturing processes deep-drawing and laying-up of thin preimpregnated woven fabrics. *Journal of Materials Processing Technology*, 118(1-3):460–471, 2001.

[224] Abdelhakim Cherouat, Houman Borouchaki, and Jean-Louis Billoët. Geometrical and mechanical draping of composite fabric. *European Journal of Computational Mechanics*, 14:693–707, 2005.

[225] Xiang Li, James Sherwood, Lu Liu, and Julie Chen. A material model for woven commingled glass-polypropylene composite fabrics using a hybrid finite element approach. *International Journal of Materials and Product Technology*, 21(123):59–64, 2004.

[226] Lisa M. Dangora, Cynthia J. Mitchell, James Sherwood, and Jason C. Parker. Deep-drawing forming trials on a cross-ply thermoplastic lamina for helmet preform manufacture. *Journal of Manufacturing Science and Engineering*, 139(3), 2017. 031009.

[227] P. Harrison, M. J. Clifford, A. C. Long, and C. D. Rudd. Constitutive modelling of impregnated continuous fibre reinforced composites micromechanical approach. *Plastics, Rubber and Composites*, 31(2):76–86, 2002.

[228] Philip Harrison. Modelling the forming mechanics of engineering fabrics using a mutually constrained pantographic beam and membrane mesh. *Composites Part A*, 81:145–157, 2016.

[229] M. V. d'Agostino, I. Giorgio, L. Greco, A. Madeo, and P. Boisse. Continuum and discrete models for structures including (quasi-) inextensible elasticae with a view to the design and modeling of composite reinforcements. *International Journal of Solids and Structures*, 59:1–17, 2015.

[230] Gabriele Barbagallo, Angela Madeo, Ismael Azehaf, Ivan Giorgio, Fabrice Morestin, and Philippe Boisse. Bias extension test on an unbalanced woven composite reinforcement: Experiments and modeling via a second-gradient continuum approach. *Journal of Composite Materials*, 51(2):153–170, 2017.

[231] Manuel Ferretti, Angela Madeo, Francesco dell'Isola, and Philippe Boisse. Modeling the onset of shear boundary layers in fibrous composite reinforcements by second-gradient theory. *Zeitschrift für angewandte Mathematik und Physik*, 65(3):587–612, 2014.

[232] David Jauffrès, James A. Sherwood, Corey D. Morris, and Julie Chen. Discrete meso-scopic modeling for the simulation of woven-fabric reinforcement forming. *International Journal of Material Forming*, 3(S2):1205–1216, 2010.

[233] Elena Syerko, Sébastien Comas-Cardona, and Christophe Binetruy. Models of mechanical properties/behavior of dry fibrous materials at various scales in bending and tension: A review. *Composites Part A*, 43(8):1365–1388, 2012.

[234] R. Tavana, S. Shaikhzadeh Najar, M. Tahaye Abadi, and M. Sedighi. Meso/macro-scale finite element model for forming process of woven fabric reinforcements. *Journal of Composite Materials*, 47(17):2075–2085, 2013.

[235] Akira Iwata, Takuya Inoue, Naim Naouar, Philippe Boisse, and Stepan V. Lomov. Meso-macro simulation of the woven fabric local deformation in draping. In *AIP Conference Proceedings of ESAFORM*, 2018. 020012.

[236] Akira Iwata, Takuya Inoue, Naim Naouar, Philippe Boisse, and Stepan V. Lomov. Coupled meso-macro simulation of woven fabric local deformation during draping. *Composites Part A*, 118:267–280, 2019.

[237] D. Wang, N. Naouar, E. Vidal-Salle, and P. Boisse. Longitudinal compression and poisson ratio of fiber yarns in meso-scale finite element modeling of composite reinforcements. *Composites Part B: Engineering*, 141:9–19, 2018.

[238] Philippe Boisse, Alain Gasser, Benjamin Hagege, and Jean-Louis Billoet. Analysis of the mechanical behavior of woven fibrous material using virtual tests at the unit cell level. *Journal of Materials Science*, 40(22):5955–5962, 2005.

[239] Pierre Badel, Emmanuelle Vidal-Sallé, and Philippe Boisse. Computational determination of in-plane shear mechanical behaviour of textile composite reinforcements. *Computational Materials Science*, 40(4):439–448, 2007.

[240] H. Lin, A. C. Long, M. Sherburn, and M. J. Clifford. Modelling of mechanical behaviour for woven fabrics under combined loading. *International Journal of Material Forming*, 1(S1):899–902, 2008.

[241] Yanchao Wang, Weizhao Zhang, Huaqing Ren, Zhengming Huang, Furong Geng, Yongxiang Li, and Zengyu Zhu. An analytical model for the tension-shear coupling of woven fabrics with different weave patterns under large shear deformation. *Applied Sciences*, 10(4):1551, 2020.

[242] Anthony K. Pickett, Gavin Creech, and Patrick de Luca. Simplified and advanced simulation methods for prediction of fabric draping. *European Journal of Computational Mechanics*, 14:677–691, 2005.

281

[243] J. Sirtautas, A. K. Pickett, and P. Lépicier. A mesoscopic model for coupled drape-infusion simulation of biaxial non-crimp fabric. *Composites Part B: Engineering*, 47:48–57, 2013.

[244] A. Margossian, S. Bel, J. M. Balvers, D. Leutz, R. Freitas, and R. Hinterhoelzl. Finite element forming simulation of locally stitched non-crimp fabrics. *Composites Part A*, 61:152–162, 2014.

[245] Patrick Böhler, Frank Härtel, and Peter Middendorf. Identification of forming limits for unidirectional carbon textiles in reality and mesoscopic simulation. *Key Engineering Materials*, 554-557:423–432, 2013.

[246] S. Allaoui, P. Boisse, S. Chatel, N. Hamila, G. Hivet, D. Soulat, and E. Vidal-Salle. Experimental and numerical analyses of textile reinforcement forming of a tetrahedral shape. *Composites Part A*, 42(6):612–622, 2011.

[247] Damien Soulat, Anthony Cheruet, and Philippe Boisse. Simulation of continuous fibre reinforced thermoplastic forming using a shell finite element with transverse stress. *Computers & Structures*, 84(13-14):888–903, 2006.

[248] F. J. Schirmaier, D. Dörr, F. Henning, and L. Kärger. A macroscopic approach to simulate the forming behaviour of stitched unidirectional non-crimp fabrics (UD-NCF). *Composites Part A*, 102:322–335, 2017.

[249] P. Boisse, R. Bai, J. Colmars, N. Hamila, B. Liang, and A. Madeo. The need to use generalized continuum mechanics to model 3D textile composite forming. *Applied Composite Materials*, 25:761–771, 2018.

[250] Renzi Bai, Julien Colmars, Naim Naouar, and Philippe Boisse. A specific 3D shell approach for textile composite reinforcements under large deformation. *Composites Part A*, 139:106135, 2020.

[251] B. Schäfer, D. Dörr, and L. Kärger. Reduced-integrated 8-node hexahedral solid-shell element for the macroscopic forming simulation of continuous fibre-reinforced polymers. In *Proceedings of 23th International Conference on Material Forming, Cottbus (Germany)*, 2020.

[252] Bastian Schäfer, Dominik Dörr, and Luise Kärger. Potential and challenges of a solid-shell element for the macroscopic forming simulation of engineering textiles. *Proceedings of 24th International Conference on Material Forming ESAFORM*, 2021.

[253] Nahiène Hamila and Philippe Boisse. Locking in simulation of composite reinforcement deformations. analysis and treatment. *Composites Part A*, 53:109–117, 2013.

[254] Ted Belytschko. *Nonlinear finite elements for continua and structures*. Wiley, Chichester, 2nd edition, 2014.

[255] Xiaobo Yu, Bruce Cartwright, Damian McGuckin, Lin Ye, and Yiu-Wing Mai. Intra-ply shear locking in finite element analyses of woven fabric forming processes. *Composites Part A*, 37(5):790–803, 2006.

[256] R.H.W. ten Thije and R. Akkerman. Solutions to intra-ply shear locking in finite element analyses of fibre reinforced materials. *Composites Part A*, 39(7):1167–1176, 2008.

[257] Hyun-Gyu Kim. A comparative study of hyperelastic and hypoelastic material models with constant elastic moduli for large deformation problems. *Acta Mechanica*, 227(5):1351–1362, 2016.

[258] Thomas J. R. Hughes and James Winget. Finite rotation effects in numerical integration of rate constitutive equations arising in large-deformation analysis. *International Journal for Numerical Methods in Engineering*, 15(12):1862–1867, 1980.

[259] W. Lee, J. Cao, P. Badel, and P. Boisse. Non-orthogonal constitutive model for woven composites incorporating tensile effect on shear behavior. *International Journal of Material Forming*, 1(1):891–894, 2008.

[260] Pierre Badel, Emmanuelle Vidal-Sallé, and Philippe Boisse. Large deformation analysis of fibrous materials using rate constitutive equations. *Computers & Structures*, 86(11-12):1164–1175, 2008.

[261] M. A. Khan, T. Mabrouki, and P. Boisse. Numerical and experimental forming analysis of woven composites with double dome benchmark. *International Journal of Material Forming*, 2(S1):201–204, 2009.

[262] Martín Machado, Luca Murenu, Michael Fischlschweiger, and Zoltan Major. Analysis of the thermomechanical shear behaviour of woven-reinforced thermoplastic-matrix composites during forming. *Composites Part A*, 86:39–48, 2016.

[263] Gerhard A. Holzapfel. *Nonlinear solid mechanics: A continuum approach for engineering*. Wiley, Chichester, 2010.

[264] R.H.W. ten Thije, R. Akkerman, and J. Huétink. Large deformation simulation of anisotropic material using an updated lagrangian finite element method. *Computer Methods in Applied Mechanics and Engineering*, 196(33-34):3141–3150, 2007.

[265] Christopher W. Macosko. *Rheology: Principles, measurements, and applications*. Advances in interfacial engineering series. VCH, New York, 1994.

[266] Y. Aimène, E. Vidal-Sallé, B. Hagège, F. Sidoroff, and P. Boisse. A hyperelastic approach for composite reinforcement large deformation analysis. *Journal of Composite Materials*, 44(1):5–26, 2009.

[267] X. Q. Peng, Z. Y. Guo, Zia-Ur-Rehman, and P. Harrison. A simple anisotropic fiber reinforced hyperelastic constitutive model for woven composite fabrics. *International Journal of Material Forming*, 3(S1):723–726, 2010.

[268] Samia Dridi, Abdelwaheb Dogui, and Philipp Boisse. Finite element analysis of bias extension test using an orthotropic hyperelastic continuum model for woven fabric. *Journal of the Textile Institute*, 102(9):781–789, 2011.

[269] Youkun Gong, Dongxiu Yan, Yuan Yao, Ran Wei, Hongling Hu, Peng Xu, and Xiongqi Peng. An anisotropic hyperelastic constitutive model with tension–shear coupling for woven composite reinforcements. *International Journal of Applied Mechanics*, 09(06):1750083, 2017.

[270] Xiongqi Peng, Zaoyang Guo, Tongliang Du, and Woong-Ryeol Yu. A simple anisotropic hyperelastic constitutive model for textile fabrics with application to forming simulation. *Composites Part B: Engineering*, 52:275–281, 2013.

[271] Youkun Gong, Xiongqi Peng, Yuan Yao, and Zaoyang Guo. An anisotropic hyperelastic constitutive model for thermoplastic woven composite prepregs. *Composites Science and Technology*, 128:17–24, 2016.

[272] S. Mathieu, N. Hamila, F. Dupé, C. Descamps, and P. Boisse. Stability of 3D textile composite reinforcement simulations: Solutions to spurious transverse modes. *Applied Composite Materials*, 23(4):739–760, 2016.

[273] A. Charmetant, J. G. Orliac, E. Vidal-Sallé, and P. Boisse. Hyperelastic model for large deformation analyses of 3D interlock composite preforms. *Composites Science and Technology*, 72(12):1352–1360, 2012.

[274] Y. Denis, E. Guzman-Maldonado, N. Hamila, J. Colmars, and F. Morestin. A dissipative constitutive model for woven composite fabric under large strain. *Composites Part A*, 105:165–179, 2018.

[275] Angela Madeo, Manuel Ferretti, Francesco dell'Isola, and Philippe Boisse. Thick fibrous composite reinforcements behave as special second-gradient materials: Three-point bending of 3D interlocks. *Zeitschrift für angewandte Mathematik und Physik*, 66(4):2041–2060, 2015.

[276] Gabriele Barbagallo, Angela Madeo, Fabrice Morestin, and Philippe Boisse. Modelling the deep drawing of a 3D woven fabric with a second gradient model. *Mathematics and Mechanics of Solids*, 22(11):2165–2179, 2016.

[277] Nahiène Hamila and Philippe Boisse. Simulations of textile composite reinforcement draping using a new semi-discrete three node finite element. *Composites Part B: Engineering*, 39(6):999–1010, 2008.

[278] N. Hamila, P. Boisse, and S. Chatel. Semi-discrete shell finite elements for textile composite forming simulation. *International Journal of Material Forming*, 2(1):169–172, 2009.

[279] P. Boisse, M. Borr, K. Buet, and A. Cherouat. Finite element simulations of textile composite forming including the biaxial fabric behaviour. *Composites Part B: Engineering*, 28(4):453–464, 1997.

[280] Peng Wang, Xavier Legrand, Philippe Boisse, Nahiène Hamila, and Damien Soulat. Experimental and numerical analyses of manufacturing process of a composite square box part: Comparison between textile reinforcement forming and surface 3D weaving. *Composites Part B: Engineering*, 78:26–34, 2015.

[281] Peng Wang, Nahiène Hamila, and Philippe Boisse. Thermoforming simulation of multilayer composites with continuous fibres and thermoplastic matrix. *Composites Part B: Engineering*, 52:127–136, 2013.

[282] Mi Ae Choi, Mi Hye Lee, Jaeeon Chang, and Seung Jong Lee. Permeability modeling of fibrous media in composite processing. *Applied Mechanics Reviews*, 79(2-3):585–598, 1998.

[283] Pavel B. Nedanov and Suresh G. Advani. Numerical computation of the fiber preform permeability tensor by the homogenization method. *Polymer Composites*, 23(5):758–770, 2002.

[284] M. V. Bruschke and S. G. Advani. Flow of generalized newtonian fluids across a periodic array of cylinders. *Journal of Rheology*, 37(3):479–498, 1993.

[285] K. Yazdchi, S. Srivastava, and S. Luding. Micro–macro relations for flow through random arrays of cylinders. *Composites Part A*, 43(11):2007–2020, 2012.

[286] K. Andriamananjara, L. Chevalier, N. Moulin, J. Bruchon, P.-J. Liotier, and S. Drapier. Numerical approach for modelling across scales infusion-based processing of aircraft primary structures. In *AIP Conference Proceedings 1896:030011*, 2017.

[287] Sabine Bschorer. *Technische Strömungslehre: Lehr- und Übungsbuch*. Lehrbuch. Springer Vieweg, Wiesbaden, 11., überarbeitete und erweiterte auflage edition, 2018.

[288] Julian Seuffert, Luise Kärger, and Frank Henning. Simulation of the influence of embedded inserts on the RTM filling behavior considering local fiber structure. *Key Engineering Materials*, 742:681–688, 2017.

285

[289] M. V. Bruschke and S. G. Advani. A finite element/control volume approach to mold filling in anisotropic porous media. *Polymer Composites*, 11(6):398–405, 1990.

[290] M. V. Bruschke and S. G. Advani. A numerical approach to model non-isothermal viscous flow through fibrous media with free surfaces. *International Journal for Numerical Methods in Fluids*, 19(7):575–603, 1994.

[291] Mark Lin, H. Thomas Hahn, and Hoon Huh. A finite element simulation of resin transfer molding based on partial nodal saturation and implicit time integration. *Composites Part A*, 29(5-6):541–550, 1998.

[292] Hua Tan and Krishna M. Pillai. Multiscale modeling of unsaturated flow of dual-scale fiber preform in liquid composite molding II: Non-isothermal flows. *Composites Part A*, 43(1):14–28, 2012.

[293] P. Cardiff, Ž. Tuković, P. de Jaeger, M. Clancy, and A. Ivanković. A lagrangian cell-centred finite volume method for metal forming simulation. *International Journal for Numerical Methods in Engineering*, 109(13):1777–1803, 2017.

[294] Justin Merotte, Pavel Simacek, and Suresh G. Advani. Resin flow analysis with fiber preform deformation in through thickness direction during compression resin transfer molding. *Composites Part A*, 41(7):881–887, 2010.

[295] Thomas J.R. Hughes, Arif Masud, and Jing Wan. A stabilized mixed discontinuous galerkin method for darcy flow. *Computer Methods in Applied Mechanics and Engineering*, 195(25-28):3347–3381, 2006.

[296] Pierre Celle, Sylvain Drapier, and Jean-Michel Bergheau. Numerical aspects of fluid infusion inside a compressible porous medium undergoing large strains. *Revue européenne de mécanique numérique*, 17(5-6-7):819–827, 2008.

[297] Abhishek Gupta and Piaras Kelly. Optimal galerkin finite element methods for non-isothermal liquid composite moulding process simulations. *International Journal of Heat and Mass Transfer*, 64:609–622, 2013.

[298] Xuan-tan Pham and Franois Trochu. Simulation of compression resin transfer molding to manufacture thin composite shells. *Polymer Composites*, 20(3):436–459, 1999.

[299] Pierre Celle, Sylvain Drapier, and Jean-Michel Bergheau. Numerical modelling of liquid infusion into fibrous media undergoing compaction. *European Journal of Mechanics - A/Solids*, 27(4):647–661, 2008.

[300] N. Meyer, L. Schöttl, L. Bretz, A. N. Hrymak, and L. Kärger. Direct bundle simulation approach for the compression molding process of sheet molding compound. *Composites Part A*, 132:105809, 2020.

[301] C. Taylor and P. Hood. A numerical solution of the navier-stokes equations using the finite element technique. *Computers & Fluids*, 1(1):73–100, 1973.

[302] D. N. Arnold, F. Brezzi, and M. Fortin. A stable finite element for the stokes equations. *Calcolo*, 21(4):337–344, 1984.

[303] Antti Hannukainen, Mika Juntunen, and Rolf Stenberg. Computations with finite element methods for the brinkman problem. *Computational Geosciences*, 15(1):155–166, 2011.

[304] S. C. Joshi, Y. C. Lam, and X.-L. Liu. Mass conservation in numerical simulation of resin flow. *Composites Part A*, 31(10):1061–1068, 2000.

[305] Edu Ruiz, V. Achim, and F. Trochu. Coupled non-conforming finite element and finite difference approximation based on laminate extrapolation to simulate liquid composite molding processes. part i: Isothermal flow. *Science and Engineering of Composite Materials*, 14(2):85–112, 2007.

[306] K. M. Pillai, C. L. Tucker, and F. R. Phelan. Numerical simulation of injection/compression liquid composite molding. part 2: Preform compression. *Composites Part A*, 32(2):207–220, 2001.

[307] A. Dereims, S. Drapier, J.-M. Bergheau, and P. de Luca. 3D robust iterative coupling of stokes, darcy and solid mechanics for low permeability media undergoing finite strains. *Finite Elements in Analysis and Design*, 94:1–15, 2015.

[308] K. M. Pillai and S. G. Advani. A model for unsaturated flow in woven fiber preforms during mold filling in resin transfer molding. *Journal of Composite Materials*, 32(19):1753–1783, 1998.

[309] Onno Ubbink. *Numerical prediction of two fluid systems with sharp interfaces*. Doctoral thesis, Imperial College London (University of London), 1997.

[310] A. Albadawi, D. B. Donoghue, A. J. Robinson, D. B. Murray, and Y.M.C. Delauré. Influence of surface tension implementation in volume of fluid and coupled volume of fluid with level set methods for bubble growth and detachment. *International Journal of Multiphase Flow*, 53:11–28, 2013.

[311] I. Chakraborty, G. Biswas, and P. S. Ghoshdastidar. A coupled level-set and volume-of-fluid method for the buoyant rise of gas bubbles in liquids. *International Journal of Heat and Mass Transfer*, 58(1-2):240–259, 2013.

[312] Matthias Ehrhardt, editor. *Progress in Computational Physics: Vol. 2: Coupled Fluid Flow in Energy, Biology and Environmental Research*. Benthma science publishers, Oak Park, 2012.

[313] Akankshya Majhi, Tarun Kumar Pardhi, and Abhijit P. Deshpande. Analysis of squeeze flow of fluids between solid and porous surfaces. *International Journal of Multiphase Flow*, 68:93–99, 2015.

[314] Thérèse Levy and Enrique Sanchez-Palencia. On boundary conditions for fluid flow in porous media. *International Journal of Engineering Science*, 13(11):923–940, 1975.

[315] Gordon S. Beavers and Daniel D. Joseph. Boundary conditions at a naturally permeable wall. *Journal of Fluid Mechanics*, 30(1):197–207, 1967.

[316] P. G. Saffman. On the boundary condition at the surface of a porous medium. *Studies in Applied Mathematics*, 50(2):93–101, 1971.

[317] M. Sahraoui and M. Kaviany. Slip and no-slip velocity boundary conditions at interface of porous, plain media. *International Journal of Heat and Mass Transfer*, 35(4):927–943, 1992.

[318] M. Le Bars and M. Grae Worster. Interfacial conditions between a pure fluid and a porous medium: implications for binary alloy solidification. *Journal of Fluid Mechanics*, 550:149—-173, 2006.

[319] G. Pacquaut, J. Bruchon, N. Moulin, and S. Drapier. Combining a level-set method and a mixed stabilized P1/P1 formulation for coupling Stokes-Darcy flows. *International Journal for Numerical Methods in Fluids*, 69(2):459–480, 2012.

[320] Jan Engmann, Colin Servais, and Adam S. Burbidge. Squeeze flow theory and applications to rheometry: A review. *Journal of Non-Newtonian Fluid Mechanics*, 132(1):1–27, 2005.

[321] Christopher W. MacMinn, Eric R. Dufresne, and John S. Wettlaufer. Large deformations of a soft porous material. *Physical Review Applied*, 5(4), 2016. 044020.

[322] C. Tucker and R. Dessenberger. Governing equations for flow and heat transfer in stationary fiber beds. *Flow and Rheology in Polymer Composites Manufacturing*, 3:237–257, 1994.

[323] Adrian M. Murtagh and Patrick J. Mallon. Chapter 5: Characterisation of shearing and frictional behaviour during sheet forming. In D. Bhattacharyya, editor, *Composite Materials Series : Composite Sheet Forming*, volume 11, pages 163–216. Elsevier, 1997.

[324] Fabian Albrecht, Clemens Zimmerling, Christian Poppe, Luise Kärger, and Frank Henning. Development of a modular draping test bench for analysis of infiltrated woven fabrics in wet compression molding. *Key Engineering Materials*, 809:35–40, 2019.

[325] Christian Poppe, Constantin Krauß, Fabian Albrecht, and Kärger Luise. Towards numerical prediction of flow-induced fiber displacements during wet compression molding (WCM). *Proceedings of 24th International Conference on Material Forming ESAFORM*, 2021.

[326] P. Boisse, N. Hamila, E. Guzman-Maldonado, A. Madeo, G. Hivet, and F. dell'Isola. The bias-extension test for the analysis of in-plane shear properties of textile composite reinforcements and prepregs: A review. *International Journal of Material Forming*, 78(5):26, 2016.

[327] G. Hivet and A. V. Duong. A contribution to the analysis of the intrinsic shear behavior of fabrics. *Journal of Composite Materials*, 45(6):695–716, 2010.

[328] Dominik Dörr, Fabian J. Schirmaier, Frank Henning, and Luise Kärger. On the relevance of modeling viscoelastic bending behavior in finite element forming simulation of continuously fiber reinforced thermoplastics. In *AIP Conference Proceedings 1896*, page 030003. ESAFORM, 2017.

[329] Christian Poppe, Dominik Dörr, Frank Henning, and Luise Kärger. A 2D modeling approach for fluid propagation during FE-forming simulation of continuously reinforced composites in wet compression moulding. In *AIP Conference Proceedings 1960:020022*, Palermo, 2018. ESAFORM.

[330] Steffen Ropers, Marton Kardos, and Tim A. Osswald. A thermo-viscoelastic approach for the characterization and modeling of the bending behavior of thermoplastic composites. *Composites Part A*, 90:22–32, 2016.

[331] J. Cao, R. Akkerman, and et. Characterization of mechanical behavior of woven fabrics: Experimental methods and benchmark results. *Composites Part A*, 39(6):1037–1053, 2008.

[332] SciPy.org. *Optimization and root finding*, 2008. https://docs.scipy.org/doc/scipy.html, Accessed: 2021-05-27.

[333] Simulia. *Contact formulation for general contact in Abaqus/Explicit, Abaqus user guide*, 2020. http://fast-lt-vm02.fast.kit.edu:2180/v2020/English.html, Accessed: 2021-01-29.

[334] Dominik Dörr, Tobias Joppich, Fabian Schirmaier, Tobias Mosthaf, Luise Kärger, and Frank Henning. A method for validation of finite element forming simulation on basis of a pointwise comparison of distance and curvature. In *AIP Conference Proceedings 1769:170011*, Nantes, France, 2016. ESAFORM.

[335] Alexander Konyukhov and Karl Schweizerhof. *Computational Contact Mechanics: Geometrically Exact Theory for Arbitrary Shaped Bodies*, volume 67 of *Lecture Notes in Applied and Computational Mechanics*. Springer, Berlin, Heidelberg, 2013.

[336] Christian Poppe, Dominik Dörr, Fabian Kraus, and Luise Kärger. Experimental and numerical investigation of the contact behavior during FE forming simulation of continuously reinforced composites in wet compression molding. In *22nd ESAFORM*, AIP Conference Proceedings, Vitoria-Gasteiz, 2019. 020002.

[337] R.H.W. ten Thije and R. Akkerman. A multi-layer triangular membrane finite element for the forming simulation of laminated composites. *Composites Part A*, 40(6-7):739–753, 2009.

[338] Fabian Kraus. *Experimentelle Charakterisierung und numerische Modellierung des Kontaktverhaltens infiltrierter CFK-Halbzeuge im Rahmen der Nasspresstechnologie mittels FEM*. Bachelor thesis (in german), Karlsruhe Institute for Technology (KIT), Institute for Vehicle System Technology (FAST), Lightweight Technology, 2018.

[339] Freia Lorenz. *Experimentelle Untersuchung des Kontaktverhaltens infiltrierter CFK-Halbzeuge im Rahmen der Nasspresstechnologie mittels FEM*. Bachelor thesis (in german), Karlsruhe Institute for Technology (KIT), Institute for Vehicle System Technology (FAST), Lightweight Technology and Fraunhofer ICT, Pfinztal, Germany, 2017.

[340] Sergio A. Rota-Chamizo. *Konstruktion und simulative Prozessauslegung eines Technologiedemonstrators für das Nasspressen endlosfaserverstärkter Kunststoffe*. Bachelor thesis (in german), Karlsruhe Institute for Technology (KIT), Institute for Vehicle System Technology (FAST), Lightweight Technology, 2018.

[341] Henrik Werner, Florian Schäfer, Frank Henning, and Luise Kärger. Material modelling of fabric deformation in forming simulation of fiber-metal laminates – A review on modelling fabric coupling mechanisms. *Proceedings of 24th International Conference on Material Forming ESAFORM*, 2021.

[342] M. Komeili and A. S. Milani. On effect of shear-tension coupling in forming simulation of woven fabric reinforcements. *Composites Part B: Engineering*, 99:17–29, 2016.

[343] Christian Poppe, Fabian Albrecht, Constantin Krauß, and Luise Kärger. A 3D Modelling Approach for Fluid Progression during Process Simulation of Wet Compression Moulding – Motivation and Approach. *Procedia Manufacturing*, 47:85–92, 2020. 23rd International Conference on Material Forming.

[344] Baoxing Chen, Eric J. Lang, and Tsu-Wei Chou. Experimental and theoretical studies of fabric compaction behavior in resin transfer molding. *Materials Science and Engineering: A*, 317(1):188–196, 2001.

[345] Siegfried Galkin, Eckart Kunze, Luise Kärger, Robert Böhm, and Maik Gude. Experimental and numerical determination of the local fiber volume content of unidirectional non-crimp fabrics with forming effects. *Journal of Composites Science*, 3(1):19, 2019.

[346] Vladimir Sauerwein. *Entwicklung einer Methodik zur Charakterisierung der oberflächlichen makroskopischen Rovingorientierung bei unidirectional endlosfaserverstärkten Verbundwerkstoffen (UD-NCF)*. Master thesis (in german), Karlsruhe Institute for Technology (KIT), Institute for Vehicle System Technology (FAST), Lightweight Technology, and Fraunhofer ICT, Pfinztal, Germany, 2019.

[347] Luise Kärger, Siegfried Galkin, Kunze Eckhard, Maik Gude, and Bastian Schäfer. Prediction of forming effects in UD-NCF by macroscopic forming simulation – capabilities and limitations. *Proceedings of 24th International Conference on Material Forming ESAFORM*, 2021.

[348] Tobias Rosenkranz. *Charakterisierung und Modellierung des Biegeverhaltens infilitrierter, textiler CFK-Halbzeuge im Rahmen der Nasspresstechnologie*. Master thesis (in german), Karlsruhe Institute for Technology (KIT), Institute for Vehicle System Technology (FAST), Lightweight Technology, 2018.

A.4   Publication list

Journal publications

- C. Poppe, D. Dörr, F. Henning, L. Kärger: Experimental and numerical investigation of the shear behaviour of infiltrated woven fabrics, *Composite Part A*, 114:327-337, 2018.

- C. Poppe, T. Rosenkranz, D. Dörr, L. Kärger: Comparative experimental and numerical analysis of bending behaviour of dry and low viscous infiltrated woven fabrics, *Composite Part A*, 124:105466, 2019.

- C. Poppe, F. Albrecht, C. Krauß, L. Kärger: A 3D process simulation model for wet compression moulding, *Composites Part A*, 145:106379, 2021

Co-authored journal publications

- C. Zimmerling, C. Poppe, O. Stein, L. Kärger: Optimisation of Manufacturing Process Parameters for Variable Component Geometries using Reinforcement Learning, *Materials and Design*, 214:110423, 2022

- F. Albrecht, C. Poppe, T. Tiemann, V. Sauerwein, P. Rosenberg, F. Henning: Flow-induced fiber displacement in non-bindered UD-NCF during Wet Compression Molding – Analysis and implications for process control, *Composite Science*, 109574, 2022

Conference contributions | With proceedings (peer-reviewed)

- C. Poppe, F. Albrecht, C. Krauß L. Kärger, Towards numerical prediction of flow-induced fiber displacements during wet compression molding (WCM), Paper presented at ESAFORM 2021 – 24th International Conference on Material Forming, 10.25518/esaform21.1938, 2021

- C. Poppe, F. Albrecht, C. Krauß, L. Kärger: A 3D Modelling Approach for Fluid Progression during Process Simulation of Wet Compression Moulding – Motivation & Approach. *Procedia Manufacturing*, 47:85-92, 2020.

- C. Poppe, D. Dörr, F. Kraus, L. Kärger: Experimental and numerical investigation of the contact behaviour during FE forming simulation of continuously reinforced composites in wet compression moulding, *AIP Conference Proceedings* 2113:020002, ESAFORM, Spain, 2019.

- C. Poppe, D. Dörr, F. Henning, L. Kärger: A 2D modeling approach for fluid propagation during FE-forming simulation of continuously reinforced composites in wet compression moulding, *AIP Conference Proceedings* 1960:020022, ESAFORM 2018, Palermo, 2018.

- C. Poppe, D. Dörr, T. Joppich, L. Kärger, F. Henning: Modelling and Validation of Gripper Induced Membrane Forces in Finite Element Forming Simulation of Continuously Reinforced Composites, *AIP Conference Proceedings* 1896:030002, ESAFORM 2017, Dublin, 2017.

Conference contributions | without proceedings

- C. Poppe, D. Dörr, L. Kärger: Systematic approach for the development of an FE-based process simulation framework for wet compression moulding of continuously reinforced composites. *Proceedings EUROMECH Colloquium 602 – Composite manufacturing processes. Analyses, modelling and simulations*, Lyon, France, 2019.

- C. Poppe, J. Fial, L. Kärger, S. Carosella, C. Zimmerling, F. Albrecht, M. Darskovic, M. Engelfried, P. Middendorf, F. : Zeit- und kosteneffiziente Prozess- und Produktentwicklung für den Hochleistungs-Faserverbund-Leichtbau mittels Nasspresstechnologie (in german), *4. Technologietag Hybrider Leichtbau*, Stuttgart, 2017.

- C. T. Poppe, C. Zimmerling, F. Albrecht, J. Hüttl, J. Fial, M. Engelfried: Zeit- und kosteneffiziente Prozess- und Produktentwicklung für den Hochleistungs-Faserverbundleichtbau im Rahmen der Nasspresstechnologie (in german), *Marktplatz Leichtbau*, Ludwigsburg, Germany, 31.01.2017.

Co-authored conference contributions | With proceedings (peer-reviewed)

- L. Kärger, S. Galkin, D. Dörr, C. Poppe: Capabilities of Macroscopic Forming Simulation for Large-Scale Forming Processes of Dry and Impregnated Textiles. *Procedia Manufacturing 2020*; 47:140-147, 2020.

- C. Zimmerling, C. Poppe, L. Kärger: Estimating Optimum Process Parameters in Textile Draping of Variable Part Geometries - A Reinforcement Learning Approach. *Procedia Manufacturing 2020*; 47:847–854, 2020.

- H.O. Werner, C. Poppe, F. Henning, L. Kärger: Material Modeling in Forming Simulation of Three-Dimensional Fiber-Metal-Laminates – A Parametric Study. *Procedia Manufacturing 2020*; 47:154–61.

- F. Albrecht, C. Zimmerling, C. Poppe, L. Kärger, F. Henning: Development of a Modular Draping Test Bench for Analysis of Infiltrated Woven Fabrics in Wet Compression Molding, *Key Engineering Materials* 80:35-40, Proceeding of 22nd Symposium on Composites, 2019.

- D. Dörr, M. Faisst, T. Joppich, C. Poppe, F. Henning, L. Kärger: Modelling Approach for Anisotropic Inter-Ply Slippage in Finite Element Forming Simulation of Thermoplastic UD-Tapes, *AIP Conference Proceedings* 1960: 020005, ESAFORM 2018, Palermo, 2018.

- J. Hüttl, F. Albrecht, C. Poppe, F. Lorzenz, B. Thoma, L. Kärger, P. Middendorf, F. Henning: Investigations on friction behavior and forming simulation of plain woven fabrics for wet compression molding. *Proceedings of SAMPE Europe* Conference, Stuttgart, 2017.

Co-authored conference contributions | without proceedings

- L. Kärger, D. Dörr, C. Poppe, J. Seuffert, A. Bernath, S. Galkin, C. Zimmerling, F. Henning: Continuous Process Simulation for Continuous Fiber

Reinforced Composites, *International VDI Conference* - Simulation in Automotive Lightweight Engineering (2018), Amsterdam, Niederlande, 25.-26.04.2018.

- D. Dörr, C. Poppe, C. Zimmerling, C. Krauß, B. Schäfer, F. Henning, L. Kärger: Advanced Macroscopic Modelling Approaches for FE Composite Forming Simulation Using Abaqus, SIMULIA *Regional User Meeting* , Hanau, Deutschland, KITopen-ID: 1000099359, 04.12.2018

Other

- C. Poppe, F. Albrecht, C. Zimmerling, J. Fial, M. Engelfried, M. Draskovic, P. Middendorf, F. Henning, L. Kärger: Prozessanalyse und -simulation der Nasspresstechnologie, Abschlusskolloquium der Forschungsbrücke, online presentation, 03.12.2020

- C. Zimmerling, C. Poppe, L. Kärger: Virtuelle Produktentwicklung mittels Simulationsmethoden und KI. *Lightweight Design* 6/2019: 14-19, ISSN (Online) 2192-8738, 2019.

- C. Zimmerling, C. Poppe, L. Kärger: Virtual Product Development Using Simulation Methods and AI. *Lightweight Design worldwide* 12/2019: 14-19, ISSN (Online) 2510-2877, 2019.

Karlsruher Schriftenreihe Fahrzeugsystemtechnik
FAST Institut für Fahrzeugsystemtechnik
(ISSN 1869-6058)

Eine vollständige Übersicht der Bände finden Sie im Verlagsshop

Die Bände sind unter www.ksp.kit.edu als PDF frei verfügbar oder als Druckausgabe bestellbar.

Karlsruher Schriftenreihe
Fahrzeugsystemtechnik

FAST
Institut für
Fahrzeugsystemtechnik

Interdisciplinary development approaches for system-efficient lightweight design unite a comprehensive understanding of materials, processes and methods. This applies particularly to continuous fibre-reinforced plastics (CoFRPs), which offer high weight-specific material properties and enable load path-optimised designs. This work is dedicated to understanding and modelling Wet Compression Moulding (WCM) to facilitate large-volume production of CoFRP structural components. WCM combines simultaneous infiltration and draping during processing, allowing for comparatively low cavity pressures (< 20 bar) and short cycle times (< 3 min.). This work covers a systematic analysis of the relevant physical process mechanisms, including modified and novel test benches for infiltrated material analysis. Moreover, a monolithic fully-coupled simulation approach for combined textile forming and resin infiltration is proposed, verified and validated. Collectively, the results support a time- and cost-efficient process and product design at an early stage. The outcomes underline the applicability and validity of the developed methods. However, they likewise indicate the scope for further development.